SCUOLA DI DOTTORATO

UNIVERSITÀ DEGLI STUDI DI MILANO-BICOCCA

Department of Biotechnologies and Biosciences

PhD program on Converging Technologies for Biomolecular Systems (TeCSBi)

XXXIII cycle

# Cellular senescence and failure in human and animal cardiac myocytes

Surname Lodrini

Name Alessandra Maria

Registration n. 753505

Tutor Prof. Marcella Rocchetti

Supervisor Dr. Lucio Barile

Coordinator Prof. Paola Branduardi

**Academic Year 2019/2020**

# Contents

# Part 1

# Cardiac Aging

## 1.1 Aging and cardiovascular diseases

Cardiovascular diseases (CVDs) are one of the main causes of mortality in the EU Member States (**Table 1**) and represent a substantial socioeconomic burden. In the year 2016 there were 1.83 million deaths resulting from CVDs in the EU-28, equivalent to 35.7% of all deaths. This percentage is considerably higher than the second listed cause of death among non-communicable diseases, cancer (malignant neoplasms; 26.0%).

The risk of developing a CVD, including stroke, hypertension, ischaemic heart disease and heart failure, largely (75.0 – 90.0%) depends on the presence of traditional risk factors (**Fig 1**). Advanced age is a reported traditional risk factor, and it is generally categorized as non-modifiable for obvious reasons [Dhingra and Vasan 2012]. Aging lowers the threshold for developing CVDs by promoting adverse remodelling in cardiac structure and function, presumably related to a decline in the cardioprotective molecular mechanisms.

The average lifespan of the human population is globally increasing, most likely because of declining fertility and increasing longevity. It has been projected that by 2035 one in every four individuals will be 65 years or older [Steenman and Lande 2017]. Therefore, it is likely that the predicted growth of the elderly population will result in an increased prevalence of CVDs.

| | Deaths (number) | Share of all deaths (%) | Standardized death rates (per 100 000 inhabitants) | | |
|---|---|---|---|---|---|
| | | | Total | < 65 yrs | ≥ 65 yrs |
| EU-28 | 1 832 835 | 35.7 | 358.3 | 43.9 | 1 656.4 |
| Belgium | 30 175 | 28.1 | 268.8 | 29.1 | 1 258.6 |
| Bulgaria | 70 509 | 66.2 | 1 094.9 | 166.3 | 4 928.3 |
| Czechia | 47 700 | 44.4 | 569.9 | 57.9 | 2 683.7 |
| Denmark | 12 569 | 23.9 | 248.3 | 28.4 | 1 155.9 |
| Germany | 339 887 | 37.2 | 381.1 | 37.8 | 1 798.6 |
| Estonia | 8 019 | 52.4 | 643.0 | 83.0 | 2 954.7 |
| Ireland | 9 218 | 30.0 | 309.0 | 31.5 | 1 454.6 |
| Greece | 43 917 | 37.1 | 351.5 | 50.6 | 1 593.7 |
| Spain | 118 824 | 29.1 | 237.3 | 27.1 | 1 105.2 |
| France | 143 967 | 24.3 | 197.2 | 24.1 | 912.1 |
| Croatia | 23 221 | 45.0 | 630.7 | 64.7 | 2 967.3 |
| Italy | 220 749 | 35.9 | 296.2 | 25.1 | 1 415.3 |
| Cyprus | 1 802 | 32.9 | 331.6 | 36.1 | 1 551.4 |
| Latvia | 15 876 | 56.1 | 848.5 | 139.2 | 3 776.5 |
| Lithuania | 23 056 | 56.7 | 845.7 | 122.7 | 3 830.4 |
| Luxembourg | 1 263 | 31.8 | 298.2 | 24.2 | 1 429.1 |
| Hungary | 62 727 | 49.4 | 737.5 | 103.9 | 3 353.2 |
| Malta | 1 209 | 36.2 | 332.7 | 33.6 | 1 567.8 |
| Netherlands | 38 954 | 26.3 | 264.4 | 24.6 | 1 254.1 |
| Austria | 33 370 | 42.0 | 397.4 | 30.7 | 1 911.2 |
| Poland | 168 280 | 43.3 | 552.7 | 76.1 | 2 520.1 |
| Portugal | 32 685 | 29.5 | 296.7 | 32.9 | 1 385.9 |
| Romania | 148 619 | 58.2 | 898.9 | 114.4 | 4 137.7 |
| Slovenia | 7 952 | 40.5 | 431.7 | 32.4 | 2 080.0 |
| Slovakia | 23 038 | 44.1 | 620.2 | 80.8 | 2 846.9 |
| Finland | 19 687 | 36.6 | 360.2 | 40.6 | 1 679.4 |
| Sweden | 31 674 | 35.0 | 318.6 | 27.8 | 1 518.9 |
| United Kingdom | 153 888 | 25.6 | 253.3 | 37.4 | 1 144.6 |

**Table 1.** Deaths resulting from CVDs in the EU-28 for the year 2016. [According to Eurostat, online data codes: hlth_cd_aro and hlth_cd_asdr2].

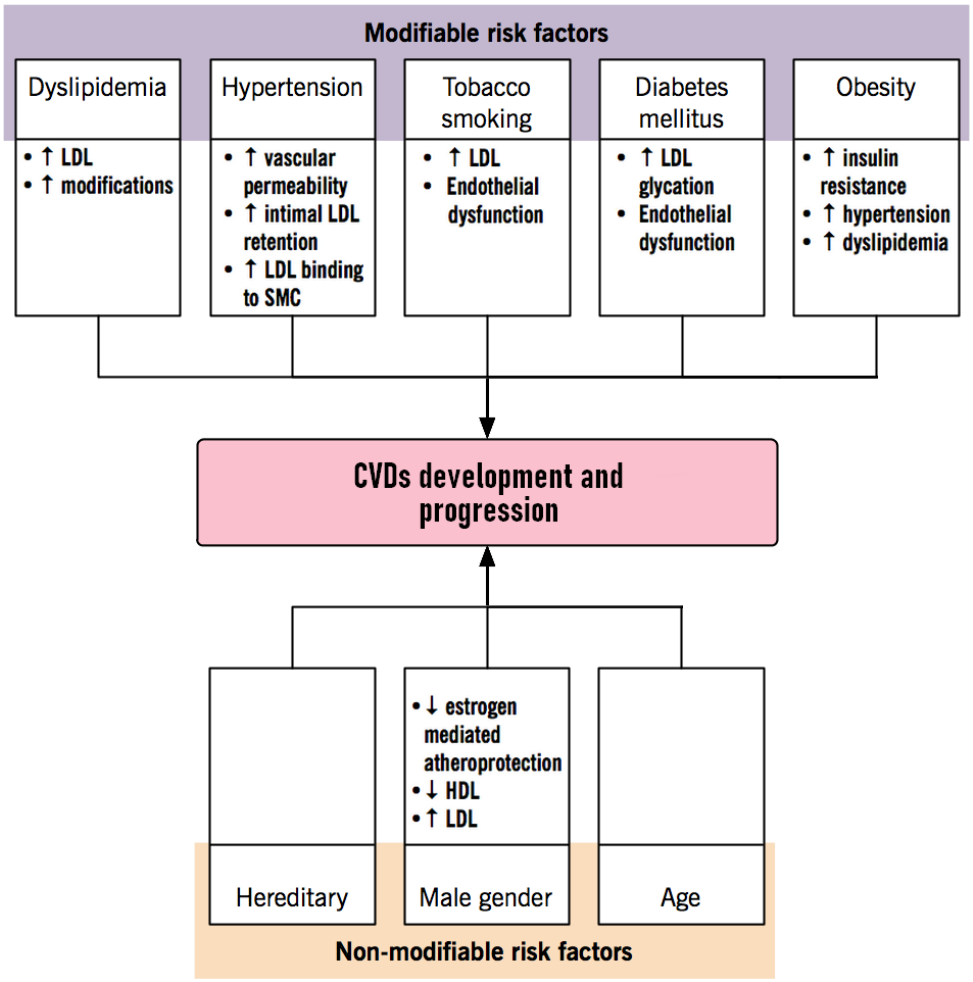


**Figure 1.** Risk factors for development and progression of CVDs. [Modified from Yelle's 'Artherosclerosis', *McMaster Pathophysiology Review.*]

## 1.2 Biological theories of aging

*Why do we age?* It is known that biological aging is the progressive manifestation of accumulated damage at a cellular level, but it is still uncertain which is the primary cause that triggers this phenomenon in living organisms. Since natural selection favours survival of the fittest, this raises the question of why natural selection did not eliminate a deleterious process like aging. The scientific community has made a number of educated guesses in order to explain this paradox. Theories about what originates aging usually fall into two categories, genetic or stochastic [Lipsky and King 2015]. Genetic (also known as 'programmed' or 'evolutionary') theories, propose that organisms have an internal clock that programs longevity, and aging is genetically determined; these theories include accumulated mutation theory, antagonistic pleiotropy, and disposable soma theory. Stochastic (or 'damage') theories propose that chance error and the accumulation of damage over time cause aging; these theories include wear-and-tear, DNA damage and repair hypothesis, cross-linking theory, rate of living theory, and free radical theory.

### 1.2.1 Genetic theories

The accumulated mutation theory proposes that aging results from accumulation of cellular damage accompanied by damage to genes coding for 'repair' functions (e.g. DNA damage response, autophagy) [Turan et al. 2019]. Since living beyond age of reproduction provides only a limited evolutionary advantage, natural selection eliminates mutations that could be detrimental early in life but exerts little evolutionary pressure on mutations causing harmful effects later in life.

The antagonistic pleiotropy theory states that there are genes with more than one effect and that some of their functions might benefit early survival but be harmful at an older age [Williams 1957]. For example, genes enhancing oxidative processes may offer a survival advantage in youth by generating greater muscle effectiveness, while generating reactive oxygen species. Antagonistic pleiotropy may also underpin the 'Hayflick limit' of cell division. Hayflick was the first to report

that human fibroblasts in culture stop dividing after ~ 50 cell divisions and then undergo replicative senescence. He also found that fibroblasts taken from the elderly stop dividing after a lesser number of divisions than those taken from young individuals, and that the replication limit approximately correlates with the lifespan of a species [Hayflick and Moorhead 1961]. The progressive shortening of Telomeres with each cell division is possibly the mechanism that explains this limit. Restrictions on cell division may suppress tumour growth early in life by offering the trade-off of cellular senescence at a later stage.

The disposable soma theory posits that organisms balance the need for repair of somatic cells with the resources needed for successful reproduction [Kirkwood and Holliday 1979]. Organisms must direct the limited amount of resources available to them to support early survival at the expense of maintaining somatic cells. After perpetuating the species, the 'soma' becomes disposable, and organisms eventually age because of accumulated damage which makes them vulnerable to disease and environmental stress.

### 1.2.2 Stochastic theories

The wear-and-tear theory of aging likens organisms to machines that 'wear out' with time, use and environmental damage [Weismann 1882]. These stressors can cause harm to cells and tissues, contributing to the age-related decline in functionality. However, unlike machines, living organisms possess endogenous repair mechanisms, and the wear-and-tear theory overlooks this ability to repair damage.

Later on, wear-and-tear was modified by incorporating the DNA damage and repair hypothesis [Hart and Setlow 1974]. Although both mitochondrial and nuclear DNA damage may contribute to cellular dysfunction, nuclear DNA is the main subject of this hypothesis. Nuclear DNA damage may be involved in the aging process either indirectly (by leading to apoptosis or cellular senescence) or directly (by disrupting cellular function). The link between DNA damage and aging is supported by studies in animal models showing there is a positive correlation between DNA repair capacity and lifespan [Hoeijmakers 2009].

According to the cross-linking (or glycosylation) theory of aging, damage can also come from sugar moieties or cross-linked proteins that can bind to the DNA and cause defects in replication, translation or proteostasis [Bjorksten and Tenhu 1990].

The rate of living theory puts across the idea that organisms have a finite amount of energy to utilize over a lifetime and energy expenditure is inversely proportional to lifespan [Rubner 1908; Pearl 1928]. This idea came from the observation that, when comparing species, tiny animals with rapid metabolisms typically have shorter lifespans than bigger animals with slower metabolisms, and it has been supported by the more recent discovery of the positive effects of caloric restriction on health and longevity [Fontana et al. 2015]. However, this theory has also been criticised by studies displaying that animals with rapid metabolisms have endogenous mechanisms that can regulate their energy expenditure and extend their lifespan [Speakman et al. 2004].

A mechanistic link between increased metabolism and aging has also been provided by the free radical theory of aging (FRTA), which states that organisms age due to accumulation of damage from free radicals prominently produced by mitochondria [Harman 1956]. This hypothesis was born from the observations that free radicals are highly reactive and cause pervasive damage to macromolecules, and that the deleterious effects of exposure to irradiation and hyperoxia can be alleviated by antioxidant administration. Although widely accepted, the FRTA has been severely critiqued in recent years, mostly pointing at failure to increase longevity by enhancing antioxidants in long-living species [Rugarli and Trifunovic 2015].

### 1.3 Cellular aging

Whatever the cause originating this phenomenon, it is widely accepted that the increased prevalence of disease, and eventual death in the elderly starts with accumulation of damage at the cellular level. Since there is a clear association between aging of the population and increasing prevalence of CVDs, cardiac aging most likely affects pathophysiological pathways also implicated in the

development of cardiovascular disease [Milholland et al. 2017]. There are numerous data on molecular pathways implicated in cardiac aging. However, these studies mostly concern analyses of animal models, whereas data on molecular changes associated with human cardiac aging are currently lacking. The major reported mechanisms by which alterations in the heart and its constituent cells manifest are altered autophagy, oxidative stress and mitochondrial dysfunction, alterations in the 5'-AMP-activated protein kinase (AMPK) signalling pathway, telomere attrition, DNA damage, impaired calcium homeostasis, and electrical instability; these defects can lead to cellular senescence with expression of a senescence-associated secretory phenotype (SASP) and apoptosis (**Fig 2**).

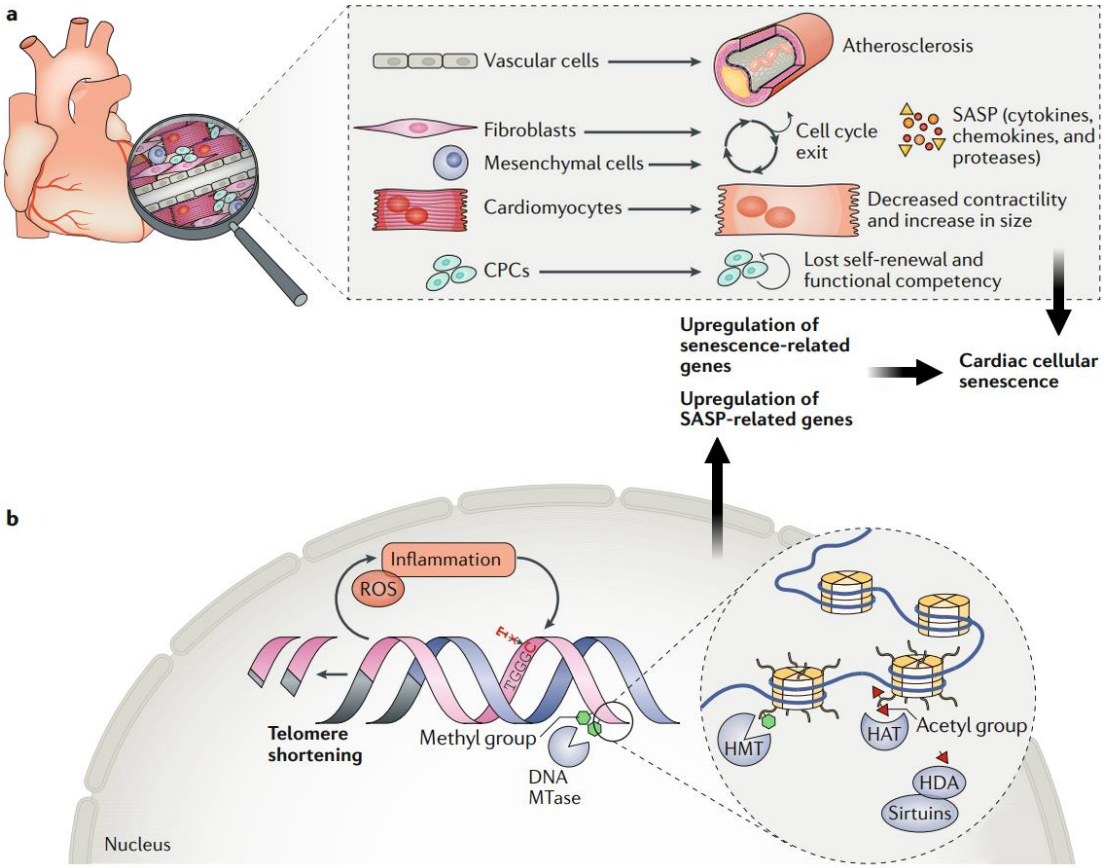


**Figure 2.** Cellular and molecular signals influencing cardiac ageing. (**a**) Cardiac cells manifest senescence by exiting the cell cycle and secreting senescence-associated secretory phenotype (SASP) factors, becoming hypertrophic and losing contractile function, and cardiac progenitor cells (CPCs) lose the capacity for self-renewal and differentiation. (**b**) At the molecular level, inflammation, and reactive oxygen species (ROS) drive DNA damage, telomere shortening, chromatin remodelling, and epigenetic changes, leading to cell cycle exit and expression of SASP and senescence-related genes. DNA MTase, DNA methyltransferase; HAT, histone acetyl transferase; HDA, histone deacetylase; HMT, histone methyltransferase. [According to Gude et al. 2018]

### 1.3.1 Decreased autophagy

Autophagy is a recycling and degradation mechanism essential for intracellular protein and organelle quality control. In this process, cytoplasmic components, like for example mitochondria, are targeted and isolated from the rest of the cell within a double-membraned vesicle called autophagosome which then fuses with a lysosome. The contents of the autolysosome are eventually degraded [Xie and Klionsky 2007].

Autophagy is upregulated when cardiac cells undergo stress, such as cardiac ischemia [Sciarretta et al. 2014], and the induction of autophagy in experimental studies has been observed to promote longevity, probably due to its clearance of damaged proteins and organelles [Rubinsztein et al. 2011]. Conversely, the downregulation of autophagy has been observed to promote the development of hypertension, atherosclerosis, cardiac hypertrophy, ischemic heart disease and heart failure [Oyabu et al. 2013; Sasaki et al. 2017].

The autophagic processes decrease in the heart with aging [Taneike et al. 2010]. Constant activation of autophagy caused by higher oxidative stress and protein misfolding may lead to exhaustion of the autophagic machinery, eventually causing suppression of autophagy itself (**Fig 3**). Activation of major inhibitors of autophagy, such as Mst1 and mTOR, or suppression of major activators of autophagy, such as Sirt1, may also cause downregulation of autophagy in the heart [Shirakabe et al. 2016]. In the end, downregulation of autophagy causes accumulation of damaged proteins and organelles, which leads to age-associated malfunction of cellular processes and may further exacerbate the aging process.

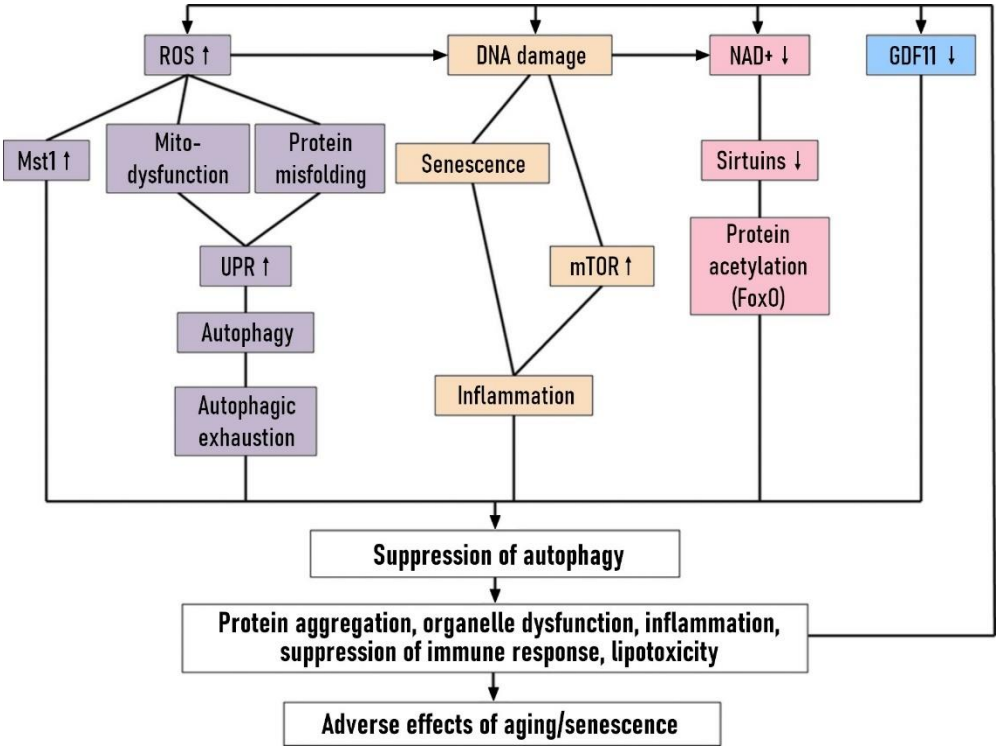


**Figure 3.** Regulation of cardiac aging by autophagy. Aging inhibits autophagy in cardiomyocytes through multiple mechanisms. Aging-induced suppression of autophagy induces accumulation of misfolded proteins and dysfunctional organelles, sterile infection caused by undigested mitochondrial DNA, inflammation, and lipotoxicity, thereby leading to a metabolically unhealthier environment, precipitous mitochondrial dysfunction and eventual cell death. GDF11 indicates growth differentiation factor 11; Mst1, macrophage-stimulating protein 1; UPR, unfolded protein response; mTOR, mammalian target of rapamycin; FoxO, forkhead box O. [According to Shirakabe et al. 2016]

### 1.3.2 Mitochondrial dysfunction and oxidative stress

Cardiac function requires an enormous amount of energy, and mitochondria are critical for the required ATP production in the myocardium. They also play a fundamental role in the survival and function of cardiomyocytes [Ren et al. 2010]. In these cells, superoxide is a key reactive oxygen species (ROS) produced by the enzyme NADPH oxidase (NOX) and the mitochondrial respiratory chain. Antioxidant enzymes, like superoxide dismutase (SOD), catalase, and glutathione peroxidase (GPx), degrade superoxide and reduce its reactivity [Brown and Griendling 2015].

With aging, the antioxidant capacity of the mitochondria in cardiomyocytes is impaired, causing an excess production but decreased elimination of ROS [Tocchi et al. 2015]. Mitochondrial DNA (mtDNA), in particular, lacks protective histones and is in proximity to high levels of ROS, resulting particularly susceptible to oxidation [Yakes and Van Houten 1997]. Besides damage to DNA (mitochondrial and nuclear), ROS also cause harm to proteins and lipids, leading to senescence, apoptosis, necrosis, inflammation, and changes in gene expression [Nakou et al. 2016]. Additionally, the impairment of respiratory efficiency following ROS-dependent damage to the mitochondria leads to further ROS production in a vicious cycle, as stated in the free radical theory of aging (FRTA) [Harman 1956]. Consequently, cardiac aging is accompanied by a general decline in mitochondrial function, and clonal expansion of dysfunctional mitochondria (**Fig 4**). This damage adds up to suppressed mitophagy and dysregulation of mitochondrial quality processes such as fusion and fission.

While all of the aforementioned theories of aging have been examined and laboriously tested, the mitochondrial FRTA, later termed oxidative stress theory, is currently one of the most popular correlative theories of the aging process. FRTA explains aging at the molecular level and results from failure to maintain oxidative defences, mitochondrial integrity, proteostasis, barrier structures, DNA repair, telomeres, immune function, metabolic regulation, and regenerative capacity.

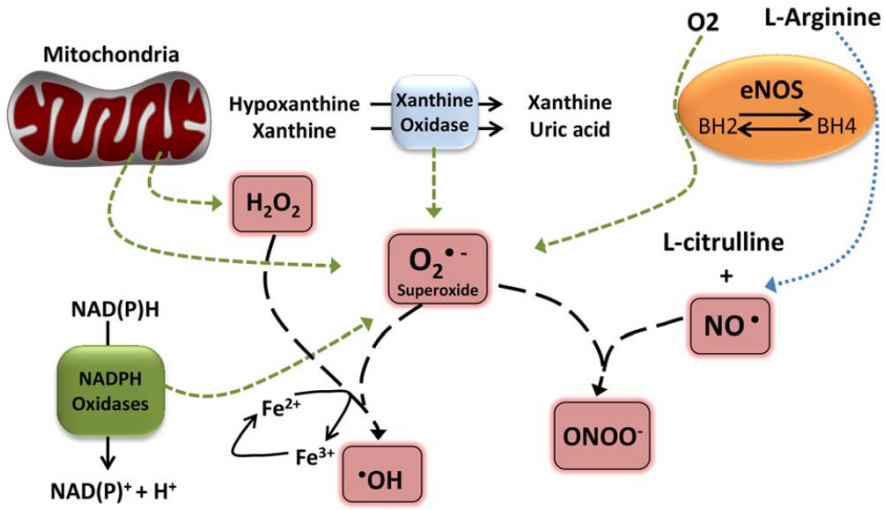


**Figure 4.** Major reactive oxygen species (ROS) generation pathways in cardiac myocytes. Mitochondria represent the predominant source of ROS in cardiomyocytes, producing superoxide ($O_2•^-$) by the premature leak of electrons from the respiratory chain at complexes I, II, or III. Mitochondrial manganese superoxide dismutase can dismutate $O_2•^-$ to hydrogen peroxide ($H_2O_2$), which can be broken down by transition metals such as $Fe^{2+}$ and converted to hydroxyl radicals (•OH). Superoxide can also be generated by the reduction of O2 by free electrons released from (a) NAD(P)H oxidases, which oxidize nicotinamide adenine dinucleotide (NADH) or nicotinamide adenine dinucleotide phosphate (NADPH) to form $NAD^+$ or $NADP^+$, (b) xanthine oxidase, which catalyses the conversion of hypoxanthine to xanthine or xanthine to uric acid, (c) endothelial nitric oxide synthase (eNOS), which switches from a coupled state (producing NO•) to an uncoupled oxide (producing $O_2•^-$) under conditions such as the reduction in l-arginine, the deficiency of cofactor tetrahydrobiopterin ($BH_4$), or increased glutathionylation of eNOS. Superoxide can also interact with preformed NO• and generate peroxynitrite $ONOO^-$. [According to Yang et al. 2015]

### 1.3.3 Alterations in the AMPK signalling pathway

AMPK is a highly conserved eukaryotic protein serine/threonine kinase, mainly known as an energy sensor that has both energy generating and conserving actions that preserve ATP during cellular stress (**Fig 5**). It is a heterotrimeric complex comprised of a catalytic α-subunit and two regulatory β- and γ-subunits. Each subunit has multiple isoforms (α1, α2, β1, β2, γ1, γ2 and γ3) encoded by different genes [Viollet et al. 2009]. The heart expresses α1/2, β1/2, γ1 and three distinct splice variants of γ2 isoforms [Li et al. 2006]. The pattern of expression is altered under pathological conditions, including HF [Kim et al. 2011; Pinter et al. 2012]. AMPK is mainly activated after its phosphorylation on Thr172 residue by upstream kinases. In the heart, the major upstream AMPK kinase is liver kinase B1 (LKB1) [Sakamoto et al. 2006].

When ATP consumption exceeds production, changes in ATP concentrations are translated by adenylate kinase into relatively larger changes in AMP. Binding of AMP not only promotes AMPK phosphorylation but also inhibits Thr172 dephosphorylation, causing a sensitive switch to the active phosphorylated form of AMPK. Although binding of ADP has been proposed to mimic some of the effects of AMP, recent reports support the notion that AMP remains the more physiologically relevant signal involved in AMPK activation [Gowans et al. 2013]. In general, activation of AMPK results in the repression of ATP-consuming anabolic processes and activation of ATP-producing catabolic processes to maintain cellular energy storage. Indeed, AMPK can phosphorylate transcription factors and therefore regulate gene expression, including FoxO3, which is involved in protection from oxidative stress by upregulating antioxidants, and PGC1-α, which regulates mitochondrial biogenesis and gluconeogenesis. Additionally, genetic mutations in AMPK genes cause metabolic disorders in both cardiac [Ahmad et al. 2005; Ma et al. 2010] and skeletal myocytes [Costford et al. 2007], while pharmacological activation of AMPK is known to improve cardiac function and upregulate cardiac autophagy in aged cardiomyocytes [Zhang J et

al. 2017], suggesting that alterations in AMPK have clinical consequences and may contribute to the decline in stress tolerance observed with aging.

Notably, many of the transcription factors regulated by AMPK are also regulated by SIRT1, a NAD-dependent deacetylase which acts as stress-response and survival protein. SIRT1 has been implicated with the pivotal ‘energy switch’ protein AMPK in studies indicating that SIRT1 may induce AMPK phosphorylation by activating one of its upstream activators, LKB1 [Lan et al. 2008; Hou et al. 2008]. Alternatively, other studies demonstrate that AMPK can activate SIRT1 by elevating intracellular $NAD^+$ levels [Fulco et al. 2008; Cantó et al. 2009].

The combined effects of AMPK and SIRT1 on PGC1-α suggest that an interdependence of these two proteins contribute to the stress response and metabolism [Scarpulla 2011]. A recent study exhibited in vivo and in vitro mechanistic evidence that PGC1α upregulation and deacetylation through the AMPK and SIRT1 cascades protects cardiomyocytes from cardiotoxic damage induced by some chemotherapy agents, such as oxidative stress and mitochondrial damage [Liu et al. 2019].

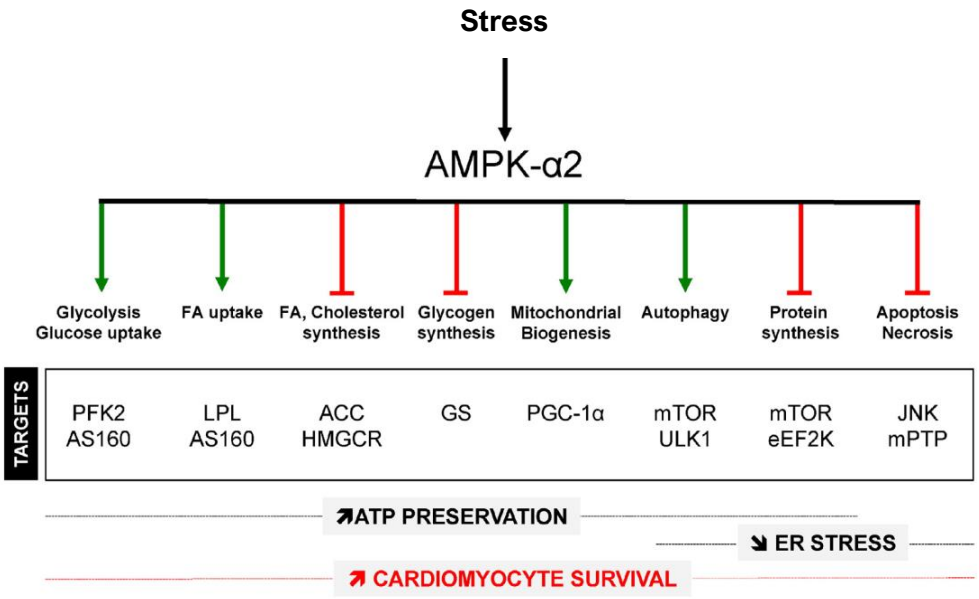


**Figure 5.** Schematic representation of key metabolic and non-metabolic targets of AMP-activated protein kinase (AMPK) in cardiac myocytes. [According to Daskalopoulos et al. 2016]

### 1.3.4 Telomere attrition

Telomeres are nucleoprotein caps present at the ends of each eukaryotic chromosome to maintain genomic integrity [Moyzis et al. 1988]. Because the DNA replication is asymmetric along double strands, a sequence at the 3′-hydroxyl end could lose 30–200 nucleotides with each DNA replication and cell division. Telomeres provide a repetitive noncoding sequence at the 3′ end to prevent the loss of critical genetically encoded information during replication. Therefore, Telomeres length (TL) has been proposed as a mitotic clock that measures how many times a cell has divided.

The enzyme telomerase is responsible for maintaining and elongating TL. Somatic cells generally have a low level of telomerase activity with limited longevity. Because telomerase activity decreases with age, TL peaks at birth, rapidly declines during puberty and slowly declines thereafter [Richardson et al. 2012]. Rich in guanine nucleotides, telomeres are also particularly vulnerable to oxidative stress due to ROS-mediated damage to single-stranded telomeric DNA [Sack et al. 2017]. When a critical TL is reached, cell cycle inhibitors are activated, and this leads to cellular senescence and eventual apoptosis through the p53 and p16 pathways [Fyhrquist et al. 2013].

Different studies have demonstrated that short telomeres induce functional decline within the cardiovascular system. When cardiac progenitor cells (CPCs) undergo Telomere attrition and eventual senescence or apoptosis, there is a consequent decline in the renewal capacity of the heart. However, this phenomena regarding the aging of CPCs is not sufficient to justify cardiac aging alone. Cardiomyocytes, on the other hand, long considered to be terminally differentiated postmitotic cells, were protagonists of experimental studies demonstrating that they possess active telomerase activity and suggesting that cardiomyocytes do indeed undergo some degree of division and regeneration throughout their lifespan [Leri et al. 2003; Bergmann et al. 2009; Sharifi-Sanjani et al. 2017]. Taken together, the Telomere shortening in CPCs and

cardiomyocytes may support the hypothesis that TL and attrition has a modest contribution toward cardiac aging.

### 1.3.5 DNA damage

DNA receives exogenous (e.g. environmental agents) and endogenous (e.g. cellular metabolic products) insults every minute ($10^4$–$10^5$ per cell per day) that can be extremely deleterious to cells. These lesions, if not correctly repaired, will interrupt genome replication and transcription and cause wide-scale chromosomal aberrations that may trigger malignant transformation or cell death. Therefore, effective sensing and repair systems have been developed during evolution to eliminate DNA damage and to maintain genome integrity.

Different types of DNA damage could be fixed by specific DNA damage response (DDR) mechanisms. Currently, four repair strategies have been elucidated in mammalian cells: base excision repair (BER) for correcting small alternations of bases, nucleotide excision repair (NER) for bulky helix-distorting lesions, and homologous recombination (HR) and non-homologous end joining (NHEJ) for double-strand break (DSB) repair [Pan et al. 2016].

When a double-strand break (DSB) occurs, it is generally repaired via the non-homologous end-joining (NHEJ) or homologous recombination (HR) pathways. NHEJ is engaged upon Ku70/Ku80 binding to DSBs followed by recruitment and activation of DNA-PK, while during HR, PARP1 assembles poly(ADP)-ribose chains on target proteins (including histone H1, H2B and PARP1 itself) to act as platforms to recruit the protein complex MRE11/Rad50/NBS1 (MRN) and subsequently activate ataxia-telangiectasia mutated kinase (ATM) and [Caldecott 2014]. Single-strand breaks (SSBs) repair is initiated by replication protein A (RPA), which recruits the Rad3-related (ATR) kinase in order to form an ATR/ATR-interacting protein (ATRIP) complex. Activation of ATM, ATR, and DNA-PK is followed by the phosphorylation of histone H2AX (γ-H2AX). Then γ-H2AX decorates the 30 kb region of chromatin-flanking DSBs and recruits early DDR proteins to the damaged sites to generate foci formation and to initiate the repair process [Shroff 2004; Podhorecka 2010]. ATM, ATR, and DNA-PK can

phosphorylate and activate the transcription factor p53 either directly or by activating the checkpoint kinases Chk1/2. p53 can upregulate the Cdk2 inhibitor (CDKII) p21, resulting in transient cell cycle arrest. If DNA damage is unrepaired, the cell cycle arrest becomes permanent, resulting in cellular senescence (**Fig 6**) [Prokhorova et al. 2015].

The spatiotemporal recruitment of sensors, transducers and effectors orchestrates a tightly controlled process to repair each type of DNA damage. Dysregulation of the DDR is closely associated with human diseases, including CVDs and aging [Ishida et al. 2014; Fang et al. 2016]. Growing evidence demonstrated that high levels of oxidative stress and abnormalities in DNA repair pathways are found in heart failure patients [Tsutsui 2011]. Their cardiac cells exhibit lower DNA repair activity, and therefore are highly sensitive to oxidative stress. Similarly, an exponential increase in chromosome aberrations and cytogenetic damage with increasing age has been amply confirmed in both humans and model organisms [Vijg and Suh 2013].

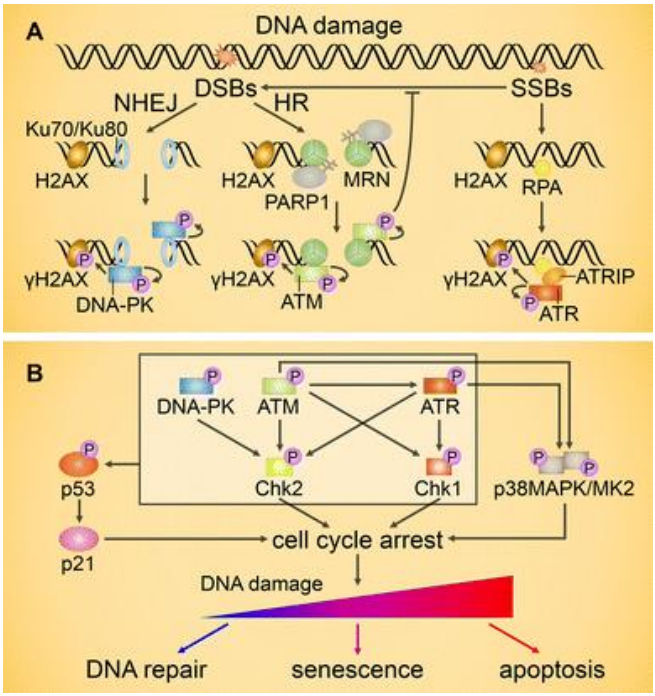


**Figure 6.** Transduction of DNA damage signals. (**a**) Activation of ataxia-telangiectasia mutated (ATM), Rad3-related (ATR) and DNA–protein kinase (DNA-PK) upon DNA damage. (**b**) ATM, ATR, and DNA-PK can phosphorylate and activate the transcription factor p53. Both ATM and ATR also contribute to the activation of the p38MAPK/MK2 kinase complex. Activation of Chk1/2 and MK2 downstream targets, as well as p53-mediated upregulation of p21, results in cell cycle arrest, which can lead to DNA repair, cellular senescence, or apoptosis. [According to Prokhorova et al. 2015]

### 1.3.6 Electrical instability

Myocardial mechanical activity is strictly dependent on electrical activity in a process called excitation-contraction coupling (ECC). The excitation process starts with an action potential (AP) which reflects the sequential activation and inactivation of inward ($Na^+$ and $Ca^{2+}$) and outward ($K^+$) ion channels [Nerbonne and Kass 2005]. Cardiomyocytes exhibit an AP morphology with 4 phases. Phase 0 is the rapid depolarizing phase that results when $Na^+$ channels activate and an influx of $Na^+$ ($I_{Na}$) causes the membrane potential depolarization. Phase 1 corresponds to the inactivation of $Na^+$ channels and outward movement of $K^+$ ions through outward current ($I_{to}$). In phase 2, a low conductance plateau phase, inward and outward ion movements are balanced mainly by L-type calcium current ($I_{CaL}$) and delayed rectifier $K^+$ channels ($I_{Kr}$ and $I_{Ks}$), respectively. Phase 3 marks the final repolarization phase of the AP, which returns to the resting potential at about -80 mV (phase 4) where the non-voltage-gated inwardly rectifying $K^+$ current ($I_{K1}$) stabilizes this resting potential.

The electrocardiogram (ECG) is a graph of voltage versus time of the electrical activity of the heart and its QT interval reflects the ventricular AP duration (APD). Since exaggerated prolongation of the QT interval can cause a distinctive polymorphic ventricular tachycardia called ‘torsades de pointes', its measure is in widespread clinical use for identifying and predicting a wide range of clinical conditions, such as electrolyte abnormalities, drug-induced cardiac toxicity, and inherited channelopaties [Shah et al. 2019].

Some studies have supported the claim that the QT interval is influenced by the person’s age. In particular, they observed an increase in QTc (QT corrected for the intrinsic heart rate) with age, which means that older individuals may be more vulnerable to situations and medications that prolong the QTc, therefore being at greater risk of developing life-threatening arrhythmias [Mangoni et al. 2003; Mason et al. 2007; Rabkin et al. 2016]. The QTc prolongation with age may be due to a combination of factors. Aging alters the myocardium and increases fibrosis [Nguyen et al. 2017] and it is associated with alterations in the amount of

sympathetic and parasympathetic tone [Can et al. 2002; Francis-Stuart et al. 2018]. Aging may also cause prolongation of APD due to increase in inward $Na^+$ currents, decrease in outward $K^+$ currents, and alterations in calcium handling (**Fig 7**) [Antzelevitch 2007].

During metabolic inhibition and mitochondrial dysfunction, ATP levels produced by the β-oxidation decrease, cells become more acidic due to production of elevated lactate levels, and the intracellular concentrations of phosphate and magnesium increase [Leyssens et al. 1996; Beauloye et al. 2001; Zima et al. 2013; Kanaporis et al. 2017]. Both reduced ATP and elevated phosphate levels can inhibit NKA ($Na^+/K^+$ ATPase) activity, leading to intracellular $Na^+$ increase [Chia et al. 2015]. Increased ROS levels can further aggravate cytosolic $Na^+$ accumulation by increasing late $I_{Na}$ ($I_{NaL}$) through direct $Na^+$ channel modification or by activating signalling molecules such as CaMKII. Therefore, there may be a feed-forward mechanism between increased cytosolic $Na^+$ levels, impaired mitochondrial metabolism, increased ROS emission, and ROS-induced elevation of cytosolic $Na^+$ [Yang et al. 2015]. Increased late $Na^+$-currents ($I_{NaL}$) contribute to prolongation of APD. Interestingly, increased intracellular $Na^+$ concentration has also been found during myocardial ischemia and heart failure [Undrovinas et al. 1992; Valdivia et al. 2005; Sokolov et al. 2013]. In these studies, elevated intracellular $Na^+$ also led to increased cytosolic $Ca^{2+}$ through decreased extrusion of $Ca^{2+}$ or through actual $Ca^{2+}$ entry with NCX activity in the reverse mode ($Na^+$ out and $Ca^{2+}$ in), causing modifications to $Ca^{2+}$ handling.

Under pathological conditions repolarizing $K^+$ currents in cardiac myocytes can be reduced, leading to delayed repolarization and prolonged APD. Increased oxidative stress is known to inhibit repolarizing voltage-gated $K^+$ (Kv) channels, leading to downregulation of $I_{to}$ and several delayed rectifier $I_K$ currents ($I_{Kr}$, $I_{Ks}$, and $I_{Kur}$) in mammalian cardiomyocytes [Cerbai et al. 1991; Li et al. 2008; Liang et al. 2008]. ROS have been shown to regulate Kv current expression by reducing transcript and protein expression of the Kv channel subunits and by modulating the phosphorylation of these proteins through PKs [Chiarugi 2005]. Cardiac Kv channels can also be regulated directly by nitric oxide (NO•), which can block the

potassium channels and therefore inhibit the currents [Nuñez et al. 2006; Gomez et al. 2008]. Overall, APD prolongation due to marked changes in the contribution of several ion currents might be the consequence of altered redox state of aged myocytes. Moreover, APD prolongation might become intrinsically pro-arrhythmogenic due to the increased beat-to-beat variability of APD, usually quantified by well-known markers, as STV (‘short term variability’) [Altomare et al. 2015].

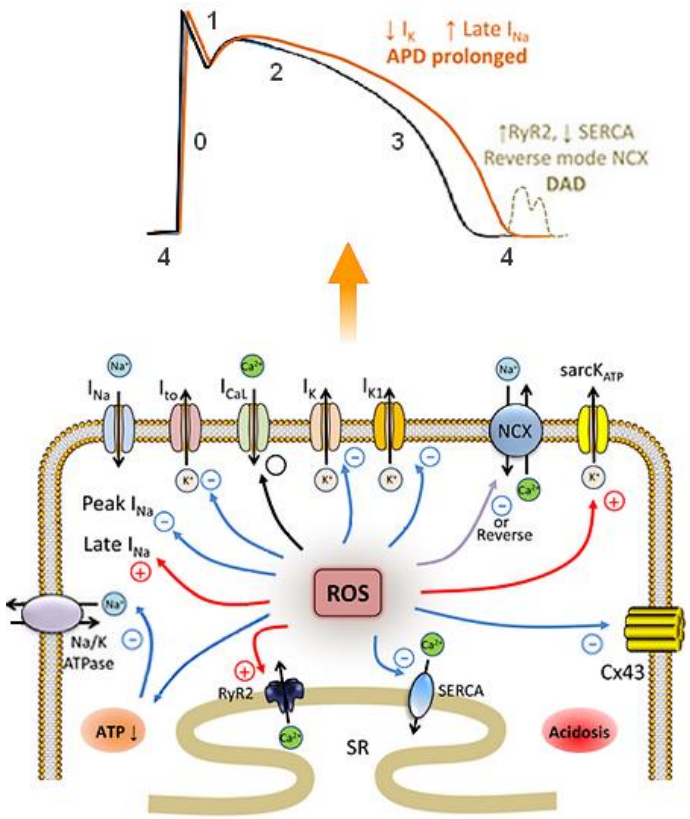


**Figure 7.** Effects of increased oxidative stress on cardiac ion channel/transporter function. Increased ROS increase $I_{NaL}$, reduces repolarizing $K^+$ currents, and inhibit NKA. Increased ROS also enhance the activity of ryanodine receptor 2 (RyR2), reduce SERCA activity, and promote the reverse mode of NCX. Reduced $K^+$ currents and increased $I_{NaL}$ lead to prolonged APD. Increased RyR2 activity, reduced SERCA function, and reverse mode NCX activity lead to cytosolic $Ca^{2+}$ overload and predispose to delayed afterdepolarizations (DADs). [Modified from Yang et al. 2015]

### 1.3.7 Altered calcium handling

The $Ca^{2+}$ entry through $I_{CaL}$, situated on invaginations of the cell membrane called T-tubules, triggers the $Ca^{2+}$ release from the sarcoplasmic reticulum (SR) through the ryanodine receptors (RyR2) in a mechanism defined as $Ca^{2+}$- induced $Ca^{2+}$ release (CICR) [Bers 2002]. The $Ca^{2+}$ influx and release from SR raise the intracellular calcium concentration and, when this concentration reaches ~1μM, $Ca^{2+}$ can bind the low affinity sites on the N-terminus of troponin C. This binding switches on the contractile machinery, which is an ATP-consuming process. For cardiac relaxation to occur, $Ca^{2+}$ must be removed from the cytoplasm. This is done through closing of RyRs and pumping of $Ca^{2+}$ mainly back into the SR by SERCA2a (sarco-endoplasmic reticulum $Ca^{2+}$-ATPase) and out of the cell by NCX (sodium–calcium exchanger).

Previous studies have shown that $Ca^{2+}$ handling may be altered in aged cardiac myocytes (**Fig 8**). For example, a recent study [Feridooni et al. 2017] showed in ventricular myocytes harvested from 27-month-old mouse hearts, that Cav1.2 channel expression and corresponding $I_{CaL}$ current are reduced, leading to minor $Ca^{2+}$ fluxes and smaller calcium transient (CaT) peaks. Despite these changes, neither SR $Ca^{2+}$ content or CaT decay rates were altered in aged mouse myocytes in that study. Conversely, other studies [Janczewski et al. 2002] reported an increase in $I_{CaL}$ and $Ca^{2+}$ influx, no change in CaT amplitude, and significantly slowed SR $Ca^{2+}$ reuptake (owing to lower SERCA levels) in aged rat myocytes. These discrepancies in experimental results may be due to species, age, degree of frailty, or experimental conditions.

Mitochondrial dysfunction may also be directly connected with age-related changes in calcium signalling. One of the proteins affected by oxidative damage with age is SERCA2a, which can be affected both in its protein expression and activity [Babusikova et al. 2012; Feridooni et al. 2015]. The activity of SERCA2a is inhibited by phospholamban (PLB) when the latter is unphosphorylated, and it has been shown that the SERCA/PLB ratio decreases with age. A decreased

SERCA functionality is associated with prolongation of relaxation and thus diastolic dysfunction.

The activity of the aforementioned calcium-handling proteins (RyR2, SERCA, PLB) is regulated through phosphorylation by calcium-/calmodulin-dependent protein kinase II (CaMKII). In concordance with an alteration of calcium signalling, aging has been found to be associated with an increased activation of CaMKII leading to augmented CaMKII-mediated phosphorylation of calcium-handling proteins [Yang et al. 2015; Yan et al. 2018]. CaMKII is activated by ROS, and it is known to play a critical role in regulating calcium-handling proteins in response to increased cardiac oxidative stress. For example, activated CaMKII increases $I_{CaL}$ by phosphorylating the Cav1.2 channel and increasing its open probability [Wu et al. 1999]. Phosphorylation of RyR2 by CaMKII increases SR calcium leak, promoting cytosolic $Ca^{2+}$ overload and delayed afterdepolarizations [Rokita and Anderson 2012; Guo et al. 2014]. Taken together, the net impact of increased oxidative stress on $Ca^{2+}$-handling proteins leads to cytosolic $Ca^{2+}$ overload and depletion of SR calcium store, resulting in detrimental changes, such as contractile dysfunction. Notably, in human heart failure the activity of these calcium-handling proteins is affected similarly to aging. SERCA activity is significantly reduced in human failing myocardium [Roe et al. 2015], and an hyperphosphorylation of RyR2 by CaMKII can be observed in both heart failure and atrial fibrillation, playing a role in $Ca^{2+}$ leaks from the SR that lead to altered contractility [Respress et al. 2012; Voigt et al. 2012].

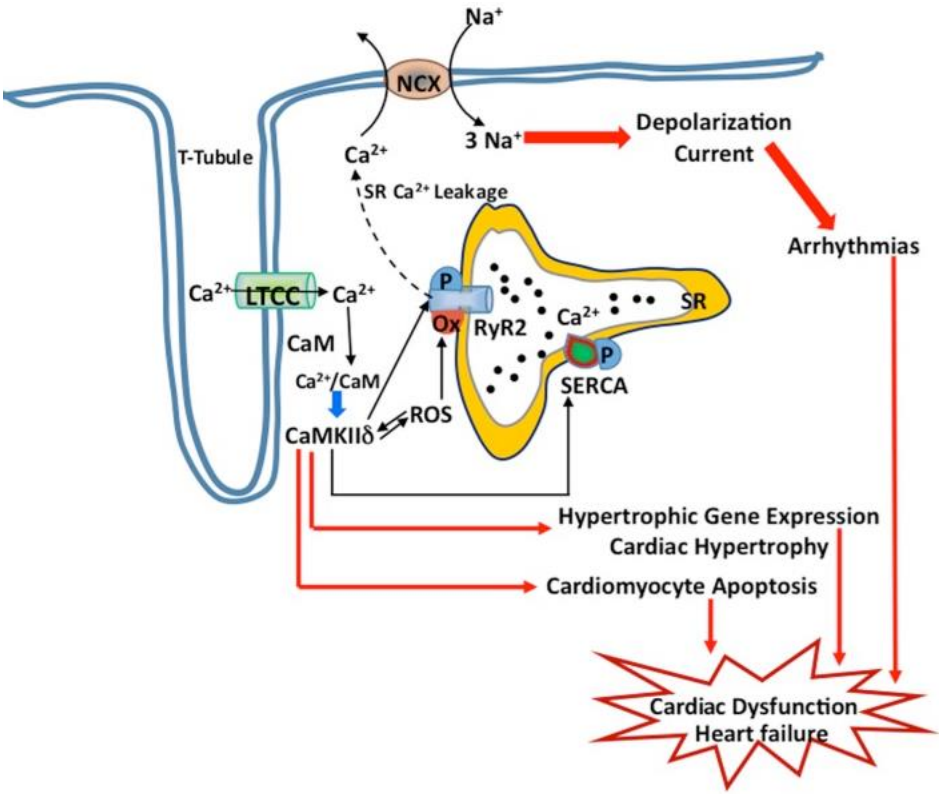


**Figure 8.** $Ca^{2+}$ transport in ventricular myocytes. Increase in intracellular $Ca^{2+}$ through L-type $Ca^{2+}$ channels, leads to CaMKIIδ activation via $Ca^{2+}$/Calmodulin (CaM) in the cardiomyocyte. ROS, which arise from other stress stimuli, can also activate CaMKIIδ, resulting in a vicious cycle of CaMKIIδ activation. Both the phosphorylation mediated by CaMKIIδ and ROS-mediated oxidation of the type 2-ryanodine receptor (RyR2) in sarcoplasmic reticulum (SR) lead to enhanced SR $Ca^{2+}$ load and in turn, cause SR $Ca^{2+}$ leak. This triggers sodium/calcium exchanger (NCX)-dependent depolarizing current (transient inward current), which can contribute to arrhythmia. Activated CaMKIIδ can also elevate transcription of cardiac hypertrophy genes and activation of apoptotic pathways. All these events contribute to failure of the heart. [According to Zhang P 2017]

### 1.3.8 Cellular senescence and SASP

As previously mentioned, an accumulation of DNA damage or defect in DNA repair promotes the aging process. Interestingly, an accumulation of DNA damage or defect in DNA repair also promotes cellular senescence. This raises the question whether senescence induced by physiological or pathological alterations may be involved in aging. Indeed, in recent years it has been suggested that accumulation of senescence cells could be considered the main cause underlying in the aging process. For this reason, sometimes the term 'senescence' is used to indicate the aging process.

Cellular senescence refers to a state of stable cell cycle arrest in which cells become resistant to growth-promoting stimuli. Physiologically, senescence prevents the expansion of damaged cells, serving an important anti-tumorigenic function. Senescence occurs in response to damaging stimuli, including telomere shortening (replicative senescence, RS) and DNA damage caused by different insults, such as chemotherapy (stress-induced premature senescence, SIPS) [Lombard et al. 2005; Blasco 2007].

Senescent cells are characterized by typical morphological and metabolic changes. It is important to note that not all senescent cells display all biomarkers of senescence. Senescence is characterized by a complex phenotype and, in addition, senescence biomarkers are not necessarily specific to senescent cells, as some markers are observed in apoptotic cells or quiescent cells, for example [Chandrasekaran et al 2017]. Only cells with stable cell cycle arrest are considered senescent and, unlike quiescent cells, senescent cells will not re-enter the cell cycle in response to grow factors.

Cell cycle arrest is mediated by the p53/$p21^{CIP1}$ and $p16^{INK4A/pRb}$ tumour suppressor pathways [Yamakoshi et al. 2009; Takeuchi et al. 2010]. Moreover, senescent cells typically have an enlarged size and flattened shape compared to their dividing cell counterparts and display accumulation of dysfunctional mitochondria and ROS. Increased lysosomal content and altered lysosomal activity is also observed, which is reflected by increased levels of β-

galactosidase (β-gal) activity at pH 6.0, leading this to be widely adopted as a biomarker of cellular senescence [Dimri et al. 1995].

Senescent cells also present a persistent DDR and accumulation of DDR-related proteins (such as γ-H2AX) in nuclear foci called DNA segments with chromatin alterations reinforcing senescence (DNA-SCARS) [Rodier et al. 2011]. Additionally, many senescent cells acquire a senescence-associated secretory phenotype (SASP) that mediates non-cell autonomous effects of senescence. These cells secrete IL-6 and IL-8, intercellular adhesion molecule 1 (ICAM-1), metalloproteases, monocyte attractants, plasminogen activator inhibitor 1, and vascular endothelial growth factor, contributing to inflammation, and promoting tissue remodeling and repair or apoptosis. Particularly through its SASP, cell senescence can aggravate chronic inflammation and accelerate aging and the development of aging-associated diseases [Watanabe et al. 2017].

## 1.4 Animal and cellular models of cardiac aging

It is critical to conduct a study on proper experimental models in order to obtain accurate information about the aging mechanisms. In general, the mainstream model systems to conduct aging studies include cells, yeast (*Saccharomyces cerevisiae*), roundworms (*Caenorhabditis elegans*), fruit flies (*Drosophila melanogaster*), mice (*Mus musculus*), rats (*Rattus norvegicus*) and dogs (*Canis lupus*).

Nonmammalian model systems, such as yeast, roundworms, and fruit flies, share a relatively large number of biological pathways with humans [Jafari et al. 2006]. Indeed, many genes and signal pathways modulating the aging process have already been identified in yeast [Jazwinski 2000], worms [Johnson et all. 2002], and fruit flies [Tower 2000], which serve as basis for further understanding human aging mechanisms. Additionally, these organisms are easier and cheaper to manipulate in large numbers than mammalian models. On the other hand, aging is a complex biological process, involving many different factors at the same time, and the physiology and phenotypes of these models are way from alike with mammals.

As to the mammal systems, such as mice, rats, and dogs, their physiology and daily activities are more parallel to humans, compared to those of nonmammalian models. Moreover, being the mainstream animals employed in laboratory for decades, the experiment protocols in which these models are involved are quite mature and stable. However, there is still no solid evidence indicating that rodents and dogs age for the same causes and mechanisms as humans [Gershon and Gershon 2002].

Recently, nonhuman primates have been regarded as a potential alternative for human aging studies [Nadon 2006]. It is claimed that Rhesus monkeys (*Macaca mulatta*) share about 90% of their genome with human beings [Roth et al. 2004]. In addition, it has already been reported that age-related changes in neurological structure and function of monkeys share great similarity with those of humans [Small et al. 2004; Smith et al. 2004]. Nevertheless, the employment of this model

in aging studies is still quite rare. First of all, those primates have comparatively long lifespan, which is a practical problem for laboratory manipulation. Secondly, the costs to conduct experiments on those animals are relatively high. Thirdly, a serious issue is the moral concern by animal rights groups.

Since nonhuman models have offered important contributions in understanding human biology and disease but do not fully mirror the complexity of human physiology and disease, the use of human material would be the most reliable way to properly understand the molecular mechanisms of cardiac aging. For different tissues, such as the myocardium, the use of primary cells from patients is limited by the amount of tissue that can be obtained and its lifespan in culture, along with the technical difficulties in accessing the tissue itself. Human induced pluripotent stem cells (hiPSCs) have the capability to self-renew indefinitely and to differentiate into derivatives of the three germ layers [Lodrini et al. 2020]. Unlike non-human animal models, cardiomyocytes derived from hiPSCs (hiPSC-CMs) offer an unprecedented platform for a comprehensive understanding of the molecular basis of human cardiac aging and CVDs.

## 1.5 References


Ahmad F, Arad M, Musi N, et al. (2005) Increased alpha2 subunit-associated AMPK activity and PRKAG2 cardiomyopathy. *Circulation*. DOI: 10.1161/CIRCULATIONAHA.105.550806

Altomare C, Bartolucci C, Sala L, et al. (2015) $I_{Kr}$ Impact on Repolarization and Its Variability Assessed by Dynamic Clamp. *Circ Arrhythm Electrophysiol.* DOI: 10.1161/CIRCEP.114.002572

Antzelevitch C (2007) Ionic, molecular, and cellular bases of QT-interval prolongation and torsade de pointes. *Europace*. DOI: 10.1093/europace/eum166

Babušíková E, Lehotský J, Dobrota D, Račay P, Kaplán P (2012) Age-associated changes in $Ca^{2+}$-ATPase and oxidative damage in sarcoplasmic reticulum of rat heart. *Physiol Res*. DOI: 10.33549/physiolres.932320

Beauloye C, Bertrand L, Krause U, et al. (2001) No-flow ischemia inhibits insulin signaling in heart by decreasing intracellular pH. *Circ Res.* DOI: 10.1161/01.res.88.5.513

Bergmann O, Bhardwaj RD, Bernard S, Zdunek S, Barnab XE et al. (2009) Evidence for cardiomyocyte renewal in humans. *Science*. DOI: 10.1126/science.1164680

Bers DM (2002) Cardiac excitation-contraction coupling. *Nature.* DOI: 10.1038/415198a

Bjorksten J and Tenhu H (1990) The crosslinking theory of aging – added evidence. *Exp Gerontol.* DOI: 10.1016/0531-5565(90)90039-5

Blasco MA (2007) Telomere length, stem cells and aging. *Nat Chem Biol.* DOI: 10.1038/nchembio.2007.38

Brown DI and Griendling KK (2015) Regulation of signal transduction by reactive oxygen species in the cardiovascular system. *Circ Res.* DOI: 10.1161/CIRCRESAHA.116.303584

Caldecott KW (2014) Protein ADP-ribosylation and the cellular response to DNA strand breaks. *DNA Repair (Amst)*. DOI: 10.1016/j.dnarep.2014.03.021

Can I, Aytemir K, Köse S, Oto A (2002) Physiological mechanisms influencing cardiac repolarization and QT interval. *Card Electrophysiol Rev.* DOI: 10.1023/a:1016341311646. PMID: 12114852

Cantó C, Gerhart-Hines Z, Feige JN, et al. (2009) AMPK regulates energy expenditure by modulating NAD+ metabolism and SIRT1 activity. *Nature*. DOI: 10.1038/nature07813

Cerbai E, Ambrosio G, Porciatti F, Chiariello M, Giotti A, Mugelli A (1991) Cellular electrophysiological basis for oxygen radical-induced arrhythmias. A patch-clamp study in guinea pig ventricular myocytes. *Circulation*. DOI: 10.1161/01.cir.84.4.1773

Chandrasekaran A, Idelchik MDPS, Melendez JA (2017) Redox control of senescence and age-related disease. *Redox Biol.* DOI: 10.1016/j.redox.2016.11.005

Chia KK, Liu CC, Hamilton EJ, et al. (2015) Stimulation of the cardiac myocyte $Na^+$-$K^+$ pump due to reversal of its constitutive oxidative inhibition. *Am J Physiol Cell Physiol*. DOI: 10.1152/ajpcell.00392.2014

Chiarugi P (2005) PTPs versus PTKs: the redox side of the coin. *Free Radic Res*. DOI: 10.1080/10715760400027987

Costford SR, Kavaslar N, Ahituv N, et al. (2007) Gain-of-function R225W mutation in human AMPKgamma(3) causing increased glycogen and decreased triglyceride in skeletal muscle. *PLoS One*. DOI: 10.1371/journal.pone.0000903

Daskalopoulos EP, Dufeys C, Bertrand L, Beauloye C, Horman S (2016) AMPK in cardiac fibrosis and repair: Actions beyond metabolic regulation. *J Mol Cell Cardiol*. DOI: 10.1016/j.yjmcc.2016.01.001

Dhingra R and Vasan RS (2012) Age as a risk factor. *Med Clin North Am.* DOI: 10.1016/j.mcna.2011.11.003

Dimri GP, Lee X, Basile G, Acosta M, Scott G, Roskelley C, Medrano EE, Linskens M, Rubelj I, Pereira-Smith O, et al. (1995) A biomarker that identifies senescent human cells in culture and in aging skin in vivo. *Proc Natl Acad Sci U S A.* DOI: 10.1073/pnas.92.20.9363

Fang EF, Scheibye-Knudsen M, Chua KF, Mattson MP, Croteau DL, Bohr VA (2016) Nuclear DNA damage signalling to mitochondria in aging. *Nat Rev Mol Cell Biol.* DOI: 10.1038/nrm.2016.14

Feridooni HA, Dibb KM, Howlett SE (2015) How cardiomyocyte excitation, calcium release and contraction become altered with age. *J Mol Cell Cardiol*. DOI: 10.1016/j.yjmcc.2014.12.004

Feridooni HA, Kane AE, Ayaz O, Boroumandi A, Polidovitch N, Tsushima RG, Rose RA, Howlett SE (2017) The impact of age and frailty on ventricular structure and function in C57BL/6J mice. *J Physiol.* DOI: 10.1113/JP274134

Francis-Stuart SD, Wang L, Woodard WR, Ng GA, Habecker BA, Ripplinger CM (2018) Age-related changes in cardiac electrophysiology and calcium handling in response to sympathetic nerve stimulation. *J Physiol*. DOI: 10.1113/JP276396

Fulco M, Cen Y, Zhao P, et al. (2008) Glucose restriction inhibits skeletal myoblast differentiation by activating SIRT1 through AMPK-mediated regulation of Nampt. *Dev Cell*. DOI: 10.1016/j.devcel.2008.02.004

Fyhrquist F, Saijonmaa O and Strandberg T (2013) The roles of senescence and telomere shortening in cardiovascular disease. *Nat Rev Cardiol.* DOI: 10.1038/nrcardio.2013.30

Gershon H, Gershon D (2002) Caenorhabditis elegans – a paradigm for aging research: advantages and limitations. *Mech Ageing Dev*. DOI: 10.1016/s0047-6374(01)00401-8

Gowans GJ, Hawley SA, Ross FA, Hardie DG (2013) AMP is a true physiological regulator of AMP-activated protein kinase by both allosteric activation and enhancing net phosphorylation. *Cell Metab*. DOI: 10.1016/j.cmet.2013.08.019

Gude NA, Broughton KM, Firouzi F, Sussman MA (2018) Cardiac ageing: extrinsic and intrinsic factors in cellular renewal and senescence. *Nat Rev Cardiol.* DOI: 10.1038/s41569-018-0061-5

Guo X, Yuan S, Liu Z, Fang Q (2014) Oxidation- and CaMKII-mediated sarcoplasmic reticulum $Ca^{2+}$ leak triggers atrial fibrillation in aging. *J Cardiovasc Electrophysiol*. DOI: 10.1111/jce.12395

Harman D (1956) Aging: a theory based on free radical and radiation chemistry. *J Gerontol.* DOI: 10.1093/geronj/11.3.298

Hart RW, Setlow RB (1974) Correlation between deoxyribonucleic acid excision-repair and lifespan in a number of mammalian species. *Proc Natl Acad Sci U S A*. DOI: 10.1073/pnas.71.6.2169

Hayflick L and Moorhead PS (1961) The serial cultivation of human diploid cell strains. *Exp Cell Res.* DOI:10.1016/0014-4827(61)90192-6

Hoeijmakers JH (2009) DNA damage, aging, and cancer. *N Engl J Med*. DOI :10.1056/NEJMra0804615

Hou X, Xu S, Maitland-Toolan KA, et al. (2008) SIRT1 regulates hepatocyte lipid metabolism through activating AMP-activated protein kinase. *J Biol Chem*. DOI: 10.1074/jbc.M802187200

Ishida T, Ishida M, Tashiro S, Yoshizumi M, Kihara Y (2014) Role of DNA damage in cardiovascular disease. *Circ J.* DOI: 10.1253/circj.cj-13-1194

Jafari M, Long AD, Mueller LD, Rose MR (2006) The pharmacology of ageing in Drosophila. *Curr Drug Targets.* DOI: 10.2174/1389450110607011479

Janczewski AM, Spurgeon HA, Lakatta EG (2002) Action potential prolongation in cardiac myocytes of old rats is an adaptation to sustain youthful intracellular $Ca^{2+}$ regulation. *J Mol Cell Cardiol.* DOI: 10.1006/jmcc.2002.2004

Jazwinski SM (2000) Metabolic mechanisms of yeast ageing. *Exp Gerontol*. DOI: 10.1016/s0531-5565(00)00146-7

Johnson TE, Henderson S, Murakami S, de Castro E, de Castro SH, Cypser J, Rikke B, Tedesco P, Link C (2002) Longevity genes in the nematode Caenorhabditis elegans also mediate increased resistance to stress and prevent disease. *J Inherit Metab Dis*. DOI: 10.1023/a:1015677828407

Kanaporis G, Treinys R, Fischmeister R, Jurevičius J (2017) Metabolic inhibition reduces cardiac L-type $Ca^{2+}$ channel current due to acidification caused by ATP hydrolysis. *PLoS One*. DOI: 10.1371/journal.pone.0184246

Kim AS, Miller EJ, Wright TM, et al. (2011) A small molecule AMPK activator protects the heart against ischemia-reperfusion injury. *J Mol Cell Cardiol*. DOI: 10.1016/j.yjmcc.2011.03.003

Kirkwood TB and Holliday R (1979) The evolution of ageing and longevity. *Proc R Soc* Lond B. DOI: 10.1098/rspb.1979.0083

Lan F, Cacicedo JM, Ruderman N, Ido Y (2008) SIRT1 modulation of the acetylation status, cytosolic localization, and activity of LKB1. Possible role in AMP-activated protein kinase activation. *J Biol Chem*. DOI: 10.1074/jbc.M805711200

Leri A, Franco S, Zacheo A, Barlucchi L, Chimenti S, Limana F, Nadal-Ginard B, Kajstura J, Anversa P, Blasco MA (2003) Ablation of telomerase and telomere loss leads to cardiac dilatation and heart failure associated with p53 upregulation. *EMBO J*. DOI: 10.1093/emboj/cdg013

Leyssens A, Nowicky AV, Patterson L, Crompton M, Duchen MR (1996) The relationship between mitochondrial state, ATP hydrolysis, $[Mg^{2+}]_i$ and $[Ca^{2+}]_i$ studied in isolated rat cardiomyocytes. J Physiol. DOI: 10.1113/jphysiol.1996.sp021669

Li J, Coven DL, Miller EJ, et al. (2006) Activation of AMPK alpha- and gamma-isoform complexes in the intact ischemic rat heart. *Am J Physiol Heart Circ Physiol*. DOI: 10.1152/ajpheart.00251.2006

Li X, Tang K, Xie B, Li S, Rozanski GJ (2008) Regulation of Kv4 channel expression in failing rat heart by the thioredoxin system. *Am J Physiol Heart Circ Physiol*. DOI: 10.1152/ajpheart.91446.2007

Liang H, Li X, Li S, Zheng MQ, Rozanski GJ (2008) Oxidoreductase regulation of Kv currents in rat ventricle. *J Mol Cell Cardiol*. DOI: 10.1016/j.yjmcc.2008.03.011

Lipsky MS and King M (2015) Biological theories of aging. *Dis Mon*. DOI: 10.1016/j.disamonth.2015.09.005

Liu D, Ma Z, Xu L, Zhang X, Qiao S, Yuan J (2019) PGC1α activation by pterostilbene ameliorates acute doxorubicin cardiotoxicity by reducing oxidative stress via enhancing AMPK and SIRT1 cascades. *Aging (Albany NY)*. DOI: 10.18632/aging.102418

Lodrini AM, Barile L, Rocchetti M, Altomare C (2020) Human Induced Pluripotent Stem Cells Derived from a Cardiac Somatic Source: Insights for an In-Vitro Cardiomyocyte Platform*. Int J Mol Sci.* DOI: 10.3390/ijms21020507

Lombard DB, Chua KF, Mostoslavsky R, Franco S, Gostissa M, Alt FW (2005) DNA repair, genome stability, and aging. *Cell*. DOI: 10.1016/j.cell.2005.01.028

López-Otín C, Blasco MA, Partridge L, Serrano M and Kroemer G (2013) The hallmarks of aging. *Cell*. DOI: 10.1016/j.cell.2013.05.039

Ma H, Wang J, Thomas DP, et al. (2010) Impaired macrophage migration inhibitory factor-AMP-activated protein kinase activation and ischemic recovery in the senescent heart. *Circulation*. DOI: 10.1161/CIRCULATIONAHA.110.953208

Mangoni AA, Kinirons MT, Swift CG, Jackson SH (2003) Impact of age on QT interval and QT dispersion in healthy subjects: a regression analysis. *Age and Ageing*. DOI: 10.1093/ageing/32.3.326

Mason JW, Ramseth DJ, Chanter DO, Moon TE, Goodman DB, Mendzelevski B (2007) Electrocardiographic reference ranges derived from 79,743 ambulatory subjects. *J Electrocardiol. DOI*: 10.1016/j.jelectrocard.2006.09.003

Milholland, B, Suh Y and Vijg J (2017) Mutation and catastrophe in the aging genome. *Exp Gerontol.* DOI: 10.1016/j.exger.2017.02.073

Moyzis RK, Buckingham JM, Cram LS, Dani M, Deaven LL, Jones MD, Meyne J, Ratliff RL, Wu JR (1988) A highly conserved repetitive DNA sequence, (TTAGGG)n, present at the telomeres of human chromosomes. *Proc Natl Acad Sci U S A*. DOI: 10.1073/pnas.85.18.6622

Nadon NL (2006) Of mice and monkeys: National Institute on Aging resources supporting the use of animal models in biogerontology research. *J Gerontol A Biol Sci Med Sci*. DOI: 10.1093/gerona/61.8.813

Nakou ES, Parthenakis FI, Kallergis EM, Marketou ME, Nakos KS and Vardas PE (2016) Healthy aging and myocardium: A complicated process with various effects in cardiac structure and physiology. *International Journal of Cardiology.* DOI: 10.1016/j.ijcard.2016.02.039

Nerbonne JM, Kass RS (2005) Molecular physiology of cardiac repolarization. *Physiol Rev.* DOI: 10.1152/physrev.00002.2005

Nguyen MN, Kiriazis H, Gao XM, Du XJ (2017) Cardiac Fibrosis and Arrhythmogenesis. *Compr Physiol.* DOI: 10.1002/cphy.c160046

Oyabu J, Yamaguchi O, Hikoso S, Takeda T, Oka T, Murakawa T et al. (2013) Autophagy-mediated degradation is necessary for regression of cardiac hypertrophy during ventricular unloading. *Biochem Biophys Res Commun.* DOI: 10.1016/j.bbrc.2013.10.135

Pan MR, Li K, Lin SY, Hung WC (2016) Connecting the Dots: From DNA Damage and Repair to Aging. *Int J Mol Sci*. DOI: 10.3390/ijms17050685

Pearl R (1928) The Rate of Living. *University of London Press, London, UK*.

Pinter K, Grignani RT, Czibik G, Farza H, Watkins H, Redwood C (2012) Embryonic expression of AMPK γ subunits and the identification of a novel γ2 transcript variant in adult heart. *J Mol Cell Cardiol*. DOI: 10.1016/j.yjmcc.2012.05.017

Podhorecka M, Skladanowski A, Bozko P (2010) H2AX Phosphorylation: Its Role in DNA Damage Response and Cancer Therapy. *J Nucleic Acids*. DOI: 10.4061/2010/920161

Pu T, Liao XH, Sun H, et al. (2017) Augmenter of liver regeneration regulates autophagy in renal ischemia-reperfusion injury via the AMPK/mTOR pathway. *Apoptosis*. DOI: 10.1007/s10495-017-1370-6

Rabkin SW, Cheng XJ, Thompson DJ (2016) Detailed analysis of the impact of age on the QT interval. *J Geriatr Cardiol*. DOI: 10.11909/j.issn.1671-5411.2016.09.013

Ren J, Pulakat L, Whaley-Connell A, Sowers JR (2010) Mitochondrial biogenesis in the metabolic syndrome and cardiovascular disease. *J Mol Med (Berl)*. DOI: 10.1007/s00109-010-0663-9

Respress JL, van Oort RJ, Li N, Rolim N, Dixit SS, deAlmeida A, Voigt N, Lawrence WS, Skapura DG, Skårdal K, Wisløff U, Wieland T, Ai X, Pogwizd SM, Dobrev D, Wehrens XH (2012) Role of RyR2 phosphorylation at S2814 during heart failure progression. *Circ Res*. DOI: 10.1161/CIRCRESAHA.112.268094

Richardson GD, Breault D, Horrocks G, Cormack S, Hole N, Owens WA (2012) Telomerase expression in the mammalian heart. *FASEB J.* DOI: 10.1096/fj.12-208843

Rodier F, Muñoz DP, Teachenor R, Chu V, Le O, Bhaumik D, Coppé JP, Campeau E, Beauséjour CM, Kim SH, Davalos AR, Campisi J (2011) DNA-SCARS: distinct nuclear structures that sustain damage-induced senescence growth arrest and inflammatory cytokine secretion. *J Cell Sci.* DOI: 10.1242/jcs.071340

Roe AT, Frisk M and Louch WE (2015) Targeting cardiomyocyte $Ca^{2+}$ homeostasis in heart failure. *Current pharmaceutical design*. DOI: 10.2174/1381612821041412041241 29

RokitaAG and Anderson ME (2012) New therapeutic targets in cardiology: arrhythmias and $Ca^{2+}$/calmodulin-dependent kinase II (CaMKII). *Circulation*. DOI: 10.1161/CIRCULATIONAHA.112.124990

Ronco C, Martin AR, Demange L, Benhida R (2016) ATM, ATR, CHK1, CHK2 and WEE1 inhibitors in cancer and cancer stem cells. *Medchemcomm*. DOI: 10.1039/c6md00439c

Roth GS, Mattison JA, Ottinger MA, Chachich ME, Lane MA, Ingram DK (2004) Aging in rhesus monkeys: relevance to human health interventions. *Science*. DOI: 10.1126/science.1102541

Rubinsztein DC, Marino G and Kroemer G (2011) Autophagy and aging. *Cell*. DOI: 10.1016/j.cell.2011.07.030

Rugarli E and Trifunovic A (2015) Is Mitochondrial Free Radical Theory of Aging Getting Old? *Biochim Biophys Acta – Bioenerg*., *Elsevier*. DOI: 10.1016/j.bbabio.2015.08.004

Rubner M (1908) Das Problem der Lebensdauer und Seine Beziehungen Zu Wachstum und Ernarhrung. *R. Oldenburg, Muenchen, Germany.*

Sack MN, Fyhrquist FY, Saijonmaa OJ, Fuster V and Kovacic JC (2017) Basic biology of oxidative stress and the cardiovascular system: Part 1 of a 3-Part Series. *J Am Coll Cardiol*. DOI: 10.1016/j.jacc.2017.05.034

Sakamoto K, Zarrinpashneh E, Budas GR, et al. (2006) Deficiency of LKB1 in heart prevents ischemia-mediated activation of AMPKalpha2 but not AMPKalpha1. *Am J Physiol Endocrinol Metab*. DOI: 10.1152/ajpendo.00443.2005

Sasaki Y, Ikeda Y, Iwabayashi M, Akasaki Y and Ohishi M (2017) The impact of autophagy on cardiovascular senescence and diseases. *Int Heart J.* DOI: 10.1536/ihj.17-246

Scarpulla RC (2011) Metabolic control of mitochondrial biogenesis through the PGC-1 family regulatory network. *Biochim Biophys Acta*. DOI: 10.1016/j.bbamcr.2010.09.019

Sciarretta S, Yee D, Shenoy V, Nagarajan N and Sadoshima J (2014) The importance of autophagy in cardioprotection. *High Blood Press Cardiovasc Prev.* DOI: 10.1007/s40292-013-0029-9

Shah SR, Park K, Alweis R (2019) Long QT Syndrome: A Comprehensive Review of the Literature and Current Evidence. *Curr Probl Cardiol.* DOI: 10.1016/j.cpcardiol.2018.04.002

Sharifi-Sanjani M, Oyster NM, Tichy ED, Bedi KC Jr, Harel O, Margulies KB, Mourkioti F (2017) Cardiomyocyte-Specific Telomere Shortening is a Distinct Signature of Heart Failure in Humans. *J Am Heart Assoc*. DOI: 10.1161/JAHA.116.005086

Shirakabe A, Ikeda Y, Sciarretta S, Zablocki DK and Sadoshima J (2016) Aging and autophagy in the heart. *Circ Res.* DOI: 10.1161/CIRCRESAHA.116.307474

Shroff R, Arbel-Eden A, Pilch D, Ira G, Bonner WM, Petrini JH, Haber JE, Lichten M (2004) Distribution and dynamics of chromatin modification induced by a defined DNA double-strand break. *Curr Biol.* DOI: 10.1016/j.cub.2004.09.047

Small SA, Chawla MK, Buonocore M, Rapp PR, Barnes CA (2004) Imaging correlates of brain function in monkeys and rats isolates a hippocampal subregion differentially vulnerable to aging. Proc Natl Acad. Sci. U S A. DOI: 10.1073/pnas.0400285101

Smith DE, Rapp PR, McKay HM, Roberts JA, Tuszynski MH (2004) Memory impairment in aged primates is associated with focal death of cortical neurons and atrophy of subcortical neurons. J Neurosci. DOI: 10.1523/JNEUROSCI.4289-03.2004

Sokolov S, Peters CH, Rajamani S, Ruben PC (2013) Proton-dependent inhibition of the cardiac sodium channel Nav1.5 by ranolazine. *Front Pharmacol*. DOI: 10.3389/fphar.2013.00078.

Speakman JR, Talbot DA, Selman C, Snart S, McLaren JS, Redman P, Krol E, Jackson DM, Johnson MS, Brand MD (2004) Uncoupled and surviving: individual mice with high metabolism have greater mitochondrial uncoupling and live longer. *Aging Cell*. DOI: 10.1111/j.1474-9728.2004.00097.x

Steenman M and Lande G (2017) Cardiac aging and heart disease in humans. *Biophys Rev.* DOI: 10.1007/s12551-017-0255-9

Takeuchi S, Takahashi A, Motoi N, Yoshimoto S, Tajima T, Yamakoshi K, Hirao A, Yanagi S, Fukami K, Ishikawa Y, Sone S, Hara E, Ohtani N (2010) Intrinsic cooperation between p16INK4a and p21Waf1/Cip1 in the onset of cellular senescence and tumor suppression in vivo*. Cancer Res.* DOI: 10.1158/0008-5472.CAN-10-0801

Taneike M, Yamaguchi O, Nakai A, Hikoso S, Takeda T, Mizote I et al. (2010) Inhibition of autophagy in the heart induces age-related cardiomyopathy. *Autophagy.* DOI: 10.4161/auto.6.5.11947

Tocchi A, Quarles EK, Basisty N, Gitari L, Rabinovitch PS (2015) Mitochondrial dysfunction in cardiac aging. *Biochim Biophys. Acta*. DOI: 10.1016/j.bbabio.2015.07.009

Tower J (2000) Transgenic methods for increasing Drosophila life span. *Mech Ageing Dev*. DOI: 10.1016/s0047-6374(00)00152-4

Turan ZG, Parvizi P, Dönertaş HM, Tung J, Khaitovich P, Somel M (2019) Molecular footprint of Medawar's mutation accumulation process in mammalian aging. *Aging Cell*. DOI: 10.1111/acel.12965

Tsutsui H, Kinugawa S, Matsushima S (2011) Oxidative stress and heart failure. *Am J Physiol Heart Circ. Physiol.* DOI: 10.1152/ajpheart.00554.2011

Undrovinas AI, Fleidervish IA, Makielski JC (1992) Inward sodium current at resting potentials in single cardiac myocytes induced by the ischemic metabolite lysophosphatidylcholine. *Circ Res*. DOI: 10.1161/01.res.71.5.1231

Valdivia CR, Chu WW, Pu J, Foell JD, Haworth RA, Wolff MR, Kamp TJ, Makielski JC (2005) Increased late sodium current in myocytes from a canine heart failure model and from failing human heart. *J Mol Cell Cardiol*. DOI: 10.1016/j.yjmcc.2004.12.012

Vijg J and Suh Y (2013) Genome instability and aging. *Annu Rev Physiol.* DOI: 10.1146/annurev-physiol-030212-183715

Viollet B, Athea Y, Mounier R, et al. (2009) AMPK: Lessons from transgenic and knockout animals. *Front Biosci (Landmark Ed)*. DOI: 10.2741/3229

Voigt N, Li N, Wang Q, Wang W, Trafford AW, Abu-Taha I, Sun Q, Wieland T, Ravens U, Nattel S, Wehrens XH, Dobrev D (2012) Enhanced sarcoplasmic reticulum $Ca^{2+}$ leak and increased $Na^{+}$-$Ca^{2+}$ exchanger function underlie delayed afterdepolarizations in patients with chronic atrial fibrillation. *Circulation*. DOI: 10.1161/CIRCULATIONAHA.111.067306

Watanabe S, Kawamoto S, Ohtani N, Hara E (2017) Impact of senescence-associated secretory phenotype and its potential as a therapeutic target for senescence-associated diseases. *Cancer Sci.* DOI: 10.1111/cas.13184

Weismann A (1889) Essays upon Heredity and Kindred Biological Problems, Volume 1. *Clarendon Press.*

Williams GC (1957) Pleiotropy, natural selection, and the evolution of senescence. *Evolution*. DOI: 10.2307/2406060

Wu Y, MacMillan LB, McNeill RB, Colbran RJ, Anderson ME (1999) CaM kinase augments cardiac L-type Ca2+ current: a cellular mechanism for long Q-T arrhythmias. *Am J Physiol*. DOI: 10.1152/ajpheart.1999.276.6.H2168Xie

Xu A and Narayanan N (1998) Effects of aging on sarcoplasmic reticulum $Ca^{2+}$-cycling proteins and their phosphorylation in rat myocardium. *Am J Physiol.* DOI: 10.1152/ajpheart.1998.275.6.H2087

Yakes FM, Van Houten B (1997) Mitochondrial DNA damage is more extensive and persists longer than nuclear DNA damage in human cells following oxidative stress. *Proc Natl Acad Sci U S A*. DOI: 10.1073/pnas.94.2.514

Yamakoshi K, Takahashi A, Hirota F, Nakayama R, Ishimaru N, Kubo Y, Mann DJ, Ohmura M, Hirao A, Saya H, Arase S, Hayashi Y, Nakao K, Matsumoto M, Ohtani N, Hara E (2009) Real-time in vivo imaging of $p16^{Ink4a}$ reveals cross talk with p53. *J Cell Biol*. DOI: 10.1083/jcb.200904105

Yan J, Zhao W, Thomson JK, et al. (2018) Stress signaling JNK2 crosstalk with CaMKII underlies enhanced atrial arrhythmogenesis. *Circ Res.* DOI: 10.1161/CIRCRESAHA.117.312536

Yang KC, Kyle JW, Makielski JC, Dudley SC Jr (2015) Mechanisms of sudden cardiac death: oxidants and metabolism. *Circ Res.* DOI: 10.1161/CIRCRESAHA.116.304691

Zhang J, Zhao P, Quan N, et al. (2017) The endotoxemia cardiac dysfunction is attenuated by AMPK/mTOR signaling pathway regulating autophagy. *Biochem Biophys Res Commun*. DOI: 10.1016/j.bbrc.2017.08.034

Zhang P (2017) CaMKII: The molecular villain that aggravates cardiovascular disease. *Exp Ther Med*. DOI: 10.3892/etm.2017.4034

Zima AV, Pabbidi MR, Lipsius SL, Blatter LA. Effects of mitochondrial uncoupling on $Ca^{2+}$ signaling during excitation-contraction coupling in atrial myocytes. *Am J Physiol Heart Circ Physiol*. DOI: 10.1152/ajpheart.00932.2012

# Part 2

# Induced pluripotent stem cells (iPSCs)

## 2.1 Reprogramming

iPSCs are pluripotent stem cells that can be generated from the reprogramming of a somatic cell. The iPSC technology was pioneered by Shinya Yamanaka's lab in 2006 by showing that the introduction of four specific genes (Oct4, Sox2, Klf4, and c-Myc), later called 'Yamanaka factors', could convert a somatic cell into a pluripotent cell [Takahashi and Yamanaka 2006].

The Yamanaka factors are transcription factors (TFs) which were found to be active in embryonic stem cells (ESCs). The combination of Oct4, Sox2 and Nanog is called 'core pluripotency gene cocktail' because these TFs are able to form an autoregulatory circuitry for pluripotency. The core pluripotency cocktail has the ability to activate genes necessary to maintain ESC-like pluripotency and to repress lineage-specific transcription factors, preventing the exit from the pluripotent state [Pan et al. 2006; Jaenisch and Young 2008]. Other factors present in reprogramming cocktails, such as c-Myc, are used to facilitate activation of this autoregulatory circuitry by stimulating gene expression and proliferation [Rahl et al. 2010].

The process to attain pluripotency has been described as consisting of three steps (**Fig 9**) [David and Polo 2014]. The first one, called initiation, is characterized by the downregulation of somatic genes, a metabolic switch from oxidative phosphorylation to glycolysis, an increase in cell proliferation, and the reactivation of telomerase activity. This stage also requires changes in cell morphology, in particular a mesenchymal-to-epithelial transition (MET) which provides for the acquisition of epithelial characteristics that lead to epigenetic modifications important for the reprogramming [Samavarchi-Tehrani et al. 2010; Downing et al. 2013]. The second phase, called maturation, involves the upregulation of endogenous pluripotency genes, such as SSEA1, Oct4, Nanog, Esrrb, and Sox2. This step is most likely the limitation of the reprogramming process since a great number of cells undergo apoptosis in this phase [Tanabe et al. 2013]. In the third and final step, called stabilization, cells undergo other changes, like rearrangements in DNA methylation and Telomeres elongation [Polo et al. 2012].

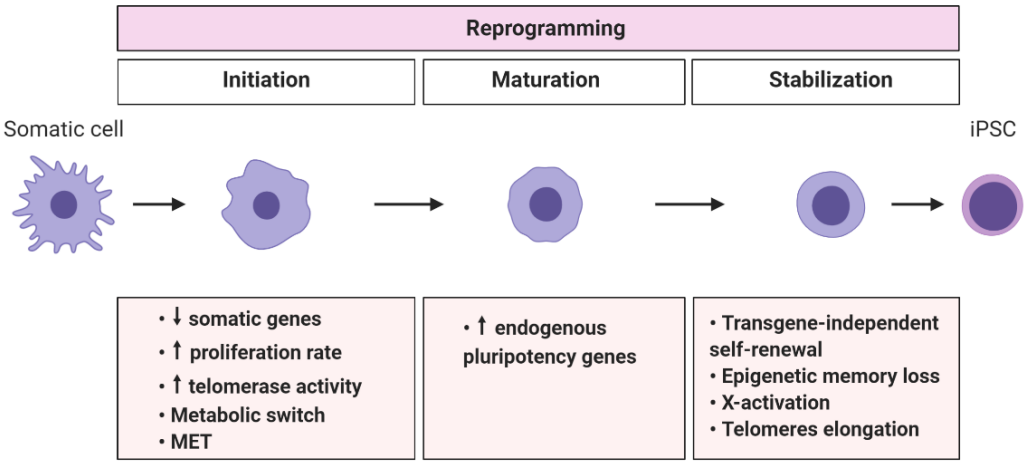


**Figure 9.** Schematization of the three phases of reprogramming and the main events by which they are characterized. [According to Lodrini et al. 2020]

## 2.2 Differentiation to iPSC-derived cardiomyocytes

The pluripotent features of human iPSCs and the possibility to derive cardiomyocytes from them (hiPSC-CMs) potentially starting from minimally invasive samples (e.g. skin biopsy) enable the creation of an in-vitro disease-specific model also fit for preclinical drug screening, thus replacing non-human cellular and animal models which present inter-species differences in cardiac cell biology and electrophysiology [Dixon and Spinale 2009; Burridge et al. 2014; Dell'Era et al. 2015].

The initial observation that stem cells could mature into beating CMs was reported when first culturing ESCs in suspension: these cells spontaneously formed three-dimensional aggregates called 'embryoid bodies' (EBs) which contained cells with functional and electrical properties similar to CMs [Itskovitz-Eldor et al. 2000]. A similar process occurring with iPSCs was later reported [Zhang et al. 2009].

Different signaling pathways and growth factors have been found involved in successfully inducing cardiac differentiation in culture (**Fig 10**) [Winnier et al. 1995; Marvin et al. 2001; Naujok et al. 2014]. To obtain ventricular-like CMs, activation of the canonical Wnt/β-catenin signaling pathway can induce gastrulation-like events in iPSCs cultured in a high-density monolayer with a serum- and feeder cell-free system [Naito et al. 2006]. Spontaneously contracting areas are generally observed after 10 days from induction and, after three weeks, these cell preparations typically consist of ~50% CMs [Yang et al. 2008]. Since all these growth factors don't elicit optimal transcript levels to induce cardiogenesis if used outside the right time frames [Schlange et al. 2000], time-dependent media supplementation is crucial to obtain an efficient lineage-specific differentiation. Commercial kits provide standardized and simplified protocols to increase the reproducibility of the differentiation procedure [Ross et al. 2019].

Since the reprogramming and re-differentiation processes can start from all type of somatic cells, this raised the question of how the somatic source may influence the phenotype of hiPSC-CMs. Although different somatic sources have shown a cardiogenic potential when reprogrammed and then exposed to appropriate

cardiac stimuli, recently it has been reported that hiPSCs from cardiac precursors may be a more suitable source to obtain more mature cardiac cells. Indeed, several sources have shown that cardiac progenitor cell (CPC)-derived hiPSCs originate CMs with an increased expression of cardiac markers in comparison to hiPSC-CMs from other tissues of the same patient, such as bone marrow and dermal fibroblasts [Sanchez-Freire et al. 2014; Meraviglia et al. 2016]. Additionally, recent works have observed variability in electrical properties and sensitivity to ion channel blockers in CMs derived from different sources [Pianezzi et al. 2019]. In this studies, CPC-derived CMs started to beat earlier and had a higher maturation degree highlighted by an increased expression of $I_{Ks}$ in comparison to HDF- and BMC-derived CMs. In support of this, exposition to the $I_{Ks}$ blocker JNJ303 resulted in a QT prolongation more pronounced in CPC-derived CMs than in HDF- and BMC-CMs. Moreover, CPC-derived CMs had a more mature calcium handling as demonstrated by the number of cells able to elicit a RyR-mediated $Ca^{2+}$ release when exposed to caffeine.

In general, although different somatic cells show a cardiogenic potential when exposed to appropriate cardiac stimuli, CPCs seem to be temporally and qualitatively more prone to differentiate into functional cardiac cells. The aforementioned works emphasized the existence of an epigenetic memory retained by iPSCs from their originary tissue, probably due to a residual tissue-specific DNA methylation that persists even through reprogramming and re-differentiation [Kim et al. 2011].

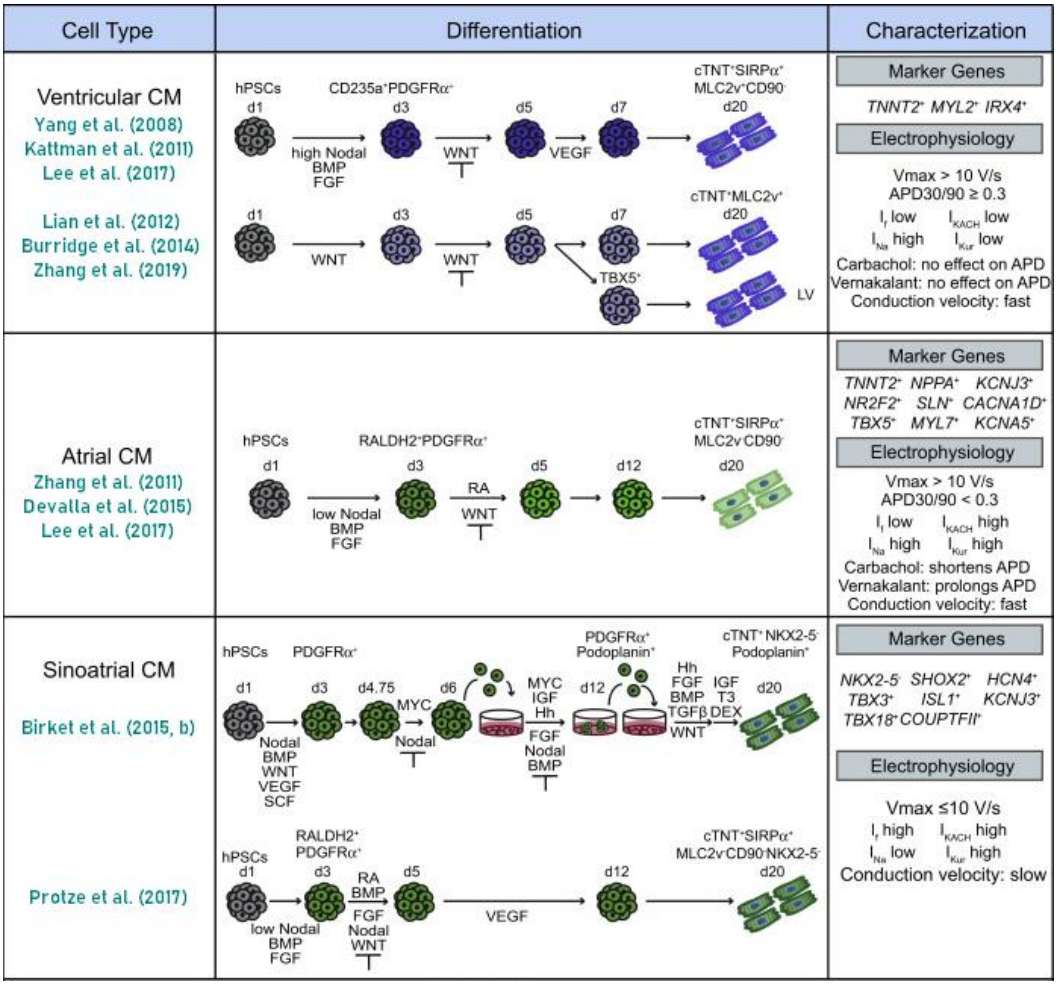


**Figure 10.** Summary of the differentiation protocols for the Generation of hiPSC-derived cardiac lineages. [According to Protze et al. 2019]

## 2.3 Characteristics and limitations of human iPSC-CMs

The spontaneous beating that appears at the beginning of the differentiation process and the positivity for cardiac troponin T (cTnT) are generally accepted as signs that hiPSCs have differentiated to CMs. The spontaneous electrical activity within newly developed hiPSC-CMs vouches for the expression of functional cardiac ion channels and transporters related to generation of action potential (AP) and contractility. Unfortunately, if more detailed analyses are conducted, it can be verified how hiPSC-CMs generated with current protocols are still quite immature and more similar to neonatal CMs than adult ones [Matsa et al. 2014; Karakikes et al. 2018; Tu et al. 2018].

Several ionic currents have been characterized in single hiPSC-CMs by using the patch-clamp technique, such as the sodium ($I_{Na}$), the calcium ($I_{Ca,L}$ and $I_{Ca,T}$) and the potassium ones ($I_{to}$, $I_{Kr}$ and $I_{Ks}$) [Davis et al. 2010; Moretti et al. 2010; Ma et al. 2011; Yazawa et al. 2011; Ivashchenko et al. 2013; Goversen et al. 2018]. The biophysical properties of each of these ion channels have been studied in relation to time of culture and it has been reported that there is an increase in ionic current densities up to 80 days of the differentiation process. Consequently, hiPSC-CMs are characterized by heterogeneous AP profiles [Otsuji et al. 2010; Ben-Ari et al. 2016; Veerman et al. 2017].

Based on the AP properties, hiPSC-CMs can be classified in either atrial-, ventricular- or nodal-like CMs, and a single cell culture can be formed by a mix of these three categories [Zhang et al. 2009; Ma et al. 2011; Burridge et al. 2014]. Nodal-like hiPSC-CMs and sinoatrial adult CMs APs are comparable, showing spontaneous electrical activity thanks to the contribution of the funny ($I_f$) and calcium ($I_{CaL}$) currents. Conversely, major differences between adult and hiPSC-derived ventricular or atrial CMs can be found. Indeed, hiPSC-CMs show more depolarized diastolic potential ($E_{diast}$) and persistent spontaneous electrical activity thanks to the expression of $I_f$ and the absence of the inward-rectifier potassium current ($I_{K1}$) [Doss et al. 2012]. As a consequence of the depolarized $E_{diast}$, AP upstroke velocity and APD in hiPSC-CMs are not completely

superimposable to those of adult CMs. Additionally, hiPSC-CMs are characterized by underdeveloped sarcomeric structure and T-tubules that may affect $Ca^2$ handling (**Fig 11**) [Bedada et al. 2016; Lee et al. 2011; Gherghiceanu et al. 2011; Lundy et al. 2013; Cadet et al. 2017].

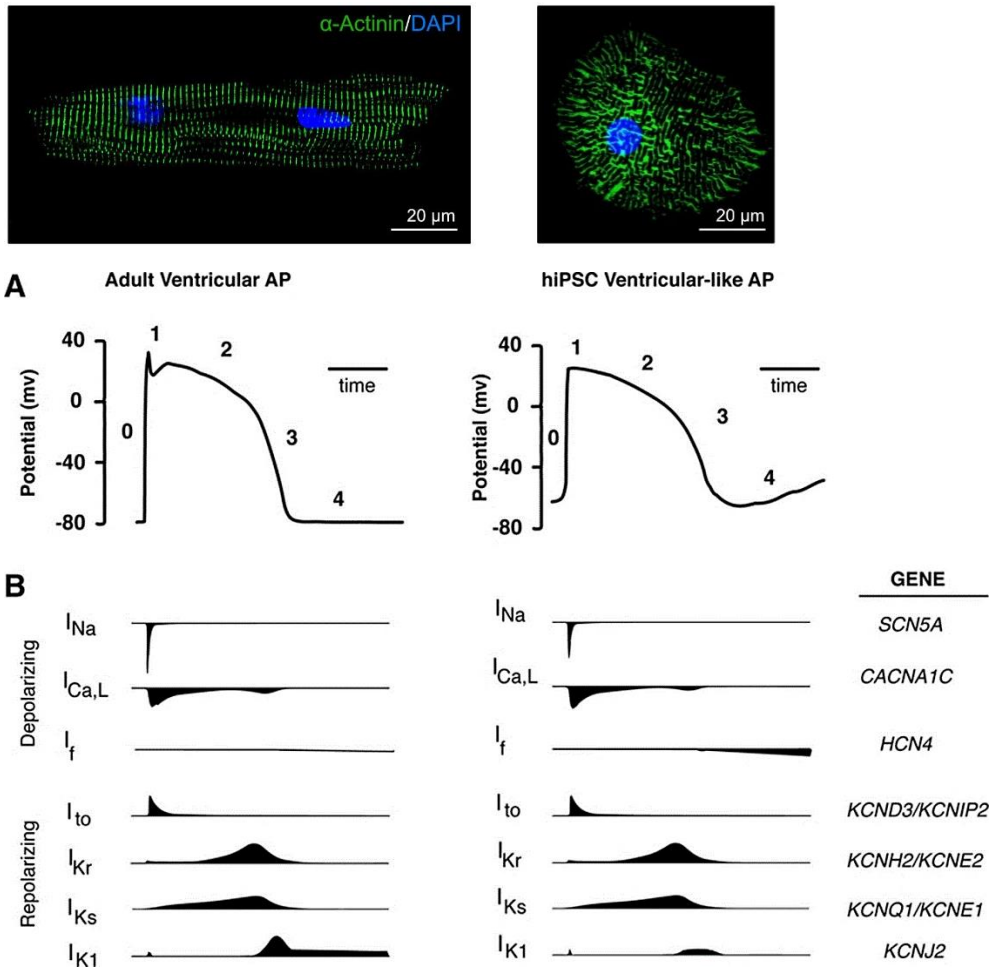


**Figure 11.** Morphology and action potentials (APs) of ventricular-like hiPSC-CMs in comparison to adult ventricular cardiomyocytes. (**a**) Schematic of ventricular APs. (**b**) The ionic currents and the genes that generate the currents with schematics of the current trajectories are shown below the APs. [According to Karakikes et al. 2015]

## 2.4 Maturation improvement

Despite their limitations, hiPSC-CMs can be still considered the experimental model that is the closest to humans for mechanisms of cardiac disease and pharmacological responses [Burridge et al. 2014; Dell'Era et al. 2015]. Several approaches are being pursued to further mature the hiPSC-derived cardiomyocytes. These include recapitulating the metabolic changes that occur within the cardiomyocytes at birth and the use of tissue engineering to expose the developing cardiomyocytes to electromechanical forces present in the heart. Highly mature CMs should display: (1) rod-shaped morphology, (2) longitudinally oriented and aligned long sarcomere structures, (3) regularly distributed mitochondria, (4) high degree of multinucleation, (5) fatty acid metabolism, (6) low proliferative capacity, (7) diastolic resting potential around -80 mV, (8) high contractile force, and (9) qualitatively normal physiological and pharmacological responses [Robertson et al. 2013].

After birth, circulating hormones and metabolites promote a switch from glycolysis to fatty acid oxidation to meet the increased energy demands of the neonatal heart [Lopaschuk and Jaswal 2010; Piquereau and Ventura-Clapier 2018]. At this stage, the cardiomyocytes also rapidly lose their proliferative capacity and advance their sarcomere organization and calcium handling for increased force of contraction. To mimic these hormonal changes, several studies have tested thyroid and steroid hormones on the differentiating hiPSC-CMs populations, managing to induce a modest maturation of CMs in terms of sarcomere organization and increase in mitochondrial capacity [Lee et al. 2010; Parikh et al. 2017; Yang et al. 2014]. Similar results can be obtained by inducing a metabolic switch through reduction of glucose and increase of fatty acids in the culture media [Correia et al. 2017; Hu et al. 2018; Mills et al. 2017; Horikoshi et al. 2019].

Other approaches to induce maturation involve the application of mechanical stimulation to the cells, mimicking the increased contractile demand of the heart after birth [Thavandiran et al. 2013; Zhang et al. 2013; Mannhardt et al.

2016; Shadrin et al. 2017; Tiburcy et al. 2017]. These studies resulted in increased expression of contractile apparatus genes, improved sarcomere organization, increased contractile force, and improvement in conduction velocities.

In addition to mechanical stimulation, electrical stimulation has been shown to improve structural and electrophysiological maturation of cardiac tissues [Nunes et al. 2013]. One of the most advanced engineered tissues reported to date was generated through the increased electrical stimulation of early-stage cardiomyocytes in a fibrin hydrogel [Ronaldson-Bouchard et al. 2018]. The resulting tissues showed highly organized sarcomeres and T-tubules, improved calcium handling, as well as mitochondria oxidative capacity similar to that of primary human cardiomyocytes.

Despite these improvements in the maturation status, these engineered tissues still show differences if compared to adult heart tissue. Further improvements may require a combination of the above maturation strategies, purification methods (e.g. pre-plating, metabolic selection, and antibody purification methods), and the inclusion of cardiac cell types different from myocytes (epicardial cells, cardiac fibroblasts, endothelial cells, and macrophages).

## 2.5 Use of hiPSC-CMs in biomedical research

hiPSC-CMs carry the exact genetic background of the patient of origin. Therefore, cell lines have been created from individuals with different cardiac diseases, such as mutations in ion channel genes or in sarcomeric proteins [Brandao et al. 2017; Rocchetti et al. 2017; Brodehl et al. 2019; Benzoni et al. 2020]. In some cases, hiPSC-derived CMs do not only recapitulate the disease phenotypes of ion channel mutations that lead to arrhythmias and sudden cardiac death, but have also indicated treatment modalities. These models of channelopathies are of particular interest because, as mentioned earlier, the pathophysiology of animal models is different than humans. For example, mouse models with mutations in KCNQ1 have significant differences in the handling of rectifying potassium currents compared to humans [Davis et al. 2011]. Since the majority of cardiac

ion channels is expressed within 2 weeks of differentiation, hiPSC-CMs immaturity has had a relatively little impact on predictive outcomes of these models, allowing them to surpass mice as preferred experimental model in the study of channelopathies [Blinova et al. 2018].

Changes in electrical properties of hiPSC-CMs can be determined reliably using electrophysiology (patch-clamp technique or multiple electrode arrays) or optical methods (voltage- or calcium-sensitive dyes) [van Meer et al. 2016]. Conversely, phenotypes resulting from cardiac hypertrophy or myopathy have been more difficult to measure. A few reports of hiPSC-CMs from patients with hypertrophic cardiomyopathy have recently emerged [Carvajal-Vergara et al. 2010]. However, not all standard criteria used to analyse cardiomyocyte hypertrophy could be performed due to the mixed population of cells obtained from the differentiation procedure, and hiPSC-CMs immature morphology which makes it difficult to capture the alterations in size or contractility.

Furthermore, hiPSC-CM have come into use in the emerging discipline of quantitative system pharmacology to test drug efficacy and safety [Li et al 2019]. This cell model has been already applied in screening the proarrhythmic potential of drugs that can inhibit ionic channels, like potassium (e.g. sotalol, dofetilide, E4031), sodium (quinidine, flecainide), and calcium channel inhibitors (verapamil, diltiazem) [Gibson et al 2014; Lu et al. 2015; Patel et al. 2019]. These drugs have been the main protagonists of the FDA's Comprehensive In-Vitro Proarrythmia Assay (CiPA) initiative, which uses a combination of in-silico and in-vitro models for the assessment of potential proarrhythmic effects of drugs [Colatsky et al. 2016]. The CiPA workflow consists of three main steps: firstly, assessment of drug's effects on the critical human ventricular ion channel currents; secondly, in-silico integration of the ion channel effects to determine the net effects on the cardiac action potential; thirdly, a check for discrepancies in fully integrated biological systems, such as hiPSC-CMs [Sager et al. 2014]. Compounds that are assessed as being at low likelihood for causing TdP and QT prolongation may receive benign labelling and move to the next steps in pharmacological studies.

The CiPA initiative represents a predictive strategy applied on hiPSC-CMs for development of therapeutic drugs potentially safety in term of cardiac function.
Currently, hiPSC-CMs are also being introduced in the field of regenerative medicine. It is known that the underlying cause of heart failure is an irreversible loss of contractile muscle mass and, at least in animal models of myocardial infarction, transplanted cardiomyocytes (CMs) can improve left ventricular (LV) function [Li et al. 1996]. However, it is tricky to find a clinically usable source of contractile cells. Cultivating human primary CMs has been a subject of decades of fruitless research, and donor CMs would be allogeneic and therefore not suitable for transplantation without immunosuppression. Therefore, it is widely accepted that the replacement of contractile myocardium requires the use of the pluripotent stem cell technology. However, maturation of hiPSC-CMs remains a challenge since only neonatal-like CMs have been derived so far. The 3D environment has been long postulated to play a vital role in generating the proper mechanical cues and driving terminal differentiation [Wang et al. 2010]. Combinatory studies are thus needed to improve hiPSC-CMs morphology and contractility, and allow their use to engineer heart tissue.

## 2.6 References


Ben-Ari M, Naor S, Zeevi-Levin N, et al. (2016) Developmental changes in electrophysiological characteristics of human-induced pluripotent stem cell-derived cardiomyocytes. *Heart Rhythm*. DOI: 10.1016/j.hrthm.2016.08.045

Benzoni P, Campostrini G, Landi S, Bertini V, Marchina E, Iascone M, Ahlberg G, Olesen MS, Crescini E, et al. (2020) Human iPSC modelling of a familial form of atrial fibrillation reveals a gain of function of $I_f$ and $I_{CaL}$ in patient-derived cardiomyocytes. *Cardiovasc Res.* DOI: 10.1093/cvr/cvz217

Blinova K, Dang Q, Millard D, et al (2018) International Multisite Study of Human-Induced Pluripotent Stem Cell-Derived Cardiomyocytes for Drug Proarrhythmic Potential Assessment. *Cell Rep.* DOI: 10.1016/j.celrep.2018.08.079

Brandão KO, Tabel VA, Atsma DE, Mummery CL and Davis RP (2017) Human pluripotent stem cell models of cardiac disease: from mechanisms to therapies. *Dis Model Mech*. DOI: 10.1242/dmm.030320

Brodehl A, Ebbinghaus H, Deutsch MA, Gummert J, Gärtner A, Ratnavadivel S and Milting H (2019) Human Induced Pluripotent Stem-Cell-Derived Cardiomyocytes as Models for Genetic Cardiomyopathies. *Int J Mol Sci*. DOI: 10.3390/ijms20184381

Burridge PW, Matsa E, Shukla P, Lin ZC, Churko JM, Ebert AD, Lan F, Diecke S, Huber B, Mordwinkin NM, Plews JR, Abilez OJ, Cui B, Gold JD, Wu JC (2014) Chemically defined generation of human cardiomyocytes. *Nat Methods*. DOI: 10.1038/nmeth.2999

Cadet JS and Kamp TJ (2017) A Recipe for T-Tubules in Human iPS Cell-Derived Cardiomyocytes. *Circ Res*. SOI: 10.1161/CIRCRESAHA.117.312177

Carvajal-Vergara X, Sevilla A, D'Souza SL, et al. (2010) Patient-specific induced pluripotent stem-cell-derived models of LEOPARD syndrome. *Nature*. DOI: 10.1038/nature09005

Colatsky T, Fermini B, Gintant G, Pierson JB, Sager P, Sekino Y, Strauss DG, Stockbridge N (2016) The Comprehensive in Vitro Proarrhythmia Assay (CiPA) initiative – Update on progress. *J Pharmacol Toxicol Methods*. DOI: 10.1016/j.vascn.2016.06.002

Correia C, Koshkin A, Duarte P, et al. (2017) Distinct carbon sources affect structural and functional maturation of cardiomyocytes derived from human pluripotent stem cells. *Sci Rep.* DOI: 10.1038/s41598-017-08713-4

David L and Polo JM (2014) Phases of reprogramming. *Stem Cell Res.* DOI: 10.1016/j.scr.2014.03.007

Davis RP, Casini S, van den Berg CW, et al. (2012) Cardiomyocytes derived from pluripotent stem cells recapitulate electrophysiological characteristics of an overlap syndrome of cardiac sodium channel disease. *Circulation*. DOI: 10.1161/CIRCULATIONAHA.111.066092

Davis RP, van den Berg CW, Casini S, Braam SR, Mummery CL (2011) Pluripotent stem cell models of cardiac disease and their implication for drug discovery and development. *Trends Mol Med*. DOI: 10.1016/j.molmed.2011.05.001

Dell'Era P, Benzoni P, Crescini E, Valle M, Xia E, Consiglio A, Memo M (2015) Cardiac disease modeling using induced pluripotent stem cell-derived human cardiomyocytes. *World J Stem Cells*. DOI: 10.4252/wjsc.v7.i2.329

Dixon JA and Spinale FG (2009) Large animal models of heart failure: a critical link in the translation of basic science to clinical practice. *Circ Heart Fail*. DOI: 10.1161/CIRCHEARTFAILURE.108.814459

Doss MX, Di Diego JM, Goodrow RJ, et al. (2012) Maximum diastolic potential of human induced pluripotent stem cell-derived cardiomyocytes depends critically on I(Kr). *PLoS One*. DOI:10.1371/journal.pone.0040288

Downing TL, Soto J, Morez C, Houssin T, Fritz A, Yuan F, Chu J, Patel S, Schaffer DV, Li S (2013) Biophysical regulation of epigenetic state and cell reprogramming. *Nat Mater*. DOI: 10.1038/nmat3777

Gherghiceanu M, Barad L, Novak A, et al. (2011) Cardiomyocytes derived from human embryonic and induced pluripotent stem cells: comparative ultrastructure*. J Cell Mol Med.* DOI: 10.1111/j.1582-4934.2011.01417.x

Gibson JK, Yue Y, Bronson J, Palmer C, Numann R (2014) Human stem cell-derived cardiomyocytes detect drug-mediated changes in action potentials and ion currents. *J Pharmacol Toxicol Methods*. DOI: 10.1016/j.vascn.2014.09.005

Goversen B, van der Heyden MAG, van Veen TAB, de Boer TP (2018) The immature electrophysiological phenotype of iPSC-CMs still hampers in vitro drug screening: Special focus on $I_{K1}$. *Pharmacol Ther*. DOI: 10.1016/j.pharmthera.2017.10.001

Jaenisch R and Young R (2008) Stem cells, the molecular circuitry of pluripotency and nuclear reprogramming. *Cell*. DOI: 10.1016/j.cell.2008.01.015

Horikoshi Y, Yan Y, Terashvili M, Wells C, Horikoshi H, Fujita S, Bosnjak ZJ, Bai X (2019) Fatty Acid-Treated Induced Pluripotent Stem Cell-Derived Human Cardiomyocytes

Exhibit Adult Cardiomyocyte-Like Energy Metabolism Phenotypes. *Cells*. DOI: 10.3390/cells8091095

Hu D, Linders A, Yamak A, et al. Metabolic Maturation of Human Pluripotent Stem Cell-Derived Cardiomyocytes by Inhibition of HIF1α and LDHA (2018) *Circ Res.* DOI: 10.1161/CIRCRESAHA.118.313249

Itskovitz-Eldor J, Schuldiner M, Karsenti D, Eden A, Yanuka O, Amit M, Soreq H, Benvenisty N (2000) Differentiation of human embryonic stem cells into embryoid bodies compromising the three embryonic germ layers. *Mol Med.* PMID: 10859025

Ivashchenko CY, Pipes GC, Lozinskaya IM, et al. (2013) Human-induced pluripotent stem cell-derived cardiomyocytes exhibit temporal changes in phenotype. *Am J Physiol Heart Circ Physiol*. DOI: 10.1152/ajpheart.00819.2012

Karakikes I, Ameen M, Termglinchan V, Wu JC (2015) Human induced pluripotent stem cell-derived cardiomyocytes: insights into molecular, cellular, and functional phenotypes. *Circ Res*. DOI: 10.1161/CIRCRESAHA.117.305365

Kim K, Zhao R, Doi A, et al. (2011) Donor cell type can influence the epigenome and differentiation potential of human induced pluripotent stem cells [published correction appears in Nat Biotechnol. 2012]. *Nat Biotechnol*. DOI: 10.1038/nbt.2052

Lee YK, Ng KM, Chan YC, et al. (2010) Triiodothyronine promotes cardiac differentiation and maturation of embryonic stem cells via the classical genomic pathway. *Mol Endocrinol*. DOI:10.1210/me.2010-0032

Lee YK, Ng KM, Lai WH, et al. (2011) Calcium homeostasis in human induced pluripotent stem cell-derived cardiomyocytes. *Stem Cell Rev Rep*. DOI: 10.1007/s12015-011-9273-3

Li RK, Jia ZQ, Weisel RD, Mickle DA, Zhang J, Mohabeer MK, Rao V, Ivanov J (1996) Cardiomyocyte transplantation improves heart function. *Ann Thorac Surg*. DOI: 10.1016/s0003-4975(96)00389-x

Li Z, Garnett C, Strauss DG (2019) Quantitative Systems Pharmacology Models for a New International Cardiac Safety Regulatory Paradigm: An Overview of the Comprehensive In Vitro Proarrhythmia Assay In Silico Modeling Approach. *CPT Pharmacometrics Syst Pharmacol*. DOI: 10.1002/psp4.12423

Lu HR, Whittaker R, Price JH, et al. (2015) High Throughput Measurement of $Ca^{2+}$ Dynamics in Human Stem Cell-Derived Cardiomyocytes by Kinetic Image Cytometery: A Cardiac Risk Assessment Characterization Using a Large Panel of Cardioactive and Inactive Compounds. *Toxicol Sci*. DOI: 10.1093/toxsci/kfv201

Lodrini AM, Barile L, Rocchetti M, Altomare C (2020) Human Induced Pluripotent Stem Cells Derived from a Cardiac Somatic Source: Insights for an In-Vitro Cardiomyocyte Platform. *Int J Mol Sci.* DOI: 10.3390/ijms21020507

Lopaschuk GD and Jaswal JS (2010) Energy metabolic phenotype of the cardiomyocyte during development, differentiation, and postnatal maturation. *J Cardiovasc Pharmacol*. DOI: 10.1097/FJC.0b013e3181e74a14

Lundy SD, Zhu WZ, Regnier M, Laflamme MA (2013) Structural and functional maturation of cardiomyocytes derived from human pluripotent stem cells. *Stem Cells Dev*. DOI: 10.1089/scd.2012.0490

Ma J, Guo L, Fiene SJ, et al. (2011) High purity human-induced pluripotent stem cell-derived cardiomyocytes: electrophysiological properties of action potentials and ionic currents. *Am J Physiol Heart Circ Physiol*. DOI: 10.1152/ajpheart.00694.2011

Mannhardt I, Breckwoldt K, Letuffe-Brenière D, et al. (2016) Human Engineered Heart Tissue: Analysis of Contractile Force. Stem Cell Reports. DOI: 10.1016/j.stemcr.2016.04.011

Marvin MJ, Di Rocco G, Gardiner A, Bush SM, Lassar AB (2001) Inhibition of Wnt activity induces heart formation from posterior mesoderm. *Genes Dev*. DOI: 10.1101/gad.855501

Matsa E, Burridge PW, Wu JC (2014) Human stem cells for modeling heart disease and for drug discovery. *Sci Transl Med*. DOI: 10.1126/scitranslmed.3008921

Meraviglia V, Wen J, Piacentini L, et al. (2016) Higher cardiogenic potential of iPSCs derived from cardiac versus skin stromal cells. *Front Biosci (Landmark Ed)*. DOI: 10.2741/4417

Mills RJ, Titmarsh DM, Koenig X, et al. (2017) Functional screening in human cardiac organoids reveals a metabolic mechanism for cardiomyocyte cell cycle arrest. *Proc Natl Acad Sci U S A. DOI*:10.1073/pnas.1707316114

Moretti A, Bellin M, Welling A, et al. (2010) Patient-specific induced pluripotent stem-cell models for long-QT syndrome. *N Engl J Med*. DOI: 10.1056/NEJMoa0908679

Naito AT, Shiojima I, Akazawa H, et al. (2006) Developmental stage-specific biphasic roles of Wnt/beta-catenin signaling in cardiomyogenesis and hematopoiesis. *Proc Natl Acad Sci U S A*. DOI: 10.1073/pnas.0605768103

Naujok O, Diekmann U, Lenzen S (2014) The generation of definitive endoderm from human embryonic stem cells is initially independent from activin A but requires canonical Wnt-signaling. *Stem Cell Rev Rep*. DOI: 10.1007/s12015-014-9509-0

Nunes SS, Miklas JW, Liu J, et al. (2013) Biowire: a platform for maturation of human pluripotent stem cell-derived cardiomyocytes. Nat Methods. DOI: 10.1038/nmeth.2524

Otsuji TG, Minami I, Kurose Y, Yamauchi K, Tada M, Nakatsuji N (2010) Progressive maturation in contracting cardiomyocytes derived from human embryonic stem cells: Qualitative effects on electrophysiological responses to drugs. *Stem Cell Res*. DOI: 10.1016/j.scr.2010.01.002

Pan G, Li J, Zhou Y, Zheng H, Pei D (2006) A negative feedback loop of transcription factors that controls stem cell pluripotency and self-renewal. *FASEB J.* DOI: 10.1096/fj.05-5543fje

Parikh SS, Blackwell DJ, Gomez-Hurtado N, et al. (2017) Thyroid and Glucocorticoid Hormones Promote Functional T-Tubule Development in Human-Induced Pluripotent Stem Cell-Derived Cardiomyocytes. *Circ Res.* DOI: 10.1161/CIRCRESAHA.117.311920

Patel D, Stohlman J, Dang Q, Strauss DG, Blinova K (2019) Assessment of Proarrhythmic Potential of Drugs in Optogenetically Paced Induced Pluripotent Stem Cell-Derived Cardiomyocytes. *Toxicol Sci*. DOI: 10.1093/toxsci/kfz076

Pianezzi E, Altomare C, Bolis S, et al. (2019) Role of somatic cell sources in the maturation degree of human induced pluripotent stem cell-derived cardiomyocytes. *Biochim Biophys Acta Mol Cell Res*. DOI: 10.1016/j.bbamcr.2019.118538

Piquereau J and Ventura-Clapier R (2018) Maturation of Cardiac Energy Metabolism During Perinatal Development. *Front Physiol.* DOI: 10.3389/fphys.2018.00959

Polo JM, Anderssen E, Walsh RM, Schwarz BA, Nefzger CM, Lim SM, Borkent M, Apostolou E, Alaei S, Cloutier J, Bar-Nur O, Cheloufi S, Stadtfeld M, Figueroa ME, Robinton D, Natesan S, Melnick A, Zhu J, Ramaswamy S, Hochedlinger K (2012) A molecular roadmap of reprogramming somatic cells into iPS cells. *Cell*. DOI: 10.1016/j.cell.2012.11.039

Protze SI, Lee JH, Keller GM (2019) Human Pluripotent Stem Cell-Derived Cardiovascular Cells: From Developmental Biology to Therapeutic Applications. *Cell Stem Cell.* DOI: 10.1016/j.stem.2019.07.010

Rahl PB, Lin CY, Seila AC, Flynn RA, McCuine S, Burge CB, Sharp PA, Young RA (2010) c-Myc regulates transcriptional pause release. *Cell*. DOI: 10.1016/j.cell.2010.03.030

Robertson C, Tran DD, George SC (2013) Concise review: maturation phases of human pluripotent stem cell-derived cardiomyocytes. *Stem Cells*. DOI: 10.1002/stem.1331

Rocchetti M, Sala L, Dreizehnter L, Crotti L, Sinnecker D, Mura M, Pane LS, Altomare C, Torre E, Mostacciuolo G, Severi S, et al. (2017) Elucidating arrhythmogenic mechanisms of long-QT syndrome CALM1-F142L mutation in patient-specific induced pluripotent stem cell-derived cardiomyocytes. *Cardiovasc Res.* DOI: 10.1093/cvr/cvx006. PMID: 28158429

Ronaldson-Bouchard K, Ma SP, Yeager K, et al. (2018) Advanced maturation of human cardiac tissue grown from pluripotent stem cells [published correction appears in Nature, 2019]. *Nature*. DOI: 10.1038/s41586-018-0016-3

Ross S, Holliday M, Lim S, Semsarian C (2019) Characterization of the first induced pluripotent stem cell line generated from a patient with autosomal dominant catecholaminergic polymorphic ventricular tachycardia due to a heterozygous mutation in cardiac calsequestrin-2. *Stem Cell Res*. DOI: 10.1016/j.scr.2019.101450

Sager PT, Gintant G, Turner JR, Pettit S and Stockbridge N (2014) Rechanneling thecardiac proarrhythmia safety paradigm: a meeting report from the cardiac safety research consortium. *Am Heart J*. DOI: 10.1016/j.ahj.2013.11.004

Samavarchi-Tehrani P, Golipour A, David L, Sung HK, Beyer TA, Datti A, Woltjen K, Nagy A, Wrana JL (2010) Functional genomics reveals a BMP-driven mesenchymal-to-epithelial transition in the initiation of somatic cell reprogramming. *Cell Stem Cell.* DOI: 10.1016/j.stem.2010.04.015

Sanchez-Freire V, Lee AS, Hu S, et al. (2014) Effect of human donor cell source on differentiation and function of cardiac induced pluripotent stem cells. *J Am Coll Cardiol*. DOI: 10.1016/j.jacc.2014.04.056

Schlange T, Andrée B, Arnold HH, Brand T (2000) BMP2 is required for early heart development during a distinct time period. *Mech Dev*. DOI: 10.1016/s0925-4773(99)00311-1

Shadrin IY, Allen BW, Qian Y, et al. (2017) Cardiopatch platform enables maturation and scale-up of human pluripotent stem cell-derived engineered heart tissues. *Nat Commun.* DOI:10.1038/s41467-017-01946-x

Tanabe K, Nakamura M, Narita M, Takahashi K, Yamanaka S (2013) Maturation, not initiation, is the major roadblock during reprogramming toward pluripotency from human fibroblasts. *Proc Natl Acad Sci U S A*. DOI: 10.1073/pnas.1310291110

Takahashi K and Yamanaka S (2006) Induction of pluripotent stem cells from mouse embryonic and adult fibroblast cultures by defined factors. *Cell*. DOI: 10.1016/j.cell.2006.07.024

Thavandiran N, Dubois N, Mikryukov A, et al. (2013) Design and formulation of functional pluripotent stem cell-derived cardiac microtissues [published correction appears in Proc Natl Acad Sci U S A, 2015]. *Proc Natl Acad Sci U S A*. DOI: 10.1073/pnas.1311120110

Tiburcy M, Hudson JE, Balfanz P, et al. (2017) Defined Engineered Human Myocardium With Advanced Maturation for Applications in Heart Failure Modeling and Repair. *Circulation*. DOI: 10.1161/CIRCULATIONAHA.116.024145

Tu C, Chao BS, Wu JC (2018) Strategies for Improving the Maturity of Human Induced Pluripotent Stem Cell-Derived Cardiomyocytes. *Circ Res*. DOI: 10.1161/CIRCRESAHA.118.313472

Van Meer BJ, Tertoolen LG, Mummery CL (2016) Concise Review: Measuring Physiological Responses of Human Pluripotent Stem Cell Derived Cardiomyocytes to Drugs and Disease. *Stem Cells*. DOI: 10.1002/stem.2403

Veerman CC, Mengarelli I, Lodder EM, et al. (2017) Switch From Fetal to Adult *SCN5A* Isoform in Human Induced Pluripotent Stem Cell-Derived Cardiomyocytes Unmasks the Cellular Phenotype of a Conduction Disease-Causing Mutation. *J Am Heart Assoc*. DOI: 10.1161/JAHA.116.005135

Wang H, Zhou J, Liu Z, Wang C (2010) Injectable cardiac tissue engineering for the treatment of myocardial infarction. *J Cell Mol Med.* DOI: 10.1111/j.1582-4934.2010.01046.x

Winnier G, Blessing M, Labosky PA, Hogan BL (1995) Bone morphogenetic protein-4 is required for mesoderm formation and patterning in the mouse. *Genes Dev*. DOI: 10.1101/gad.9.17.2105

Yang L, Soonpaa MH, Adler ED, et al. (2008) Human cardiovascular progenitor cells develop from a KDR+ embryonic-stem-cell-derived population. *Nature*. DOI: 10.1038/nature06894

Yang X, Rodriguez M, Pabon L, Fischer KA, Reinecke H, Regnier M, Sniadecki NJ, Ruohola-Baker H, Murry CE (2014) Tri-iodo-l-thyronine promotes the maturation of human cardiomyocytes-derived from induced pluripotent stem cells. *J Mol Cell Cardiol*. DOI: 10.1016/j.yjmcc.2014.04.005

Yazawa M, Hsueh B, Jia X, et al. (2011) Using induced pluripotent stem cells to investigate cardiac phenotypes in Timothy syndrome. *Nature*. DOI: 10.1038/nature09855

Zhang J, Wilson GF, Soerens AG, Koonce CH, Yu J, Palecek SP, Thomson JA, Kamp TJ (2009) Functional cardiomyocytes derived from human induced pluripotent stem cells. *Circ Res.* DOI: 10.1161/CIRCRESAHA.108.192237

Zhang D, Shadrin IY, Lam J, Xian HQ, Snodgrass HR, Bursac N (2013) Tissue-engineered cardiac patch for advanced functional maturation of human ESC-derived cardiomyocytes. *Biomaterials*. DOI: 10.1016/j.biomaterials.2013.04.026

# Part 3

# Doxorubicin and cardiac dysfunction

## 3.1 Cancer therapy-related cardiac dysfunction (CTRCD)

Doxorubicin (Dox), which is an anthracycline antibiotic derived from *Streptomyces*, is among the most potent chemotherapeutic agents. However, the clinical utility of anthracyclines is hampered by cardiotoxicity, manifesting initially as asymptomatic cardiac dysfunction and evolving irreversibly to congestive heart failure [Armenian and Bathia 2018]. The mechanism by which Dox exerts cytotoxic (antitumoral and cardiotoxic) effects appears to be multifactorial, involving binding and intercalation with DNA, inhibition of DNA synthesis and repair, generation of ROS, inhibition of autophagy, and disturbance of calcium homeostasis (**Fig 12**) [Gewirtz 1999; Wenningmann et al. 2019].

The cellular target of Dox is topoisomerase-II (Top2). Dox binds both DNA and Top2 to form the ternary Top2-Dox-DNA cleavage complex, which can trigger cell death. Top2α is highly expressed in cancer cells and required for cell division to block DNA replication [Tewey et al. 1984; Capranico et al. 1992]. Adult mammalian CMs express Top2β which can be also targeted by Dox, as demonstrated by studies showing how Top2β-deleted cell lines and mouse models are resistant to Dox-induced cell death [Lyu et al. 2007; Zhang et al. 2012]. The Top2β-Dox-DNA cleavage complex can induce DNA DSBs in cardiomyocytes, leading to cell death via p53-activated caspases [Cunha-Oliveira et al. 2018].

Additionally, Dox-induced increase in apoptosis may be caused by the upregulation of death receptors (DRs), including TNF receptor 1 (TNFR1), Fas, DR4 and DR5. Death receptors are crucial mediators of apoptosis under physiological conditions. Individual DRs can be activated by their cognate ligands TNFα, Fas ligand (FasL), and TNF-related apoptosis-inducing ligand (TRAIL) that trigger activation of a caspase cascade, cleavage of cellular proteins, and ultimately apoptosis of target cells [Annibaldi and Walczak 2020]. Using hiPS-CMs, recent studies identified upregulation of DRs and subsequent apoptosis as a novel mechanism by which doxorubicin elicits toxicity in human cardiomyocytes [Zhao et al. 2017].

As Dox penetrates into the mithochondria, ROS-producing enzymes transform this molecule into a semiquinone. Semiquinones can be readily reacted with oxygen to create superoxide anions ($O_2^-$), which can be neutralized into more stable and less toxic hydrogen peroxide ($H_2O_2$) by SOD, or further transferred to ROS in a sequence of reactions known as the redox cycle. Dangerously, $H_2O_2$ and $O_2^-$ may produce highly reactive and toxic hydroxyl radicals (OH·). These generated ROS then react with mitochondrial biomolecules in the vicinity, resulting in protein, mtDNA, and lipid peroxidation [Songbo et al. 2019]. Since Dox has also been reported to inhibit the autophagic process in CMs, damaged mitochondria may accumulate inside the cell, further exacerbating Dox-induced dysfunction [Li et al. 2016; Gu et al. 2018].

Calcium dysregulation is another well-known and established mechanism contributing to DOX cardiotoxicity [Wallace 2007]. It has been postulated that doxorubicin and its metabolite, doxorubicinol, can deleteriously alter the activity of calcium handling proteins. Both RyR2 and SERCA are known binding targets of doxorubicin [Gambliel et al. 2002; Hanna et al. 2014], with the drug causing decreased SR $Ca^{2+}$ content and increased cytoplasmic $Ca^{2+}$ concentration during diastole [Wang et al. 2001; Sag et al. 2011]. Decreased gene expression levels of calcium handling proteins, like SERCA and NCX, have also been appointed as underlying cause of altered calcium homeostasis, as observed in a rabbit model of Dox-induced cardiomyopathy following treatment with DOX [Arai et al. 1998]. This altered gene expression pattern is most likely due to the genomic damage caused by Dox. Taken together, these alterations induced by anthracyclines lead to cellular damage and cardiac dysfunction.

To enhance its therapeutic efficiency, Dox is administered in combination with other pharmacological compounds in the treatment of breast cancer. Following anthracycline treatment, the human epidermal growth factor receptor 2 (HER2; ErbB2)/neu inhibitor Trastuzumab (Trz) improves outcomes in women with surgically removed HER2-positive breast cancer [Romond et al. 2005]. Trz is a monoclonal antibody targeting HER2, inducing an immune-mediated response

that causes internalization and downregulation of HER2. Cells treated with Trz undergo arrest during the G1 phase of the cell cycle via activation of p21 and p27 [Bange et al. 2001]. It has also been suggested that Trz may downregulate AKT, therefore inhibiting cell proliferation [Kute et al. 2004]. Since the simultaneous delivery of Doxo and Trz results in enhanced cardiotoxicity, the current clinical protocols involve their sequential administration. However, Dox–Trz combined therapy is still associated with high risk of LV dysfunction in up to 25% of breast cancer patients [Advani et al. 2016], along with an increased risk of arrhythmia [Santoro et al. 2017]. The specific roles and effects of Dox and Trz in cardiotoxicity induced by their combined administration remain to be fully characterized.

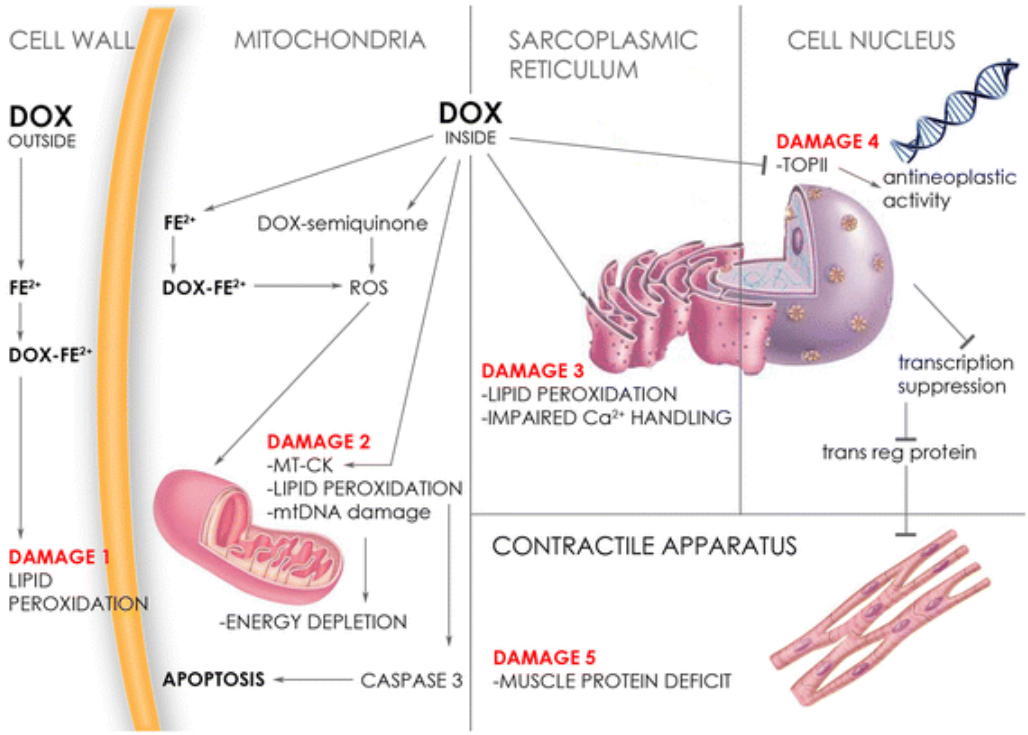


**Figure 12.** Mechanisms underlying anthracycline-induced myocyte toxicity. DOX: doxorubicin; MT-CK: mitochondrial creatine kinase; $Fe^{2+}$: iron; ROS: reactive oxygen species; $Ca^{2+}$: calcium; TOPII: topoisomerase II; trans reg protein: transcriptional regulatory protein. [According to Framarino-Dei-Malatesta et al. 2017]

## 3.2 Dox-induced cellular senescence

Despite solid evidence proving the induction of apoptosis in cardiomyocytes exposed to Dox in-vitro, there is controversy over the amount of contribution of this cellular process in Dox-induced cardiotoxicity in-vivo [Auner et al. 2001]. It has recently been suggested that senescence may be a novel mechanism of cardiotoxicity induced by low doses of Dox. As mentioned earlier, cellular senescence can be divided into two categories: replicative senescence (RS), which is programmed at a specific time when telomeric ends are exposed, and stress-induced premature senescence (SIPS), which is independent from TL [Campisi and d'Adda di Fagagna 2007]. SIPS is usually due to damaging stimuli, such as chemotherapy, which result in changes in the expression levels of regulatory proteins, leading to the impairment of cell functions, including the regenerative capacity [Vigneron et al. 2005; Spallarossa et al. 2010].

It has been reported that low or high doses of Dox induce either senescence or apoptosis, respectively, in myocytes. Studies on neonatal mouse CMs showed that when exposed to low concentrations (0.25–1 μM) of Dox, the cells do not enter apoptotic program but exhibit a senescence-like phenotype [Maejima et al. 2008; Spallarossa et al. 2009]. There are also reports concerning Dox-dependent senescence of vascular smooth muscle cells (VSMCs) from human umbilical artery, which compared stress-induced premature senescence (SIPS) to replicative senescence (RS) [Hodjat et al. 2012; Bielak-Zmijewska et al. 2013]. These studies observed classical markers of cellular senescence in both RS and Dox-induced SIPS, such as SA-β-gal activity, DNA damage foci, DDR pathway activation, changed morphology, increased superoxide production, SASP, increased cell granularity and increased micronucleation.

There are different hypotheses about the underlying causes of Dox-induced SIPS. Studies performed on tumour cells indicate that low doses of Dox, as well as several other anti-cancer agents, induce mitotic catastrophe, a phenomenon that is characterized by chromosomal abnormalities and abnormal mitosis which leads to late cell death. The same studies demonstrated that cells that ultimately die of

mitotic catastrophe initially show a senescence-like phenotype [Eom et al. 2005]. Other publications also suggest that genomic damage to telomeres may also play a role in the SIPS program [Lechel et al. 2005].

CMs and VSMCs are not the only targets of Dox-induced SIPS. The adult heart contains a population of primitive cells with stem cell characteristics that are responsible for tissue homeostasis in normal conditions and mediate myocardial regeneration in pathological states [Beltrami et al. 2003; Pfister et al. 2005; Bearzi et al. 2007; Smith et al. 2007]. Increasing evidence indicates that senescence of CPCs is a fundamental process that contributes to the onset and progression of aging and heart failure [Cesselli et al. 2001; Chimenti et al. 2003; Urbanek et al. 2005; Gonzalez et al. 2008]. It has been shown in different models that Dox-dependent SIPS is not restricted to cardiomyocytes, but severely affects also resident CPCs. Dox exposure impaired vascular development and reduced the number of CPCs in juvenile mice, resulting in a higher susceptibility of the heart to stress in the adult life [Huang et al. 2010]. In anthracycline-exposed rats, Dox decreased the number of functionally competent CPCs by inhibiting their proliferation together with accumulation of oxidative DNA damage, apoptosis and progressive cellular senescence. The depletion and premature senescence of the CPC population interfered with the physiological turnover of the myocardium in these animals [De Angelis et al. 2010]. A similar phenotype can be seen in CPCs isolated from patients and treated with Dox in-vitro, with premature senescence and impaired function as the long-lasting effects [Piegari et al. 2013].

In light of this evidence, the induction of SIPS has been proposed as a novel mechanism of cardiotoxicity induced by low doses of Dox.

## 3.3 References


Advani PP, Ballman KV, Dockter TJ, Colon-Otero G and Perez EA (2016) Long-Term Cardiac Safety Analysis of NCCTG N9831 (Alliance) Adjuvant Trastuzumab Trial. *J Clin Oncol.* DOI: 10.1200/JCO.2015.61.8413

Annibaldi A, Walczak H (2020) Death Receptors and Their Ligands in Inflammatory Disease and Cancer. *Cold Spring Harb Perspect Biol*. DOI: 10.1101/cshperspect.a036384

Arai M, Tomaru K, Takizawa T, et al. (1998) Sarcoplasmic reticulum genes are selectively down-regulated in cardiomyopathy produced by doxorubicin in rabbits. *J Mol Cell Cardiol*. DOI: 10.1006/jmcc.1997.0588

Armenian S and Bhatia S (2018) Predicting and Preventing Anthracycline-Related Cardiotoxicity. *Am Soc Clin Oncol Educ Book*. DOI: 10.1200/EDBK_100015

Auner HW, Tinchon C, Linkesch W, Halwachs-Baumann G, Sill H. Correspondence re: O. J. Arola et al., acute doxorubicin cardiotoxicity involves cardiomyocyte apoptosis. Cancer Res., 60: 1789-1792, 2000. *Cancer Res*. PMID: 11280807

Bange J, Zwick E, Ullrich A (2001) Molecular targets for breast cancer therapy and prevention. *Nat Med*. DOI: 10.1038/87872

Bearzi C, Rota M, Hosoda T, Tillmanns J, Nascimbene A, De Angelis A, Yasuzawa-Amano S, Trofimova I, Siggins RW, Lecapitaine N, Cascapera S, Beltrami AP, D'Alessandro DA, Zias E, Quaini F, Urbanek K, Michler RE, Bolli R, Kajstura J, Leri A, Anversa P (2007) Human cardiac stem cells. *Proc Natl Acad Sci USA.* DOI: 10.1073/pnas.0706760104

Beltrami AP, Barlucchi L, Torella D, Baker M, Limana F, Chimenti S, Kasahara H, Rota M, Musso E, Urbanek K, Leri A, Kajstura J, Nadal-Ginard B, Anversa P (2003) Adult cardiac stem cells are multipotent and support myocardial regeneration. *Cell*. DOI: 10.1016/S0092-8674(03)00687-1

Bielak-Zmijewska A, Wnuk M, Przybylska D, et al. (2014) A comparison of replicative enescence and doxorubicin-induced premature senescence of vascular smooth muscle cells isolated from human aorta. *Biogerontology*. DOI: 10.1007/s10522-013-9477-9

Campisi J, d'Adda di Fagagna F (2007) Cellular senescence: when bad things happen to good cells. *Nat Rev Mol Cell Biol*. DOI: 10.1038/nrm2233

Capranico G, Tinelli S, Austin CA, Fisher ML, Zunino F (1992) Different patterns of gene expression of topoisomerase II isoforms in differentiated tissues during murine development. *Biochim Biophys Acta*. DOI:10.1016/0167-4781(92)90050-a

Cesselli D, Beltrami AP, D'Aurizio F, Marcon P, Bergamin N, Toffoletto B, Pandolfi M, Puppato E, Marino L, Signore S, Livi U, Verardo R, Piazza S, Marchionni L, et al. (2011) Effects of age and heart failure on human cardiac stem cell function. *Am J Pathol.* DOI: 10.1016/j.ajpath.2011.03.036

Chimenti C, Kajstura J, Torella D, Urbanek K, Heleniak H, Colussi C, Di Meglio F, Nadal-Ginard B, Frustaci A, Leri A, Maseri A, Anversa P (2003) Senescence and death of primitive cells and myocytes lead to premature cardiac aging and heart failure. *Circ Res*. DOI: 10.1161/01.RES.0000093985.76901.AF

Cunha-Oliveira T, Ferreira LL, Coelho AR, Deus CM, Oliveira PJ (2018) Doxorubicin triggers bioenergetic failure and p53 activation in mouse stem cell-derived cardiomyocytes. *Toxicol Appl Pharmacol*. DOI: 10.1016/j.taap.2018.04.009

De Angelis A, Piegari E, Cappetta D, Marino L, Filippelli A, Berrino L, Martins-Ferreira J, Zheng H, Hosoda T, Rota M, Urbanek K, Kajstura J, Leri A, Rossi F, Anversa P (2010) Anthracycline cardiomyopathy is mediated by depletion of the cardiac stem cell pool and is rescued by restoration of progenitor cell function. *Circulation*. DOI: 10.1161/CIRCULATIONAHA.109.895771

Eom YW, Kim MA, Park SS, et al. (2005) Two distinct modes of cell death induced by doxorubicin: apoptosis and cell death through mitotic catastrophe accompanied by senescence-like phenotype. *Oncogene*. DOI: 10.1038/sj.onc.1208627

Framarino-Dei-Malatesta M, Sammartino P, Napoli A (2017) Does anthracycline-based chemotherapy in pregnant women with cancer offer safe cardiac and neurodevelopmental outcomes for the developing fetus? *BMC Cancer*. DOI: 10.1186/s12885-017-3772-9

Gambliel HA, Burke BE, Cusack BJ, et al. (2005) Doxorubicin and C-13 deoxydoxorubicin effects on ryanodine receptor gene expression. *Biochem Biophys Res Commun*. DOI: 10.1006/bbrc.2002.6380

Gewirtz DA (1999) A critical evaluation of the mechanisms of action proposed for the antitumor effects of the anthracycline antibiotics adriamycin and daunorubicin. *Biochem Pharmacol*. DOI: 10.1016/s0006-2952(98)00307-4

Gonzalez A, Rota M, Nurzynska D, Misao Y, Tillmanns J, Ojaimi C, Padin-Iruegas ME, Mu¨ller P, Esposito G, Bearzi C, Vitale S, Dawn B, Sanganalmath SK, et al. (2008) Activation of cardiac progenitor cells reverses the failing heart senescent phenotype and prolongs lifespan. *Circ Res*. DOI: 10.1161/CIRCRESAHA.107.165464

Gu J, Fan YQ, Zhang HL, et al. (2018) Resveratrol suppresses doxorubicin-induced cardiotoxicity by disrupting E2F1 mediated autophagy inhibition and apoptosis promotion. *Biochem Pharmacol*. DOI: 10.1016/j.bcp.2018.02.025

Hanna AD, Lam A, Tham S, Dulhunty AF, Beard NA (2014) Adverse effects of doxorubicin and its metabolic product on cardiac RyR2 and SERCA2A. *Mol Pharmacol*. DOI: 10.1124/mol.114.093849

Hodjat M, Haller H, Dumler I, Kiyan Y (2013) Urokinase receptor mediates doxorubicin-induced vascular smooth muscle cell senescence via proteasomal degradation of TRF2. *J Vasc Res*. DOI: 10.1159/000343000

Huang C, Zhang X, Ramil JM, Rikka S, Kim L, Lee Y, Gude NA, Thistlethwaite PA, Sussman MA, Gottlieb RA, Gustafsson AB (2010) Juvenile exposure to anthracyclines impairs cardiac progenitor cell function and vascularization resulting in greater susceptibility to stress-induced myocardial injury in adult mice. *Circulation*. DOI: 10.1161/CIRCULATIONAHA.109.902221

Lechel A, Satyanarayana A, Ju Z, et al. (2005) The cellular level of telomere dysfunction determines induction of senescence or apoptosis in vivo. *EMBO Rep*. DOI: 10.1038/sj.embor.7400352

Li DL, Wang ZV, Ding G, et al. (2016) Doxorubicin Blocks Cardiomyocyte Autophagic Flux by Inhibiting Lysosome Acidification. *Circulation*. DOI: 10.1161/CIRCULATIONAHA.115.017443

Lyu YL, Kerrigan JE, Lin CP, et al. (2007) Topoisomerase IIbeta mediated DNA double-strand breaks: implications in doxorubicin cardiotoxicity and prevention by dexrazoxane. *Cancer Res*. DOI: 10.1158/0008-5472.CAN-07-1649

Maejima Y, Adachi S, Ito H, Hirao K, Isobe M (2008) Induction of premature senescence in cardiomyocytes by doxorubicin as a novel mechanism of myocardial damage. *Aging Cell*. DOI: 10.1111/j.1474-9726.2007.00358.x

Pessah IN, Durie EL, Schiedt MJ, Zimanyi I (1990) Anthraquinone-sensitized $Ca^{2+}$ release channel from rat cardiac sarcoplasmic reticulum: possible receptor-mediated mechanism of doxorubicin cardiomyopathy. *Mol Pharmacol*. PMID: 2157959

Pfister O, Mouquet F, Jain M, Summer R, Helmes M, Fine A, Colucci WS, Liao R (2005) CD31- but not CD31+ cardiac side population cells exhibit functional cardiomyogenic differentiation. *Circ Res*. DOI: 10.1161/01.RES.0000173297.53793.fa

Piegari E, De Angelis A, Cappetta D, et al. (2013) Doxorubicin induces senescence and impairs function of human cardiac progenitor cells. *Basic Res Cardiol*. DOI: 10.1007/s00395-013-0334-4

Romond EH, Perez EA, Bryant J, et al. (2005) Trastuzumab plus adjuvant chemotherapy for operable HER2-positive breast cancer. *N Engl J Med*. DOI: 10.1056/NEJMoa052122

Sag CM, Köhler AC, Anderson ME, Backs J, Maier LS (2011) CaMKII-dependent SR Ca leak contributes to doxorubicin-induced impaired Ca handling in isolated cardiac myocytes. *J Mol Cell Cardiol*. DOI: 10.1016/j.yjmcc.2011.07.016

Santoro C, Arpino G, Esposito R, Lembo M, Paciolla I, Cardalesi C, de Simone G, Trimarco B, De Placido S and Galderisi M (2017) 2D and 3D strain for detection of subclinical anthracycline cardiotoxicity in breast cancer patients: a balance with feasibility. *Eur Heart J Cardiovasc Imaging.* DOI: 10.1093/ehjci/jex033

Smith RR, Barile L, Cho HC, Leppo MK, Hare JM, Messina E, Giacomello A, Abraham MR, Marban E (2007) Regenerative potential of cardiosphere-derived cells expanded from percutaneous endomyocardial biopsy specimens. *Circulation*. DOI: 10.1161/CIRCULATIONAHA.106.655209

Spallarossa P, Altieri P, Aloi C, et al. (2009) Doxorubicin induces senescence or apoptosis in rat neonatal cardiomyocytes by regulating the expression levels of the telomere binding factors 1 and 2. *Am J Physiol Heart Circ Physiol*. DOI: 10.1152/ajpheart.00068.2009

Spallarossa P, Altieri P, Barisione C, Passalacqua M, Aloi C, Fugazza G, Frassoni F, Podestà M, Canepa M, Ghigliotti G, Brunelli C (2010) p38 MAPK and JNK antagonistically control senescence and cytoplasmic $p16I^{NK4A}$ expression in doxorubicin-treated endothelial progenitor cells. *PLoS One*. DOI: 10.1371/journal.pone.0015583

Songbo M, Lang H, Xinyong C, Bin X, Ping Z, Liang S (2019) Oxidative stress injury in doxorubicin-induced cardiotoxicity. *Toxicol Lett*. DOI: 10.1016/j.toxlet.2019.02.013

Tewey KM, Rowe TC, Yang L, Halligan BD, Liu LF (1984) Adriamycin-induced DNA damage mediated by mammalian DNA topoisomerase II. *Science*. DOI:10.1126/science.6093249

Urbanek K, Torella D, Sheikh F, De Angelis A, Nurzynska D, Silvestri F, Beltrami CA, Bussani R, Beltrami AP, Quaini F, Bolli R, Leri A, Kajstura J, Anversa P (2005) Myocardial regeneration by activation of multipotent cardiac stem cells in ischemic heart failure. *Proc Natl Acad Sci U S A*. DOI: 10.1073/pnas.0500169102

Vigneron A, Roninson IB, Gamelin E, Coqueret O (2005) Src inhibits adriamycin-induced senescence and G2 checkpoint arrest by blocking the induction of p21waf1. *Cancer Res*. DOI: 10.1158/0008-5472.CAN-05-0461

Wallace KB (2007) Adriamycin-induced interference with cardiac mitochondrial calcium homeostasis. *Cardiovasc Toxicol*. DOI: 10.1007/s12012-007-0008-2

Wang GX, Wang YX, Zhou XB, Korth M (2001) Effects of doxorubicinol on excitation--contraction coupling in guinea pig ventricular myocytes. *Eur J Pharmacol*. DOI: 10.1016/s0014-2999(01)01096-2

Wenningmann N, Knapp M, Ande A, Vaidya TR, Ait-Oudhia S (2019) Insights into Doxorubicin-induced Cardiotoxicity: Molecular Mechanisms, Preventive Strategies, and Early Monitoring. *Mol Pharmacol*. DOI: 10.1124/mol.119.115725

Zhang S, Liu X, Bawa-Khalfe T, et al. (2012) Identification of the molecular basis of doxorubicin-induced cardiotoxicity. *Nat Med*. DOI: 10.1038/nm.2919

# Part 4

# Cardioprotection

## 4.1 Protection of the senescent heart from injury

The WHO has identified very cost-effective strategies for prevention and control of CVDs through diminishing the influence of modifiable risk factors. They described two types of interventions: population-wide and individual, which are recommended to be used in combination to reduce the greatest cardiovascular disease burden. Population-wide interventions include comprehensive tobacco control policies, taxation to reduce the intake of foods that are high in fat, sugar and salt, building walking and cycle paths to increase physical activity, strategies to reduce harmful use of alcohol, and providing healthy school meals to children. At the individual level, individual health-care interventions need to be targeted to those at high total cardiovascular risk. While aging and its consequences cannot be altogether stopped, one can presumably delay the normal cardiac aging process. Several studies in animal models have shown the potential of different therapeutic approaches to delay or partially revert aging, ranging from dietary restrictions to pharmacologic interventions (such as rapamycin, enalapril, and SS-31), recombinant protein therapy (IGF-1 and GDF-11), gene therapy (miRNAs), and cardiac stem cell therapy. While experimental data from animal models shows that aging can be modified by these strategies, to date no known intervention slows, stops or reverses the aging process in humans. In fact, researchers find some treatments, such as supplemental antioxidants, to be ineffective or even harmful [Henkel et al. 2019]. Future studies will be required to evaluate the translational potentials of these interventions.

As a general rule for cardiac aging interventions, short-term treatments beginning at late life will have higher translational potential compared with long-term or life-long treatments. This is particularly relevant to systemic treatments or treatments that target multiple pathways, as a briefer treatment will lower the chances of irreversible side effects [Chiao and Rabinovitch 2015]. Therefore, it is important to study the kinetics and pharmacodynamics of the treatment to determine the minimal effective dose and duration, as well as the persistence of the treatment to determine the optimum therapeutic regimen.

### 4.1.1 Clearance of senescence cells

Despite their harsh internal and external microenvironments, senescent cells are viable. They survive even though they have active DNA damage responses, heightened metabolic flux, and increased local levels of SASP inflammatory cytokines and other factors that are able to induce apoptosis. Indeed, senescent cells are more resistant to stresses such as serum deprivation than non-senescent cells [Wang 1995; Fridman and Lowe 2003]. In vivo, senescent cells appear to be removed by the immune system, rather than apoptosis or necrosis [Xue et al. 2007]. Therefore, it has been hypothesized that anti-apoptotic, pro-survival mechanisms could be upregulated in senescent cells and interfering with these protective endogenous mechanisms.

It has been shown in animal models that removal of senescent cells, targeted using a transgenic suicide gene or senolytic molecules, can protect against the aging phenotype and therefore lead to rejuvenating of the organism [Baker et al. 2011; Thannickal 2013; Zhu et al. 2015]. Additionally, these studies produce direct evidence for the role of senescence in the organismal aging.

### 4.1.2 Dietary restrictions

The relationship between dietary patterns and cardiac aging is less well-studied. There are multiple observational studies to support a favourable association between long-term adherence to a Mediterranean diet with the absence of incident chronic disease [Assman et al. 2018; Samieri et al. 2013]. Epidemiologic trials dating back several decades have supported the health benefits of a diet rich in unsaturated fats and low in red meat, dairy, and sweets [Tracy 2013]. More recently, the PREDIMED (Prevencion con Dieta Mediterranea) study reported that a Mediterranean diet lowered rates of mortality due to the composite endpoint of MI, stroke, or CVD [Estruch et al. 2018]. It has been reported that the Mediterranean diet has anti-inflammatory and antioxidant effects, which explain its protective effects. Some studies have demonstrated a significant reduction in circulating levels of inflammatory markers, including IL-6 and IL-8, with long-term adherence to Mediterranean diet, along with antioxidant effects probably due to

assumption of polyphenols [Casas et al. 2017; Billingsley and Carbone 2018]. Indeed, other studies observed how moderate consumption of coffee, which is rich in polyphenols, significantly decreased risk of CVD, while high consumption significantly increased the risk [Kouli et al. 2018].

Caloric restriction (CR) has also been described to attenuate cardiac aging, and CR mimetics are currently a major drug target. In animal models, dietary restriction reprograms the transcriptome, extends lifespan and decreases the burden of age-related diseases [Heiss et al. 2017; Ma et al. 2020]. Of note, the activity of Sirtuins, which act as stress-response and survival proteins, is higher in caloric restriction states [Oellerich and Potente 2012; Preyat and Leo 2013]. Hence, CR may delay changes to cardiac and vascular function via promoting antioxidant defense mechanisms. Moreover, CR has been demonstrated to reduce cardiac apoptosis and myocardial interstitial fibrosis, while promoting angiogenesis [Alfaras et al. 2016]. There have been recent medications that mimic caloric restriction with the aim of delaying cardiac aging. For example, resveratrol, a polyphenol found in grapes, is being studied as it mimics caloric restriction by promoting FoxO and SIRT activity and expression [Tseng et al. 2014; Sin et al. 2015].

### 4.1.3 Stem cells transplants

Since the proliferating and self-healing capacity of cardiomyocytes in adults is limited, increasing interest has been focused in exploiting the potential of autologous or allogeneic transplants of stem cells for heart repair and regeneration through restoration of cardiomyocytes and damaged myocardial tissue.

Stem cells are specified as undifferentiated cells possessing the ability to generate, sustain, and replace terminally differentiated cells via unlimited replication. They show two basic features, perpetual self-renewal, and capability of differentiation into a specialized cell type under appropriate stimuli [Lanza and Atala 2013]. In cardiac regenerative medicine, the therapeutic use of pluripotent

stem cells (ESCs and iPSCs), potentially able to differentiate into all cell types of an organism (including mesodermal derived cardiomyocytes), is currently limited mainly due to the risk of immune rejection, genetic instability, tumorigenic potential, low induction efficiency, and ethical issues [Musunuru et al. 2018; Machiraju and Greenway 2019]. However, the safety and efficacy of multipotent or unipotent adult stem cells has already been intensively investigated in clinical trials over the last 15 years, with promising results from bone marrow mesenchymal stem cells (BMCs) [López et al. 2013]. BMCs are attractive for therapeutic use in cardiac regenerative medicine due to their relatively easy accessibility and further isolation from autologous bone marrow or blood. Accordingly, their potential to optimize heart function, angiogenic potential for a vascular regeneration, and favourable tolerance by the immune system holds additional benefit [Wernly et al. 2019]. However, exact mechanisms of cardiac repair by transplanted cells are still controversially discussed facing inconsistent results regarding therapeutic efficacy. Several independent studies have demonstrated that, while providing significant improvement in heart function, injection of MSC into the damaged myocardium results only in limited differentiation, mainly into vascular lineages [Tao et al. 2016].

### 4.1.4 Extracellular vesicles

Alternative mechanisms and explanations for the beneficial effects of stem cell transplants despite low levels of differentiation are being investigated. Stem cell-derived paracrine effect has emerged as a very promising strategy for the reactivation of endogenous mechanisms of repair and regeneration in several disease models [Gnecchi et al. 2008; Mirotsou et al. 2011; Bollini et al. 2013; Barile et al. 2014; Gallet et al. 2017; Barile et al. 2018]. In these studies, transplanted stem cells have been demonstrated to contribute to tissue regeneration by modulatory effects rather than direct differentiation into new functional tissue. This discovery has led to a significant paradigm shift, from exploring the stem cell

genome to analysing the stem cell 'secretome' as the whole of growth factors and chemo-attractant molecules produced by paracrine secretion.

In the analysis of stem cell secretomes, there has been a growing interest on the characterization of extracellular vesicles (EV). EV are membrane-bound cellular components enriched with soluble bioactive factors (e.g. proteins, lipids) and RNA (regulatory miRNA, and mRNA) eliciting wide-ranging effects while mediating horizontal inter-cellular transfer of genetic information to recipient cells and modulating their function [Tetta et al. 2013]. EVs are secreted as micro-sized (microvesicles, Ø 0.2–1 μm) and nanosized (exosomes, Ø 40–150 nm) particles. Microvesicles are released as shedding vesicles by direct budding of the plasma membrane, while exosomes are produced in endosomal multivesicular bodies (MVB) and secreted as the MVB fuses with the plasma membrane [Lotvall et al. 2014]. The isolation and characterization of exosomes (Exo) is still difficult, and distinct techniques such as chromatography, centrifugation, precipitation, and affinity-isolation are used, often in combination [Lawson et al. 2016; Takov et al. 2018; Balbi 2020]. Still, given their similar size and density, none of these techniques purifies Exo completely from microvesicles, lipoproteins, and macromolecular complexes. Even the use of flow-cytometry is limited because of Exo's extremely small size and, although these vesicles express surface markers, these proteins usually hint more towards the cell of origin than they are exosome-specific [Arraud et al. 2014; Kowal et al. 2016]. Despite these methodological difficulties, exosomes have already been extensively evaluated and reviewed in the field of cardiovascular medicine.

Recent studies have shown that the beneficial effects observed in preclinical models of ischemic heart disease following stem cell transplantation are mediated by EVs, progenitor cell-derived exosomes in particular. These beneficial effects include the activation of pro-survival, angiogenic, anti-inflammatory and anti-fibrotic pathways, and the stimulation of resident endogenous progenitors, overall enhancing organ function [Rani et al. 2015]. EVs from adult mesenchymal stem cells (CPCs and BMCs) have been demonstrated to provide cardioprotection against acute myocardial infarction [Lai et al. 2010; Arslan et al. 2013; Bian et al.

2013; Barile et al. 2018], enhance wound healing [Zhang et al. 2014], counteract graft-versus-host-disease (GVHD) [Kordelas et al. 2014], reduce renal injury [Bruno et al. 2012], mediate liver regeneration [Tan et al. 2014], stimulate neural plasticity following stroke [Xin et al. 2012], and counteract Doxo-induced cardiotoxicity [Lazzarini et al. 2016]. Since cell-free delivery of bioactive cargos by EVs recapitulates the same beneficial responses of stem cell transplantation, they offer remarkable benefits over conventional cell therapy as immunologically-unresponsive agents [Bobis-Wozowicz et al. 2015].

## 4.2 References


Alfaras I, Di Germanio C, Bernier M, Csiszar A, Ungvari Z, Lakatta EG et al. (2016) Pharmacological strategies to retard cardiovascular aging. *Circ Res.* DOI: 10.1161/CIRCRESAHA.116.307475

Arraud N, Linares R, Tan S, et al. (2014) Extracellular vesicles from blood plasma: determination of their morphology, size, phenotype, and concentration. *J Thromb Haemost*. DOI: 10.1111/jth.12554

Assmann KE, Adjibade M, Andreeva VA, Hercberg S, Galan P and Kesse-Guyot E (2018) Association between adherence to the mediterranean diet at midlife and healthy aging in a cohort of french adults. *J Gerontol A Biol Sci Med Sci.* DOI: 10.1093/gerona/glx066

Arslan F, Lai RC, Smeets MB, Akeroyd L, Choo A, Aguor ENE, et al. (2013) Mesenchymal stem cell-derived exosomes increase ATP levels, decrease oxidative stress and activate PI3K/Akt pathway to enhance myocardial viability and prevent adverse remodeling after myocardial ischemia/reperfusion injury. *Stem Cell Res.* DOI: 10.1016/j.scr.2013.01.002

Balbi C and Vassalli G (2020) Exosomes: Beyond stem cells for cardiac protection and repair. *Stem Cells*. DOI: 10.1002/stem.3261

Barile L, Lionetti V, Cervio E, Matteucci M, Gherghiceanu M, Popescu LM, et al. (2014) Extracellular vesicles from human cardiac progenitor cells inhibit cardiomyocyte apoptosis and improve cardiac function after myocardial infarction. *Cardiovasc Res,* DOI: 10.1093/cvr/cvu167

Barile L, Cervio E, Lionetti V, Milano G, Ciullo A, Biemmi V, Bolis S, Altomare C, Matteucci M, Di Silvestre D, Brambilla F, Fertig TE, Torre T, Demertzis S, Mauri P, Moccetti T, Vassalli G (2018) Cardioprotection by cardiac progenitor cell-secreted exosomes: role of pregnancy-associated plasma protein-A. *Cardiovasc Res.* DOI: 10.1093/cvr/cvy055

Baker DJ, Wijshake T, Tchkonia T, LeBrasseur NK, Childs BG, van de Sluis B, Kirkland JL, van Deursen JM (2011) Clearance of p16Ink4a-positive senescent cells delays ageing-associated disorders. *Nature*. DOI: 10.1038/nature10600

Bian S, Zhang L, Duan L, Wang X, Ying M, and Yu H (2013) Extracellular vesicles derived from human bone marrow mesenchymal stem cells promote angiogenesis in a rat myocardial infarction model. *J Mol Med.* DOI: 10.1007/s00109-013-1110-5

Billingsley HE and Carbone S (2018) The antioxidant potential of the Mediterranean diet in patients at high cardiovascular risk: an in-depth review of the PREDIMED. *Nutr. Diabetes.* DOI: 10.1038/s41387-018-0025-1

Bobis-Wozowicz S, Kmiotek K, Sekula M, Kedracka-Krok S, Kamycka E, Adamiak M, et al. (2015) Human Induced Pluripotent Stem Cell-Derived Microvesicles Transmit RNAs and Proteins to Recipient Mature Heart Cells Modulating Cell Fate and Behavior. *Stem Cells*. DOI: 10.1002/stem.2078

Bollini S, Gentili C, Tasso R and Cancedda R (2013) The Regenerative Role of the Fetal and Adult Stem Cell Secretome. *J Clin Med.* DOI: 10.3390/jcm2040302

Casas R, Urpi-Sarda M, Sacanella E, Arranz S, Corella D, Castaner O et al. (2017) Anti-inflammatory effects of the mediterranean diet in the early and late stages of atheroma plaque development. *Mediators Inflamm.* DOI: 10.1155/2017/3674390

Chiao YA, Rabinovitch PS (2015) The Aging Heart.*Cold Spring Harb Perspect Med*. DOI: 10.1101/cshperspect.a025148

Estruch R, Ros E, Salas-Salvado J, Covas MI, Corella D, Aros F et al. (2018) Primary prevention of cardiovascular disease with a Mediterranean diet supplemented by extra-virgin olive oil or nuts. *N Engl J Med.* DOI: 10.1056/NEJMoa1800389

Fridman JS and Lowe SW (2003) Control of apoptosis by p53. *Oncogene*. DOI: 10.1038/sj.onc.1207116

Gallet R, Dawkins J, Valle J, Simsolo E, de Couto G, Middleton R, et al. (2017) Exosomes secreted by cardiosphere-derived cells reduce scarring, attenuate adverse remodelling, and improve function in acute and chronic porcine myocardial infarction. *Eur Heart J.* DOI: 10.1093/eurheartj/ehw240

Gnecchi M, Zhang Z, Ni A and Dzau VJ (2008) Paracrine mechanisms in adult stem cell signaling and therapy. *Circ. Res.* DOI: 10.1161/CIRCRESAHA.108.176826

Heiss C, Spyridopoulos I and Haendeler J (2017) Interventions to slow cardiovascular aging: dietary restriction, drugs and novel molecules. *Exp Gerontol.* DOI: 10.1016/j.exger.2017.06.015

Henkel R, Sandhu IS, Agarwal A (2019) The excessive use of antioxidant therapy: A possible cause of male infertility? *Andrologia*. DOI: 10.1111/and.13162

Kordelas L, Rebmann V, Ludwig AK, Radtke S, Ruesing J, Doeppner TR, et al. (2014) MSC-derived exosomes: a novel tool to treat therapy-refractory graft-versus-host disease. *Leukemia*. DOI: 10.1038/leu.2014.41

Kouli GM, Panagiotakos D, Chrysohoou C, Tsigos C, Tousoulis D and Pitsavos C (2018) J-shaped relationship between habitual coffee consumption and 10-year (2002-2012)

cardiovascular disease incidence: The ATTICA study. *Clin Nutr ESPEN.* DOI: 10.1016/j.clnesp.2018.01.040

Kowal J, Arras G, Colombo M, et al. (2016) Proteomic comparison defines novel markers to characterize heterogeneous populations of extracellular vesicle subtypes. *Proc Natl Acad Sci U S A*. DOI: 10.1073/pnas.1521230113

Lai RC, Arslan F, Lee MM, Sze, NSK, Choo A, Chen TS, et al. (2010) Exosomes secreted by MSC reduces myocardial ischemia/reperfusion injury. *Stem Cell Res. DOI*: 10.1016/j.scr.2009.12.003

Lanza R and Atala A (2013) Essentials of Stem Cell Biology. *Academic Press*, Cambridge, MA, USA.

Lawson C, Vicencio JM, Yellon DM, Davidson SM (2016) Microvesicles and exosomes: new players in metabolic and cardiovascular disease. *J Endocrinol.* DOI: 10.1530/JOE-15-0201

Lazzarini E, Balbi C, Altieri P, Pfeffer U, Gambini E, Canepa M, et al. (2016) The human amniotic fluid stem cell secretome effectively counteracts doxorubicin-induced cardiotoxicity. *Sci Rep. DOI*: 10.1038/srep29994.

Lötvall J, Hill AF, Hochberg F, Buzás EI, Di Vizio D, Gardiner C, et al. (2014) Minimal experimental requirements for definition of extracellular vesicles and their functions: a position statement from the International Society for Extracellular Vesicles. *J Extracell Vesicles.* DOI: 10.3402/jev.v3.26913

López Y, Lutjemeier B, Seshareddy K, Trevino EM, Hageman KS, Musch TI, Borgarelli M, Weiss ML (2013) Wharton's jelly or bone marrow mesenchymal stromal cells improve cardiac function following myocardial infarction for more than 32 weeks in a rat model: a preliminary report. *Curr Stem Cell Res Ther*. DOI: 10.2174/1574888x11308010007

Ma S, Sun S, Geng L, et al. (2020) Caloric Restriction Reprograms the Single-Cell Transcriptional Landscape of Rattus Norvegicus Aging. *Cell*. DOI: 10.1016/j.cell.2020.02.008

Machiraju P and Greenway SC (2019) Current methods for the maturation of induced pluripotent stem cell-derived cardiomyocytes. *World J Stem Cells*. DOI: 10.4252/wjsc.v11.i1.33

Mirotsou M, Jayawardena TM, Schmeckpeper J, Gnecchi M and Dzau VJ (2011) Paracrine mechanisms of stem cell reparative and regenerative actions in the heart. *J Mol Cell Cardiol.* DOI: 10.1016/j.yjmcc.2010.08.005

Musunuru K, Sheikh F, Gupta RM, et al. (2018) Induced Pluripotent Stem Cells for Cardiovascular Disease Modeling and Precision Medicine: A Scientific Statement from the American Heart Association. *Circ Genom Precis Med*. DOI: 10.1161/HCG.0000000000000043

Oellerich MF and Potente M (2012) FOXOs and sirtuins in vascular growth, maintenance, and aging. *Circ Res.* DOI: 10.1161/CIRCRESAHA.111.246488

Preyat N, Leo O (2013) Sirtuin deacylases: a molecular link between metabolism and immunity. *J Leukoc Biol*. DOI: 10.1189/jlb.1112557

Rani S, Ryan AE, Griffin MD and Ritter T (2015) Mesenchymal Stem Cell-derived Extracellular Vesicles: Toward Cell-free Therapeutic Applications. *Mol Ther.* DOI: 10.1038/mt.2015.44

Samieri C, Sun Q, Townsend MK, Chiuve SE, Okereke OI, Willett WC et al. (2013) The association between dietary patterns at midlife and health in aging: an observational study. *Ann Intern Med.* DOI: 10.7326/0003-4819-159-9-201311050-00004

Sin TK, Yung BY and Siu PM (2015) Modulation of SIRT1-Foxo1 signaling axis by resveratrol: implications in skeletal muscle aging and insulin resistance. *Cell Physiol Biochem.* DOI: 10.1159/000369718

Takov K, Yellon DM, Davidson SM (2018) Comparison of small extracellular vesicles isolated from plasma by ultracentrifugation or size-exclusion chromatography: yield, purity and functional potential. *J Extracell Vesicles*. DOI: 10.1080/20013078.2018.1560809

Tan CY, Lai RC, Wong W, Dan YY, Lim SK, and Ho HK (2014) Mesenchymal stem cell-derived exosomes promote hepatic regeneration in drug-induced liver injury models. *Stem Cell Res.* DOI: 10.1186/scrt465.

Tao H, Han Z, Han ZC and Li Z (2016) Proangiogenic Features of Mesenchymal Stem Cells and Their Therapeutic Applications. *Stem Cells Int. DOI*: 10.1155/2016/1314709.

Tetta C, Ghigo E, Silengo L, Deregibus MC and Camussi G (2013) Extracellular vesicles as an emerging mechanism of cell to-cell communication. *Endocrine*. DOI: 10.1007/s12020-012-9839-0

Thannickal VJ (2013) Mechanistic links between aging and lung fibrosis. *Biogerontology*. DOI: 10.1007/s10522-013-9451-6

Tracy SW (2013) Something new under the sun? The Mediterranean diet and cardiovascular health. *N Engl J Med.* DOI: 10.1056/NEJMp1302616

Tseng AH, Wu LH, Shieh SS and Wang DL (2014) SIRT3 interactions with FoxO3 acetylation, phosphorylation and ubiquitinylation mediate endothelial cell responses to hypoxia. *Biochem. J.* DOI: 10.1042/BJ20140213

Wang E (1995) Senescent human fibroblasts resist programmed cell death, and failure to suppress bcl2 is involved. *Cancer Res*. PMID: 7757977

Wernly B, Mirna M, Rezar R, et al. (2019) Regenerative Cardiovascular Therapies: Stem Cells and Beyond. *Int J Mol Sci.* DOI: 10.3390/ijms20061420

Xin H, Li Y, Buller B, Katakowski M, Zhang Y, Wang X, et al. (2012) Exosome-mediated transfer of miR-133b from multipotent mesenchymal stromal cells to neural cells contributes to neurite outgrowth. *Stem Cells*. DOI: 10.1002/stem.1129

Xue W, Zender L, Miething C, et al. (2007) Senescence and tumour clearance is triggered by p53 restoration in murine liver carcinomas [published correction appears in *Nature*, 2011]. *Nature*. DOI: 10.1038/nature05529

Zhang B, Wang M, Gong A, Zhang X, Wu X, Zhu Y, Shi H, Wu L, Zhu W, Qian H, Xu W (2014) HucMSC-Exosome Mediated-Wnt4 Signaling Is Required for Cutaneous Wound Healing. *Stem Cells*. DOI: 10.1002/stem.1771

# Part 5

# Scope of thesis and experimental design

The main goal of this PhD project has been the development of an in-vitro human model of cardiac senescence. This model will serve as a platform to both identify molecular mechanisms of human aging and test promising alternative therapies for cardioprotection and regeneration of the injured myocardium.

Firstly, we proceeded to generate the senescence in-vitro model using human induced pluripotent stem cells (hiPSCs) from cardiac explants from patients. hiPSC were subsequently differentiated to functional cardiomyocytes (CM). We induced premature senescence in hiPSC-CMs by exposing them to a sub-lethal concentration of Doxorubicin (Dox) in culture. Dose dependent experiments were performed to adjust the dose and to obtain a consistent senescent model. Senescence markers at molecular, structural, and electrophysiological levels, along with changes in intracellular $Ca^{2+}$ dynamics, ROS production and mitochondrial integrity were evaluated.

Secondly, we utilized the generated senescence model to investigate the cardioprotective and possible anti-aging effects mediated by exosomes (Exo). Exo were isolated from cardiac progenitor cells (CPCs) and characterized. Then, senescent hiPSC-CMs were treated by exposure to Exo and markers of senescence and cellular integrity were re-evaluated.

During my PhD I was also involved in other research studies in order to characterize:

(1) Dox-induced cardiotoxicity in an in-vivo rat model; in particular, cardiotoxicity was evaluated following Dox injection alone or in combination with Trastuzumab (See 'Part 7', paper submitted to *Basic Research in Cardiology,* BRIC-D-20-00593);

(2) the pathophysiological mechanisms of a multifactorial familial form of atrial fibrillation (AF), with particular attention to the identification of putative triggering cellular mechanisms, using patient-derived iPSC-CMs (See 'Published Papers', Cardiovasc Res 2020 May 1;116(6):1147-1160);

(3) SERCA2a stimulation by Istaroxime in a model of diabetic diastolic dysfunction (See 'Published Papers', paper under revision at *Cardiovasc Res*, 2020-0042).

# Part 6

## Stress-induced premature senescence is associated with a prolonged QT interval in a model of human cardiac aging

Alessandra Maria Lodrini[1,2#]; Edoardo Lazzarini[2#]; Sara Bolis[2,3]; Sara Vagni[1]; Giuseppe Vassalli[3,4]; Claudia Altomare[3]; Marcella Rocchetti[1]*; Lucio Barile[2,4,5]*

[1]Department of Biotechnology and Biosciences, Università degli Studi di Milano-Bicocca, Milano, Italy. [2]Laboratory for Cardiovascular Theranostics, Cardiocentro Ticino Foundation, Lugano, Switzerland; [3]Laboratory of Cellular and Molecular Cardiology, Cardiocentro Ticino Foundation, Lugano, Switzerland; [4]Faculty of Biomedical Sciences, Università della Svizzera Italiana, Lugano, Switzerland. [5]Institute of Life Science, Scuola Superiore Sant'Anna, Pisa, Italy.

# The first two Authors contributed equally to the study

* Corresponding Authors

Addresses for correspondence:

Marcella Rocchetti, University of Milano-Bicocca, Piazza della Scienza 2, 20126 Milano, Italy.

marcella.rocchetti@unimib.it

Lucio Barile, Cardiocentro Ticino, via Tesserete 48, 6900 Lugano, Switzerland.

lucio.barile@cardiocentro.org

Running title: iPSC-derived cardiomyocytes as a platform for studying myocardial aging
Keywords: iPS-derived Cardiomyocytes; Senescence; Ageing Heart; Exosomes
Conflicts of interest: Nothing to declare

Paper submitted to *Aging Cell* (ACE-20-0832).

## 6.1 Abstract

Aging of the heart involves adverse remodeling in cardiomyocytes (CMs), resulting in heart failure, which increases with age. This study exploits CMs from human induced pluripotent stem cells (iCMs) as a tool to reproduce and characterize mechanisms involved in aging and to be used as an in-vitro platform for cardioprotective approaches. Human somatic cells were reprogrammed into human induced pluripotent stem cells and subsequently differentiated in iCMs. A senescent-like phenotype (SenCMs) was induced by short exposure (3 hours) to doxorubicin (Dox) at the sub-lethal concentration of 0.2 μM. Dox treatment induced expression of cyclin-dependent kinase inhibitors p21 and p16, and increased positivity to senescence-associated beta-galactosidase (SA-β-gal) when compared to untreated iCM. SenCMs showed an increase in oxidative stress markers and a depolarized mitochondrial membrane potential, which resulted in decreased ATP production. Functionally, SenCMs showed impaired calcium handling and prolonged QTc as compared to iCM. The latter effect was ascribable at augmented sodium current ($I_{NaL}$) and concomitant reduction in delayed rectifier potassium current ($I_{Kr}$). Exosomes derived from cardiac progenitor cells (Exo-CPC) were tested as 'senostatic' agent. Exposure to Exo at the dose of ~$2\times10^3$ particles/cell mitigated electrophysiological impairment SenCMs. Overall, we showed that SenCMs recapitulate the phenotype of aged primary CMs in terms of senescence markers, electrical properties and metabolic features. Additionally, we provided evidence that Exo-CPC can ameliorate age-related cardiac anomalies.

## 6.2 Introduction

Cardiovascular diseases (CVDs) remain the leading cause of death, disability, and morbidity among chronic diseases [Roth et al., 2017]. Advanced age has been identified as one of the traditional risk factors for the development of CVDs [Dhingra & Vasan, 2012]. It is estimated that by the year 2035, nearly one in four individuals will be 65 years of age or older, and this change in the world demographics will result in a large increase in the prevalence of age-related cardiovascular disabilities with a high impact on the utilization of healthcare resources [Steenman & Lande, 2017]. In this context, it would be crucial to implement strategies that limit myocardial dysfunction in the elderly. A critical step in developing these approaches is understanding the age-related pathophysiological changes to unveil the mechanisms underlying the increased susceptibility of the aged heart to injury [Jahangir, Sagar, & Terzic, 2007].

Primary drivers of tissue damage in aging, such as oxidative stress, DNA damage, mitochondrial dysfunction, and metabolic dysregulation, play a role in inducing cellular senescence. Senescence represents a cellular response to such stimuli, thereby being defined as an 'antagonistic' hallmark of aging [McHugh & Gil, 2018]. However, the discovery that senescent cells aberrantly accumulate in aging tissues has substantiated the hypothesis that senescence itself can drive aging [Childs, Durik, Baker, & van Deursen, 2015; McHugh & Gil, 2018]. Indeed, accumulating senescent cells secrete pro-inflammatory molecules triggering the senescence-associated secretory phenotype (SASP), with deleterious effects on the tissue microenvironment leading to age-dependent functional impairment [Kuilman, Michaloglou, Mooi, & Peeper, 2010]. Premature senescence participates in heart remodeling after myocardial infarction [Cui et al., 2018] and cancer therapy-induced cardiotoxicity [Mitry et al., 2020]. Therefore, studying the mechanisms underlying cellular senescence in cardiomyocytes (CMs) might pave the way for understanding the intricacies of age-related changes in the human cardiovascular system's physiology.

Currently, the most used approaches to study cellular senescence are the direct comparison of young and naturally aging animals or the exploiting of aging prone transgenic organisms [Reed et al., 2011]. However, the cardiovascular phenotype in aged animals mimics only partially the changes occurring in humans. CMs derived from human induced pluripotent stem cells (iCMs) offer an unprecedented platform that overcomes not only species-specific limitations but also the technical difficulties of accessing human primary CMs as well as their limited lifespan in culture. This study aimed to develop an in vitro tool for understanding human cardiac senescence's molecular basis that may affect age-related CVDs. Based on extensive published data showing that doxorubicin (Dox) can induce senescence in neonatal murine CMs [Maejima, Adachi, Ito, Hirao, & Isobe, 2008], cardiac progenitor cells (CPCs) [Piegari et al., 2013], and vascular smooth muscle cells [Bielak-Zmijewska et al., 2014], we used sub-apoptotic doses of Dox as an inducer of senescent-like phenotype in human iCMs. We explored phenotypic and functional properties of senescent CMs (SenCM) in comparison to untreated control iCMs. Moreover, we provided preliminary data showing that CPC-derived exosomes (Exo), known as critical mediators of cardioprotective effect of stem/progenitor cells in acute and chronic models of cardiac injury [Barile et al., 2014; Ciullo et al., 2019; Milano et al., 2020], possess modest but present features as ‘senostatic’ agent. To our knowledge, the present study is the first to report that premature senescence can be induced in human iCMs, showing the potential of this platform to investigate in vitro therapeutic approaches aimed at reducing the detrimental accumulation of senescent cells in aging organs and elucidate molecular mechanisms underlying senescence in human cardiomyocytes.

## 6.3 Results

### 6.3.1 Sub-lethal concentrations of Dox induces cell cycle arrest in human iCMs accompanied by negligible cytotoxicity

We successfully generated three different lines of human induced pluripotent stem cells (hiPS) from cardiac somatic cells source as previously described [Pianezzi et al., 2020]. hiPS were reprogrammed to functional cardiomyocytes (iCMs) using a small molecules protocol (see Methods). Phenotypic and functional characteristics of iCMs were described by recent studies from our lab [Altomare et al., 2016; Pianezzi et al., 2020].

Premature senescence was induced in iCMs by a short-time exposure to sub-lethal doses of Dox followed by drug washout (**Supplementary Figure 1A**). Cells were analyzed for the expression of senescence-associated beta-galactosidase (SA-β-gal) and simultaneously monitored for cell death hallmarks. As compared to untreated control iCMs, cell-viability decreased upon exposure to Dox in a dose-dependent manner (**Figure 1A**), whereas the activity of SA-β-gal tended to increase and peaked at 0.2 μM (**Figure 1B**). Overall, these data showed that 0.2 μM Dox induces expression of well-known senescence biomarkers with minimal cytotoxicity. Thus, iCMs treated with 0.2 μM Dox are hereinafter referred to as senescent-like CMs (SenCMs). Unless otherwise specified, measurements were performed 4 days following Dox treatment.

Since iCMs possess residual capability of DNA synthesis leading to poly-nucleation and limited cell division, we assessed the effect of Dox on the capacity of iCM to incorporate the thymidine analogue 5-ethynyl-2′-deoxyuridine (EdU). 0.2 μM Dox treatment dramatically decreased the incorporation of EdU by 16-fold as compared to untreated iCMs (**Figure 1C**).

### 6.3.2 SenCMs display components of senescence-associated pathways

To test whether SenCMs exhibit a typical features of Dox-induced DNA-damage that might trigger the onset of senescence processes [Chandrasekaran, Idelchik,

& Melendez, 2017; Watanabe, Kawamoto, Ohtani, & Hara, 2017], we performed a series of experiments assessing the phosphorylation of histone H2AX on serine 139 (γ-H2AX), the induction of cyclin-dependent kinase inhibitors (CDKIs), and the expression of SASP-associated cytokines.

Dox treatment increased the number of γ-H2AX-positive nuclear foci more than 5-fold as compared to control iCMs (**Figure 2A**). Accumulation of γ-H2AX in SenCMs was associated with augmented expression of $p21^{cip1/waf1}$ and $p16^{INK4a}$ at both mRNA and protein levels (**Figure 2B-E**). Unexpectedly, the transcript levels of $p16^{INK4a}$ peaked at 24 hours after treatment and rescued at the basal level at 48 hours (**Figure 2D**). SenCMs were also characterized by an increased expression of SASP-associated genes. Levels of expression of IL-8 and SERPIN-1 mRNAs were 4-fold higher in SenCMs vs. iCMs (**Figure 2F**). Finally, as an exacerbated release of atrial natriuretic peptides (ANP) and brain/B-type natriuretic peptides (BNP) is often associated with cardiac aging [Li et al., 2017], we explored whether this also occurs in SenCMs. The transcript of ANP and BNP have a trend toward the increase upon treatment with Dox, although not significant (**Figure 2G**).

### 6.3.3 Dox-induced senescence is associated with mitochondrial dysfunction and oxidative stress in SenCMs

Mitochondria are essential determinants of cellular homeostasis in CMs due to the high energetic demand of these cells. The senescence process is generally associated with detrimental alterations in mitochondrial function and increased production of reactive oxygen species (ROS) [Tocchi, Quarles, Basisty, Gitari, & Rabinovitch, 2015]. Therefore, we evaluated the extent to which these aspects affect our model by measuring intracellular ROS levels and evaluating mitochondrial integrity.

SenCMs had significantly increased ROS levels as compared to iCMs (**Figure 3A**). Contextually, the membrane potential ($\Delta\Psi m$) of mitochondria, assessed using the potential-sensitive dye JC-10, became significantly depolarized in

SenCMs (**Figure 3B**), suggesting a potential disruption in organelle integrity. Indeed, SenCMs had a generalized decline of metabolic capacity, as shown by the significant decrease in the cellular ATP/AMP ratio (**Figure 3C**). The imbalance in the energetic fluxes in SenCMs was associated with increased activity of the 5'-AMP-activated protein kinase (AMPK) as highlighted by the positive ratio between the Thr172 phosphorylated AMPK (pAMPK) and the total protein level (**Figure 3E**). However, the increased activity was not accompanied by concomitant increase in protein expression level (**Figure 3D**). This suggests that cytosolic AMP levels could intrinsically increase AMPK activity by inducing its allosteric activation [Kim, Yang, Kim, Kim, & Ha, 2016].

### 6.3.4 Dox-induced senescence affects electrical properties and intracellular $Ca^{2+}$ dynamics of SenCMs

Aging is associated with an increased incidence of cardiac arrhythmias and heart failure. Indeed, the ability of senescent CMs to respond to stressors is compromised by ionic remodelling, abnormalities in calcium handling, and defective sarcoplasmic reticulum (SR)-mitochondria crosstalk [Mirza, Strunets, Shen, & Jahangir, 2012; Ruiz-Meana et al., 2019]. Dox is also known to cause arrhythmias in humans as well as animal models [Doherty et al., 2015; Zhu, Shou, Payne, Caldwell, & Field, 2008]. Using the technology of microelectrode arrays (MEA), we sought to explore whether Dox-induced senescence may affect QT intervals by measuring its equivalent at cellular level, the field potential duration (FPD). We found that electrophysiological properties of multicellular preparations of SenCMs were significantly altered as compared to iCMs, with a time-dependent increase of the corrected FPD (or QTcB) (**Figure 4A**). Notably, the prolongation of QTcB worsened over time and reached a steady-state value 5-7 days after single Dox exposure at day 0, while the RR interval was not significantly affected by Dox treatment (**Supplementary Figure 1I**).

As the QT interval reflects the duration of the action potential (AP) at a single-cell level, we further investigated by patch-clamp analysis the specific contribution of

inward and outward ionic currents that might explain the QT prolongation observed at multicellular level. As first attempt we investigated the rapid delayed rectifier $K^+$ current ($I_{Kr}$) I/V relationship, mediated by the HERG (also known as KCNH2) channel. We found that SenCMs showed significant downregulation of $I_{Kr}$ density (3 µM E4031-sensitive current) in comparison to control iCMs 5-7 days after Dox treatment (**Figure 4B**). Moreover, the protein expression level of the HERG channel at this time point was reduced in SenCMs vs. iCMs (**Figure 4C**). As it was the first time that a decrease in expression of KCNH2 was associated with senescent CMs, we took advantage of our in-house biobank of human atrial appendage tissue specimens to verify a possible correlation between the protein levels and the age of the donors. Consistent with the in vitro data, we found a significant inverse correlation between KCNH2 expression and age of the patient (**Figure 4D**).

A second cause of prolonged QT in CMs might be ascribable to an increased inward current during the plateau phase of the AP. Thus, we evaluated the Dox-induced modulation of the late component of $Na^+$ current ($I_{NaL}$), a good candidate accordingly to its sensitivity to the cellular redox state [Yang et al., 2015]. $I_{NaL}$ was isolated as TTX (2 µM)-sensitive current ($I_{TTX}$) by applying slow voltage ramps. Inward $I_{TTX}$ might be representative of both $Na^+$ window current at negative potentials and $I_{NaL}$ at more positive potential [Rocchetti et al., 2014]. Inward $I_{TTX}$ measured at 0 mV (representative of INaL) significantly increased in SenCMs compared to iCMs 5-7 days following Dox treatment (**Figure 4E**). Accordingly, the proportion of CAMKII phosphorylated on the Thr286 of its alpha subunit (pCAMKII), a well-known modulator of $I_{NaL}$ [Hegyi et al., 2018], tended to increase in SenCMs (**Figure 4F**). Overall, the combination of $I_{Kr}$ downregulation and $I_{NaL}$ enhancement may justify the Dox-induced senescence-dependent electrical remodeling leading to QT prolongation.

Next, we studied the intracellular $Ca^{2+}$ dynamics in FLUO-4 voltage clamped iCMs. In comparison to controls, $Ca^{2+}$ transient (CaT) amplitude and sarcoplasmic reticulum $Ca^{2+}$ content (Ca SR), evaluated through a caffeine (10 mM) pulse, were significantly reduced in SenCMs 5-7 days after treatment, leading to a similar

fractional release (0.41±0.04 vs 0.44±0.04, ns). Both $Ca^{2+}$ influx through L-type $Ca^{2+}$ channel (**Figure 4G**) and peak $I_{CaL}$ density (-9.8±1.4 pA/pF vs -11.1±1.1 pA/pF, ns) at 0 mV were not significantly affected in SenCMs. These results suggest reduced SR $Ca^{2+}$ uptake in SenCMs, probably as a consequence of SERCA2a downregulation, as previously reported in aged animal models [Hamilton & Terentyev, 2019].

### 6.3.5 CPC-derived exosomes ameliorate mitochondrial health and energy status in SenCMs

Cardiac progenitor cells (CPCs)-derived Exosomes (Exo) are secreted nanovesicles known for their cardioprotective effects in different models of acute cardiac ischemia [Barile et al., 2018; Barile et al., 2014; Gallet et al., 2017]. Moreover, CPC-Exo has shown to attenuate Dox-induced oxidative stress in cardiomyocytes [Milano et al., 2020].

Based on these recently published data, we addressed whether Exo could also rescue the senescent phenotype induced by Dox in human iCMs. To explore this hypothesis, SenCMs were exposed to CPC-Exo ($2\times10^3$ Exo/cell) 24 hrs after Dox treatment (**Supplementary Figure 1A**). CPC-derived Exo significantly prevented Dox-induced increase of ROS levels (**Figure 5A**) and significantly blunted Dox-induced mitochondrial membrane potential depolarization in SenCMs (**Figure 5B**). Consistently, ATP/AMP ratio was rescued at basal level (**Figure 5C**), and activity of AMPK (**Figure 5D**) was normalized towards the values of iCMs. However, SenCMs exposed to CPC-Exo did not differ from their untreated counterpart in terms of a $p21^{cip1/waf1}$ and SA-β-Gal expression (**Figure 5E-F**, **Supplementary Figure 1D**), cell viability (**Supplementary Figure 1E**), and number of γ-H2AX-positive nuclear foci (**Supplementary Figure 1F**). Conversely, restoration of cellular energetic balance directly affected $I_{NaL}$, which was restored towards the values of control cells along with CAMKII activity (**Figure 5G-H**), probably justifying the protective effects of Exo on Dox-induced

QT prolongation (**Figure 5I**). Concurrently, Dox-induced $I_{Kr}$ downregulation was not affected by Exo treatment (**Supplementary Figure 1G-H**).

## 6.4 Discussion

Stressors such as DNA-damaging agents [Wlaschek et al., 2000], overexpression of oncogenic genes [Spyridopoulos, Isner, & Losordo, 2002], and oxidants [Chen, Tu, & Liu, 2000] can induce age-independent senescence. Stress-induced premature senescence (SIPS) not only plays a role in the arrest of cell cycle and cell propagation in replicating tissues, but also impairs the functionality of organs with scarce residual replicative capacity, as it is the heart. SIPS is considered a novel mechanism in the heart remodelling after acute myocardial infarction (Cui et al., 2018) and cancer therapy-induced cardiotoxicity [Mitry et al., 2020]. Maejima et al. reported that murine neonatal cardiomyocytes (CMs) that undergo SIPS have common features of replicative-senescence, including upregulation of cell-cycle regulatory inhibitors, expression of SA-β-gal, and the attenuation of telomerase activity [Maejima et al., 2008]. Here we extended existing data to human iPS-derived cardiomyocytes (iCMs), overcoming potential specie-specific limitations, and exploring functional electrophysiological properties of artificially aged human CMs. This report showed that sub-toxic concentration of doxorubicin induced expression of either p21 and p16 in human CMs and causes cellular senescence. Senescent cells displayed components of DNA-damage response (DDR), such as γH2AX foci. The first consequence of these effects, is that the residual cardiomyocyte renewal – which has been demonstrated occurring in humans by approximately 0.5% to 2% per year [Bergmann et al., 2009] and accounting for a stable turnover of cardiomyocytes in the healthy adult heart [Eschenhagen et al., 2017] – might be impaired by SIPS. In fact, the synthesis of new DNA was dramatically abrogated in iCMs following Dox treatment (Figure 1C). Additionally, as SenCMs showed mitochondrial damage in terms of a reduction in mitochondrial membrane potential and consequently impaired energy production capability. The model can mimic the peculiar effects of aging on mitochondria during the development of heart failure [Doenst, Nguyen, & Abel, 2013].

Importantly, we provide evidence showing that stress-induced senescence affects ionic currents in human CMs. We observed a reduction of the rapid delayed rectifier $K^+$ current ($I_{Kr}$) and enhancement of the late $Na^+$ current ($I_{NaL}$) in SenCMs vs. control ones, resulting in a prolonged QTc interval. The latter constitutes a downright novel finding that supports at a cellular level a recent population study by Rabkin and colleagues [Rabkin, Cheng, & Thompson, 2016]. They applied a rigorous analytical method to compare six QTc formulae and clearly showed that older individuals have a greater QTc. A significant association between QTc and age was evident in both sexes and regardless of whether they considered a linear or non-linear relationship [Rabkin et al., 2016]. This finding was sustained by our data in human tissue showing a significant inverse relationship between age and KCNH2 expression (Figure 4D). Although some aspects of the study from Rabkin and colleagues remain controversial as other investigators have reported no association between age and QTc [Huang, Lin, Pan, & Chen, 2010; Tran, White, Chow, & Kluger, 2001], our data supports the hypothesis that elderly patients are more vulnerable to situations and medications that might prolong the QTc, leading to increased propensity to arrhythmias.

Electrical activity was associated to alteration in $Ca^{2+}$ handling in SenCMs. In particular, while $Ca^{2+}$ influx was not significantly altered, SR $Ca^{2+}$ content and release were reduced in SenCMs, thus suggesting a compromised functionality of SERCA2a pumping activity in senescent CMs. A similar finding has been reported in animal models [Hamilton & Terentyev, 2019] and can justify the diastolic relaxation impairment in the aged population [Kitzman, 2000].

Moreover, our data sheds light on the significance of having an in vitro platform for exploring cellular senescence and its link with aging-associated pathologies, as well as to dissect specific drug effects on aging tissues and organs. Contextually, we found that exosomes derived from CPCs, which have been previously demonstrated to be cardioprotective in acute and chronic models of heart injury [Barile, Gherghiceanu, Popescu, Moccetti, & Vassalli; Ciullo et al., 2019; Gallet et al., 2017; Gao et al., 2020; Milano et al., 2020], partially antagonized Dox-induced senescence in human CMs. This new information

integrates previous findings that CPC-Exo attenuates anthracycline-related oxidative stress in CMs [Milano et al., 2020]. This primary effect of Exo, likely due to these vesicles enveloping numerous proteins involved in redox processes (e.g. SOD2) [Milano et al., 2020], significantly affects the electrophysiological properties of aged CMs, thus giving insights and new perspectives for the therapeutic use of exosomes in cardiovascular disease.

Finally, our data substantiate that senescence of cardiac cells is an event of primary importance for the occurrence of anthracycline-related cardiomyopathy [Altieri et al., 2016].

## 6.5 Methods and Materials

### 6.5.1 Generation and characterization of human iPS cells

Right cardiac atrial appendage tissue specimens were collected from patients who underwent surgical repair of heart valves and had no concomitant coronary artery disease. Patients gave written informed consent. Cardiac progenitor cells (CPCs) were derived as cellular outgrowth from the explants using an ex vivo primary tissue culture technique, as previously described [Barile et al., 2014; Pianezzi et al., 2019]. Atrial tissue was rinsed with phosphate buffer saline (PBS) and cut into small pieces that were placed into a 100-mm cell culture dish (Corning). To facilitate cell outgrowth, atrial tissue was treated with Trypsin/EDTA (SIGMA Life Science) for 2–3 min. Tissue pieces were then moved to a 100-mm dish coated with 0,02% gelatin and cultured in IMDM medium (Iscove's Modified Dulbecco's Medium) supplemented with 20% fetal bovine serum (FBS) and 1% penicillin/streptomycin (all from Life Technologies). The culture medium was changed twice a week. After 25–30 days of culture, CPCs were enzymatically detached using Trypsin/EDTA and transferred to a gelatin-coated 35-mm dish (Corning, $2.5\times10^5$ cells/dish). After an additional 48 h, CPCs were transduced with the integration-free Sendai virus cocktail hKOS:hc-Myc:hKlf4 at a MOI of 5:5:3 (CytoTune-iPS 2.0 Sendai Reprogramming Kit, Thermo Fisher Scientific), as per manufacturer's instructions. The virus was removed after 24 h and the medium was changed daily in the next 7 days. A week after transduction, medium was changed to StemFlex (Thermo Fisher Scientific). Individual colonies with ESC-like morphology typically appeared after 25-35 days and were transferred manually into 12-well plates coated with Matrigel (hESC Qualified Matrix, Corning) and expanded. Established human iPS cell lines were maintained in 33-mm Matrigel-coated plates (Falcon), passaged with TrypLe solution (TrypLE Express Enzyme 1x, Thermo Fisher Scientific) and cultured in StemFlex medium.

### 6.5.2 Directed differentiation of iPS cells into CMs

Directed differentiation of human iPS cells into iCMs was performed via WNT signaling pathway modulation. Differentiation was initiated at 90% confluence in 12-well Matrigel-coated plates with a differentiation medium composed of RPMI 1640 supplemented with B-27 minus insulin (Thermo Fisher Scientific) with 4 μM CHIR99021 (Merck Millipore) for 48 h and subsequently 5 μM IWP4 (Merck Millipore) for 48 h [Lian et al., 2013]. The medium was changed to a maintenance medium composed of RPMI 1640 with B-27 plus insulin (Thermo Fisher Scientific) at day 7. Metabolic selection of CMs was performed using a selection medium composed of RPMI 1640 without glucose (Thermo Fisher Scientific), 0.5 mg/ml human recombinant albumin, 0.2 mg/ml L-ascorbic acid 2-phosphate, and 4 mM lactate (Sigma-Aldrich) from days 10 to 17. Afterwards, hiPSC-CMs were cultured in maintenance medium at least to day 30 for further maturation.

### 6.5.3 Exo purification

Medium conditioned by CPCs was obtained by culturing cells in DMEM (Dulbecco's Modified Eagle's Medium, Thermo Fisher Scientific). After 7 days the conditioned medium was centrifuged at 3000 g for 15 min, filtered through a 0.2 mm membrane (BD Biosciences) and processed using ultracentrifugation at 100 000 g for 90 min. The exosomes (Exo) pellet was re-suspended in 100–500 μL of phosphate-buffered saline (PBS, pH 7.4) and stored at -80°C. Three different Exo preparations were pooled and used for every experimental procedure. Nanoparticle tracking analysis was performed using NanoSight LM10 (Malvern Instruments, Worcestershire, UK).

### 6.5.4 Dox-induced senescence model

Optimal conditions to obtain a doxorubicin (Dox)-induced senescent phenotype were determined by testing different experimental protocols. Of the tested conditions (including different concentrations of Dox, acute or chronic treatment, acute treatment with Dox exposure for different time periods), we obtained the best results with acute exposure of iCMs to 0.2 μM Dox for 3 hours. Briefly,

spontaneously beating iCMs were enzymatically dissociated (Multi Tissue Dissociation Kit 3, Miltenyi Biotec) and then plated in Synthemax II-SC Substrate (Corning)-coated wells ($5\times10^4$ cells/$cm^2$). After 24-48 hours, part of the wells had the maintenance medium replaced with Dox-containing maintenance medium to obtain senescent-like cardiomyocytes (SenCMs). After 3 hours from Dox administration, all cells were washed twice with PBS and placed back in fresh maintenance medium. One day after the Dox treatment, part of the SenCMs was randomly selected and exposed to CPC-Exo ($2\times10^3$ Exo/cell) for 24 hours. Treated cells were then characterized at different time-points.

### 6.5.5 SA-β-gal staining

iCMs were stained for senescence-associated β-galactosidase (SA-β-gal) activity as previously described [Dimri et al., 1995]. Briefly, after appropriate DOX exposure, the cells were washed twice with PBS, fixed with 2% formaldehyde and 0.2% glutaraldehyde in PBS, and washed twice in PBS. Cells were stained in X-gal staining solution (1 mg/ml X-gal, 40 mmol/l citric acid/sodium phosphate, 5 mmol/l potassium ferricyanide, 5 mmol/l potassium ferrocyanide, 150 mmol/l NaCl, 2 mmol/l $MgCl_2$, pH 6.0). After 6 hours, cells were washed twice with PBS. For a sensitive determination of the total cell number, cells were counterstained with 1 µg/ml Hoechst 33342 (Molecular Probes). Stained cells were examined using Lionheart FX Automated Microscope (BioTek Instruments Inc., Winooski, VT, USA).

### 6.5.6 Cell viability

Cellular viability was assessed by double labeling of cells with 1 µM calcein-AM, 1µg/ml Hoechst 33342 and 1.2 µM DRAQ7. Viable total and dead cells were counted using the Lionheart FX Automated Microscope (BioTek Instruments Inc., Winooski, VT, USA).

### 6.5.7 Immunochemistry

After appropriate treatment, iCMs were washed twice with PBS and then fixed for 5 min at RT using a PFA-4%/sucrose-2% solution. Fixed cells were incubated for 10 min with glycine 0.1 M and then washed with PBS for 5 min. Cells were then permeabilized with 3 washes of 0.1% Triton X (Triton X detergent, Sigma-Aldrich) in PBS for 10 min each, followed by a 5-min wash with PBS. Cells were then blocked in bovine serum albumin (BSA) 2% (Sigma-Aldrich) for 1 h at RT. Subsequently, they were incubated with PBS containing 0.1% Tween, 0.2% BSA, and the primary antibody for 2 h at 37 °C. To assess cardiac differentiation, cells were stained using antibodies against Sarcomeric Actin (α-S-Actin) (Abcam 9465) and cardiac Troponin T (cTnT) (13-11 Thermo Fisher), while to assess presence of DNA damage, cells were stained using antibodies against γ-H2AX (9718 Cell Signaling ). Nuclei were counterstained with DAPI (1:1000), EdU (1 μM) where supplied 24h post-doxorubicin treatment and revealed with Click-it kit (Thermo Fisher) following manufacturer protocol to measure active DNA synthesis. Stained cells were examined using Lionheart FX Automated Microscope (BioTek Instruments Inc., Winooski, VT, USA).

### 6.5.8 Real time PCR analysis

For RNA extraction, iCMs were washed twice using a 1:1 DMEM/F12 solution, and RNA was extracted by adding 1 mL of TRI-Reagent (Sigma-Aldrich) as per manufacture instructions. For reverse transcription, 1 μg of RNA was reverse-transcribed using GoScript Reverse Transcription System kit (Promega) as per manufacture instructions. To perform real-time PCR, the following mix was used: 6 μL DEPC water, 5 μL SYBR Green, 2 μL of cDNA diluted 1:50 in DEPC water, 1 μL primers forward 10mM, and 1 μL primers reverse 10mM. Amplification and detection of specific products were performed in triplicate using a CFX Connect™ Real-Time PCR Detection System (Bio-Rad Labs). The threshold cycle (Ct) of each gene was automatically defined and normalized to the control gene GAPDH (ΔCt value). To compare gene expression levels among different treatments, ΔΔCt values in treated CMs were calculated as the differences between the ΔCt

value in these groups and the ΔCt value in untreated CMs following Livak method (ref doi: 10.1006/meth.2001.1262.). Primers sequences are shown in **Supplementary Table 1**.

### 6.5.9 Western blot analysis

Total proteins were extracted by lysing cells and then heated at 95 °C for 5 min with Laemmli SDS sample buffer 6× with 0.375 M Tris-HCl pH 6.8, 12% SDS, 60% glycerol, 0.6 M DTT, 20% (v/v) beta-mercaptoethanol 70.2% (w/v) bromophenol blue (VWR International LCC). Proteins were separated on 4–20% Mini-PROTEAN® TGX™ Precast Gel (Bio-Rad), and transferred onto a PVDF membrane with a semi-dry transfer system (Bio-Rad). The membranes were blocked for 1 h with Intercept (TBS) Blocking Buffer (Licor), and incubated with the primary rabbit polyclonal Abs at 4 °C overnight (anti-p16, 1:1000, Proteintech; anti-p21, 1:1000, Abcam; anti-KCNH2, 1:200, Alomone; anti-AMPK, 1:1000, Cell Signaling; anti-CAMKII, 1:2000, Abcam). Membranes were then rinsed and incubated with appropriated secondary antibodies at RT for 2 h. Subsequently, the membranes were rinsed and analysed using the Odyssey CLx Detection System (LI-COR Biosciences).

### 6.5.10 ATP/AMP ratio

iCMs were lysed by incubation with an ultrapure water buffer containing perchloric acid 2.5% for 10 min, followed by a freeze (-20 °C)-thaw cycle. The lysate was then incubated with KH2CO3 for 5 min, resulting in crystal and $CO_2$ formation. At the end of the reaction, the supernatant was centrifuged (18000 G for 15 min) to remove any precipitate. For ATP detection, the supernatant was incubated with an ultrapure water buffer containing (mM) 100 Tris, 50 glucose, 0.2 $NADP^+$, 5 $MgCl_2$, 0.27 $HK/G_6PDH$. The increase in absorbance over time indicated the reduction of NADPH and it correlated with the ATP levels in the supernatant. For AMP detection, the supernatant was incubated with an ultrapure water buffer containing (mM) 100 Tris, 0.15 NADH, 0.2 ATP, 1 PEP, 5 MgCl2, 0.27

PK/LDH, 0.27 AK. The decrease in absorbance over time indicated the oxidation of NADH and it correlated with the AMP levels in the supernatant.

### 6.5.11 ROS detection assay

iCMs were seeded in 96-well/clear bottom plates for fluorescent measurements. Cells were washed twice with PBS and then incubated at 37°C in the dark with the ROS staining buffer containing dihydroethidium (5 μM After 30 min of incubation, designated positive control wells were treated with TBHT (100 μM). After 30 additional minutes, iCMs were gently washed with PBS. The fluorescence was measured using the Infinite M-series fluorescent plate reader (TECAN) using an excitation wavelength of 480-520 nm and an emission wavelength of 580-600 nm.

### 6.5.12 JC10 assay

Designed positive control cells were incubated with maintenance medium containing CCCP (carbonyl cyanide m-chlorophenyl hydrazine) at 37 °C for 1 hour. All wells were then washed twice with PBS and incubated with the JC10 dye (Abcam) as per manufacturer instructions. After 45 minutes of incubation, the fluorescence was measured using the Infinite M-series fluorescent plate reader (TECAN) using an excitation wavelength of 490 nm and an emission wavelength of 520-570 nm.

### 6.5.13 Microelectrode arrays

Field potentials (extracellular recordings) of spontaneously beating clusters of iCMs (cardiac bodies, CBs) were recorded at 37 °C using a 60MEA100/10iR-Ti-gr 64-electrode Microelectrode Arrays (MEA, Multi Channel Systems). CBs were seeded in the Syntemax-coated MEA chambers (volume 500 μl) for at least 4 days before appropriate DOX treatment and recordings. The latter were performed in maintenance medium. For each time-point, measurements were taken 10 minutes after signals had reached a steady state value. The duration of

field potentials (FPD), reflecting the electrical systole, was measured from the onset of the sharp positive deflection to the peak of the secondary slow deflection. This measurement is representative of the electrocardiographic QT interval. The rate corrected QT intervals (QTc) were calculated by applying Bazett's correction ($QTc = QT/\sqrt{RR}$). MEA data analysis was performed with MC Rack, MC Data Tool (both by Multi Channel Systems) and Clampfit 10.7 (Molecular Devices).

### 6.5.14 Membrane currents

iCMs were voltage-clamped in the whole-cell configuration at physiological temperature. iCMs were superfused at 2 ml/min with the extracellular Tyrode's solution containing (mM) 154 NaCl, 4 KCl, 1 $MgCl_2$, 2 $CaCl_2$, 5 HEPES-NaOH, 5.5 D-glucose (pH 7.4). Pipette solution contained (mM): 110 K-aspartate, 23 KCl, 3 $MgCl_2$, 2 $CaCl_2$, 5 HEPES-KOH, 5 EGTA-KOH, 5 ATP $Na^+$-salt, 5 phosphocreatine $Na^+$ salt, 0.4 GTP $Na^+$ salt (pH 7.35). Membrane capacitance ($C_m$) and series resistance were measured in every cell and left uncompensated. Signals were acquired with Axopatch 200A (Molecular Devices) connected to a Digidata 1200 (Molecular Devices) and filtered at 2 kHz via pClamp 8 (Molecular Devices). Current densities (pA/pF) were obtained by normalizing current amplitudes to $C_m$. The rapid delayed rectifier $K^+$ current ($I_{Kr}$) was recorded as E-4031 (3 µM)-sensitive current by applying depolarizing steps from -40 mV to +40 mV in the presence of $I_{Ks}$ and $I_{CaL}$ blockers (1 µM) HMR1556 and (1 µM) nifedipine respectively. $I_{Kr}$ I/V relationships were obtained by measuring tail currents at -40 mV. The late component of the $Na^+$ current ($I_{NaL}$) was isolated as TTX (2 µM)-sensitive current ($I_{TTX}$) by applying slow voltage ramps (28 mV/s) from -100 mV to +40 mV. $I_{TTX}$ at 0 mV was taken as representative of $I_{NaL}$, while peak $I_{TTX}$ value, occurring at more negative potentials, was assumed to reflect the $Na^+$ 'window component' ($I_{Naw}$) as previously described [Rocchetti et al., 2014].

### 6.5.15 Intracellular $Ca^{2+}$ dynamics

Cytosolic $Ca^{2+}$ and membrane current were simultaneously recorded in V-clamped iCMs loaded with Fluo4-AM (10 μM). iCMs were superfused at 2 ml/min with the Tyrode's solution added with 2 mM 4-AP and 1 mM $BaCl_2$ to block $K^+$ currents. Pipette solution contained (mM) 110 K-aspartate, 23 KCl, 3 $MgCl_2$, 0.04 $CaCl_2$, 5 HEPES-KOH, 0.1 EGTA-KOH, 5 ATP $Na^+$-salt, 5 phosphocreatine $Na^+$ salt, 0.4 GTP $Na^+$ salt, 0.01 Fluo4-$K^+$ salt (pH 7.3). Resting fluorescence at -80 mV was used as reference ($F_0$) for signal normalization ($F/F_0$) after subtraction of background. $Ca^{2+}$ transients (CaT) and $I_{CaL}$ were recorded during 300 ms steps to 0 mV following 50 ms step to -35 mV to inactivate $Na^+$ channels. $I_{CaL}$ was isolated as nifedipine (10 μM)-sensitive current; nmols of $Ca^{2+}$ entering the cell (CaL influx) were quantified integrating $I_{CaL}$ during the step. Sarcoplasmic reticulum (SR) $Ca^{2+}$ content (CaSR) was estimated by both integrating the $Na^+/Ca^{2+}$ exchanger (NCX) current ($I_{NCX}$) and measuring CaT amplitude elicited by caffeine (10 mM) pulse, obtaining comparable results.

### 6.5.16 Statistical analysis

Data are expressed as the mean ± standard error of the mean (SEM) of independent experiments. The differences between groups were tested with unpaired t-test or one-way ANOVA analysis as appropriate. Post-hoc comparison between individual means was performed with Tukey test. A p-value $< 0.05$ was considered statistically significant.

## 6.6 Figure Legends

**Figure 1: Response of human iPS-derived cardiomyocytes (iCMs) to doxorubicin (Dox).** Response of human iPS-derived cardiomyocytes (iCMs) to doxorubicin (Dox). Cells were incubated with low concentrations (0.2, 0.5, or 1 µM) of Dox for 3 hours, then washed and placed back in fresh maintenance medium. The analysis was performed four days after treatment. (A) Viable cells were labeled with Calcein-AM/DRAQ7 as described in Methods and Materials. The percentages of dead cells (ratio of DRAQ7 positive and Calcein negative cells on the total number of cells) are shown in the bar graphs representing means of four independent experiments ± SEM. (B) Representative bright-field microscopy images of SA β-gal staining in iCMs and in 0.2 µM Dox-treated cells. The percentages of SA β-gal-positive cells are shown in the bar graphs representing the mean of four independent experiments ± SEM. (C) EdU incorporation in iCM and Dox-treated cells. Cells were stained for cTnT followed by counterstaining with DAPI. Quantitative analysis of double-positive cells for EdU and cTnT is shown in the bar graphs representing four independent experiments ± SEM. * $P < 0.05$, ** $P < 0.01$ vs. iCMs. # $P < 0.05$ vs. 0.2 µM Dox.

**Figure 2: Induction of senescence markers in SenCMs.** (A) Representative images of immunostaining of iCMs with γ-H2AX antibody followed by counterstaining with DAPI 4 days after 0.2 µM Dox treatment. The number of γ-H2AX-positive foci per cell was calculated. Data are means of four independent experiments ± SEM. (B) p21 mRNA relative copy number in SenCMs 1, 2 and 4 days after Dox treatment, referenced to iCMs. Data are means of four independent experiments ± SEM. (C) Western blot showing p21 expression levels 4 days after treatment. Quantitative data of five independent experiments ± SEM (densitometric values for the protein of interest normalized for histone H3). (D) p16 mRNA relative copy number in SenCMs 1, 2 and 4 days after treatment, referenced to control iCMs. Data are means of four independent experiments ± SEM. (E) Western blot showing p16 expression levels 1 day after treatment.

Quantitative data of three independent experiments ± SEM (densitometric values for the protein of interest normalized for GAPDH). (F) SASP-associated genes mRNA relative copy number in SenCMs 4 days after treatment, referenced to iCMs. Data are means of three independent experiments ± SEM. (G) ANP and BNP mRNA relative copy number in SenCMs 4 days after Dox treatment, referenced to iCMs. Data are means of four independent experiments ± SEM. * P < 0.05, ** P < 0.01 vs. iCMs.

**Figure 3: Induction of mitochondrial damage in SenCMs.** (A) 4 days after Dox treatment cells were incubated with DHE for intracellular $H_2O_2$ detection as described in Methods and Materials. Data shown in the bar graph are means of six independent experiments ± SEM. (B) Cells were incubated with the potential-sensitive dye JC-10 and mitochondrial membrane potential (ΔΨm) was quantified 2- and 4-days post treatment. The graph represents the means of 3 and 5 independent experiments respectively ± SEM. (C) Cells were lysed 4 days after treatment and intracellular ATP and AMP levels were measured as described in Methods and Materials. Data are means of four independent experiments ± SEM. (D) AMPKα1 and AMPKα2 mRNA relative copy numbers in SenCMs 4-days post treatment, referenced to control iCMs. Data are means of three independent experiments ± SEM. (E) pThr172 AMPK:$AMPK_{tot}$ protein expression levels. Quantitative data of three independent experiments ± SEM (densitometric values for the proteins of interest normalized for GAPDH). * P < 0.05, ** P < 0.01 vs. iCMs.

**Figure 4: Alterations in electrical activity and intracellular $Ca^{2+}$ handling SenCMs.** (A) The electrical activity of spontaneously beating clusters of CMs was recorded using MEA for 7 consecutive days after Dox treatment. Data are means of five independent experiments ± SEM. QTcB: QT-interval corrected by Bazett's formula. Representative examples of field potentials in iCMs and SenCMs at day 1 and 7 are shown. (B) E-4031 (3μM)-sensitive currents ($I_{Kr}$) activated according to the protocol shown on top and relative I/V relationships in iCMs (N = 21) and SenCMs (N = 26) 5-7 days after treatment. (C) HERG (KCNH2) protein expression

levels in iCMs and SenCMs 5 days after treatment. Quantitative data of four independent experiments ± SEM (densitometric values for the protein of interest normalized for histone H3). (D) HERG (KCNH2) protein expression levels in human patient-derived atrial explants (densitometric values for the proteins of interest normalized for histone H3). The linear correlation (black line) and confidence intervals (dotted lines) are shown. (E) TTX (2 μM)-sensitive current ($I_{TTX}$) activated during slow voltage ramps (28 mV/sec) from a holding potential of -100 mV. Mean I/V relationships for iCMs (N = 13) and SenCMs (N = 13) 5-7 days after treatment are shown. Statistics of $I_{TTX}$ at 0 mV, representative of $I_{NaL}$, are reported on the right. (F) pThr286 CAMKII:CAMKII protein expression levels in SenCMs 4 days after treatment in comparison to iCMs. Quantitative data are four independent experiments ± SEM (densitometric values for the proteins of interest normalized for GAPDH). (G) Simultaneously recorded membrane currents and $Ca^{2+}$ transients (CaT) according to the voltage clamp protocol shown on top in Fluo4-loaded iCMs. Statistics of CaL influx, CaT amplitude and caffeine-induced CaT amplitude (estimating CaSR) in iCMs (N = 22) and SenCMs (N = 14) 5-7 days after Dox treatment. * $P < 0.05$, ** $P < 0.01$ vs. iCMs.

**Figure 5: CPC-Exo prevented Dox-induced changes in SenCMs.** SenCMs were treated with CPC-Exo ($2\times10^3$ Exo/cell) 24 hours after Dox treatment. (A) Intracellular ROS ($H_2O_2$) changes (DHE fluorescence) were detected 4 days after Dox treatment. Data are means of >4 independent experiments ± SEM. (B) Mitochondrial membrane potential (ΔΨm) changes (JC-10 fluorescence) analysed 2- and 4-days post treatment. Data are means of >3 independent experiments ± SEM. (C) Intracellular ATP:AMP ratio measured 4 days after Dox treatment. Data are means of >3 independent experiments ± SEM. (D) pThr172 AMPK:AMPK protein expression levels 4 days post Dox treatment. Data are means of 3 independent experiments ± SEM. Data reported in panels A-D w/o CPC-Exo are those shown in Figure 3A-D. (E) p21 expression levels 4 days after Dox treatment. Quantitative data of >3 independent experiments ± SEM (densitometric values for the protein of interest normalized for histone H3). Data

w/o CPC-Exo reported here are those shown in Figure 2C. (F) Percentage of SA β-gal positive cells 4 days post treatment. Data are means of >3 independent experiments ± SEM. Data w/o CPC-Exo reported here are those shown in Figure 1B. (G) TTX (2 μM)-sensitive current ($I_{TTX}$) I/V relationships 5-7 days after treatments and statistics of $I_{TTX}$ at 0 mV, representative of $I_{NaL}$, are shown (N = 13 for each group). Data w/o CPC-Exo reported here are those shown in Figure 4E. (H) pThr286 CAMKII:CAMKII protein expression levels. Quantitative data are four independent experiments ± SEM (densitometric values for the proteins of interest normalized for GAPDH). Data w/o CPC-Exo reported here are those shown in Figure 4F. (I) Electrical activity of spontaneously beating clusters of iCMs recorded using MEA for 7 consecutive days. Data are means of five independent experiments ± SEM. QTcB: QT-interval corrected by Bazett's formula. Data w/o CPC-Exo reported here are those shown in Figure 4A. * $P < 0.05$, ** $P < 0.01$ vs. iCMs. # $P < 0.05$ vs. SenCMs.

## 6.7 Figures

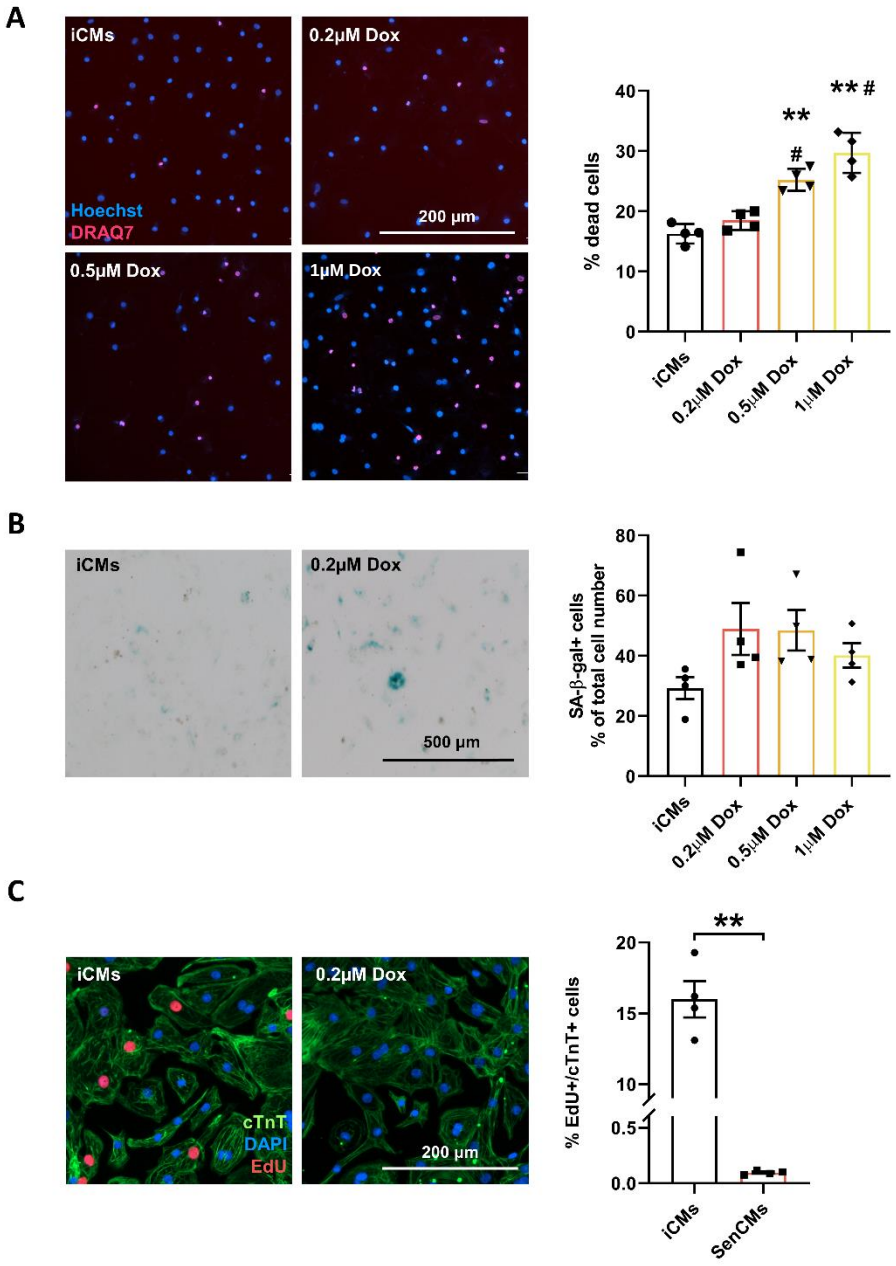


Figure 1

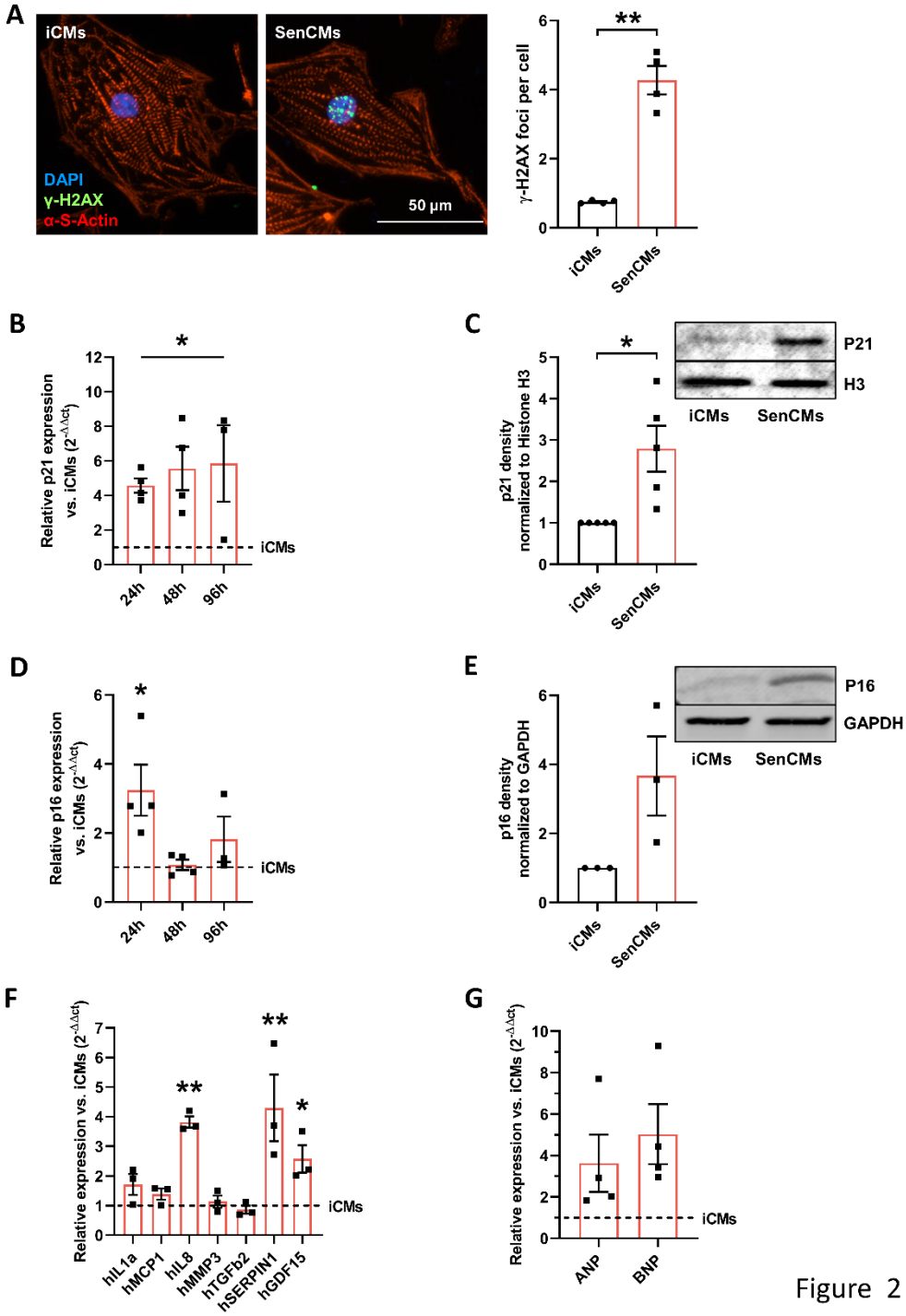
A
iCMs
SenCMs
DAPI
γ-H2AX
α-S-Actin
50 μm
γ-H2AX foci per cell
**
iCMs
SenCMs
B
Relative p21 expression vs. iCMs (2^-ΔΔct)
*
iCMs
24h
48h
96h
C
p21 density normalized to Histone H3
*
P21
H3
iCMs
SenCMs
D
Relative p16 expression vs. iCMs (2^-ΔΔct)
*
iCMs
24h
48h
96h
E
p16 density normalized to GAPDH
P16
GAPDH
iCMs
SenCMs
F
Relative expression vs. iCMs (2^-ΔΔct)
**
**
*
iCMs
hIL1a
hMCP1
hIL8
hMMP3
hTGFb2
hSERPIN1
hGDF15
G
Relative expression vs. iCMs (2^-ΔΔct)
iCMs
ANP
BNP

Figure 2

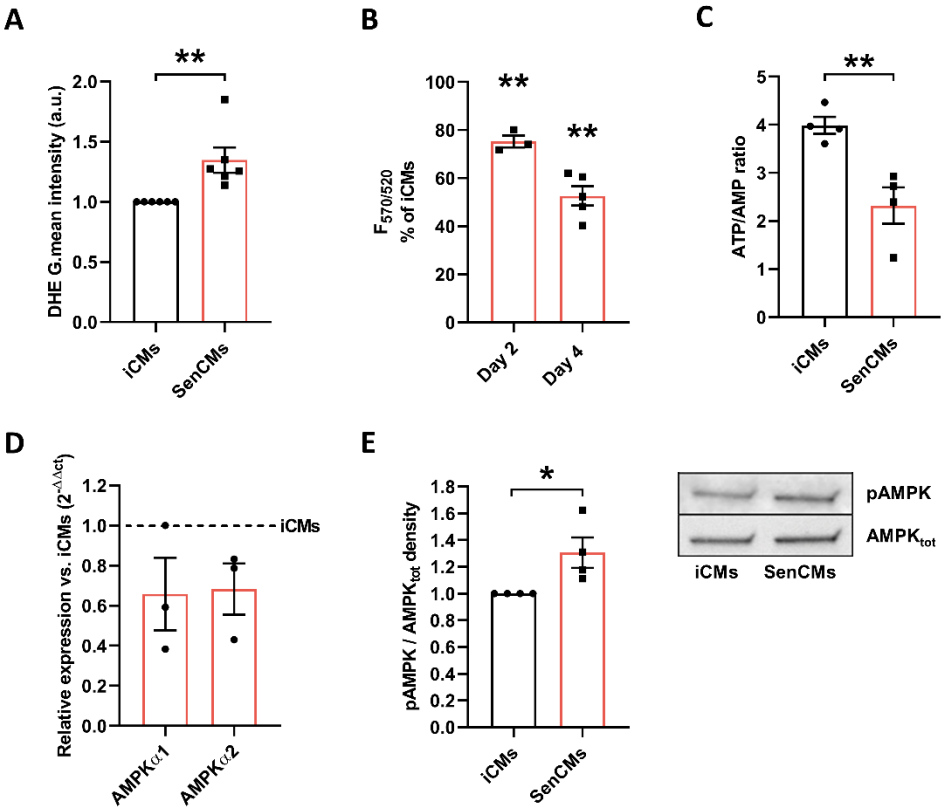
A
DHE G.mean intensity (a.u.)
2.0
1.5
1.0
0.5
0.0
**
iCMs
SenCMs
B
F570/520
% of iCMs
100
80
60
40
20
0
**
**
Day 2
Day 4
C
ATP/AMP ratio
5
4
3
2
1
0
**
iCMs
SenCMs
D
Relative expression vs. iCMs (2-ΔΔct)
1.2
1.0
0.8
0.6
0.4
0.2
0.0
iCMs
AMPKα1
AMPKα2
E
pAMPK / AMPKtot density
1.8
1.6
1.4
1.2
1.0
0.8
0.6
0.4
0.2
0.0
*
iCMs
SenCMs
pAMPK
AMPKtot
iCMs
SenCMs

Figure 3

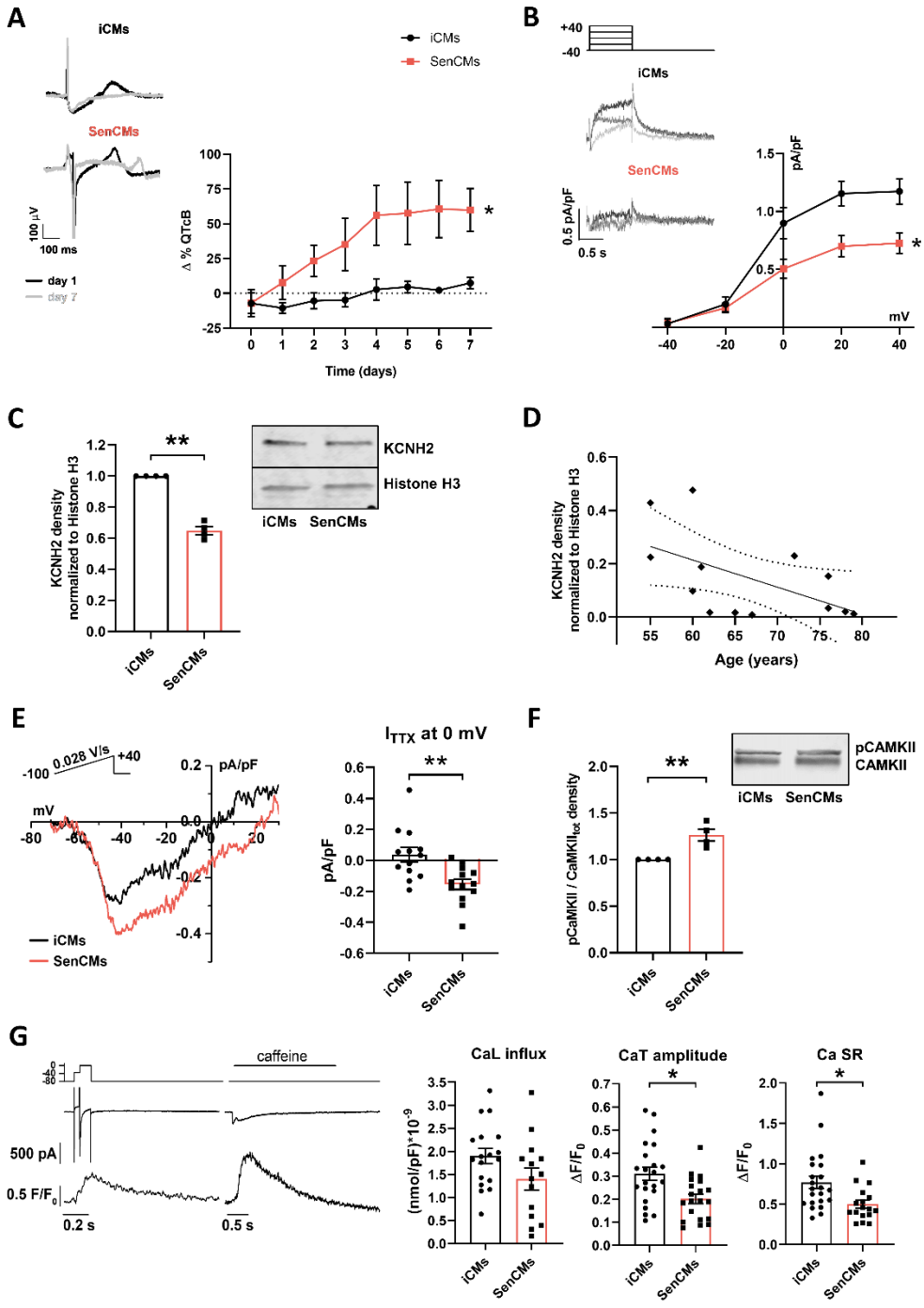
A
iCMs
SenCMs
100 µV
100 ms
day 1
day 7
iCMs
SenCMs
Δ % QTcB
Time (days)
B
+40
-40
iCMs
SenCMs
0.5 pA/pF
0.5 s
pA/pF
mV
C
KCNH2
Histone H3
iCMs SenCMs
KCNH2 density normalized to Histone H3
D
KCNH2 density normalized to Histone H3
Age (years)
E
0.028 V/s
-100
+40
mV
pA/pF
iCMs
SenCMs
I_TTX at 0 mV
pA/pF
F
pCAMKII
CAMKII
iCMs SenCMs
pCaMKII / CaMKII_tot density
G
caffeine
500 pA
0.5 F/F0
0.2 s
0.5 s
CaL influx
(nmol/pF)*10^-9
CaT amplitude
ΔF/F0
Ca SR
ΔF/F0
iCMs
SenCMs

Figure 4

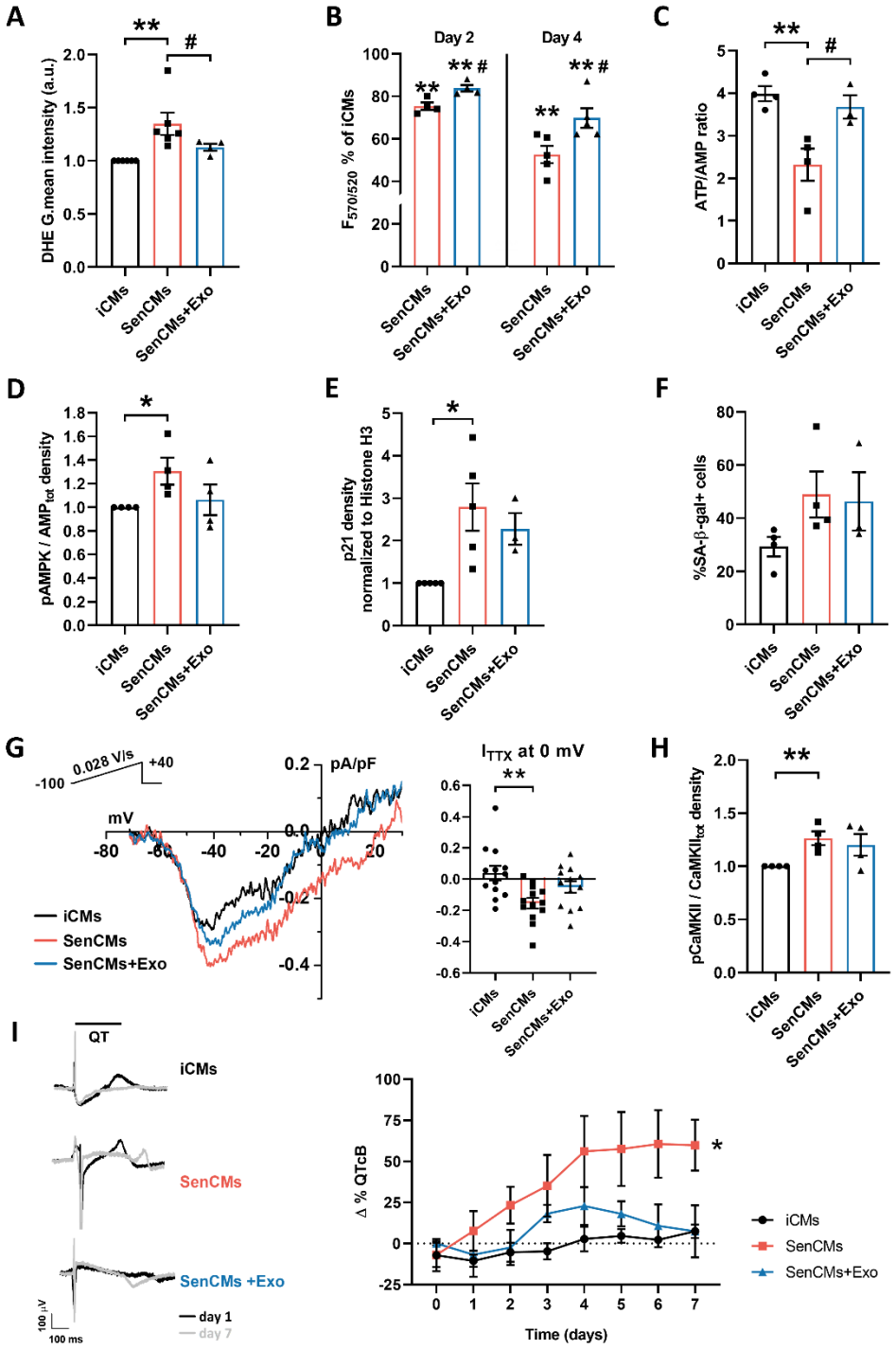
A
DHE G.mean intensity (a.u.)
iCMs
SenCMs
SenCMs+Exo
B
Day 2
Day 4
F570/520 % of iCMs
C
ATP/AMP ratio
D
pAMPK / AMPtot density
E
p21 density normalized to Histone H3
F
%SA-β-gal+ cells
G
0.028 V/s
-100
+40
mV
pA/pF
iCMs
SenCMs
SenCMs+Exo
ITTX at 0 mV
H
pCaMKII / CaMKIItot density
I
QT
iCMs
SenCMs
SenCMs +Exo
day 1
day 7
100 μV
100 ms
Δ % QTcB
Time (days)

Figure 5

## 6.8 Supplementary Figures and Tables legends

**Supplementary Figure 1:** (A) To obtain SenCMs, iCMs were incubated with 0.2 μM Dox for 3 hours, then washed and placed back in fresh maintenance medium. After 24 hours, part of the SenCMs were exposed to CPC-derived Exo ($2\times10^3$ Exo/cell). Cells were characterized in the week following treatments. (B) Immunostaining of iCMs derived from CPCs for α-S-Actin (red) and cTnT (green) followed by nuclear staining with DAPI (blue). Myofibrillar striations are visible. (C) Characterization of extracellular vescicels (EVs) derived from conditioned media of CPCs using Nanoparticle tracking analysis. Mean size of EVs is 160 ± 2.0 nm, corresponding to Exo. (D) EdU incorporation following Dox and Dox+Exo treatments. Quantitative analysis of double positive cells for EdU and cTnT are shown in the bar graph representing means of four independent experiments ± SEM. (E) 4 days after treatment, viable cells were labeled with Calcein AM as described in the Methods and Materials section. The total numbers of Calcein-positive cells as a percentage of control are shown in the bar graphs. Data are >3 independent experiments ± SEM. (F) Number of γ-H2AX-positive foci per cell. Data are means of four independent experiments ± SEM. (G) $I_{Kr}$ I/V relationships of iCMs (N = 21), SenCMs (N = 26), and SenCMs+Exo (N = 28) 5-7 days after treatment. (H) HERG (KCNH2) protein expression levels. Quantitative data of four independent experiments ± SEM (densitometric values for the proteins of interest normalized for GAPDH). (I) The electrical activity of spontaneously beating clusters of CMs was recorded using MEA for 7 consecutive days after Dox treatment, and the RR interval was measured. Data are means of five independent experiments ± SEM. * $P < 0.05$, ** $P < 0.01$ vs. iCMs.

**Supplementary Table 1:** Real Time PCR primer sequences.

## 6.9 Supplementary Figures and Tables

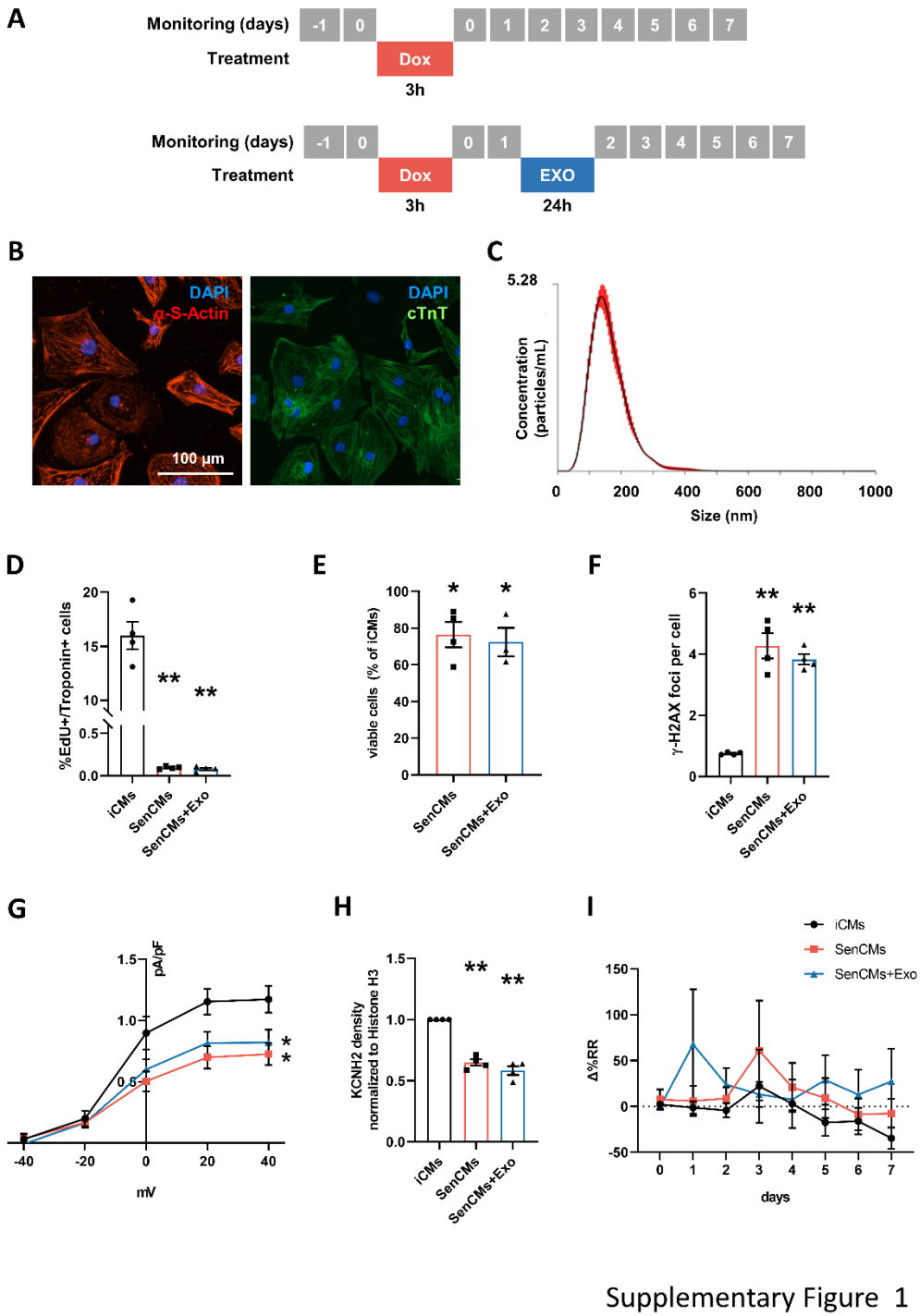


Supplementary Figure 1

| Gene | Forward (5'-3') | Reverse (5'-3') |
|---|---|---|
| AMPKα1 | ACAGCCGAGAAGCAGAAACA | TTGCCAACCTTCACTTTGCC |
| AMPKα2 | TTGACAGGCCATAAAGTGGCA | TCGAACAATTCACCTCCAGACA |
| ANP | CCATATTGGAGCAAATCCCGT | TGGTCTAGCAGGTTCTTGAAAT |
| BNP | GATGGCACATAGTTCAAGCTG | TAAAACAACCTCAGCCCGTCA |
| GDF15 | AGGTGAGAACCTTCTGGGGTT | CCTGGGAGTCTGTGCTTTTGG |
| IL-1α | CTTCTGGGAAACTCACGGCA | AGCACACCCAGTAGTCTTGC |
| IL-8 | TCTGGACCCCAAGGAAAACTG | TCACTGGCATCTTCACTGATTCTT |
| MCP1 | CCTTCATTCCCCAAGGGCTC | CTTCTTTGGGACACTTGCTGC |
| MMP3 | TGAAATTGGCCACTCCCTGG | GGAACCGAGTCAGGTCTGTG |
| P16 | CTTCGGCTGACTGGCTGG | TCATCATGACCTGGATCGGC |
| P21 | CACTTCCTCTGCTCTGCTGC | GCTGGTCTGCCTCCGTTTT |
| Serpin1 | TTGCAGGATGGAACTACGGG | GTGGCAGGCAGTACAAGAGT |
| Sirt1 | TGACCTCCTCATTGTTATTGGG | TTCATGGGGTATGGAACTTGG |
| TGFβ2 | CATCTACAACAGCACCAGGGA | CAACTGGGCAGACAGTTTCGG |

Supplementary Table 1

## 6.10 Funding

This work was supported by grants Velux Stiftung of the CardioCentro Ticino Foundation (Lugano, Switzerland), as well as Fondo Ricerca di Ateneo of University of Milano-Bicocca (Milano, Italy).

## 6.11 References


Altieri, P., Barisione, C., Lazzarini, E., Garuti, A., Bezante, G. P., Canepa, M., . . . Ameri, P. (2016). Testosterone Antagonizes Doxorubicin-Induced Senescence of Cardiomyocytes. *J Am Heart Assoc, 5*(1). doi:10.1161/JAHA.115.002383

Altomare, C., Pianezzi, E., Cervio, E., Bolis, S., Biemmi, V., Benzoni, P., . . . Vassalli, G. (2016). Human-induced pluripotent stem cell-derived cardiomyocytes from cardiac progenitor cells: effects of selective ion channel blockade. *Europace, 18*(suppl 4), iv67-iv76. doi:10.1093/europace/euw352

Barile, L., Cervio, E., Lionetti, V., Milano, G., Ciullo, A., Biemmi, V., . . . Vassalli, G. (2018). Cardioprotection by cardiac progenitor cell-secreted exosomes: role of pregnancy-associated plasma protein-A. *Cardiovasc Res, 114*(7), 992-1005. doi:10.1093/cvr/cvy055

Barile, L., Gherghiceanu, M., Popescu, L. M., Moccetti, T., & Vassalli, G. Human cardiospheres as a source of multipotent stem and progenitor cells. *Stem Cells Int, 2013*, 916837. doi:10.1155/2013/916837

Barile, L., Lionetti, V., Cervio, E., Matteucci, M., Gherghiceanu, M., Popescu, L. M., . . . Vassalli, G. (2014). Extracellular vesicles from human cardiac progenitor cells inhibit cardiomyocyte apoptosis and improve cardiac function after myocardial infarction. *Cardiovasc Res, 103*(4), 530-541. doi:10.1093/cvr/cvu167

Bergmann, O., Bhardwaj, R. D., Bernard, S., Zdunek, S., Barnabe-Heider, F., Walsh, S., . . . Frisen, J. (2009). Evidence for cardiomyocyte renewal in humans. *Science, 324*(5923), 98-102. doi:10.1126/science.1164680

Bielak-Zmijewska, A., Wnuk, M., Przybylska, D., Grabowska, W., Lewinska, A., Alster, O., . . . Sikora, E. (2014). A comparison of replicative senescence and doxorubicin-induced premature senescence of vascular smooth muscle cells isolated from human aorta. *Biogerontology, 15*(1), 47-64. doi:10.1007/s10522-013-9477-9

Chandrasekaran, A., Idelchik, M., & Melendez, J. A. (2017). Redox control of senescence and age-related disease. *Redox Biol, 11*, 91-102. doi:10.1016/j.redox.2016.11.005

Chen, Q. M., Tu, V. C., & Liu, J. (2000). Measurements of hydrogen peroxide induced premature senescence: senescence-associated beta-galactosidase and DNA synthesis index in human diploid fibroblasts with down-regulated p53 or Rb. *Biogerontology, 1*(4), 335-339. doi:10.1023/a:1026590501344

Childs, B. G., Durik, M., Baker, D. J., & van Deursen, J. M. (2015). Cellular senescence in aging and age-related disease: from mechanisms to therapy. *Nat Med, 21*(12), 1424-1435. doi:10.1038/nm.4000

Ciullo, A., Biemmi, V., Milano, G., Bolis, S., Cervio, E., Fertig, E. T., . . . Barile, L. (2019). Exosomal Expression of CXCR4 Targets Cardioprotective Vesicles to Myocardial Infarction and Improves Outcome after Systemic Administration. *Int J Mol Sci, 20*(3). doi:10.3390/ijms20030468

Cui, S., Xue, L., Yang, F., Dai, S., Han, Z., Liu, K., . . . Chen, Y. (2018). Postinfarction Hearts Are Protected by Premature Senescent Cardiomyocytes Via GATA 4-Dependent CCN 1 Secretion. *J Am Heart Assoc, 7*(18), e009111. doi:10.1161/JAHA.118.009111

Dhingra, R., & Vasan, R. S. (2012). Age as a risk factor. *Med Clin North Am, 96*(1), 87-91. doi:10.1016/j.mcna.2011.11.003

Dimri, G. P., Lee, X., Basile, G., Acosta, M., Scott, G., Roskelley, C., . . . et al. (1995). A biomarker that identifies senescent human cells in culture and in aging skin in vivo. *Proc Natl Acad Sci U S A, 92*(20), 9363-9367.

Doenst, T., Nguyen, T. D., & Abel, E. D. (2013). Cardiac metabolism in heart failure: implications beyond ATP production. *Circ Res, 113*(6), 709-724. doi:10.1161/CIRCRESAHA.113.300376

Doherty, K. R., Talbert, D. R., Trusk, P. B., Moran, D. M., Shell, S. A., & Bacus, S. (2015). Structural and functional screening in human induced-pluripotent stem cell-derived cardiomyocytes accurately identifies cardiotoxicity of multiple drug types. *Toxicol Appl Pharmacol, 285*(1), 51-60. doi:10.1016/j.taap.2015.03.008

Eschenhagen, T., Bolli, R., Braun, T., Field, L. J., Fleischmann, B. K., Frisen, J., . . . Hill, J. A. (2017). Cardiomyocyte Regeneration: A Consensus Statement. *Circulation, 136*(7), 680-686. doi:10.1161/CIRCULATIONAHA.117.029343

Gallet, R., Dawkins, J., Valle, J., Simsolo, E., de Couto, G., Middleton, R., . . . Marban, E. (2017). Exosomes secreted by cardiosphere-derived cells reduce scarring, attenuate adverse remodelling, and improve function in acute and chronic porcine myocardial infarction. *Eur Heart J, 38*(3), 201-211. doi:10.1093/eurheartj/ehw240

Gao, L., Wang, L., Wei, Y., Krishnamurthy, P., Walcott, G. P., Menasche, P., & Zhang, J. (2020). Exosomes secreted by hiPSC-derived cardiac cells improve recovery from myocardial infarction in swine. *Sci Transl Med, 12*(561). doi:10.1126/scitranslmed.aay1318

Hamilton, S., & Terentyev, D. (2019). Altered Intracellular Calcium Homeostasis and Arrhythmogenesis in the Aged Heart. *Int J Mol Sci, 20*(10). doi:10.3390/ijms20102386

Hegyi, B., Banyasz, T., Izu, L. T., Belardinelli, L., Bers, D. M., & Chen-Izu, Y. (2018). beta-adrenergic regulation of late Na(+) current during cardiac action potential is mediated by both PKA and CaMKII. *J Mol Cell Cardiol, 123*, 168-179. doi:10.1016/j.yjmcc.2018.09.006

Huang, J. H., Lin, Y. Q., Pan, N. H., & Chen, Y. J. (2010). Aging modulates dispersion of ventricular repolarization in the very old of the geriatric population. *Heart Vessels, 25*(6), 500-508. doi:10.1007/s00380-010-0026-z

Jahangir, A., Sagar, S., & Terzic, A. (2007). Aging and cardioprotection. *J Appl Physiol (1985), 103*(6), 2120-2128. doi:10.1152/japplphysiol.00647.2007

Kim, J., Yang, G., Kim, Y., Kim, J., & Ha, J. (2016). AMPK activators: mechanisms of action and physiological activities. *Exp Mol Med, 48*, e224. doi:10.1038/emm.2016.16

Kitzman, D. W. (2000). Diastolic dysfunction in the elderly. Genesis and diagnostic and therapeutic implications. *Cardiol Clin, 18*(3), 597-617, x. doi:10.1016/s0733-8651(05)70164-8

Kuilman, T., Michaloglou, C., Mooi, W. J., & Peeper, D. S. (2010). The essence of senescence. *Genes Dev, 24*(22), 2463-2479. doi:10.1101/gad.1971610

Li, X., Lan, Y., Wang, Y., Nie, M., Lu, Y., & Zhao, E. (2017). Telmisartan suppresses cardiac hypertrophy by inhibiting cardiomyocyte apoptosis via the NFAT/ANP/BNP signaling pathway. *Mol Med Rep, 15*(5), 2574-2582. doi:10.3892/mmr.2017.6318

Lian, X., Zhang, J., Azarin, S. M., Zhu, K., Hazeltine, L. B., Bao, X., . . . Palecek, S. P. (2013). Directed cardiomyocyte differentiation from human pluripotent stem cells by modulating Wnt/beta-catenin signaling under fully defined conditions. *Nat Protoc, 8*(1), 162-175. doi:10.1038/nprot.2012.150

Maejima, Y., Adachi, S., Ito, H., Hirao, K., & Isobe, M. (2008). Induction of premature senescence in cardiomyocytes by doxorubicin as a novel mechanism of myocardial damage. *Aging Cell, 7*(2), 125-136. doi:10.1111/j.1474-9726.2007.00358.x

McHugh, D., & Gil, J. (2018). Senescence and aging: Causes, consequences, and therapeutic avenues. *J Cell Biol, 217*(1), 65-77. doi:10.1083/jcb.201708092

Milano, G., Biemmi, V., Lazzarini, E., Balbi, C., Ciullo, A., Bolis, S., . . . Vassalli, G. (2020). Intravenous administration of cardiac progenitor cell-derived exosomes protects against doxorubicin/trastuzumab-induced cardiac toxicity. *Cardiovasc Res, 116*(2), 383-392. doi:10.1093/cvr/cvz108

Mirza, M., Strunets, A., Shen, W. K., & Jahangir, A. (2012). Mechanisms of arrhythmias and conduction disorders in older adults. *Clin Geriatr Med, 28*(4), 555-573. doi:10.1016/j.cger.2012.08.005

Mitry, M. A., Laurent, D., Keith, B. L., Sira, E., Eisenberg, C. A., Eisenberg, L. M., . . . Edwards, J. G. (2020). Accelerated cardiomyocyte senescence contributes to late-onset doxorubicin-induced cardiotoxicity. *Am J Physiol Cell Physiol, 318*(2), C380-C391. doi:10.1152/ajpcell.00073.2019

Pianezzi, E., Altomare, C., Bolis, S., Balbi, C., Torre, T., Rinaldi, A., . . . Vassalli, G. (2020). Role of somatic cell sources in the maturation degree of human induced pluripotent stem cell-derived cardiomyocytes. *Biochim Biophys Acta Mol Cell Res, 1867*(3), 118538. doi:10.1016/j.bbamcr.2019.118538

Piegari, E., De Angelis, A., Cappetta, D., Russo, R., Esposito, G., Costantino, S., . . . Rossi, F. (2013). Doxorubicin induces senescence and impairs function of human cardiac progenitor cells. *Basic Res Cardiol, 108*(2), 334. doi:10.1007/s00395-013-0334-4

Rabkin, S. W., Cheng, X. J., & Thompson, D. J. (2016). Detailed analysis of the impact of age on the QT interval. *J Geriatr Cardiol, 13*(9), 740-748. doi:10.11909/j.issn.1671-5411.2016.09.013

Reed, A. L., Tanaka, A., Sorescu, D., Liu, H., Jeong, E. M., Sturdy, M., . . . Sutliff, R. L. (2011). Diastolic dysfunction is associated with cardiac fibrosis in the senescence-accelerated mouse. *Am J Physiol Heart Circ Physiol, 301*(3), H824-831. doi:10.1152/ajpheart.00407.2010

Rocchetti, M., Sala, L., Rizzetto, R., Staszewsky, L. I., Alemanni, M., Zambelli, V., . . . Zaza, A. (2014). Ranolazine prevents INaL enhancement and blunts myocardial remodelling in a model of pulmonary hypertension. *Cardiovasc Res, 104*(1), 37-48. doi:10.1093/cvr/cvu188

Roth, G. A., Johnson, C., Abajobir, A., Abd-Allah, F., Abera, S. F., Abyu, G., . . . Murray, C. (2017). Global, Regional, and National Burden of Cardiovascular Diseases for 10 Causes, 1990 to 2015. *J Am Coll Cardiol, 70*(1), 1-25. doi:10.1016/j.jacc.2017.04.052

Ruiz-Meana, M., Minguet, M., Bou-Teen, D., Miro-Casas, E., Castans, C., Castellano, J., . . . Garcia-Dorado, D. (2019). Ryanodine Receptor Glycation Favors Mitochondrial Damage in the Senescent Heart. *Circulation, 139*(7), 949-964. doi:10.1161/CIRCULATIONAHA.118.035869

Spyridopoulos, I., Isner, J. M., & Losordo, D. W. (2002). Oncogenic ras induces premature senescence in endothelial cells: role of p21(Cip1/Waf1). *Basic Res Cardiol, 97*(2), 117-124. doi:10.1007/s003950200001

Steenman, M., & Lande, G. (2017). Cardiac aging and heart disease in humans. *Biophys Rev, 9*(2), 131-137. doi:10.1007/s12551-017-0255-9

Tocchi, A., Quarles, E. K., Basisty, N., Gitari, L., & Rabinovitch, P. S. (2015). Mitochondrial dysfunction in cardiac aging. *Biochim Biophys Acta, 1847*(11), 1424-1433. doi:10.1016/j.bbabio.2015.07.009

Tran, H., White, C. M., Chow, M. S., & Kluger, J. (2001). An evaluation of the impact of gender and age on QT dispersion in healthy subjects. *Ann Noninvasive Electrocardiol, 6*(2), 129-133. doi:10.1111/j.1542-474x.2001.tb00097.x

Watanabe, S., Kawamoto, S., Ohtani, N., & Hara, E. (2017). Impact of senescence-associated secretory phenotype and its potential as a therapeutic target for senescence-associated diseases. *Cancer Sci, 108*(4), 563-569. doi:10.1111/cas.13184

Wlaschek, M., Hommel, C., Wenk, J., Brenneisen, P., Ma, W., Herrmann, G., & Scharffetter-Kochanek, K. (2000). Isolation and identification of psoralen plus ultraviolet A (PUVA)-induced genes in human dermal fibroblasts by polymerase chain reaction-based subtractive hybridization. *J Invest Dermatol, 115*(5), 909-913. doi:10.1046/j.1523-1747.2000.00120.x

Zhu, W., Shou, W., Payne, R. M., Caldwell, R., & Field, L. J. (2008). A mouse model for juvenile doxorubicin-induced cardiac dysfunction. *Pediatr Res, 64*(5), 488-494. doi:10.1203/PDR.0b013e318184d732

# Part 7

## Structural and electrophysiological changes in a model of cardiotoxicity induced by anthracycline combined with trastuzumab

Claudia Altomare[1], Alessandra Maria Lodrini[2,3], Giuseppina Milano[1,4], Vanessa Biemmi[3], Edoardo Lazzarini[3], Sara Bolis[1,3], Nicolò Pernigoni[1], Eleonora Torre[2], Martina Arici[2], Mara Ferrandi[5], Lucio Barile[3,6], Marcella Rocchetti[§2], Giuseppe Vassalli[§1,6,7]

[1]Laboratory of Cellular and Molecular Cardiology, Cardiocentro Ticino Foundation, Lugano, Switzerland; [2]Dept. of Biotechnology and Biosciences, Università degli Studi di Milano – Bicocca, Milano, Italy; [3]Laboratory of Cardiovascular Theranostics, Cardiocentro Ticino Foundation, Lugano, Switzerland; [4]Laboratory of Cardiovascular Research, Lausanne University Hospital, Lausanne, Switzerland; [5]Windtree Therapeutics Inc., Warrington, Pennsylvania, USA; [6]Faculty of Biomedicine, Università della Svizzera Italiana (USI), Lugano, Switzerland; [7]Center for Molecular Cardiology, University of Zurich, Zurich, Switzerland.

§ Corresponding authors.

Address for correspondence: Giuseppe Vassalli, Cardiocentro Ticino, via Tesserete 48, 6900 Lugano, Switzerland. giuseppe.vassalli@cardiocentro.org

Running title: Anthracyclines/trastuzumab cardiotoxicity

Keywords: Doxorubicin; trastuzumab; cardiotoxicity; T-tubules; electrophysiology; calcium handling

Conflicts of interest: Nothing to declare

Paper submitted to *Basic Research in Cardiology* (BRIC-D-20-00593).

## 7.1 Abstract

Combined treatment with anthracyclines (e.g., doxorubicin; Dox) and trastuzumab (Trz), a humanized anti-human epidermal growth factor receptor 2 (HER2; ErbB2) antibody, in patients with HER2-positive cancer is limited by cardiotoxicity, as manifested by contractile dysfunction and arrhythmia. The respective roles of the two agents in the cardiotoxicity of the combined therapy are incompletely understood.

To assess cardiac performance, T-tubule organization, electrophysiological changes and intracellular $Ca^{2+}$ handling in cardiac myocytes using an *in vivo* rat model of Dox/Trz-related cardiotoxicity. Adult rats received 6 doses of either Dox or Trz, or the two agents sequentially. Dox-mediated left ventricular (LV) dysfunction was aggravated by Trz administration. Dox treatment, but not Trz, induced T-tubule disarray. Moreover, Dox, but not Trz monotherapy, induced prolonged action potential duration (APD), increased incidence of delayed afterdepolarizations (DADs) and beat-to-beat variability of repolarization (BVR), and slower $Ca^{2+}$ transient decay. Although APD, DADs, BVR and $Ca^{2+}$ transient decay recovered over time after the cessation of Dox treatment, subsequent Trz administration exacerbated these abnormalities. Trz, but not Dox, reduced $Ca^{2+}$ transient amplitude and SR $Ca^{2+}$ content. Both agents increased $Ca^{2+}$ waves and downregulated SERCA. Finally, Dox increased resting $Ca^{2+}$ waves, $Ca^{2+}$ spark frequency, spark-mediated sarcoplasmic reticulum (SR) leak, and long-lasting $Ca^{2+}$ release events (so-called $Ca^{2+}$ 'embers').

These results suggest that Dox, but not Trz, may cause T-tubule disarray in cardiac myocytes *in vivo* while also inducing overall larger changes in electrical parameters and intracellular $Ca^{2+}$ handling. While Dox-induced changes in electrical parameters are reversible, subsequent Trz administration prevents their recovery. These findings illustrate the specific roles of Dox and Trz, and their interactions in cardiotoxicity and arrhythmogenicity.

## 7.2 Introduction

Anthracyclines (e.g., doxorubicin; Dox) are among the most efficient and frequently used chemotherapeutic agents, being prescribed to more than 40% of women with breast cancer [Giordano, Lin, Kuo, Hortobagyi, & Goodwin, 2012]. Following anthracyclines and cyclophosphamide treatment, the human epidermal growth factor receptor 2 (HER2; ErbB2)/neu inhibitor trastuzumab (Trz), in combination with paclitaxel, improves outcomes in women with surgically removed HER2-positive breast cancer [Romond et al., 2005]. However, both anthracyclines-related cardiotoxicity, including chronic congestive heart failure and Trz-related cardiotoxicity [Mor-Avi et al., 2011; Sawaya et al., 2012; Thavendiranathan et al., 2013], limit the clinical use of these agents. Because the simultaneous delivery of the two drugs results in enhanced cardiotoxicity, currently used clinical protocols involve their sequential administration. However, Dox/Trz combined therapy is still associated with a risk of LV dysfunction in up to one-quarter of breast cancer patients [Advani, Ballman, Dockter, Colon-Otero, & Perez, 2016; Ewer & Ewer, 2015; Ghigo, Li, & Hirsch, 2016; Rayson et al., 2008; Saeed, Premecz, Goyal, Singal, & Jassal, 2014], along with an increased risk of arrhythmia [Muraru et al., 2014; Santoro et al., 2017]. In this regard, acute arrhythmogenicity of Dox administration has been reported [Steinberg, Cohen, Wasserman, Cohen, & Ross, 1987]. In a recent study from the Mayo Clinic, episodes of nonsustained VT (Ventricular Tachicardia), AF (Atrial Fibrillation), and sustained VT or ventricular fibrillation were seen in 73.9%, 56.6%, and 30.4% of patients with anthracycline-related cardiomyopathy who had implantable cardioverter defibrillators [Mazur et al., 2017]. Rare cases of malignant ventricular arrhythmias associated with Trz treatment have also been reported [Piotrowski et al., 2012]. However, electrophysiological changes induced by Dox/Trz combined therapy are poorly characterized.

The underlying mechanisms of anthracyclines-induced cardiotoxicity are incompletely understood but increased oxidative stress, abnormal intracellular $Ca^{2+}$ homeostasis and mitochondrial energetics, degradation of ultrastructural

proteins, direct DNA damage via inhibition of topoisomerase 2β, and inhibition of pro-survival pathways such as neuregulin 1 (NRG) and ErbB [Cappetta, De Angelis, et al., 2017; Cardinale et al., 2010; Dubey et al., 2016] may be involved. In this regard, ErbB2 overexpression protected against Dox-related cardiotoxicity [Belmonte et al., 2015], whereas Trz-mediated inhibition of ErbB2 signaling interfered with the protective effects of ErbB2 and NRG, potentiating Dox-related toxicity in rat ventricular cardiac myocytes (CMs) [Rochette et al., 2015; Sawyer, Zuppinger, Miller, Eppenberger, & Suter, 2002].

The respective roles of Dox and Trz in cardiotoxicity induced by their combined administration remain to be fully elucidated. Here, we investigated these roles in T-tubule disarray, electrophysiological alterations and changes in intracellular $Ca^{2+}$ handling using an *in vivo* rat model that mimics currently applied clinical regimens, specifically with respect to the sequential delivery of the two agents. Electrical measurements were performed at a single cell level. Dox treatment induced severe T-tubule disarray, significant electrical abnormalities, and limited changes in $Ca^{2+}$ handling. Although Trz monotherapy induced comparatively modest changes, administration of this agent following Dox pre-treatment exacerbated the abnormalities observed after the initial Dox treatment. These results suggest that CMs pre-stressed by Dox may become susceptible to Trz-mediated toxicity, including electrical instability.

## 7.3 Results

### 7.3.1 Trz treatment aggravates Dox-induced LV dysfunction

Echocardiographic results are shown in **Fig 1b**. Compared to Ctrl, Dox-treated animals showed increases in LVESV from d 19 to d 37, and in LVEDV at d 19, d 30 and d 37, along with decreases in LVEF and LVFS at all time points. In the absence of Dox pre-treatment, Trz-treated animals showed an increase in LVESV at d30 (i.e., one day after administration of the last Trz dose), and non-significant trends toward decreases in LVEF and LVFS using one-way ANOVA for multiple groups (however, such trends resulted statistically significant vs. Ctrl using a two-group analysis; **Suppl Fig S1**). These changes were reversible over time. Animals receiving Dox/Trz combined therapy showed increases in LVESV and LVEDV, along with decreases in LVEF and LVFS which were significantly greater than those induced by Dox monotherapy, indicating additive effects by the two agents. Heart rate, body weight, tibia length, and heart weight did not significantly differ among groups (**Suppl Table S1**).

### 7.3.2 Trz treatment enhances Dox-induced ROS generation by CMs

ROS levels in LV CMs increased with a clear trend in the Dox/Trz group, and to a lesser extent in the Dox group at d19 (the time point of the first Trz administration in the Dox/Trz group), but not at d37 (**Suppl Fig S2**), demonstrating a decrease in ROS levels over time. In the absence of Dox pre-treatment, however, ROS levels were only marginally affected by Trz.

### 7.3.3 Dox treatment, but not Trz, induces TT disarray

Representative confocal region of interest (ROI) of 3-di-ANEPPDHQ–treated CMs in the different groups are shown in **Fig 2a**. Disruption of TT architecture in the Dox and Dox/Trz groups, but not in the Trz group, can be appreciated visually. Representative spatial Fast Fourier Transform analyses of TT-power in LV and RV

CMs are shown in **Fig 2b**. Quantitative analysis confirmed that Dox, but not Trz, treatment induces TT disarray (**Fig 2c**).

### 7.3.4 Trz treatment enhances Dox-induced APD prolongation and DADs

AP recordings in isolated CMs from either ventricle showed increases in both $APD_{50}$ and $APD_{90}$ in the Dox group at d19, but not at d37 (**Fig 3a,b**), indicating reversible effects. LV CMs and RV CMs were analyzed separately because electrical measurements are influenced by ventricular loading conditions. In the absence of Dox pre-treatment, Trz did not affect APD, whereas it significantly prolonged it while also decreasing AP amplitude and $dV/dt_{max}$ in RV CMs in Dox pre-treated rats (**Suppl Table S2**). Depolarizing events during diastole and systole were recorded as DADs and early afterdepolarizations (EADs), respectively. The percentage of cells exhibiting DADs at 1Hz-stimulation was increased in Dox-treated animals at d19, but not at d37. In analogy to its effect on APD, Trz increased the frequency of DADs selectively in rats pre-treated with Dox (**Fig 3c,d**). Similar changes were found for beat-to-beat variability of repolarization (BVR), which reflects $APD_{90}$ time-variability (i.e., electrical instability) and represents a pro-arrhythmic parameter (Johnson et al., 2010). The dispersion of $APD_{90}$ values around the identity line in Poincaré plots was increased in the Dox group at d19 and in the Dox/Trz group, but not in the Dox group at d37 neither in Trz monotherapy (**Fig 4a**). Quantitative STV data are shown in **Fig 4b**. The slope of the linear correlation between BVR and $APD_{90}$ was comparable in all groups (**Suppl Fig S3**), indicating that increases in BVR were strictly dependent on APD prolongation. These results indicate pro-arrhythmic conditions in both the Dox and Dox/Trz groups.

### 7.3.5 Effects of Dox and Trz on intracellular $Ca^{2+}$ handling

In principle, TT disarray and changes in APD, DADs, and BVR can impact intracellular $Ca^{2+}$ handling. We analyzed evocated $Ca^{2+}$ transients (CaT) at 1, 2 and 4 Hz in field-stimulation, as well as caffeine-induced CaT which reflect SR

$Ca^{2+}$ content (CaSR; **Suppl Fig S4**). Trz treatment resulted in significant decreases in CaT amplitude and CaSR in LV CMs, and to a slightly lesser extent in RV CMs, with only marginal changes observed in the Dox and Dox/Trz groups (**Fig 5a**). These results suggest that Trz may limit $Ca^{2+}$ influx (Kitani et al., 2019). Studies of the CaT decay kinetics showed a lower decay half-time ($T_{0.5}$) in Ctrl LV CMs compared to Ctrl RV CMs, in line with previous data showing a faster SR $Ca^{2+}$ sequestration in LV CMs compared to RV CMs (Sathish, Xu, Karmazyn, Sims, & Narayanan, 2006). CaT decay in both Dox and Dox/Trz groups of LV CMS, but not in the Trz group, was slower than in Ctrl (**Fig 5b**), suggesting Dox-induced changes in $Ca^{2+}$ removal. SERCA protein levels were significantly decreased in LV CMs in both Dox and Dox/Trz groups, with clear trends toward SERCA downregulation also observed in both LV and RV Trz CMs (**Fig 5c**). The percentage of LV CMs exhibiting $Ca^{2+}$ waves was increased in all treated groups, with a similar increase in RV CMs from Dox d37 rats. The frequency of resting CaT in LV CMs was increased in both Dox and Dox/Trz groups (**Fig 5d**). These findings are in good agreement with our results on DAD frequency (**Fig 3c,d**). They indicate limited effects of Dox and Trz on $Ca^{2+}$ handling, as evidenced by steady-state CaT amplitude and SR $Ca^{2+}$ content measurements.

### 7.3.6 Dox, but not Trz, induces $Ca^{2+}$ sparks

The effects of Dox on $Ca^{2+}$ waves and resting CaT led us to investigate SR stability by quantifying spontaneous SR $Ca^{2+}$ release events visualized as $Ca^{2+}$ sparks. Representative images of $Ca^{2+}$ sparks in the different groups are shown in **Fig 6a**. Increased frequencies of $Ca^{2+}$ sparks were readily apparent in the Dox and Dox/Trz group, whereas Trz alone did not significantly impact this parameter. Spark mass was increased in LV CMs from Trz-treated animals, with similar trends in Dox-treated ones (Llach et al., 2019), but not in the Dox/Trz group. Dox, and to a lesser extent Trz, induced an increased spark-mediated SR $Ca^{2+}$ leak quantified by the spark mass*spark frequency index (**Fig 6b**). Dox, but not Trz, increased the number of so-called $Ca^{2+}$ 'embers', defined as $Ca^{2+}$ sparks with

FDHM>20 ms (the peak value of FDHM distribution [Louch et al., 2013]; **Fig 6c and S5**). The full duration at half maximum (FDHM) and the decay time constant ($tau_{decay}$), two markers of altered RyR openings, were increased in Dox-treated animals (**Suppl Table S3**). These results suggest that Dox, but not Trz, may affect spontaneous $Ca^{2+}$ release events favoring SR $Ca^{2+}$ leak.

## 7.4 Discussion

Cardiotoxicity limits the application of anthracycline-based chemotherapy and anti-HER2 therapy combined regimens. Here, we investigated selected aspects of this condition including TT organization, electrophysiological changes, and intracellular $Ca^{2+}$ handling using an *in vivo* rat model that mimics clinically used combined regimens. Dox treatment induced LV dysfunction lasting for more than 37 days. Trz monotherapy likewise impaired contractile function, albeit less severely than Dox, and for a shorter period of time. The sequential administration of the two agents impaired LV function to a greater extent than did either agent alone, demonstrating additive effects. These changes were paralleled by changes in ROS levels in CMs. These results are in line with previous data in *Erb2*-mutated mice [Ozcelik et al., 2002] and in human induced pluripotent stem cell (hiPSC)-derived CMs suggesting that pre-existing cellular stress induced by Dox may exacerbate Trz-related cardiotoxicity by inhibiting protective pathways, e.g., Erb2/4 [Hsu, Huang, Yen, Cheng, & Hsieh, 2018; Kurokawa, Shang, Yin, & George, 2018; Tocchetti et al., 2012]. Moreover, lapatinib, another HER2 inhibitor, potentiated Dox-related cardiotoxicity via iNOS signaling [Hsu et al., 2018].

Dox treatment, but not Trz, induced sustained TT disarray that accounted for, at least in part, LV dysfunction in this group. An association between TT disarray and heart failure of various etiologies including dilated cardiomyopathy has been reported previously in both human patients and animal models [Bryant et al., 2014; Caldwell et al., 2014; Crocini et al., 2014; Crossman et al., 2015; He et al., 2001; Heinzel et al., 2008; Ibrahim et al., 2010; Louch et al., 2006; Sachse et al., 2012; Shah et al., 2014; Song et al., 2006; Wagner et al., 2012]. Time course studies revealed that TT disruption preceded the development of heart failure, suggesting a causative role for the former in disease progression [Shah et al., 2014; Wei et al., 2010]. In addition, altered TT structure has been shown to impair AP propagation [Crocini, Ferrantini, Coppini, & Sacconi, 2017; Ferrantini et al., 2013; Manfra, Frisk, & Louch, 2017]. In the present study, Dox treatment resulted in APD prolongation in CMs. These results are in line with previous data on Dox-

induced QT-interval prolongation in guinea pigs and reduced $I_{Ks}$ component in stably transfected HEK293 cells [Ducroq et al., 2010]. Another study reported increased $I_{NaL}$ leading to changes in $Ca^{2+}$ and $Na^{+}$ handling in a model of Dox-induced LV diastolic dysfunction [Cappetta, Esposito, et al., 2017]. In our model, Dox-mediated APD prolongation was associated with increases in the frequency of DADs as a reflection of spontaneously released $Ca^{2+}$ being extruded by sodium-calcium exchanger (NCX), as well as in BVR as an index of arrhythmogenicity. Trz treatment did not significantly impact APD, DADs, and BVR in the absence of Dox pre-treatment. In pre-treated rats, however, it induced changes in these parameters similar to those induced by Dox itself. Of note, these Trz-induced changes in pre-treated rats were observed after a full recovery in these electrical parameters following Dox treatment, suggesting that the latter exacerbated subsequent Trz toxicity. Clinical evidence of arrhythmia in Trz-treated patients has been reported [Piotrowski et al., 2012].

Our analysis of intracellular $Ca^{2+}$ handling revealed that Dox treatment increased both the amplitude of $Ca^{2+}$ transients and SR $Ca^{2+}$ content in RV CMs, but not in LV CMs. Chamber-specificity in $Ca^{2+}$ handling was also observed in controls CMs by analysis of CaT decay kinetics, in line with previous data on SR uptake function [Molina, Heijman, & Dobrev, 2016]. Unlike Dox, Trz treatment resulted in a decrease in both the amplitude of $Ca^{2+}$ transients and SR $Ca^{2+}$ content in LV CMs. These findings are in good agreement with previous data using sorafenib, a distinct tyrosine kinase inhibitor that reduced $Ca^{2+}$ transient amplitude and SR $Ca^{2+}$ content in human atrial CMs and in mouse ventricular CMs, inducing a reversible negative inotropic effect [Schneider et al., 2018]. Moreover, $Ca^{2+}$ transient decay was slower after Dox/Trz combined therapy, and to a lesser extent after Dox monotherapy but not after Trz monotherapy compared to controls. During cell relaxation, released $Ca^{2+}$ is recycled into the SR by the action of SERCA and extruded from the cell by NCX membrane protein. Both Dox alone and Dox/Trz combined therapy significantly reduced SERCA protein levels in LV CMs, with a non-significant trend in the same direction for Trz monotherapy. In our study, although SERCA protein level was downregulated in all LV groups,

$Ca^{2+}$ handling was preserved at all pacing rates in all groups except Trz, probably as a consequence of concurrent APD prolongation [Ronchi, Badone, Bernardi, & Zaza, 2018]. Therefore, Dox and further Dox/Trz depressed systolic function in terms of LVFS was not supported by relevant $Ca^{2+}$ handling derangement in isolated LV CMs, suggesting the contribution of other mechanisms to justify the in vivo cardiac disorder. Dox treatment also induced increases in spontaneous $Ca^{2+}$ waves and $Ca^{2+}$ sparks which reflect SR instability. Previous studies have shown that low density of poorly organized TT favors de-synchronized and protracted $Ca^{2+}$ release in failing CMs [Louch et al., 2004; Louch et al., 2006; Lyon et al., 2009; Song et al., 2006], which has been linked to the slowed and decreased amplitude of contraction typical of the failing heart [Bokenes et al., 2008; Mork, Sjaastad, Sejersted, & Louch, 2009]. $Ca^{2+}$ spark mass, which reflects the amount of $Ca^{2+}$ released within an individual spark, was increased by Trz in LV CMs, with a trend in the same direction for Dox. Previous data in isolated CMs suggest that ROS-dependent activation of CAMKII pathway may result in CaMKII-dependent SR $Ca^{2+}$ leak contributing to Dox-mediated impairment of $Ca^{2+}$ handling [Sag, Kohler, Anderson, Backs, & Maier, 2011]. Accordingly, in the present study, Dox induced an increase in prolonged spontaneous $Ca^{2+}$ events (so-called $Ca^{2+}$ 'embers') previously described in congestive heart failure [Louch et al., 2013], but not in chemotherapy-related cardiotoxicity. $Ca^{2+}$ 'embers' likely contributed to spontaneous SR $Ca^{2+}$ leak, which was increased in all treated groups.

In conclusion, our data using an *in vivo* rat model of chemotherapy-related cardiotoxicity show that Dox treatment induces oxidative stress, LV dysfunction, TT disarray, electrical changes, and modest changes in intracellular $Ca^{2+}$ handling. Trz treatment alone induces a lesser degree of LV dysfunction, no TT disarray, no significant electrical changes, while affected intracellular $Ca^{2+}$ handling. However, Dox pre-treatment exacerbates Trz-related cardiotoxicity. These results highlight different yet interrelated effects by the two agents in Dox/Trz-related cardiotoxicity, including arrhythmogenicity.

## 7.5 Methods

### 7.5.1 Animal experiments

The animal protocol was approved by the Committee on the Ethics of Animal Experiments of the Canton Ticino, Switzerland (TI32/18). The study was carried out in strict accordance with the recommendations in the Guide for the Care and Use of Laboratory Animals of the Directive 2010/63/EU. The study protocol is depicted schematically in **Fig 1a**. Sprague Dawley female rats (10-12 weeks old; from Charles River Laboratories) were subdivided into 4 groups. In the Dox group, rats were injected IP with 6 doses of Dox hydrochloride (Sigma-Aldrich), one dose each other day (from d1 to d11), for a cumulative dosage of 20 mg/kg, followed by 6 doses of phosphate-buffered saline (PBS; pH 7.4), one dose each other day (from d19 to d29), as described (Milano et al., 2020). In the Trz group, rats received 6 doses of PBS (from d1 to d11) followed by 6 doses of Trz (Roche), one dose each other day (from d19 to d29), for a cumulative dosage of 20 mg/kg. In the combined Dox/Trz group, rats received 6 doses of Dox hydrochloride (from d1 to d11) followed by 6 doses of Trz (from d19 to d29). Control rats received 12 doses of PBS at the time points corresponding to drug administration in treated groups (from d1 to d11, and from d19 to d19). Notably, Trz monotherapy was started at d19 of the study protocol to match the time point of Trz administration in the combined therapy group. However, Trz-mediated changes in LV function at later points were measured in a separate series of experiments.

### 7.5.2 Echocardiography

Heart function was monitored by echocardiography using a VEVO 2100 high-resolution imaging system (VisualSonics) at d0, d12, d19, d30, and d37, as described. Anesthesia was induced using 2% isoflurane mixed with 100% oxygen in an induction chamber. Rats were then placed on a heat pad in the supine position and kept at 37°C to minimize fluctuations of body temperature. Data acquisition was performed in rats lightly anesthetized with 0.5% to 1% isoflurane

in order to maintain HR ≥350 bpm. Two-dimensional short-axis M-mode echocardiography was performed and LV end-systolic (LVESV) and end-diastolic (LVEDV) volumes, ejection fraction (LVEF) and fractional shortening (LVFS) were determined, as previously described (Barile et al., 2018).

### 7.5.3 CM isolation

Isolated CMs from *in vivo* treated rats were analyzed at d19 (early Dox time point), and at d37 (late Dox time point, early Trz time point, combined Dox/Trz treatment). For CM isolation, rats were anesthetized using a cocktail of ketamine (100 mg/kg) and xylazine (75 mg/kg) and humanly euthanized by cervical dislocation. Hearts were harvested and perfused *ex vivo* in a Langendorff mode, as previously described (Rocchetti et al., 2014). CMs were isolated separately from LV and RV free walls. Rod-shaped, $Ca^{2+}$ tolerant CMs were used for patch-clamp measurements and confocal microscopy less than 12 hrs after tissue dissociation.

### 7.5.4 Reactive oxygen species (ROS)

To assess oxidative stress, CMs were stained with 2′-7′-Dichlorodihydrofluorescein diacetate (2 μM H2-DCF) in the following solution (in mM): 40 KCl, 3 $MgCl_2$, 70 KOH, 20 $KH_2PO_4$, 0.5 EGTA, 50 L-Glutamic acid, 20 Taurine, 10 HEPES, 10 D-glucose (pH 7.4) for 30 min. Dead CMs were detected after incubation with 7-Aminoactinomycin D (7-AAD) for 10 min. Fluorescence intensity was measured using Cytoflex flow cytometer (Beckman Coulter; λ excitation = 488nm / λ emission = 525 nm for DCF and λ excitation = 488nm / λ emission = 647nm for 7-AAD). Data were analyzed with Kaluza software (Beckman Coulter) and shown as the geometric mean of fluorescence intensity in the 7-AAD-negative subpopulation.

### 7.5.5 T-tubule analysis

To investigate the impact of each treatment on the organization of T-tubules (TT), sarcolemmal membranes were marked by incubating CMs with 20 μM 3-di-

ANEPPDHQ (Life Technologies, Carlsbad) and TT oriented transversely along z-lines were visualized (Rocchetti et al., 2014). 3-di-ANEPPDHQ was dissolved in the following solution (in mM): 40 KCl, 3 $MgCl_2$, 70 KOH, 20 $KH_2PO_4$, 0.5 EGTA, 50 L-Glutamic acid, 20 Taurine, 10 HEPES, 10 D-glucose (pH 7.4) for 10 min at RT (Sacconi et al., 2012). Cell contraction was prevented by adding blebbistatin (17 μM; Sigma). CMs were washed with the same solution before confocal microscopy analysis. Images of loaded CMs were acquired by laser-scanning microscopy (images: 1024 X 10124 pixels, 78μm x 78μm) using a confocal microscope (Nikon C2 plus) with a 40x oil-immersion objective. Eight-bit gray-scaled images were analyzed by spatial Fast Fourier Transform analysis to quantify periodic components of pixel variance. To compensate for staining differences among cells, a raw power spectrum was generated with ImageJ (v.1.4) and normalized to its central peak. TT density was quantified by normalizing the area under the harmonic relative to the spatial frequency of 0.5 $\mu m^{-1}$ (between 0.3 and 0.7 $\mu m^{-1}$) to the area of the entire spectrum (Rocchetti et al., 2014). TT power was calculated as the periodic transverse component of TT organization. T-index was calculated as TT power ratio between the area under the periodic (0.5 $\mu m^{-1}$) component and the area of the entire spectrum.

### 7.5.6 Electrical activity

Action potentials (AP) were recorded by pacing CMs at 1Hz in current-clamp conditions. AP duration measured at 90% and 50% of the repolarization phase ($APD_{90}$ and $APD_{50}$, respectively), diastolic potential ($E_{diast}$) and maximal AP phase 0 depolarization velocity ($dV/dt_{max}$) were determined. Single cells were superfused with standard Tyrode's solution containing (in mM): 154 NaCl, 4 KCl, 2 $CaCl_2$, 1 $MgCl_2$, 5.5 D-glucose, and 5 HEPES-NaOH (pH 7.35). Experiments were carried out in whole-cell configuration; the pipette solution contained (in mM): 23 KCl, 110 KAsp, 0.4 $CaCl_2$, 3 $MgCl_2$, 5 HEPES-KOH, 1 EGTA-KOH, 0.4 NaGTP, 5 $Na_2ATP$, 5 $Na_2PC$, 5.5 D-glucose (pH 7.3). Delayed afterdepolarizations (DADs) were defined as diastolic depolarizations with amplitude $\geq$1mV. The

percentage of cells exhibiting DADs was quantified. Beat-to-beat variability of repolarization (BVR) was expressed as the short-term variability (STV) of $APD_{90}$ (i.e., the mean orthogonal deviation from the identity line (Altomare et al., 2015; Heijman et al., 2013)), calculated as follows:

$$STV = \sum(|APD_{n+1} - APD_n|/\left[n_{beats}\, x\, \sqrt{2}\right]$$

for 30 consecutive APs ($n_{beats}$) at steady-state level. STV data are shown using $APD_n$ versus $APD_{n+1}$ (Poincaré) plots.

### 7.5.7 Intracellular $Ca^{2+}$ handling analyses

CMs were incubated in Tyrode solution for 45 min with the membrane-permeant form of the dye, Fluo4-AM (10 µmol/L), and then washed for 30 min to allow for the de-esterification process. Fluo4 emission was collected through a 535 nm band pass filter, converted to voltage, low-pass filtered (100 Hz) and digitized at 2 kHz after further low-pass digital filtering (FFT, 50 Hz). Intact CMs were field-stimulated at 1, 2 and 4 Hz at 37°C during superfusion with standard Tyrode's solution. $Ca^{2+}$ transient (CaT) amplitude at steady-state and the sarcoplasmic reticulum (SR) $Ca^{2+}$ content (CaSR) estimated by an electronically timed 10 mmol/L caffeine pulse were evaluated at each cycle length. The diastolic fluorescence was used as reference ($F_0$) for signal normalization ($F/F_0$) after subtraction of background luminescence. For intergroup comparisons, $Ca^{2+}$ handling parameters measured at each cycle length in a treated group were normalized to values measured in Ctrl. Rate-dependency of CaT decay kinetic was expressed as half-time decay ($T_{0.5}$). Frequency of resting $Ca^{2+}$ waves was assessed under resting conditions (for 1 min) before pacing. A $Ca^{2+}$ wave was defined as a $Ca^{2+}$ oscillation occurring at rest with an amplitude >3 SD over resting fluorescence levels ($F_{rest}$). Comparable results were obtained using amplitude cutoffs up to 5 $F_{rest}$ SD. Frequency of spontaneous CaT occurring at rest (resting CaT) was assessed as an additional parameter of SR instability and $Ca^{2+}$ overload.

### 7.5.8 $Ca^{2+}$ sparks

Spontaneous unitary $Ca^{2+}$ release events ($Ca^{2+}$ sparks) were recorded at RT in Fluo4-AM (10μM)-loaded CMs under resting conditions. Tyrode bath solution contained 2 mM $CaCl_2$. Images were acquired at 60x magnification in line-scan mode (xt) at 0.5 kHz by confocal Nikon A1R microscope. Each cell was scanned along a longitudinal line and #10 xt frames (512 pxls x 512 pxls) were acquired. Background fluorescence was measured. Confocal setting parameters were kept constant among experimental groups. Images were analyzed by SparkMaster plugin (Fiji) software (Picht, Zima, Blatter, & Bers, 2007). Automatic spark detection threshold was 3.8. Only in-focus $Ca^{2+}$ sparks (amplitude >0.3) were included in analyses. The following spark parameters were measured: frequency (event number/s/100μm), amplitude (ΔF/F0), full width at half-maximal amplitude (FWHM; μm), full duration at half-maximal amplitude (FDHM; ms), full width (FW; μm) and full duration (FD; ms), time-to-peak (TtP, ms), and decay time constant (τ; ms). Spark mass ($\Delta F/F_0$*$\mu m^3$), an index of $Ca^{2+}$ spark volume (Hollingworth, Peet, Chandler, & Baylor, 2001), was calculated as spark amplitude*1.206* $FWHM^3$. Spark-mediated SR $Ca^{2+}$ leak was calculated as the product of spark mass and frequency.

### 7.5.9 Western blotting

Proteins from CM extracts were separated by SDS-polyacrylamide gel electrophoresis (4-12% Bis-Tris Criterion BIO-RAD gels), blotted for 1 hr, incubated with polyclonal anti-SERCA2 primary antibody (N-19; Santa Cruz Biotechnology) at 4°C overnight, followed by incubation with a specific secondary antibody labelled with fluorescent markers (Alexa Fluor or IRDye) for 1 hr. Signal intensity was quantified by Odyssey Infrared Imaging System (LI-COR). SERCA2 protein levels were normalized to actin levels, as measured using polyclonal anti-actin Ab (Sigma). Data are shown as percent changes vs. Ctrl.

### 7.5.10 Statistical analysis

Results are shown as mean ± SE. Unpaired Student's t-test was used to test for significant differences in two-group analyses. One-way ANOVA was used to test for significance among multiple groups, with post-hoc comparison analyses using Bonferroni's multiple comparison test. $Chi^2$-test was used for comparison of categorical variables. Statistical significance was defined as $p < 0.05$.

## 7.6 Figure Legends

**Fig 1: Effects of Dox and Trz on LV function. a** Schema depicting the experimental protocol. Dox and Trz were administered sequentially (from d1 to d11, and from d19 to d29, respectively). The timing of Trz administration was the same in the Dox/Trz and Trz groups. **b** Echocardiographic results for LV end-systolic volume (LVESV), LV end-diastolic volume (LVEDV), LV ejection fraction (LVEF), and LV fractional shortening (LVFS) in different groups at varying time points. Data are mean ± SEM; **p*<0.05 *vs* Ctrl; # *p*<0.05 Dox *vs* Trz; § *p*<0.05 Dox/Trz *vs* Dox (Ctrl, *n* = 5; Dox, *n* = 7; Trz, *n* = 8; Dox/Trz, *n* = 6). Additional data generated at later time points after Trz administration are shown in Suppl. Fig. S1.

**Fig 2: Effects of Dox and Trz on T-tubule (TT) organization. a** Confocal regions of interest (ROI) of a 3-di-ANEPPDHQ–treated LV CM from a Ctrl rat, and representative higher-magnification LV CM confocal ROI in all groups. Disruption of TT organization in the Dox and Dox/Trz groups, but not in the Trz group, is apparent. **b** Mean TT power spectra in LV and RV CMs in Dox (red), Trz (black) and Dox/Trz groups (green) at the indicated time points, superimposed to those in the Ctrl group (blue). **c)** Quantitative analysis of the TT periodic component (TT-index) in LV and RV CMs. Data on the Dox group are shown at d19 and at d37. Bars are mean ± SEM (*n* = ≥15 cells from ≥3 rats/group; **p*<0.05; ***p*<0.01).

**Fig 3: Effects of Dox and Trz on action potential duration (APD). a** Electrical recordings of stimulated (1 Hz) APs in LV and RV CMs in all groups. Measurements were performed at d19 and at d37 (before and after Trz administration, respectively). **b** Quantitative analysis of $APD_{50}$ and $APD_{90}$ showing increases in the Dox group (at d19) and in the Dox/Trz group (at d37). **c** Electrical recordings showing DAD at 1 Hz-stimulation, as well as EAD and trigger activity (TA) at 2 Hz-stimulation in the Dox/Trz group. **d** Quantitative analysis of cells (%) exhibiting DADs at 1 Hz-stimulation. Data were acquired at d19 and at d37 (see

above). Bars are mean ± SEM ($n$ = ≥12 cells from ≥3 rats/group; *$p$<0.05; **$p$<0.01).

**Fig 4**: Effects of Dox and Trz on beat-to-beat variability of repolarization (BVR). **a** Poincaré plots showing the dispersion of $APD_{90}$ values around the identity line in LV and RV CMs in all groups. **b** Quantitative analysis of short-term variability (STV) of APD values. STV was increased in the Dox group at d19 and in the Dox/Trz group at d37. Data are shown at d19 and at d37. Bars are mean ± SEM ($n$ = ≥12 from ≥3 rats/group; *$p$<0.05).

**Fig 5**: **Effects of Dox and Trz on intracellular $Ca^{2+}$ handling. a** Quantitative analysis of $Ca^{2+}$ transient (CaT) amplitude and SR $Ca^{2+}$ content (CaSR) estimated by a caffeine pulse at different pacing rates (1, 2, and 4 Hz) in field stimulated LV and RV CMs. Dox increased both CaT amplitude and CaSR in RV CMs but not in LV CMs, whereas Trz reduced them in LV CMs. **b** rate dependency of CaT decay kinetics (CaT decay half time, $T_{0.5}$) in both RV and LV CMs. LV CaT decay was slower in the Dox and Dox/Trz groups, but not in the Trz group, compared to Ctrl. **c** Immunoblots showing SERCA protein levels ($n$ = 2-4 rats/group; data in the Trz group and respective Ctrl were analyzed separately). Densitometric analysis. **d** Left panel: Example of $Ca^{2+}$ wave (arrow) and spontaneous CaT occurring at resting. Quantitative analysis of cells (%) exhibiting spontaneous $Ca^{2+}$ waves and resting CaT in both LV and RV CMs. Data on the Dox group are shown at d19 and at d37. Bars are mean ± SEM ($n$ >17 cells/group; *$p$<0.05)

**Fig 6: Effects of Dox and Trz on $Ca^{2+}$ sparks. a** Confocal xt-images of FLuo4-AM loaded LV CMs in all groups. **b** Quantitative analyses of $Ca^{2+}$ sparks frequency (% of Ctrl), spark mass, and sparks-mediated SR $Ca^{2+}$ leak ($n$ = 14-24 cells from 3-5 rats per group). **c** Quantitative analysis of $Ca^{2+}$ 'embers' (i.e., $Ca^{2+}$ sparks with FDHM>20 ms). Data on the Dox group are shown at d19 and at d37. Bars are mean ± SEM (*$p$<0.05).

## 7.7 Figures

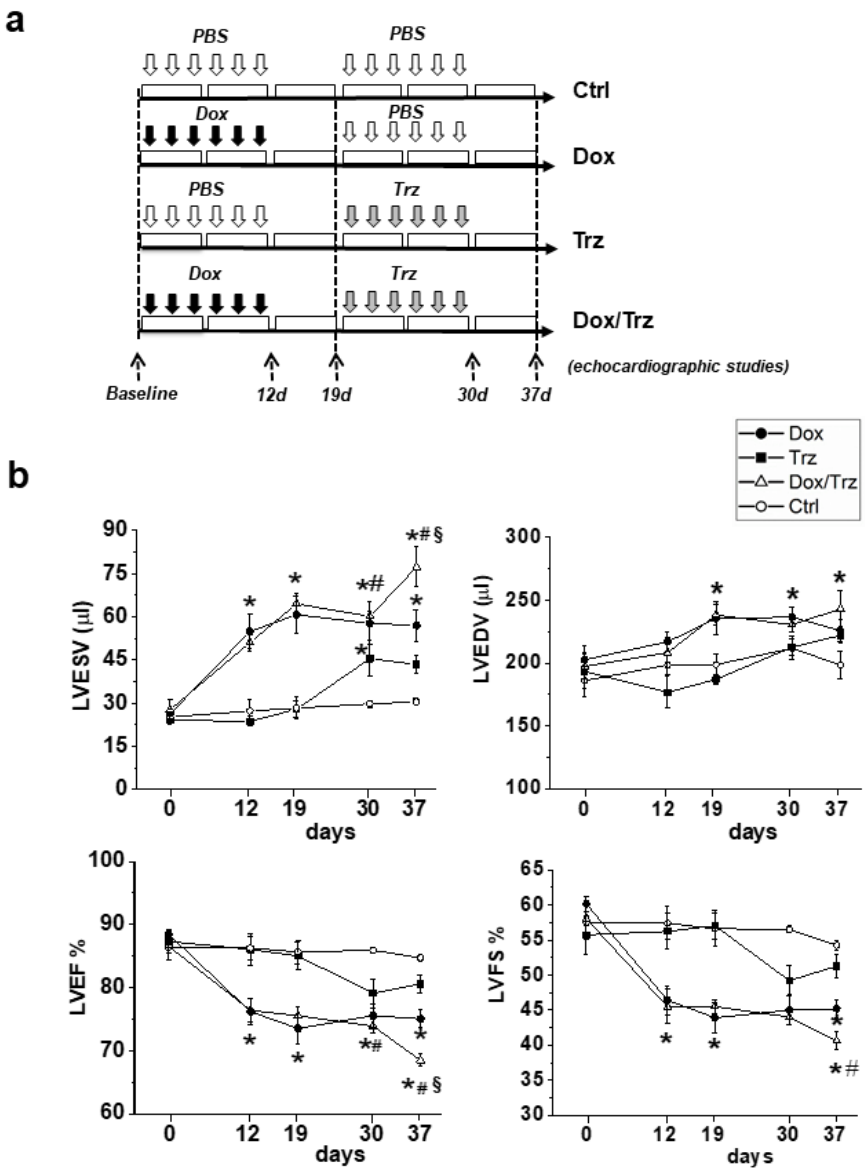


Fig 1

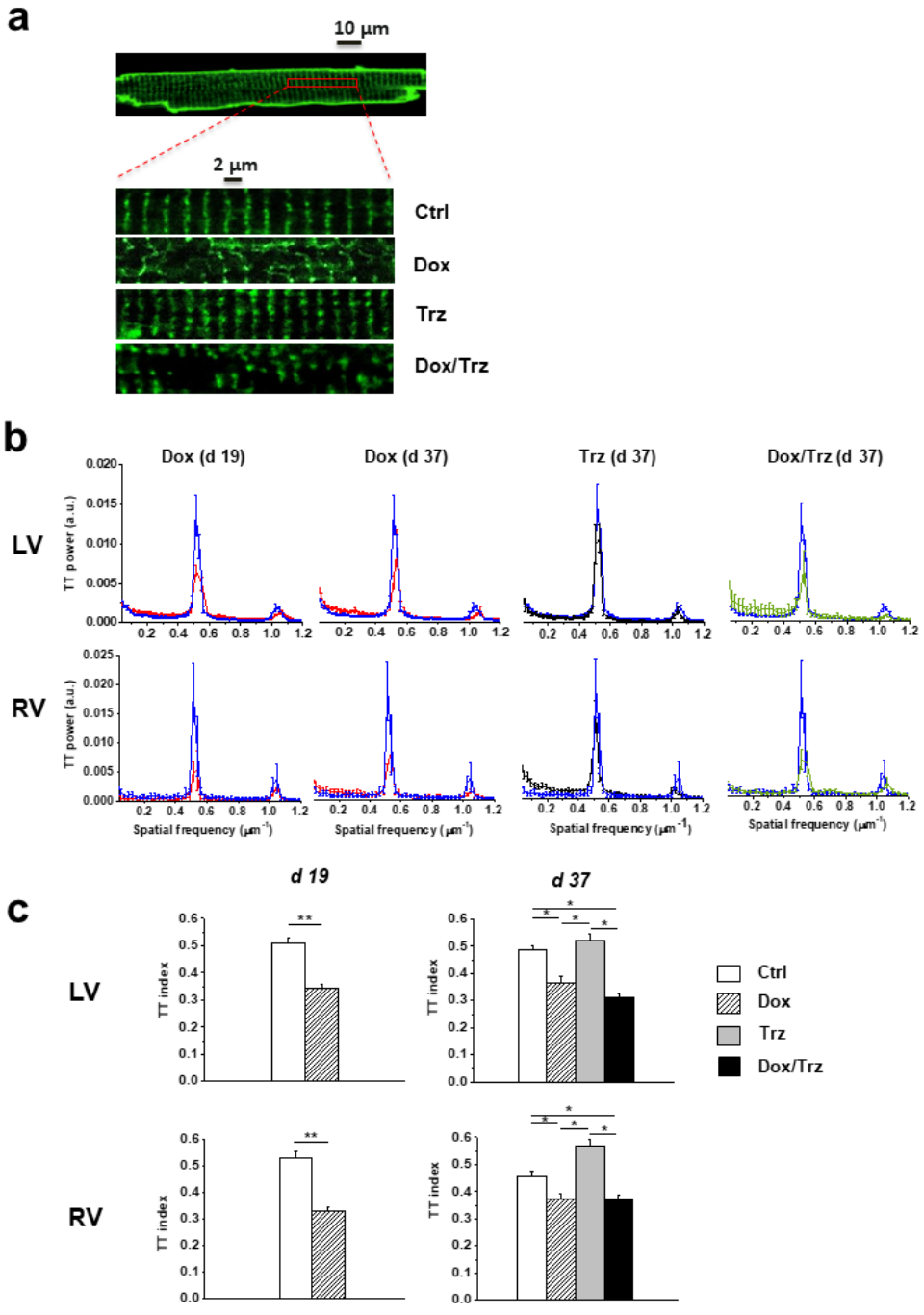
a
10 µm
2 µm
Ctrl
Dox
Trz
Dox/Trz
b
Dox (d 19)
Dox (d 37)
Trz (d 37)
Dox/Trz (d 37)
LV
RV
TT power (a.u.)
Spatial frequency (µm-1)
c
d 19
d 37
LV
RV
TT index
Ctrl
Dox
Trz
Dox/Trz

Fig 2

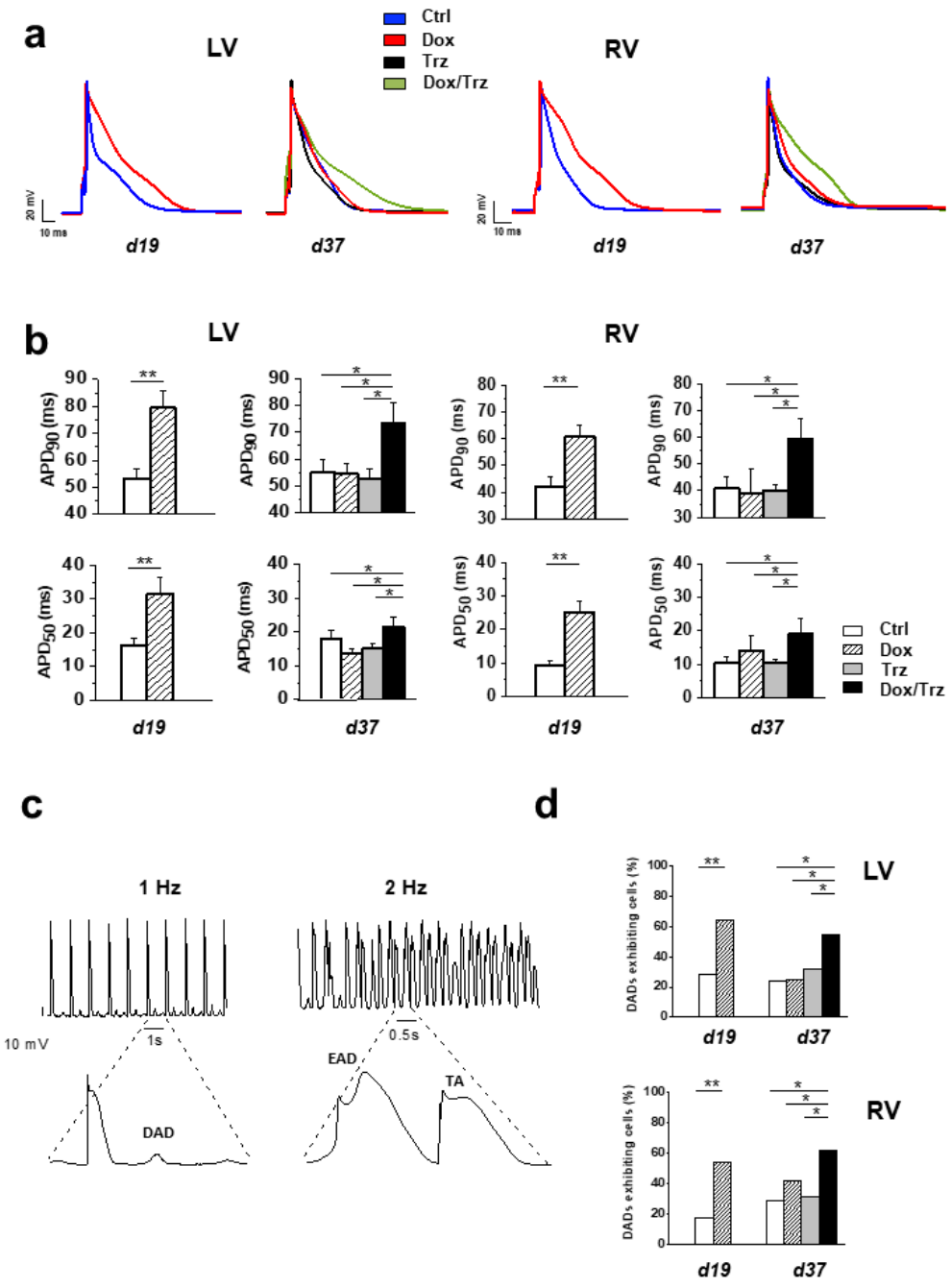
a
LV
RV
Ctrl
Dox
Trz
Dox/Trz
20 mV
10 ms
d19
d37
b
LV
RV
APD90 (ms)
APD50 (ms)
d19
d37
Ctrl
Dox
Trz
Dox/Trz
c
1 Hz
2 Hz
10 mV
1s
0.5s
DAD
EAD
TA
d
DADs exhibiting cells (%)
LV
RV
d19
d37

Fig 3

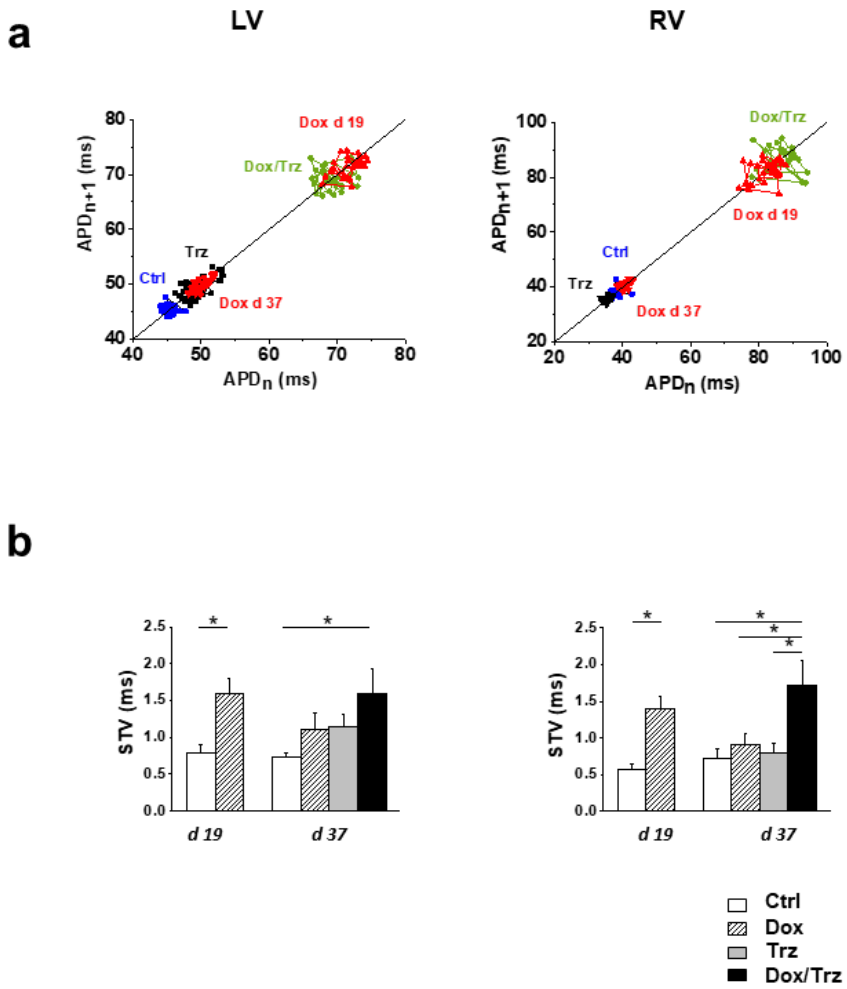
a
LV
RV
Dox d 19
Dox/Trz
Trz
Ctrl
Dox d 37
APDn+1 (ms)
APDn (ms)
b
STV (ms)
d 19
d 37
Ctrl
Dox
Trz
Dox/Trz

Fig 4

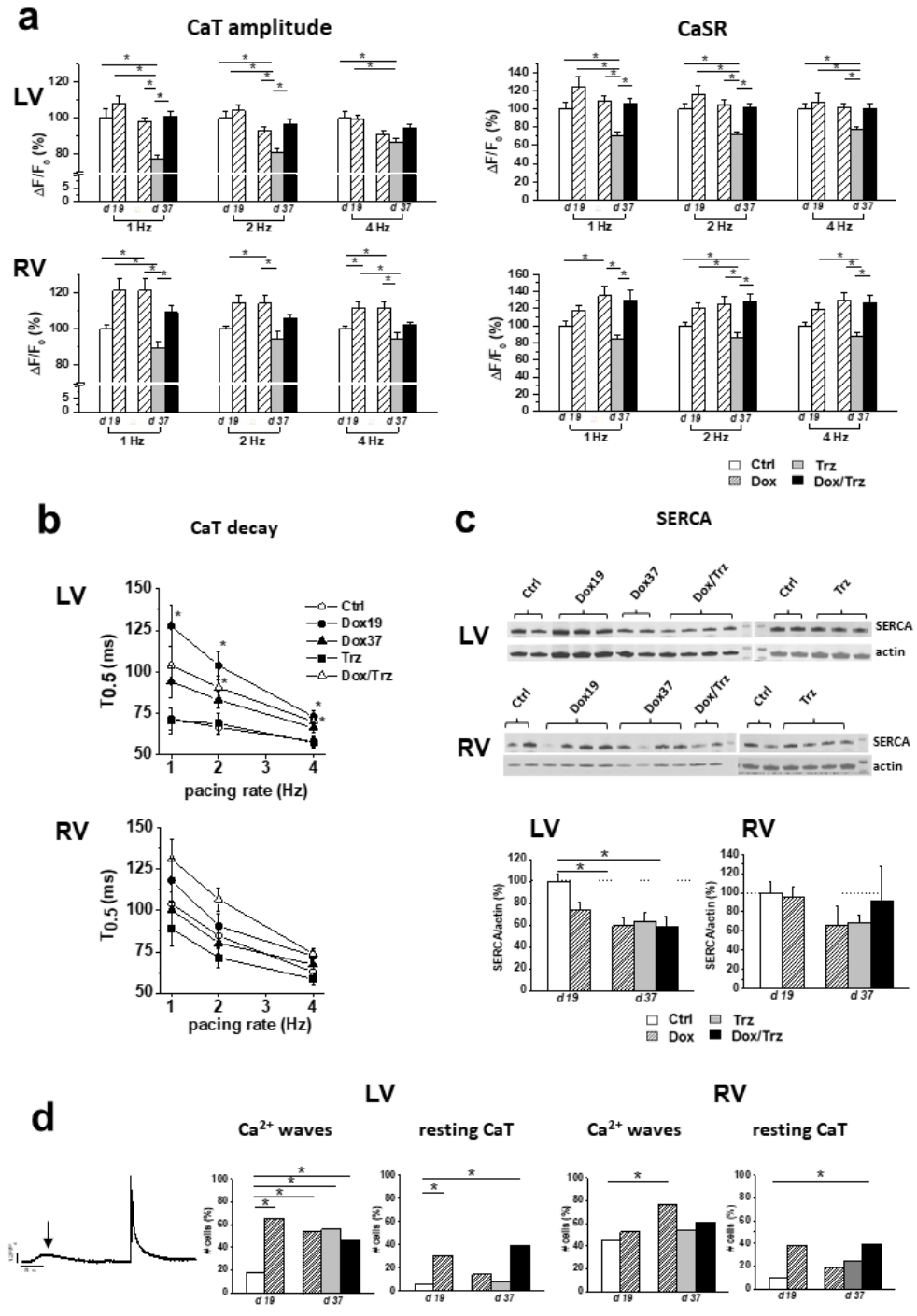
a
CaT amplitude
CaSR
LV
RV
ΔF/F0 (%)
d 19
d 37
1 Hz
2 Hz
4 Hz
Ctrl
Dox
Trz
Dox/Trz
b
CaT decay
T0.5 (ms)
pacing rate (Hz)
Dox19
Dox37
c
SERCA
actin
SERCA/actin (%)
d
Ca2+ waves
resting CaT
# cells (%)

Fig 5

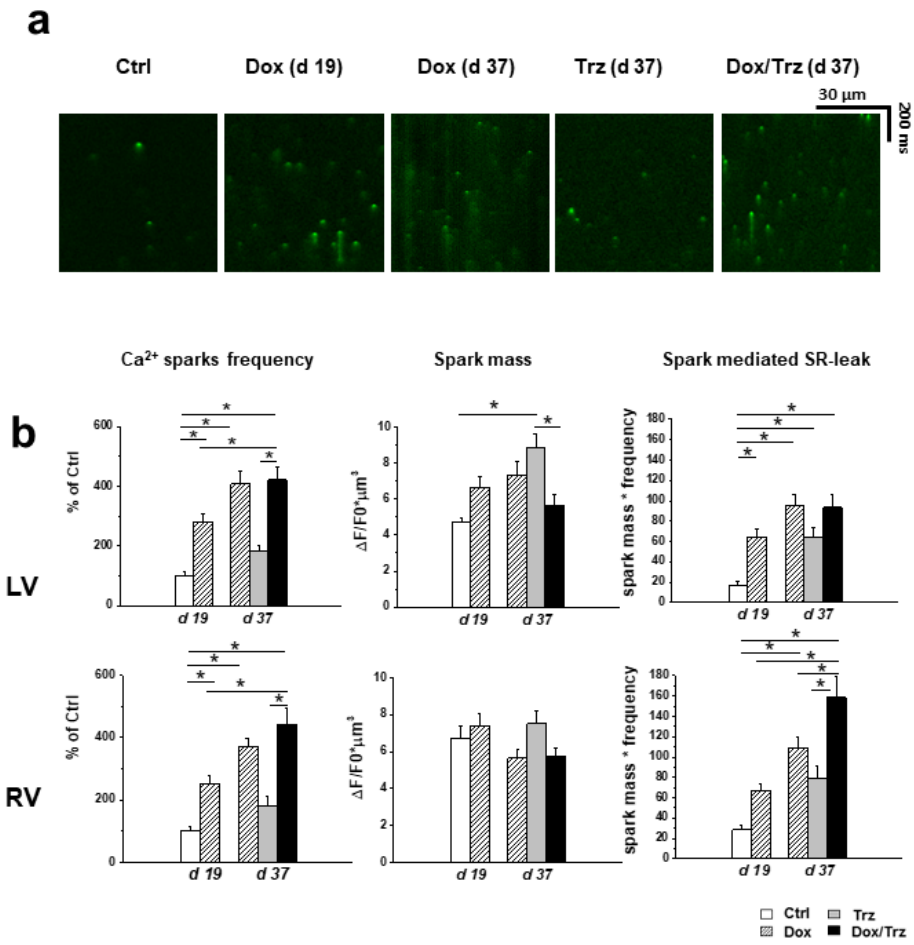
a
Ctrl
Dox (d 19)
Dox (d 37)
Trz (d 37)
Dox/Trz (d 37)
30 µm
200 ms
b
Ca2+ sparks frequency
Spark mass
Spark mediated SR-leak
LV
RV
% of Ctrl
ΔF/F0*µm³
spark mass * frequency
d 19
d 37
Ctrl
Dox
Trz
Dox/Trz
c
LV
RV
embers incidence (% vs sparks)
d 19
d 37

Fig 6

## 7.8 Supplementary Figures and Tables legends

**Suppl Fig S1:** Supplemental echocardiographic analysis of LV function after Trz administration. **a** Schema depicting the experimental protocol. This analysis was performed because the study protocol shown in Fig 1a involved Trz administration starting at d19, which implied a shorter follow-up for this group compared to the Dox group. **b** Echocardiographic results for LV end-systolic volume (LVESV), LV end-diastolic volume (LVEDV), LV ejection fraction (LVEF), and Fractional Shortening (FS). LV and FS functions recover over time after Trz administration. Data are mean ± SEM; *p<0.05 vs Ctrl (Ctrl, n = 5; Trz, n = 3).

**Suppl Fig S2:** ROS generation in CMs. ROS generation in CMs was measured 8 days after the last dose of drug administration in each treated group. In the Dox group, measurements performed at d37, showed reversibility of early changes. Data (% increase over Ctrl) are mean ± SEM.

**Suppl Fig S3:** Correlations between STV of APD and APD values. Plots of STV of APD vs APD values at 1 Hz in LV and RV CMs from all groups. The slope values of each correlation are reported.

**Suppl Fig S4:** $Ca^{2+}$ handling protocol in field-stimulated CMs. Fluo4-loaded intact CMs were field-stimulated at 1, 2, and 4 Hz at physiological temperature. SR $Ca^{2+}$ content was assessed at each cycle length by an electronically timed 10 mmol/L caffeine pulse.

**Suppl Fig S5:** $Ca^{2+}$ spark FDHM distribution. $Ca^{2+}$ spark full duration at half maximum (FDHM) distribution yielded from sparks detected in a Ctrl CM, defining the cut-off value of $Ca^{2+}$ 'embers' used in subsequent analyses shown in Fig 6c.

**Suppl Table S1:** Rat body weight (BW), heart weight (HW), and LV/RV mass ratio. Rat body weight (BW), tibia length (TL), heart weight (HW)/BW ratio, HW/TL radio,

and LV/RV mass ratio in the different groups. No significant differences among groups were observed.

**Suppl Table S2:** Action potential (AP) parameters Electrophysiological parameters yielded from AP recordings in LV and RV treated with Dox, Trz and combination of both at different time points. (APD90 and APD50, durations of AP measured at 90% and 50% of the repolarization phase; Ediast, diastolic potential; dV/dtmax, maximal AP phase 0 upstroke velocity; APA, AP amplitude. Data are expressed as mean ± SE; *p<0.05 vs Ctrl, #p<0.05 vs Trz.

**Suppl Table S3:** Properties of $Ca^{2+}$ sparks. FWHM: full width at half-maximum amplitude; FDHM: full duration at half-maximum amplitude; TtP: time to peak; Tau: decay time constant. Data are expressed as mean ± SE; *p<0.05 *vs* Ctrl.

## 7.9 Supplementary Figures and Tables

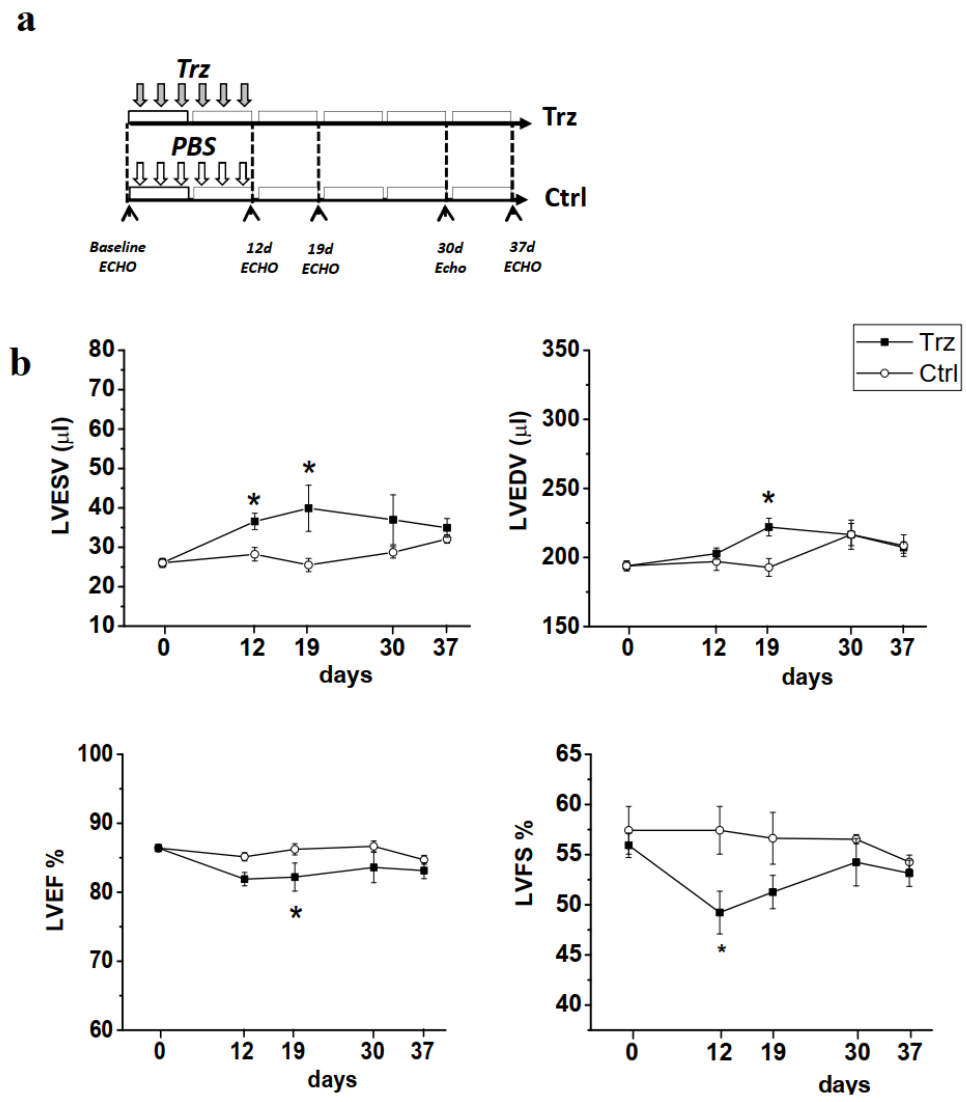


Suppl Fig S1

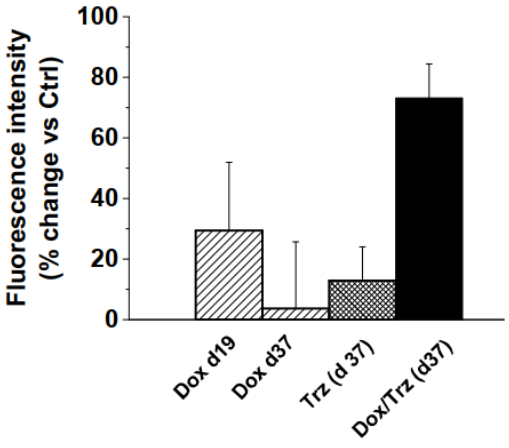
Fluorescence intensity
(% change vs Ctrl)
100
80
60
40
20
0
Dox d19
Dox d37
Trz (d 37)
Dox/Trz (d37)

Suppl Fig S2

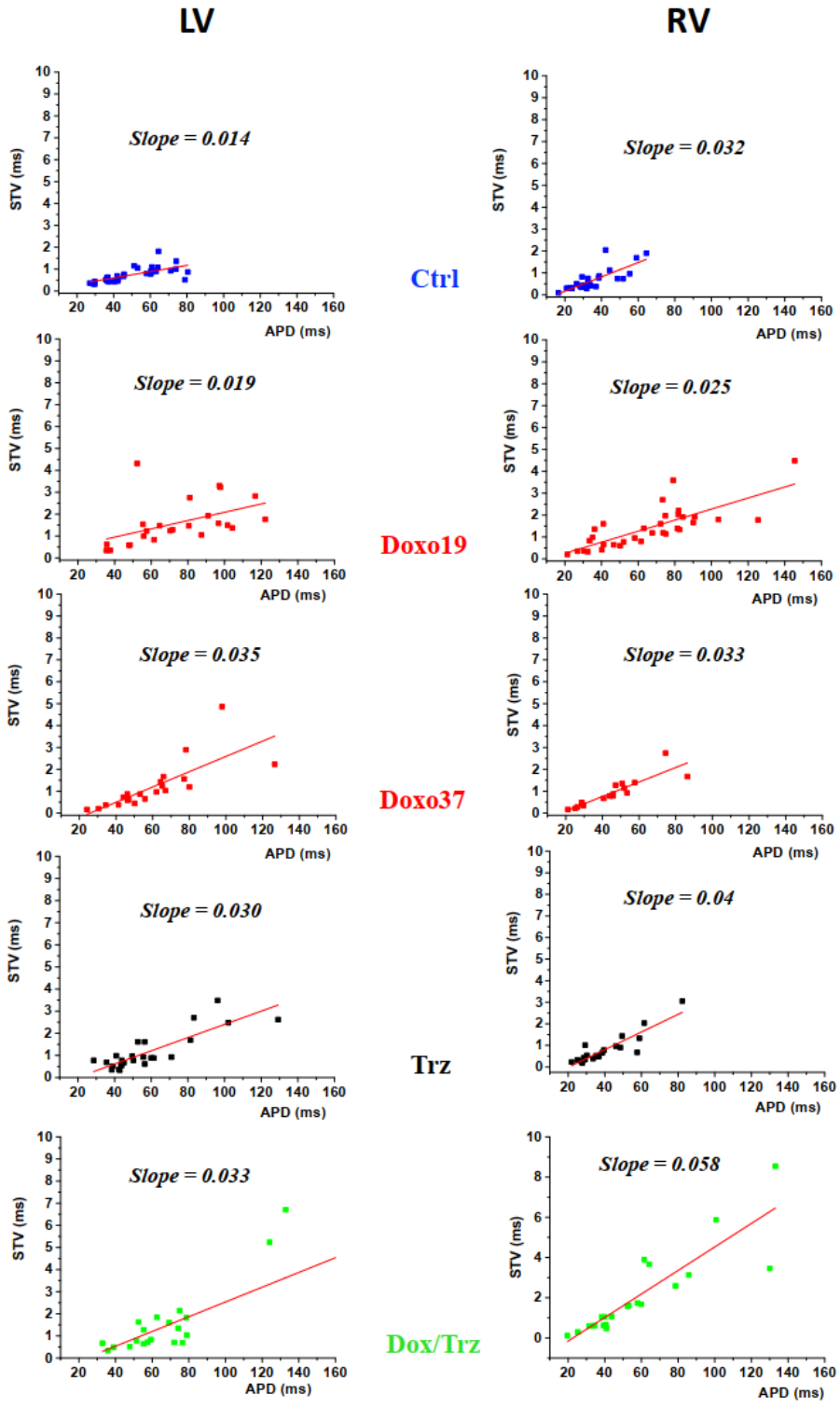
LV
RV
Slope = 0.014
Slope = 0.032
Ctrl
Slope = 0.019
Slope = 0.025
Doxo19
Slope = 0.035
Slope = 0.033
Doxo37
Slope = 0.030
Slope = 0.04
Trz
Slope = 0.033
Slope = 0.058
Dox/Trz
STV (ms)
APD (ms)

Suppl Fig S3

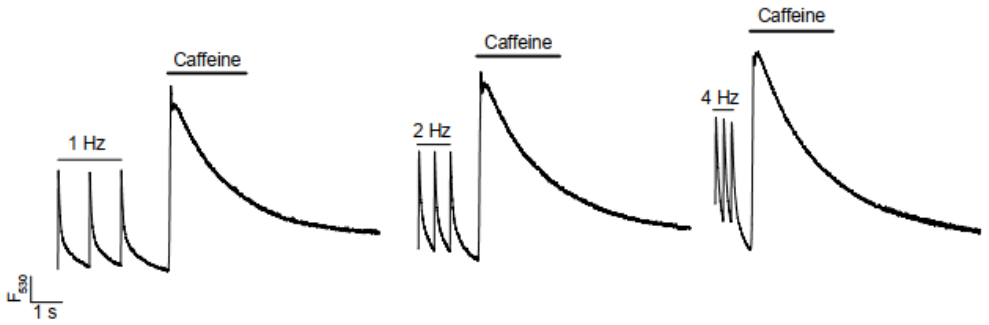


Suppl Fig S4

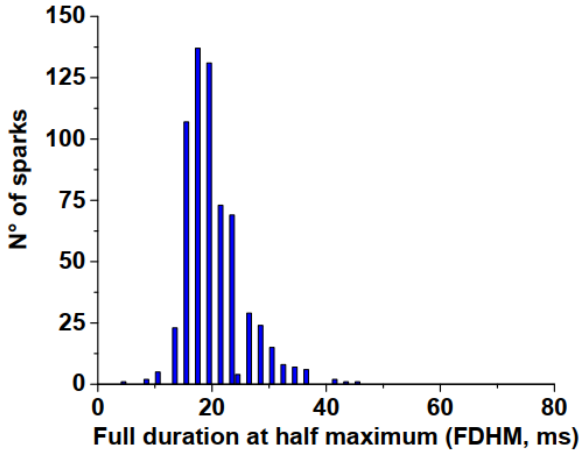
N° of sparks
150
125
100
75
50
25
0
0
20
40
60
80
Full duration at half maximum (FDHM, ms)

Suppl Fig S5

| | Ctrl (N=6) | Dox19 (N=4) | Dox37 (N=5) | Trz (N=4) | Dox/Trz (N=5) |
|---|---|---|---|---|---|
| **BW (Kg)** | 0.27 ± 0.02 | 0.26 ± 0.01 | 0.32 ± 0.007 | 0.29 ± 0.01 | 0.32 ± 0.004 |
| **TL (cm)** | 3.9 ± 0.09 | 3.9 ± 0.09 | 4.08 ± 0.1 | 3.92 ± 0.15 | 3.96 ± 0.06 |
| **HW/BW (g/Kg)** | 4.6 ± 0.36 | 4.6 ± 0.37 | 4.14 ± 0.3 | 4.79 ± 0.23 | 4.39 ± 0.33 |
| **HW/TL (g/cm)** | 0.31 ± 0.01 | 0.30 ± 0.02 | 0.32 ± 0.02 | 0.35 ± 0.01 | 0.35 ± 0.02 |
| **RV/LV (%)** | 33.9 ± 3.9 | 33.9 ± 1.7 | 41.4 ± 7.5 | 38.9 ± 1.9 | 37.3 ± 4.6 |

Suppl Table S1

| LV | | $APD_{90}$ (ms) | $APD_{50}$ (ms) | $APD_{50/90}$ | $E_{diast}$ (mV) | $dV/dt_{max}$ (V/s) | APA (mV) | N cells |
|---|---|---|---|---|---|---|---|---|
| Ctrl | d19 | 53.2 ± 3.8 | 16.3 ± 2.1 | 0.29 ± 0.02 | -76.8 ± 2.1 | 241.5 ± 17 | 119.4 ± 1.7 | n = 20 |
| | d37 | 55.3 ± 4.5 | 18 ± 2.4 | 0.32 ± 0.03 | -75.9 ± 1.2 | 260.2 ± 19.1 | 121 ± 2 | n = 20 |
| Trz | d19 | 59 ± 4.4 | 15.1 ± 2 | 0.24 ± 0.02 | -77.2 ± 0.8 | 222.8 ± 14.7 | 119.3 ± 1.3 | n = 31 |
| | d37 | 51 ± 3.9 | 15.7 ± 2 | 0.3 ± 0.02 | -73.4 ± 1.4 | 196.6 ± 22 | 116.3 ± 2.5 | n = 17 |
| Dox | d19 | 79.5 ± 6.5 *# | 31.5 ± 4.7 | 0.36 ± 0.02 # | -74.7 ± 0.5 # | 220.4 ± 12.7 | 117.7 ± 1.2 | n = 38 |
| | d37 | 54.7 ± 3.6 | 13.6 ± 1.5 | 0.25 ± 0.02 | -74 ± 1.5 | 194.6 ± 12.1 | 113.4 ± 1.3 * | n = 11 |
| Dox/Trz | d37 | 73.2 ± 7.5 * | 21.6 ± 2.7 | 0.3 ± 0.02 | -75.1 ± 0.6 | 218.3 ± 12.3 | 115.2 ± 1.1 | n = 31 |
| RV | | $APD_{90}$ (ms) | $APD_{50}$ (ms) | $APD_{50/90}$ | $E_{diast}$ (mV) | $dV/dt_{max}$ (V/s) | APA (mV) | N cells |
| Ctrl | d19 | 41.8 ± 4 | 9.2 ± 1.3 | 0.22 ± 0.02 | -75 ± 1.1 | 206.3 ± 24 | 114.8 ± 2.1 | n = 17 |
| | d37 | 40.7 ± 4.2 | 10.3 ± 1.8 | 0.26 ± 0.03 | -73.8 ± 1.2 | 286.2 ± 18.8 | 120.9 ± 1.4 | n = 22 |
| Trz | d19 | 40.8± 2.5 | 9.5 ± 0.9 | 0.23 ± 0.02 | -78 ± 1 | 218 ± 13 | 116.6 ± 1.4 | n = 31 |
| | d37 | 46.3± 3.2 | 14 ± 2.4 | 0.3 ± 0.03 | -72.4 ± 1.2 | 205 ± 27.8 | 113.4 ± 3.8 | n = 10 |
| Dox | d19 | 60.5 ± 4.3 *# | 25.2 ± 3.2 *# | 0.36 ± 0.02 *# | -76 .1± 0.8 | 197.8 ± 11 | 115.6 ± 1 | n = 40 |
| | d37 | 43 ± 3.7 | 13.8 ± 4.7 | 0.32 ± 0.05 | -75.1± 3 | 219.8 ± 38.8 | 115 ± 4.3 | n = 10 |
| Dox/Trz | d37 | 59.5 ± 7.3 * | 20.6 ± 3.5 | 0.31 ± 0.03 | -73.4 ± 2 | 171.7 ± 14 ** | 109.6 ± 2 ** | n = 20 |

Suppl Table S2

| LV | Ampl ($F/F_0$) | FWHM (µm) | FDHM (ms) | FullWidth (µm) | FullDur (ms) | TtP (ms) | Tau (ms) | Spark mass*rate | N rat/sparks |
|---|---|---|---|---|---|---|---|---|---|
| Ctrl | 0.8 ± 0.01 | 1.76 ± 0.01 | 20.3 ± 0.2 | 3.8 ± 0.04 | 54.1 ± 0.8 | 10.6 ± 0.2 | 20.1 ± 0.25 | 14.5 ± 2.5 | 3/807 |
| Dox d19 | 0.86 ± 0.01 | 1.82 ± 0.02 | 22.6 ± 0.16* | 4.33 ± 0.03 | 65.3 ± 0.72 | 12.11 ± 0.2 | 22.8 ± 0.2* | 64.5 ± 7.5 | 4/1626 |
| Dox d37 | 0.73 ± 0.01 | 1.81 ± 0.01 | 22.6 ± 0.14* | 3.4 ± 0.03 | 48 ± 0.5 | 11.05 ± 0.1 | 22.2 ± 0.2* | 95.3 ± 10.7 | 4/1915 |
| Trz | 0.77 ± 0.01 | 2.06 ± 0.01 | 21.3 ± 0.21 | 3.9 ± 0.04 | 47.3 ± 0.7 | 11.5 ± 0.2 | 20 ± 0.3 | 63.9 ± 9.4 | 3/917 |
| Dox/Trz d37 | 0.72 ± 0.01 | 1.7 ± 0.01 | 23.8 ± 0.2* | 3.2 ± 0.03 | 51.8 ± 0.64 | 11 ± 0.2 | 24.14 ± 0.2* | 93.2 ± 12.4 | 4/1435 |
| RV | Ampl ($F/F_0$) | FWHM (µm) | FDHM (ms) | FullWidth (µm) | FullDur (ms) | TtP (ms) | Tau (ms) | Spark mass*rate | N rat/sparks |
| Ctrl | 0.94 ± 0.02 | 1.84 ± 0.01 | 22.6 ± 0.3 | 4.14 ± 0.04 | 61.4 ± 1 | 11.11 ± 0.16 | 22.8 ± 0.4 | 5.28 ± 1.46 | 3/878 |
| Dox d19 | 0.8± 0.54 | 1.9 ± 0.3 | 26 ± 2* | 4.1 ± 0.68 | 65.2 ± 4.03 | 12.2 ± 1.9 | 27.4 ± 3.45* | 75.11 ± 7.2 | 4/1770 |
| Dox d37 | 0.7 ± 0.01 | 1.81 ± 0.01 | 24.4 ± 0.21* | 3.26 ± 0.02 | 49.8 ± 0.52 | 11.72 ± 0.14 | 23.83 ± 0.3* | 108.35 ± 13.6 | 4/1719 |
| Trz | 0.7 ± 0.01 | 2 ± 0.01 | 21.3 ± 0.2 | 3.5 ± 0.03 | 43.1 ± 0.5 | 11.2 ± 0.16 | 19.8 ± 0.3 | 79.6 ± 11.5 | 3/1295 |
| Dox/Trz d37 | 0.6 ± 0.006 | 1.91 ± 0.01 | 27.4 ± 0.22* | 3.20 ± 0.02 | 52.2 ± 0.61 | 11.53 ± 0.14 | 29.35 ± 0.5* | 158.9 ± 20.22 | 4/2182 |

Suppl Table S3

## 7.10 Funding

This work was supported by grants of the Swiss Cancer League, as well as of the Cecilia-Augusta Foundation and the San Salvatore Foundation (Lugano, Switzerland) and Fondo Ricerca di Ateneo of University of Milano-Bicocca (Milano, Italy).

## 7.11 References


Advani, P. P., Ballman, K. V., Dockter, T. J., Colon-Otero, G., & Perez, E. A. (2016). Long-Term Cardiac Safety Analysis of NCCTG N9831 (Alliance) Adjuvant Trastuzumab Trial. *J Clin Oncol, 34*(6), 581-587. doi:10.1200/JCO.2015.61.8413

Altomare, C., Bartolucci, C., Sala, L., Bernardi, J., Mostacciuolo, G., Rocchetti, M., . . . Zaza, A. (2015). IKr Impact on Repolarization and Its Variability Assessed by Dynamic Clamp. *Circ Arrhythm Electrophysiol, 8*(5), 1265-1275. doi:10.1161/CIRCEP.114.002572

Barile, L., Cervio, E., Lionetti, V., Milano, G., Ciullo, A., Biemmi, V., . . . Vassalli, G. (2018). Cardioprotection by cardiac progenitor cell-secreted exosomes: role of pregnancy-associated plasma protein-A. *Cardiovasc Res, 114*(7), 992-1005. doi:10.1093/cvr/cvy055

Belmonte, F., Das, S., Sysa-Shah, P., Sivakumaran, V., Stanley, B., Guo, X., . . . Gabrielson, K. (2015). ErbB2 overexpression upregulates antioxidant enzymes, reduces basal levels of reactive oxygen species, and protects against doxorubicin cardiotoxicity. *Am J Physiol Heart Circ Physiol, 309*(8), H1271-1280. doi:10.1152/ajpheart.00517.2014

Bokenes, J., Aronsen, J. M., Birkeland, J. A., Henriksen, U. L., Louch, W. E., Sjaastad, I., & Sejersted, O. M. (2008). Slow contractions characterize failing rat hearts. *Basic Res Cardiol, 103*(4), 328-344. doi:10.1007/s00395-008-0719-y

Bryant, S., Kimura, T. E., Kong, C. H., Watson, J. J., Chase, A., Suleiman, M. S., . . . Orchard, C. H. (2014). Stimulation of ICa by basal PKA activity is facilitated by caveolin-3 in cardiac ventricular myocytes. *J Mol Cell Cardiol, 68*, 47-55. doi:10.1016/j.yjmcc.2013.12.026

Caldwell, J. L., Smith, C. E., Taylor, R. F., Kitmitto, A., Eisner, D. A., Dibb, K. M., & Trafford, A. W. (2014). Dependence of cardiac transverse tubules on the BAR domain protein amphiphysin II (BIN-1). *Circ Res, 115*(12), 986-996. doi:10.1161/CIRCRESAHA.116.303448

Cappetta, D., De Angelis, A., Sapio, L., Prezioso, L., Illiano, M., Quaini, F., . . . Urbanek, K. (2017). Oxidative Stress and Cellular Response to Doxorubicin: A Common Factor in the Complex Milieu of Anthracycline Cardiotoxicity. *Oxid Med Cell Longev, 2017*, 1521020. doi:10.1155/2017/1521020

Cappetta, D., Esposito, G., Coppini, R., Piegari, E., Russo, R., Ciuffreda, L. P., . . . De Angelis, A. (2017). Effects of ranolazine in a model of doxorubicin-induced left ventricle diastolic dysfunction. *Br J Pharmacol, 174*(21), 3696-3712. doi:10.1111/bph.13791

Cardinale, D., Colombo, A., Torrisi, R., Sandri, M. T., Civelli, M., Salvatici, M., . . . Cipolla, C. M. (2010). Trastuzumab-induced cardiotoxicity: clinical and prognostic implications of troponin I evaluation. *J Clin Oncol, 28*(25), 3910-3916. doi:10.1200/JCO.2009.27.3615

Crocini, C., Coppini, R., Ferrantini, C., Yan, P., Loew, L. M., Tesi, C., . . . Sacconi, L. (2014). Defects in T-tubular electrical activity underlie local alterations of calcium release in heart failure. *Proc Natl Acad Sci U S A, 111*(42), 15196-15201. doi:10.1073/pnas.1411557111

Crocini, C., Ferrantini, C., Coppini, R., & Sacconi, L. (2017). Electrical defects of the transverse-axial tubular system in cardiac diseases. *J Physiol, 595*(12), 3815-3822. doi:10.1113/JP273042

Crossman, D. J., Young, A. A., Ruygrok, P. N., Nason, G. P., Baddelely, D., Soeller, C., & Cannell, M. B. (2015). T-tubule disease: Relationship between t-tubule organization and regional contractile performance in human dilated cardiomyopathy. *J Mol Cell Cardiol, 84*, 170-178. doi:10.1016/j.yjmcc.2015.04.022

Dubey, R., Lebensohn, A. M., Bahrami-Nejad, Z., Marceau, C., Champion, M., Gevaert, O., . . . Rohatgi, R. (2016). Chromatin-Remodeling Complex SWI/SNF Controls Multidrug Resistance by Transcriptionally Regulating the Drug Efflux Pump ABCB1. *Cancer Res, 76*(19), 5810-5821. doi:10.1158/0008-5472.CAN-16-0716

Ducroq, J., Moha ou Maati, H., Guilbot, S., Dilly, S., Laemmel, E., Pons-Himbert, C., . . . Le Grand, M. (2010). Dexrazoxane protects the heart from acute doxorubicin-induced QT prolongation: a key role for I(Ks). *Br J Pharmacol, 159*(1), 93-101. doi:10.1111/j.1476-5381.2009.00371.x

Ewer, M. S., & Ewer, S. M. (2015). Cardiotoxicity of anticancer treatments. *Nat Rev Cardiol, 12*(9), 547-558. doi:10.1038/nrcardio.2015.65

Ferrantini, C., Crocini, C., Coppini, R., Vanzi, F., Tesi, C., Cerbai, E., . . . Sacconi, L. (2013). The transverse-axial tubular system of cardiomyocytes. *Cell Mol Life Sci, 70*(24), 4695-4710. doi:10.1007/s00018-013-1410-5

Ghigo, A., Li, M., & Hirsch, E. (2016). New signal transduction paradigms in anthracycline-induced cardiotoxicity. *Biochim Biophys Acta, 1863*(7 Pt B), 1916-1925. doi:10.1016/j.bbamcr.2016.01.021

Giordano, S. H., Lin, Y. L., Kuo, Y. F., Hortobagyi, G. N., & Goodwin, J. S. (2012). Decline in the use of anthracyclines for breast cancer. *J Clin Oncol, 30*(18), 2232-2239. doi:10.1200/JCO.2011.40.1273

He, J., Conklin, M. W., Foell, J. D., Wolff, M. R., Haworth, R. A., Coronado, R., & Kamp, T. J. (2001). Reduction in density of transverse tubules and L-type Ca(2+) channels in canine

tachycardia-induced heart failure. *Cardiovasc Res, 49*(2), 298-307. doi:10.1016/s0008-6363(00)00256-x

Heijman, J., Zaza, A., Johnson, D. M., Rudy, Y., Peeters, R. L., Volders, P. G., & Westra, R. L. (2013). Determinants of beat-to-beat variability of repolarization duration in the canine ventricular myocyte: a computational analysis. *PLoS Comput Biol, 9*(8), e1003202. doi:10.1371/journal.pcbi.1003202

Heinzel, F. R., Bito, V., Biesmans, L., Wu, M., Detre, E., von Wegner, F., . . . Sipido, K. (2008). Remodeling of T-tubules and reduced synchrony of Ca2+ release in myocytes from chronically ischemic myocardium. *Circ Res, 102*(3), 338-346. doi:10.1161/CIRCRESAHA.107.160085

Hollingworth, S., Peet, J., Chandler, W. K., & Baylor, S. M. (2001). Calcium sparks in intact skeletal muscle fibers of the frog. *J Gen Physiol, 118*(6), 653-678. doi:10.1085/jgp.118.6.653

Hsu, W. T., Huang, C. Y., Yen, C. Y. T., Cheng, A. L., & Hsieh, P. C. H. (2018). The HER2 inhibitor lapatinib potentiates doxorubicin-induced cardiotoxicity through iNOS signaling. *Theranostics, 8*(12), 3176-3188. doi:10.7150/thno.23207

Ibrahim, M., Al Masri, A., Navaratnarajah, M., Siedlecka, U., Soppa, G. K., Moshkov, A., . . . Terracciano, C. M. (2010). Prolonged mechanical unloading affects cardiomyocyte excitation-contraction coupling, transverse-tubule structure, and the cell surface. *FASEB J, 24*(9), 3321-3329. doi:10.1096/fj.10-156638

Johnson, D. M., Heijman, J., Pollard, C. E., Valentin, J. P., Crijns, H. J., Abi-Gerges, N., & Volders, P. G. (2010). I(Ks) restricts excessive beat-to-beat variability of repolarization during beta-adrenergic receptor stimulation. *J Mol Cell Cardiol, 48*(1), 122-130. doi:10.1016/j.yjmcc.2009.08.033

Kitani, T., Ong, S. G., Lam, C. K., Rhee, J. W., Zhang, J. Z., Oikonomopoulos, A., . . . Wu, J. C. (2019). Human-Induced Pluripotent Stem Cell Model of Trastuzumab-Induced Cardiac Dysfunction in Patients With Breast Cancer. *Circulation, 139*(21), 2451-2465. doi:10.1161/CIRCULATIONAHA.118.037357

Kurokawa, Y. K., Shang, M. R., Yin, R. T., & George, S. C. (2018). Modeling trastuzumab-related cardiotoxicity in vitro using human stem cell-derived cardiomyocytes. *Toxicol Lett, 285*, 74-80. doi:10.1016/j.toxlet.2018.01.001

Llach, A., Mazevet, M., Mateo, P., Villejouvert, O., Ridoux, A., Rucker-Martin, C., . . . Gomez, A. M. (2019). Progression of excitation-contraction coupling defects in doxorubicin cardiotoxicity. *J Mol Cell Cardiol, 126*, 129-139. doi:10.1016/j.yjmcc.2018.11.019

Louch, W. E., Bito, V., Heinzel, F. R., Macianskiene, R., Vanhaecke, J., Flameng, W., . . . Sipido, K. R. (2004). Reduced synchrony of Ca2+ release with loss of T-tubules-a comparison to Ca2+ release in human failing cardiomyocytes. *Cardiovasc Res, 62*(1), 63-73. doi:10.1016/j.cardiores.2003.12.031

Louch, W. E., Hake, J., Mork, H. K., Hougen, K., Skrbic, B., Ursu, D., . . . Sejersted, O. M. (2013). Slow Ca(2)(+) sparks de-synchronize Ca(2)(+) release in failing cardiomyocytes: evidence for altered configuration of Ca(2)(+) release units? *J Mol Cell Cardiol, 58*, 41-52. doi:10.1016/j.yjmcc.2013.01.014

Louch, W. E., Mork, H. K., Sexton, J., Stromme, T. A., Laake, P., Sjaastad, I., & Sejersted, O. M. (2006). T-tubule disorganization and reduced synchrony of Ca2+ release in murine cardiomyocytes following myocardial infarction. *J Physiol, 574*(Pt 2), 519-533. doi:10.1113/jphysiol.2006.107227

Lyon, A. R., MacLeod, K. T., Zhang, Y., Garcia, E., Kanda, G. K., Lab, M. J., . . . Gorelik, J. (2009). Loss of T-tubules and other changes to surface topography in ventricular myocytes from failing human and rat heart. *Proc Natl Acad Sci U S A, 106*(16), 6854-6859. doi:10.1073/pnas.0809777106

Manfra, O., Frisk, M., & Louch, W. E. (2017). Regulation of Cardiomyocyte T-Tubular Structure: Opportunities for Therapy. *Curr Heart Fail Rep, 14*(3), 167-178. doi:10.1007/s11897-017-0329-9

Mazur, M., Wang, F., Hodge, D. O., Siontis, B. L., Beinborn, D. S., Villarraga, H. R., . . . Herrmann, J. (2017). Burden of Cardiac Arrhythmias in Patients With Anthracycline-Related Cardiomyopathy. *JACC Clin Electrophysiol, 3*(2), 139-150. doi:10.1016/j.jacep.2016.08.009

Milano, G., Biemmi, V., Lazzarini, E., Balbi, C., Ciullo, A., Bolis, S., . . . Vassalli, G. (2020). Intravenous administration of cardiac progenitor cell-derived exosomes protects against doxorubicin/trastuzumab-induced cardiac toxicity. *Cardiovasc Res, 116*(2), 383-392. doi:10.1093/cvr/cvz108

Molina, C. E., Heijman, J., & Dobrev, D. (2016). Differences in Left Versus Right Ventricular Electrophysiological Properties in Cardiac Dysfunction and Arrhythmogenesis. *Arrhythm Electrophysiol Rev, 5*(1), 14-19. doi:10.15420/aer.2016.8.2

Mor-Avi, V., Lang, R. M., Badano, L. P., Belohlavek, M., Cardim, N. M., Derumeaux, G., . . . Zamorano, J. L. (2011). Current and evolving echocardiographic techniques for the quantitative evaluation of cardiac mechanics: ASE/EAE consensus statement on methodology and indications endorsed by the Japanese Society of Echocardiography. *J Am Soc Echocardiogr, 24*(3), 277-313. doi:10.1016/j.echo.2011.01.015

Mork, H. K., Sjaastad, I., Sejersted, O. M., & Louch, W. E. (2009). Slowing of cardiomyocyte Ca2+ release and contraction during heart failure progression in postinfarction mice. *296*(4), H1069-1079. doi:10.1152/ajpheart.01009.2008

Muraru, D., Cucchini, U., Mihaila, S., Miglioranza, M. H., Aruta, P., Cavalli, G., . . . Badano, L. P. (2014). Left ventricular myocardial strain by three-dimensional speckle-tracking echocardiography in healthy subjects: reference values and analysis of their physiologic and technical determinants. *J Am Soc Echocardiogr, 27*(8), 858-871 e851. doi:10.1016/j.echo.2014.05.010

Ozcelik, C., Erdmann, B., Pilz, B., Wettschureck, N., Britsch, S., Hubner, N., . . . Garratt, A. N. (2002). Conditional mutation of the ErbB2 (HER2) receptor in cardiomyocytes leads to dilated cardiomyopathy. *Proc Natl Acad Sci U S A, 99*(13), 8880-8885. doi:10.1073/pnas.122249299

Picht, E., Zima, A. V., Blatter, L. A., & Bers, D. M. (2007). SparkMaster: automated calcium spark analysis with ImageJ. *Am J Physiol Cell Physiol, 293*(3), C1073-1081. doi:10.1152/ajpcell.00586.2006

Piotrowski, G., Gawor, R., Slomka, R., Banasiak, M., Strzelecki, P., Gawor, Z., & Potemski, P. (2012). [Cardioverter-defibrillator in the treatment of arrhythmia induced by trastuzumab used in the adjuvant setting in a patient with positive human epidermal growth factor receptor type-2 breast cancer]. *Kardiol Pol, 70*(7), 756-757. PMID: 22825957

Rayson, D., Richel, D., Chia, S., Jackisch, C., van der Vegt, S., & Suter, T. (2008). Anthracycline-trastuzumab regimens for HER2/neu-overexpressing breast cancer: current experience and future strategies. *Ann Oncol, 19*(9), 1530-1539. doi:10.1093/annonc/mdn292

Rocchetti, M., Sala, L., Rizzetto, R., Staszewsky, L. I., Alemanni, M., Zambelli, V., . . . Zaza, A. (2014). Ranolazine prevents INaL enhancement and blunts myocardial remodelling in a model of pulmonary hypertension. *Cardiovasc Res, 104*(1), 37-48. doi:10.1093/cvr/cvu188

Rochette, L., Guenancia, C., Gudjoncik, A., Hachet, O., Zeller, M., Cottin, Y., & Vergely, C. (2015). Anthracyclines/trastuzumab: new aspects of cardiotoxicity and molecular mechanisms. *Trends Pharmacol Sci, 36*(6), 326-348. doi:10.1016/j.tips.2015.03.005

Romond, E. H., Perez, E. A., Bryant, J., Suman, V. J., Geyer, C. E., Jr., Davidson, N. E., . . . Wolmark, N. (2005). Trastuzumab plus adjuvant chemotherapy for operable HER2-positive breast cancer. *N Engl J Med, 353*(16), 1673-1684. doi:10.1056/NEJMoa052122

Ronchi, C., Badone, B., Bernardi, J., & Zaza, A. (2018). Action Potential Prolongation, beta-Adrenergic Stimulation, and Angiotensin II as Co-factors in Sarcoplasmic Reticulum Instability. *Front Physiol, 9*, 1893. doi:10.3389/fphys.2018.01893

Sacconi, L., Ferrantini, C., Lotti, J., Coppini, R., Yan, P., Loew, L. M., . . . Pavone, F. S. (2012). Action potential propagation in transverse-axial tubular system is impaired in heart failure. *Proc Natl Acad Sci U S A, 109*(15), 5815-5819. doi:10.1073/pnas.1120188109

Sachse, F. B., Torres, N. S., Savio-Galimberti, E., Aiba, T., Kass, D. A., Tomaselli, G. F., & Bridge, J. H. (2012). Subcellular structures and function of myocytes impaired during heart failure are restored by cardiac resynchronization therapy. *Circ Res, 110*(4), 588-597. doi:10.1161/CIRCRESAHA.111.257428

Saeed, M. F., Premecz, S., Goyal, V., Singal, P. K., & Jassal, D. S. (2014). Catching broken hearts: pre-clinical detection of doxorubicin and trastuzumab mediated cardiac dysfunction in the breast cancer setting. *Can J Physiol Pharmacol, 92*(7), 546-550. doi:10.1139/cjpp-2013-0470

Sag, C. M., Kohler, A. C., Anderson, M. E., Backs, J., & Maier, L. S. (2011). CaMKII-dependent SR Ca leak contributes to doxorubicin-induced impaired Ca handling in isolated cardiac myocytes. *J Mol Cell Cardiol, 51*(5), 749-759. doi:10.1016/j.yjmcc.2011.07.016

Santoro, C., Arpino, G., Esposito, R., Lembo, M., Paciolla, I., Cardalesi, C., . . . Galderisi, M. (2017). 2D and 3D strain for detection of subclinical anthracycline cardiotoxicity in breast cancer patients: a balance with feasibility. *Eur Heart J Cardiovasc Imaging, 18*(8), 930-936. doi:10.1093/ehjci/jex033

Sathish, V., Xu, A., Karmazyn, M., Sims, S. M., & Narayanan, N. (2006). Mechanistic basis of differences in Ca2+ -handling properties of sarcoplasmic reticulum in right and left ventricles of normal rat myocardium. *Am J Physiol Heart Circ Physiol, 291*(1), H88-96. doi:10.1152/ajpheart.01372.2005

Sawaya, H., Sebag, I. A., Plana, J. C., Januzzi, J. L., Ky, B., Tan, T. C., . . . Scherrer-Crosbie, M. (2012). Assessment of echocardiography and biomarkers for the extended prediction of cardiotoxicity in patients treated with anthracyclines, taxanes, and trastuzumab. *Circ Cardiovasc Imaging, 5*(5), 596-603. doi:10.1161/CIRCIMAGING.112.973321

Sawyer, D. B., Zuppinger, C., Miller, T. A., Eppenberger, H. M., & Suter, T. M. (2002). Modulation of anthracycline-induced myofibrillar disarray in rat ventricular myocytes by neuregulin-1beta and anti-erbB2: potential mechanism for trastuzumab-induced cardiotoxicity. *Circulation, 105*(13), 1551-1554. doi:10.1161/01.cir.0000013839.41224.1c

Schneider, C., Wallner, M., Kolesnik, E., Herbst, V., Machler, H., Pichler, M., . . . Rainer, P. P. (2018). The Anti-Cancer Multikinase Inhibitor Sorafenib Impairs Cardiac Contractility by Reducing Phospholamban Phosphorylation and Sarcoplasmic Calcium Transients. *Sci Rep, 8*(1), 5295. doi:10.1038/s41598-018-23630-w

Shah, S. J., Aistrup, G. L., Gupta, D. K., O'Toole, M. J., Nahhas, A. F., Schuster, D., . . . Wasserstrom, J. A. (2014). Ultrastructural and cellular basis for the development of abnormal myocardial mechanics during the transition from hypertension to heart failure. *306*(1), H88-100. doi:10.1152/ajpheart.00642.2013

Song, L. S., Sobie, E. A., McCulle, S., Lederer, W. J., Balke, C. W., & Cheng, H. (2006). Orphaned ryanodine receptors in the failing heart. *Proc Natl Acad Sci U S A, 103*(11), 4305-4310. doi:10.1073/pnas.0509324103

Steinberg, J. S., Cohen, A. J., Wasserman, A. G., Cohen, P., & Ross, A. M. (1987). Acute arrhythmogenicity of doxorubicin administration. *Cancer, 60*(6), 1213-1218. doi:10.1002/1097-0142(19870915)60:6<1213::aid-cncr2820600609>3.0.co;2-v

Thavendiranathan, P., Grant, A. D., Negishi, T., Plana, J. C., Popovic, Z. B., & Marwick, T. H. (2013). Reproducibility of echocardiographic techniques for sequential assessment of left ventricular ejection fraction and volumes: application to patients undergoing cancer chemotherapy. *J Am Coll Cardiol, 61*(1), 77-84. doi:10.1016/j.jacc.2012.09.035

Tocchetti, C. G., Ragone, G., Coppola, C., Rea, D., Piscopo, G., Scala, S., . . . Maurea, N. (2012). Detection, monitoring, and management of trastuzumab-induced left ventricular dysfunction: an actual challenge. *Eur J Heart Fail, 14*(2), 130-137. doi:10.1093/eurjhf/hfr165

Wagner, E., Lauterbach, M. A., Kohl, T., Westphal, V., Williams, G. S., Steinbrecher, J. H., . . . Lehnart, S. E. (2012). Stimulated emission depletion live-cell super-resolution imaging shows proliferative remodeling of T-tubule membrane structures after myocardial infarction. *Circ Res, 111*(4), 402-414. doi:10.1161/CIRCRESAHA.112.274530

Wei, S., Guo, A., Chen, B., Kutschke, W., Xie, Y. P., Zimmerman, K., . . . Song, L. S. (2010). T-tubule remodeling during transition from hypertrophy to heart failure. *Circ Res, 107*(4), 520-531. doi:10.1161/CIRCRESAHA.109.212324

# Part 8

# Published Papers

1. Torre E, Arici M, **Lodrini AM**, Ferrandi M, Barassi P, Hsu SC, Chang GJ, Boz E, Sala E, Vagni S, Altomare C, Mostacciuolo G, Bussadori C, Ferrari P, Bianchi G, Rocchetti M. "SERCA2a stimulation by istaroxime improves intracellular $Ca^{2+}$ handling and diastolic dysfunction in a model of diabetic cardiomyopathy". Under revision at *Cardiovasc Res*, 2020-0042.

2. **Lodrini AM**, Barile L, Rocchetti M, Altomare C. "Human Induced Pluripotent Stem Cells Derived from a Cardiac Somatic Source: Insights for an In-Vitro Cardiomyocyte Platform". *Int J Mol Sci*. 2020 Jan 13;21(2):507. doi: 10.3390/ijms21020507.

3. Benzoni P, Campostrini G, Landi S, Bertini V, Marchina E, Iascone M, Ahlberg G, Olesen MS, Crescini E, Mora C, Bisleri G, Muneretto C, Ronca R, Presta M, Poliani PL, Piovani G, Verardi R, Di Pasquale E, Consiglio A, Raya A, Torre E, **Lodrini AM**, Milanesi R, Rocchetti M, Baruscotti M, DiFrancesco D, Memo M, Barbuti A, Dell'Era P. "Human iPSC modelling of a familial form of atrial fibrillation reveals a gain of function of $I_f$ and $I_{CaL}$ in patient-derived cardiomyocytes". *Cardiovasc Res*. 2020 May 1;116(6):1147-1160. doi: 10.1093/cvr/cvz217.

# SERCA2a stimulation by istaroxime improves intracellular $Ca^{2+}$ handling and diastolic dysfunction in a model of diabetic cardiomyopathy

Eleonora Torre[1], Martina Arici[1], Alessandra Maria Lodrini[1], Mara Ferrandi[2], Paolo Barassi[2], Shih-Che Hsu[3], Gwo-Jyh Chang[4], Elisabetta Boz[5], Emanuela Sala[1], Sara Vagni[1], Claudia Altomare[6], Gaspare Mostacciuolo[1], Claudio Bussadori[5], Patrizia Ferrari[2], Giuseppe Bianchi[2], Marcella Rocchetti[1].

[1] Department of Biotechnology and Biosciences, Università degli Studi di Milano-Bicocca, Milan, Italy. [2] Windtree Therapeutics Inc., Warrington, Pennsylvania, USA. [3] CVie Therapeutics Limited, Taipei, Taiwan. [4] Chang Gung University, Tao-Yuan, Taiwan. [5] Clinica Veterinaria Gran Sasso, Milano, Italy. [6] Fondazione Cardiocentro Ticino, Lugano, Switzerland.

**Short title:** SERCA2a stimulation by istaroxime in STZ-treated rats

**Category:** Original article

**Address for correspondence:**

Marcella Rocchetti, PhD
University of Milano Bicocca
Dept. of Biotechnologies and Biosciences
P.za della Scienza, 2
20126 Milano, Italy
+39 0264483313
marcella.rocchetti@unimib.it

## Abstract

*Aims*

Diabetic cardiomyopathy is a multifactorial disease characterized by an early onset of diastolic dysfunction (DD) that precedes the development of systolic impairment. Mechanisms that can restore cardiac relaxation improving intracellular $Ca^{2+}$ dynamics represent a promising therapeutic approach for cardiovascular diseases associated to DD. Istaroxime has the double property to accelerate $Ca^{2+}$ uptake into sarcoplasmic reticulum (SR) through the SR $Ca^{2+}$ pump (SERCA2a) stimulation and to inhibit $Na^+/K^+$ ATPase (NKA). The project aims to characterize istaroxime effects at a concentration (100 nM) marginally affecting NKA, in order to highlight its effects dependent on the stimulation of SERCA2a in a model of mild diabetes.

*Methods and Results*

Streptozotocin (STZ) treated diabetic rats were studied at 9 weeks after STZ injection in comparison to controls (CTR). Istaroxime effects were evaluated *in vivo* and in left ventricular (LV) preparations. STZ animals showed 1) marked DD not associated to cardiac fibrosis, 2) LV mass reduction associated to reduced LV cell dimension and T-tubules loss, 3) reduced LV SERCA2 protein level and activity and 4) slower SR $Ca^{2+}$ uptake rate, 5) LV action potential (AP) prolongation and increased short-term variability (STV) of AP duration, 6) increased diastolic $Ca^{2+}$, 7) unaltered SR $Ca^{2+}$ content and stability in intact cells. Acute istaroxime infusion (0.11 mg/kg/min for 15 min) reduced DD in STZ rats. Accordingly, in STZ myocytes istaroxime (100 nM) stimulated SERCA2a activity and blunted STZ-induced abnormalities in LV $Ca^{2+}$ dynamics. In CTR myocytes, istaroxime increased diastolic $Ca^{2+}$ level due to NKA blockade albeit minimal, while its effects on SERCA2a were almost absent.

*Conclusions*

SERCA2a stimulation by istaroxime improved STZ-induced DD and intracellular $Ca^{2+}$ handling anomalies. Thus, SERCA2a stimulation can be considered a promising therapeutic approach for DD treatment.

**Translational perspective**

Deficient sarcoplasmic reticulum (SR) $Ca^{2+}$ uptake has been identified in cardiomyocytes from failing human hearts with impaired diastolic relaxation (e.g. diabetic hearts) and has been associated with a decreased SERCA2a expression and activity and/or with a higher SERCA2a inhibition by phospholamban. Thus, SERCA2a may represent a pharmacological target for interventions aimed at improving cytosolic $Ca^{2+}$ compartmentalization into the SR to limit diastolic dysfunction pathologies. In this contest, istaroxime is the first-in-class luso-inotropic agent targeting SERCA2a that has already demonstrated its efficacy in clinical trials and may be useful to clarify the relevance of SERCA2a stimulation in controlling cytosolic $Ca^{2+}$ level.

# 1. Introduction

Diabetes affects globally more than 300 million people and type 1 diabetes (T1D) accounts for up to 10% of cases[1]. Heart failure (HF) is the predominant cardiovascular complication of diabetes and represents the leading cause of morbidity and mortality. Diabetic cardiomyopathy (DCM) is a complex and multifactorial disease characterized by an early onset of diastolic dysfunction (DD), which precedes the development of systolic impairment[2–5].

The molecular and pathophysiological mechanisms underlying diabetes include abnormalities in the regulation of $Ca^{2+}$ homeostasis in cardiomyocytes and the consequent alteration of ventricular excitation-contraction coupling (ECC). In the diabetic heart, a dysregulation of $Ca^{2+}$ cycling includes a reduction of SERCA2 activity, which may be accompanied by a decreased SERCA2 protein expression (mostly SERCA2a isoform)[6,7]. A key role in the regulation of SERCA2a activity is played by phospholamban (PLN), a protein that behaves like its endogenous inhibitor when it is in its non-phosphorylated state[8]. In most diabetic models, PLN expression level appears increased while its phosphorylation state is reduced, thus contributing to the inhibition of SERCA2a function[6–8]. This defect generates an impairment of sarcoplasmic reticulum (SR) $Ca^{2+}$ refilling that results in slow diastolic relaxation. An abnormal $Ca^{2+}$ distribution may facilitate cardiac arrhythmias appearance and myocyte apoptosis[9,10].

Therefore, SERCA2a may represent a molecular target for a pharmacological intervention aimed at increasing the mechanical function and the energetic efficiency of the diabetic heart characterized by a defective SR $Ca^{2+}$ loading. To date, the current medications have shown a limited efficacy in preventing the progression to HF in patients with DCM and diabetic complications[10–12]. New hypotheses have been recently proposed in HF aimed at improving cardiac contractility[13–19], however, all these attempts are still far from being considered as beneficial treatment options available for clinicians and the treatment of HF and DCM remains an open field of research. The development of a small-molecule as SERCA2a activator represents a promising strategy for HF and DCM treatment. Along this line, istaroxime is the first-

in-class original luso-inotropic agent, shown to be highly effective and safe in patients[20]. Istaroxime is endowed of a double mechanism of action that consists in the ability to inhibit $Na^+$-$K^+$ ATPase (NKA) and enhance SERCA2a ATPase activity[21], this last obtained through the relief of PLN inhibitory effect on SERCA2a[22], without inducing spontaneous $Ca^{2+}$ release from SR[21,23]. In healthy and failing animal models and in patients with acute HF syndrome, istaroxime improves systolic and diastolic performance[20,24–28] and efficiency of cardiac contraction with a low oxygen consumption[26], minimizing the risk of arrhythmias or ischemia, without affecting other cardiovascular functions[29–32].

In the present study, we characterized the STZ model on different levels of biological organization, such as: (i) *in vivo*, to evaluate STZ-induced DD, (ii) in isolated left ventricular (LV) cardiomyocytes, to evaluate structure, intracellular $Ca^{2+}$ dynamics, electrical activity and (iii) in LV and renal preparations (cell-free systems) to assess SERCA2a and NKA activity. We tested whether SERCA2a stimulation by a small molecule can improve the altered intracellular $Ca^{2+}$ handling responsible for the DD in STZ-treated rats. To this end, istaroxime was tested (i) *in vivo* after iv infusion in STZ rats, (ii) in LV myocytes at a concentration marginally affecting NKA to highlight its effects mostly dependent on SERCA2a stimulation and (iii) in the cell-free systems.

## 2. Materials and Methods

All experiments involving animals (methods detailed in the on line Supplementary Material) conformed to the guidelines for Animal Care endorsed by the University of Milano-Bicocca and to the Directive 2010/63/EU of the European Parliament on the protection of animals used for scientific purposes. Male Sprague Dawley rats (150-175 gr) were used to generate a STZ-induced T1D cardiomyopathy model according to the Health Minister of Italy permission.

Methods details are described in the Online Supplementary Material.

### 2.1 STZ rat model

T1D was induced through a single STZ (Sigma-Aldrich, 50 mg/kg) injection into a rat-tail vein; littermate control (CTR) rats received only citrate buffer (vehicle). Overnight fasting or non-fasting glycaemia was measured after 1 week by Contour XT system (Bayer). Animals were considered diabetic with fasting glycaemia values > 290 mg/dL.

### 2.2 Echocardiography

Eight weeks after vehicle/STZ injection, rats were submitted to a transthoracic echocardiographic and Tissue Doppler evaluation, performed under urethane anesthesia (1.25 g/kg i.p.) (M9 Mindray Echographer equipped with a 10 MHz probe, P10-4s Transducer, Mindray, China). Systolic and diastolic parameters were measured in CTR and diabetic (STZ) animals by a blinded investigator. Details are shown in the on line Supplementary Material.

A group of STZ rats was subjected to istaroxime infusion at 0.11 mg/kg/min for 15 min accordingly to a previous study[25]. Drug was infused through a polyethylene 50 cannula inserted into a jugular vein under urethane anesthesia. Echocardiographic and Tissue Doppler parameters were measured under basal condition (before) and following 15 min istaroxime administration.

### 2.3 Morphometric parameters

Rats were euthanized by cervical dislocation under anesthesia with ketamine-xylazine (130-7.5 mg/kg i.p) 9 weeks after STZ injection. Body weight (BW), heart weight (HW), LV weight (LVW) and kidney weight (KW) were measured. Body weight gain (BW gain) was obtained by subtracting the initial BW from the BW at sacrifice. HW and KW were normalized to tibia length (TL) to assess respectively cardiac and kidney indexes in CTR and STZ groups.

### 2.4 Myocyte dimensions and T-tubules (TT) analysis

Sarcolemmal membranes were stained by incubating isolated LV myocytes with 20 μmol/L di-3-ANEPPDHQ[33] (Life Technologies, Carlsbad, United States) to measure cell dimensions and T-tubules (TT) organization/periodicity by a method based on Fast Fourier Transform[34].

### 2.5 SERCA2a and $Na^+/K^+$ pump (NKA) activity measurement

SERCA2a activity was measured *in vitro* as $^{32}$P-ATP hydrolysis at different $Ca^{2+}$ concentrations (100-3000 nM) in heart homogenates as previously described[25]. $Ca^{2+}$ concentration-response curves were fitted by using a logistic function to estimate SERCA2a $Ca^{2+}$ affinity ($K_d$ $Ca^{2+}$) and $V_{max}$.

NKA activity was assayed *in vitro* by measuring the release of $^{32}$P-ATP, as previously described[35]. The concentration of compound causing 50% inhibition of the NKA activity ($IC_{50}$) was calculated by using a logistic function.

### 2.6 Intracellular $Na^+$ and $Ca^{2+}$ dynamics

Intracellular $Na^+$ ($Na^+_i$) and $Ca^{2+}$ ($Ca^{2+}_i$) dynamics were evaluated by incubating LV myocytes with the membrane-permeant form of the dyes Ion NaTRIUM Green-2 AM (5 µM) and Fluo4-AM (10 µmol/L) respectively.

$Na^+_i$ dynamics were monitored in I-clamp under physiological condition (Tyrode's solution) and in V-clamp under modified Tyrode's solution suitable to measure NKA current ($I_{NKA}$) at the same time.

$Ca^{2+}_i$ dynamics were analysed in field stimulated (2 Hz) and in patch-clamped myocytes. In field stimulated cells, SR $Ca^{2+}$ loading and stability were evaluated through a post-rest potentiation protocol (Fig S1). $Ca_T$ parameters and SR $Ca^{2+}$ content ($Ca_{SR}$) were estimated at steady state (2Hz) and following caffeine (10 mM) superfusion respectively. Moreover, incidence of spontaneous $Ca^{2+}$ release (SCR) events was evaluated in each group during resting pauses and diastole.

To better highlight changes in $Ca^{2+}$ handling not affected by modifications on electrical activity, $Ca^{2+}_i$ dynamic was also evaluated in voltage-clamped cells. Firstly, action potential (AP) clamp experiments were performed to verify whether $Ca_T$ amplitude and $Ca_{SR}$ were dependent on AP durations (APDs). To this end, two AP waveforms were used to dynamic voltage clamp STZ myocytes: a "short AP" and a "long AP" representative of the CTR and STZ group in terms of AP characteristics respectively. $Ca^{2+}_i$ dynamics were then evaluated in voltage-clamped cells by standard V-clamp protocols.

Finally, to estimate SR uptake function in the absence of NCX and NKA function, SR reloading protocol was applied in V-clamped cells by removing $Na^+$ from both sides of the sarcolemma (Fig. S2)[21]. Kinetics of SR $Ca^{2+}$ reloading was evaluated; in particular, we considered the time constant of $Ca_T$ decay ($\tau_{decay}$) reflecting in this setting $Ca^{2+}$ transport rate across the SR membrane, a functional index of SERCA2a activity.

### 2.7 $Ca^{2+}$ sparks rate and characteristics

Spontaneous unitary $Ca^{2+}$ release events ($Ca^{2+}$ sparks) were recorded at room temperature in Fluo 4-AM (10 μM) loaded myocytes at resting condition. Tyrode's bath solution contained 1 mM $CaCl_2$.

### 2.8 Action potential rate-dependency and variability

Action potentials (APs) were recorded in I-clamp condition by pacing myocytes at 1, 2, 4 and 7 Hz during Tyrode superfusion. Rate-dependency of AP duration (APD) at 50% ($APD_{50}$) and 90% ($APD_{90}$) of repolarization and diastolic potential ($E_{diast}$) were evaluated at steady state. Moreover, at each rate, a minimum of 30 APs were recorded at steady state to evaluate the short-term variability (STV) of $APD_{90}$, a well-known proarrhythmic index[36], according to Eq. 1:

$$STV=\sum(|APD_{(n+1)}-APD_n|)/[n_{beats}*\sqrt{2}] \qquad \text{(Eq. 1)}$$

Incidence of delayed afterdepolarizations (DADs) was evaluated.

### 2.9 Statistical analysis

Normal distribution of the results was checked by using the Shapiro-Wilk test. Paired or unpaired Student's *t*-test, one-way or two-way ANOVA were applied as appropriate test for significance between means. Post-hoc comparison between individual means was performed by Tukey or Sidak multiple comparison tests. $Chi^2$-test was used for comparison of categorical variables. Results are expressed as mean ± SEM. A value of $P<0.05$ was considered significant.

Except when specified, in vitro istaroxime effects were analyzed by incubating cells with the drug for at least 30 min, thus group comparison analysis was performed. Number of animals (N) and cells (n) are shown in each figure legend.

# 3. Results

## 3.1 Morphometric parameters

Diabetic rats were obtained by a single injection of STZ (50 mg/kg) into a tail vein and were compared to CTR rats receiving only vehicle. Fasting and non-fasting glycaemia increased significantly one week after STZ administration (Table 1).

At the time of STZ administration, body weight (BW) was comparable among CTR and STZ groups (data not shown), while 9 weeks after STZ infusion, BW gain was largely different among groups because of a BW significantly lower in STZ than in CTR (Table 1). Tibia length (TL) was also measured as a rat growth index and resulted slightly reduced in STZ compared to CTR (Table 1). Heart weight (HW) was significantly lower in STZ than in CTR (Table 1), even when HW was normalized to TL (Table 1). Analogously, left ventricular (LV) weight (LVW), normalized to HW, was significantly reduced in STZ in comparison to CTR (Table 1).

Likewise, LV cell length, volume, cross-sectional area (CSA) and cell membrane capacitance ($C_m$), a further index of cell dimension, were significantly reduced in STZ in comparison to CTR (Table 1).

Conversely, kidney weight (KW) did not differ between the two groups, but KW/TL ratio resulted modestly increased in STZ rats versus CTR, suggesting STZ-induced kidney hypertrophy (Table 1).

It was further investigated whether the decrease of cardiac weight/mass observed in STZ rats might be associated with cardiac fibrosis deposition. To this end, a western blot analysis for collagen type 1 and matrix metallopeptidase 9 (MMP-9) protein expression level was conducted on LV homogenates from CTR and STZ rats (Fig S3). The results indicate that any significant difference of collagen type 1 and MMP-9 protein content could be detected between the two rat groups.

### 3.2 STZ induces diastolic dysfunction (DD), reverted by acute istaroxime infusion

The echocardiographic parameters were measured in CTR and STZ rats 8 weeks after STZ injection (Table 2). Wall thickness for the interventricular septum (IVST) and posterior wall (PWT) both in diastole and systole did not differ between CTR and STZ rats (Table 2). Analogously, LV end-diastolic and systolic diameter (LVEDD, LVESD) remained unchanged (Table 2).

The calculated fractional shortening (FS) did not differ while the TDI contraction velocity (s') was reduced in STZ animals when compared to CTR, thus suggesting an overall systolic function only partially compromised in STZ rats at this stage (Table 2).

The transmitral Doppler parameters were altered in STZ rats indicating an impairment of diastolic function. In particular, in STZ rats, while early (E) peak diastolic velocity was unchanged, E wave deceleration time (DT) was prolonged, thus, the mitral deceleration index (DT/E) and the deceleration slope (E/DT) tended respectively to increase and decrease; late peak diastolic velocity (A) was significantly increased and thus, E/A ratio resulted significantly reduced (Table 2). Tissue Doppler examination showed in STZ rats a significant reduction of early diastolic myocardial velocity (e') and a significant increase of late diastolic myocardial velocity (a'), similarly to A wave. Thus, a significant reduction of e'/a' ratio and increase of the E/e' ratio was observed in STZ rats in comparison to CTR (Table 2).

The overall cardiac function indicated that stroke volume (SV), ejection fraction (EF) and cardiac output (CO) were not significantly affected in STZ rats although heart rate (HR) was reduced. Echocardiographic data mostly indicate that, at this time point, STZ induced a diabetic cardiomyopathy characterized by DD and mostly preserved systolic function. Furthermore, the diastolic impairment observed in STZ rats at this early stage was not associated with cardiac fibrosis (Fig S3).

To analyze early *in vivo* effects of istaroxime in reducing STZ-induced DD, istaroxime was infused in STZ rats at 0.11 mg/kg/min[25] and echocardiographic

parameters were collected 15 min later. The results (Table 2) showed that the compound was able to revert the DD documented in STZ rats with a significant reduction of DT and DT/E and an increase of E/DT and e' (Table 2). No effect on CO, SV and HR was observed following istaroxime infusion at this early time point (Table 2). Moreover, to exclude changes due to time dependent effects of urethane, echocardiographic parameters were collected every 5 minutes in a set of animals not treated with the drug. Up to 20 minutes in urethane anesthesia, diastolic and systolic parameters remained constant (Fig S4). It should be noted that in a parallel study we estimated istaroxime plasma level in male rats after 1-hour infusion at 0.11 mg/kg/min, resulting 780 nM (N=3, unpublished data); this suggests that its concentration at 15 min infusion should be reasonably around 200 nM.

### 3.2 Istaroxime affinity for rat NKA

To identify the *in vitro* istaroxime concentration suitable to limit its effects dependent on NKA inhibition, $I_{NKA}$ was isolated in CTR rat LV myocytes and the concentration-response curve for istaroxime was evaluated as previously shown for guinea-pig[30] and mouse myocytes[23]. A saturating concentration of ouabain (1 mM) was used (Fig S5) to evaluate the $I_{NKA}$ inhibition by istaroxime as percentage of the ouabain-induced change. Moreover, a subgroup of cells was incubated with Ion NaTRIUM Green-2 to monitor $Na^+_i$ changes under istaroxime or ouabain superfusion. The estimated $IC_{50}$ for $I_{NKA}$ inhibition by istaroxime was 32 ± 4 μM (Fig 1A); a similar value was detected in cardiac (84 ± 20 μM) (inset Fig 1A) and renal preparations (55 ± 19 μM, Fig S6). Moreover, while NKA inhibition by 100 nM istaroxime was detectable by measuring $I_{NKA}$ in isolated myocytes (-6.9 ± 1.2%, $p<0.05$, N=14), istaroxime effects on NKA were not detectable up to 1 μM in cardiac and renal preparations.

In isolated rat ventricular myocytes $Na^+_i$ increased slightly under cumulative istaroxime concentrations (20 μM istaroxime +2.2 ± 0.7%, $p<0.05$, N=5), while it was evident under saturating ouabain concentration (+8.6 ± 1.4%, $p<0.05$, N=5) (Fig 1A).

Consistently with the aim of the study, istaroxime effects on STZ-induced changes were evaluated by testing the compound at concentrations marginally affecting NKA (100 or 500 nM).

### 3.3 STZ induces SERCA2a downregulation and T-tubules loss

LV homogenates from CTR and STZ rats were used to measure SERCA2a and PLN protein level by Western blot analysis. Representative Western blots from CTR and STZ samples and the relative densitometric analysis indicized for actin content are shown in Fig 1B. SERCA2a protein expression resulted significantly reduced in STZ versus CTR samples (-45%, $p<0.001$); while monomeric (m) PLN levels were unchanged, pentameric (p) PLN levels were slightly increased (+22%, $p<0.05$). As a consequence, both mPLN/SERCA2a and pPLN/SERCA2a ratio were significantly increased (+89% and +128% respectively, $p<0.001$), suggesting higher SERCA2a inhibitory activity by PLN in STZ group. Moreover, in STZ samples, while the fraction of phosphorylated $Thr^{17}$-mPLN ($pThr^{17}$-mPLN/mPLN) resulted unchanged, the fraction of phosphorylated $Ser^{16}$-mPLN ($pSer^{16}$-mPLN/mPLN) was reduced (-42%, $p<0.05$), thus highlighting reduced PKA-dependent SERCA2a modulation in STZ. Most of these measurements were also performed in isolated LV myocytes showing comparable results as those shown in LV homogenates (Fig S7).

SERCA2a activity was measured in cardiac SR homogenates from CTR and STZ rats as $^{32}$P-ATP hydrolysis assay (Fig 1C). In comparison to CTR preparations, SERCA2a $V_{max}$ was significantly decreased (-25%, $p<0.05$) in STZ, while the $K_d$ $Ca^{2+}$ did not differ (Fig S8). Overall, SERCA2a protein level and activity were reduced in STZ preparations, a result in line with echocardiographic parameters showing STZ-induced DD.

Disarray of the T-tubular (TT) system has been described in several failure models and was generally characterized by loss of the transverse component. A sharp pattern of transverse striations was observed in CTR myocytes (Fig 1D); accordingly, in these myocytes, pixel variance was largely represented by the periodic component, whose period was consistent with transverse TT arrangement. LV disarray of the

transverse TT was visually obvious in STZ myocytes, a result confirmed by the quantitative analysis of the power of the periodic component (Fig 1D).

### 3.4 Istaroxime effects on STZ-induced changes in $Ca^{2+}$ dynamics

Istaroxime (500 nM) stimulated SERCA2a activity in cardiac SR homogenates from STZ diabetic rats by increasing SERCA2a $V_{max}$ (+25%, $p<0.01$) to a value similar to CTR rats (Fig 1C) without affecting $Ca^{2+}$ affinity (575 ± 98 nM vs 450 ± 51 nM, NS, Fig S8). Conversely, in CTR rat preparations, $V_{max}$ (Fig 1C) and $K_d$ (Fig S8) parameters were unchanged in the presence of istaroxime.

Istaroxime effects on STZ-induced DD were then evaluated at the cellular level by measuring the SR ability to accumulate resting $Ca^{2+}$ through a post-rest potentiation protocol in field stimulated myocytes (Fig 2). As shown in Fig 2A, following increasing resting pauses, the amplitude of the first $Ca_T$ increased progressively in CTR myocytes; accordingly to STZ-induced SERCA2a downregulation, post-rest potentiation was reduced in STZ myocytes at all resting intervals (Fig 2A). Istaroxime at 100 nM failed to affect post-rest potentiation in CTR myocytes, while it improved the ability of SR to accumulate $Ca^{2+}$ especially at long resting pauses in STZ myocytes, in agreement with its stimulatory action on SERCA2a.

At steady-state, STZ increased $Ca_D$ and CaT decay time ($t_{0.5}$), while leaving unchanged $Ca_T$ amplitude and $Ca_{SR}$ (Fig 2B-C). Istaroxime (100 nM) significantly increased $Ca_D$ in CTR myocytes, while blunted STZ-induced $Ca_D$ enhancement in STZ myocytes. This was furtherly appreciable monitoring the time course of $Ca_D$ enhancement during the SR reloading process following caffeine superfusion (Fig 2D). On the other hand, $Ca_T$ amplitude, decay kinetics and $Ca_{SR}$ were not significantly affected by istaroxime in both CTR and STZ myocytes. Overall, STZ-induced SERCA2a down-regulation resulted in cytosolic $Ca_D$ enhancement probably due to a reduced ability of SR to compartmentalize $Ca^{2+}$ into the SR; however, SR $Ca^{2+}$ content was preserved. In parallel, the effect of istaroxime on $Ca_D$ in CTR myocytes was likely attributable to a partial NKA blockade, that was blunted in STZ myocytes by the simultaneous action on SERCA2a.

SCR events were evaluated in CTR and STZ cells. SCR events were absent in CTR while a not significant number of events occurred in STZ myocytes; istaroxime not affected their incidence in both CTR and STZ myocytes.

### 3.5 STZ induces changes in electrical activity affecting intracellular $Ca^{2+}$ dynamics. Analysis of istaroxime effects.

Potential changes in electrical activity in STZ myocytes might mask expected changes directly resulting from SERCA2a down-regulation (e.g. changes in $Ca_{SR}$).
Thus, to verify STZ-induced changes in electrical activity, AP rate dependency was evaluated in STZ myocytes in comparison to CTR. STZ induced a significant APD prolongation at all stimulation rates (Fig 3A), accordingly to voltage-dependent $K^+$ channels down-regulation[37,38]. Moreover, rate dependency of $E_{diast}$ observed in CTR myocytes was absent in STZ myocytes, probably due to STZ-induced NKA down-regulation[39]. In both CTR and STZ myocytes, istaroxime at 100 nM not affected APD, while slightly depolarized $E_{diast}$ especially in STZ myocytes (Fig 3A).
All these measurements were done following istaroxime incubation for at least 30 min to allow drug accumulation inside the cell and stimulate SERCA2a. On the other hand, to better understand drug effects on diastolic potential, likely attributable to NKA inhibition, a group of CTR myocytes were loaded with Ion NaTRIUM Green-2 and membrane potential plus $Na^+_i$ were simultaneously recorded at 7Hz (to highlight the contribution of NKA to diastolic potential) under basal condition and following istaroxime (100 nM) superfusion; ouabaine at saturating concentration was also tested as reference compound inhibiting NKA (Fig 3B). Istaroxime at 100 nM slightly depolarized $E_{diast}$ ($\Delta$ -0.58 ± 0.1 mV, n=8, $p<0.05$) in comparison to ouabaine superfusion ($\Delta$ -13.5 ± 1.2 mV, n=13, $p<0.05$); in parallel, a significant $Na^+_i$ enhancement was detectable during ouabaine only (+3 ± 0.5% n=13, $p<0.05$).
Overall, as expected, STZ treatment largely affects ion channels and pumps resulting in AP shape changes; istaroxime at 100 nM substantially leaved unchanged STZ-induced AP changes and further slightly depolarized $E_{diast}$, resulting from a minimal (about -7%) NKA inhibition.

The short-term variability (STV) of APD was evaluated in all groups, as a well-known pro-arrhythmic index. In comparison to CTR, STZ increased STV of APD at all pacing rates (Fig 3C); in both CTR and STZ myocytes STV was not significantly affected by istaroxime, even though tended to be reduced in STZ myocytes. As expected, STV was directly correlated to $APD_{90}$ in all groups; the slope of this correlation tended to increase in STZ group without reaching statistical significance (0.016 vs 0.012, ns) and it was not significantly affected by istaroxime in both groups. These results suggest the absence of major mechanisms other than APD prolongation significantly affecting STV in all groups[37].

Likewise, to SCR incidence, delayed afterdepolarizations (DADs) were completely absent in CTR myocytes and were present only in few cells in STZ groups (data not shown).

Given the STZ-induced APD prolongation, we verified if AP duration could effectively affect intracellular $Ca^{2+}$ handling in STZ myocytes. To this end, AP-clamp measurements were performed (Fig 4A). $Ca_T$ were evocated in the same cell by using as voltage commands waveforms named "short" AP (CTR AP) and "long" AP (STZ AP) (see Methods). In comparison to the short AP waveform, the long AP one caused a huge increase in $Ca_T$ amplitude (+66 ± 9.4%, $p<0.05$) and $Ca_{SR}$ (+36 ± 9.8%, $p<0.05$), confirming the hypothesis that the prolonged AP in STZ myocytes affected intracellular $Ca^{2+}$ handling.

### 3.6 STZ-induced $Ca^{2+}$ handling changes under control of membrane potential are reverted by istaroxime SERCA2a stimulation

To clarify direct effects of SERCA2a down-regulation and its stimulation by istaroxime on intracellular $Ca^{2+}$ handling, analysis on voltage clamped myocytes was performed (Fig 4B) through a standard V-clamp protocol. Cells were superfused with Tyrode's solution to allow evaluation of both SR and NCX function. As shown in Fig 4B, STZ induced $Ca_T$ and $Ca_{SR}$ amplitude reduction, leaving unchanged fractional release. Influx through L-type $Ca^{2+}$ channels ($Ca_L$ influx) was not affected in STZ group, leading to an excitation-release (ER) gain that tended to be reduced in comparison to CTR. Moreover, in STZ myocytes $I_{CaL}$ peak density at 0 mV was

significantly reduced, but the current decay tended to be slower; in particular, the fast decay time constant ($\tau_{fast}$), reflecting $Ca^{2+}$-dependent inactivation, tended to increase in comparison to CTR myocytes (Fig S9). Thus, all $I_{CaL}$ changes justify a global unaltered $Ca^{2+}$ influx in STZ myocytes under these settings. Finally, the slope of the linear correlation between NCX current ($I_{NCX}$) and the $Ca_{SR}$ ($\Delta I_{NCX}/\Delta Ca_{SR}$) was similar in CTR and STZ myocytes (Fig S10), suggesting that SERCA2a down-regulation was not associated to changes in NCX activity in STZ myocytes. Treatment of STZ myocytes with istaroxime blunted differences between CTR and STZ.

Lastly, to estimate SR $Ca^{2+}$ uptake function in the absence of NCX and NKA function, SR reloading protocol was applied in V-clamped cells by removing $Na^+$ from both sides of the sarcolemma as previously described[21]. As shown in Fig 4C, after SR depletion by caffeine superfusion, in comparison to CTR myocytes, the SR reloading process was slower in STZ myocytes, clearly confirming the SERCA2a down-regulation. In particular, in STZ myocytes, the rate of $Ca_T$ increment was reduced and this was associated with a slower enhancement of the ER gain. Moreover, the decay time constant, mostly representing SR $Ca^{2+}$ uptake function, increased at each pulse, accordingly to a reduced SERCA2a function in STZ myocytes. Stimulation of SERCA2a by istaroxime caused faster SR reloading and all parameters were restored to CTR condition.

### 3.7 SERCA2a activity affects $Ca^{2+}$ sparks characteristics

As shown before, both DADs and SCR events were detected only in few STZ myocytes, suggesting that SR stability is mostly preserved in this DCM model. To further analyze this point, $Ca^{2+}$ sparks rate and characteristics were evaluated in all groups (Fig 5). Compared to CTR, STZ myocytes showed $Ca^{2+}$ sparks with reduced amplitude, width, duration and spark mass (Fig 5B), in agreement with a reduced SR $Ca^{2+}$ content at resting. Istaroxime, by stimulating SERCA2a, partially restored $Ca^{2+}$ sparks characteristics in STZ myocytes. In particular, istaroxime-induced SERCA2a stimulation emerged also by the analysis of $Ca^{2+}$ sparks decay that significantly

became faster in the presence of the compound. Sparks rate was not significantly affected by STZ and istaroxime.

# 4. Discussion

Aim of the present study was to assess the effect of SERCA2a stimulation mediated by istaroxime in improving intracellular $Ca^{2+}$ dynamics in a diabetic rat model characterized by impaired diastolic function.

Several therapeutic approaches that increase SERCA2a function have been recently investigated[18,40–43]. However, despite of the intense research on discovering small molecules or gene therapy aimed at selectively activating SERCA2a, no promising clinical outcomes have been reached so far.

Istaroxime is the first-in-class original luso-inotropic agent targeting SERCA2a, in addition to NKA inhibition, that has shown efficacy and safety in clinical trials on patients with acute HF syndrome[20,28]. In the past, *in vitro* istaroxime effects were largely characterized at concentrations showing dual mechanism of action[21,23,27,29,30]. In the present study, lusitropic SERCA2a-dependent istaroxime effects were evaluated by testing istaroxime both *in vitro* and *in vivo* at concentrations marginally affecting NKA. Estimated drug plasma level at 15 min infusion and drug concentrations adopted for *in vitro* assays were largely comparable.

To our knowledge, no other small molecules active on SERCA2a at submicromolar concentration are available.

### 4.1 STZ-induced DCM. DD is associated to down-regulated SERCA2a expression and activity and is improved by istaroxime infusion

STZ rats showed a clear DD highlighted by changes in mitral inflow, in line with published results, reporting that DCM often manifests first as DD (Table 2). Our echo measurements evidenced marked alterations on DD indexes in STZ rats. In particular, we showed a significant transmitral Doppler flow enhancement of E wave deceleration time (DT) and reduced E/A ratio in STZ rats. Analogously, TDI parameters, relatively unaffected by load, indicated a significant reduction of early diastolic myocardial velocity (e') and e'/a' with an increase of E/e' ratio in STZ rats.

Systolic function appeared almost unaffected in STZ as compared to CTR rats, as indicated by FS and CO values (Table 2). Moreover, we observed a marked bradycardia (Table 2), consistent with the impaired autonomic function and down-regulation of the expression of the pacemaker channel HCN4[44].

Consistently with STZ-induced DD, in heart preparations and in cardiomyocytes from STZ rats, we observed a clear reduction of SERCA2 protein expression level, an increase of mPLN/SERCA2 ratio and a reduction of $Ser^{16}$ phosphorylated mPLN (Fig 1 and Fig S7). Conversely, CaMKII-dependent $Thr^{17}$ phosphorylation of mPLN was similar between STZ and CTR rats (Fig 1). These biochemical alterations were associated with the reduction of SERCA2a ATPase activity observed in heart preparations from STZ compared to CTR rats (Fig 1) and indicate that these may translate into the impairment of diastolic function seen by the echocardiographic examination.

DCM is reported to be associated with cardiac fibrosis which is responsible for increased LV stiffness and decreased ventricular wall compliance resulting in systolic and, in particular, DD[45]. However, in the present study, no change of collagen type 1 and MMP-9 protein expression has been observed in LV from CTR and STZ rats, indicating that 8 weeks after STZ injection may be a time not long enough to develop this alteration. Moreover, several indexes indicated the absence of a concrete LV hypertrophy in STZ rats, because the increase in HW/BW was strictly dependent on BW loss. Otherwise, we observed reduced HW/TL and LV/HW ratios, results confirmed at the cellular level with reduced cell membrane capacitance ($C_m$), CSA, cell volume and TT organization. These results are supported by a recent study showing reduced sinoatrial cell membrane capacitance in STZ-treated mice[44]. Loss of viable cardiomyocytes in STZ rats is also a possibility as previously shown[46].

Collectively, these results indicate that our model of STZ-induced DCM is characterized by impaired diastolic function associated with the down-regulation of the SERCA2a expression and activity. This model is therefore suitable for testing the cardiac effects of SERCA2a stimulation by istaroxime. Istaroxime infused at 0.11 mg/kg/min for 15 min in STZ rats reverted the DD, inducing a significant reduction of DT and DT/E and an increase of e' (Table 2). The favorable mechanistic profile of

istaroxime action is once again corroborated by our results in ameliorating DD in a DCM model.

### 4.2 STZ-induced changes in $Ca^{2+}$ dynamics and electrical activity. Istaroxime effects at a concentration marginally affecting NKA.

Consequences of STZ-induced SERCA2a downregulation were functionally analyzed in isolated LV myocytes. In particular, the post-potentiation protocol clearly highlighted the reduced ability of SR to accumulate $Ca^{2+}$ at resting in STZ myocytes in comparison to CTR ones. This resulted in $Ca_D$ enhancement when pacing cells at 2 Hz (Fig 2); in spite of this, $Ca_{SR}$ left unchanged, probably as a consequence of STZ-induced changes in electrical activity. Indeed, STZ induced marked APD prolongation at all stimulation rates (Fig 3A), according to voltage dependent $K^+$ channels down-regulation[37]. Moreover, the lack of $E_{diast}$ rate dependent hyperpolarization in STZ myocytes is in agreement with STZ-induced NKA down-regulation[39].

AP-clamp experiments clearly demonstrated the relevance of AP waveform in controlling intracellular $Ca^{2+}$ dynamics (Fig 4A). Indeed, AP prolongation caused a sharp intracellular $Ca^{2+}$ loading. Thus, STZ induced changes in electrical activity might indirectly affect intracellular $Ca^{2+}$ dynamics. In agreement with this, following the control of membrane potential (Fig 4B), direct effects of STZ-induced SERCA2a downregulation were detected on $Ca^{2+}$ handling. In particular, by clamping myocytes at -40 mV, STZ induced $Ca_{SR}$ and $Ca_T$ amplitude reduction, effects that were unseen in intact field stimulated cells. Moreover, incubating myocytes in extracellular and intracellular $Na^+$ free solutions to remove NCX and NKA contribution (Fig 4C), SR $Ca^{2+}$ uptake reloading kinetic following caffeine-induced SR depletion was clearly depressed in STZ myocytes.

Istaroxime stimulated SERCA2a in cardiac preparations from STZ rats by re-establishing the STZ-induced reduction of its maximal activity ($V_{max}$) without affecting its affinity for $Ca^{2+}$ ($K_d$). Moreover, no effects on SERCA2a activity were detected in CTR heart preparation (Fig 1), indicating that the stimulatory action on SERCA2a is more remarkable when a pathological alteration (i.e. STZ-induced

SERCA2a downregulation) is present. Analogously, in dog cardiac SR vesicles, the stimulatory effect of istaroxime prevailed in the failing vs healthy dog[22]. However, in healthy guinea pig cardiac microsomes istaroxime stimulated SERCA2a by reducing the $K_d$[21]. The different effect of the compound on SERCA2a kinetic parameters in rat and dog ($V_{max}$ enhancement) versus guinea pig ($K_d$ reduction) may not exclude species-specific differences in SERCA2a-PLN functional complex formation along the heart preparation, affecting istaroxime interaction. Furthermore, these kinetic changes across species might depend on how the compound interferes with species-specific SERCA2a-PLN complex domains. Although Ferrandi et al.[22] has already shown that istaroxime stimulates SERCA2a activity through a direct interaction with SERCA2a/PLN complex, favoring a partial dissociation of PLN from SERCA2a, further structural studies are still necessary to full understand istaroxime molecular mechanism of action.

At the cellular level, istaroxime stimulated SR $Ca^{2+}$ uptake as clearly shown by applying the post-rest potentiation protocol to STZ myocytes (Fig 2). Moreover, as explain above, SERCA2a stimulation by the drug was fully remarkable by controlling membrane potential changes in voltage clamped myocytes (Fig 4). Indeed, istaroxime, by stimulating SERCA2a, mostly restored STZ-induced changes in $Ca_{SR}$ and $Ca_T$ amplitude and it accelerated the SR uptake function, effects all compatible with a sharp enhancement of $Ca^{2+}$ uptake by the SR, as expected from stimulation of SERCA2a activity.

STZ-induced $Ca_D$ enhancement was blunted by istaroxime in paced STZ myocytes; by contrast, $Ca_D$ was significantly increased by the drug in CTR myocytes. Moreover, istaroxime slightly depolarized $E_{diast}$ in both CTR and STZ myocytes, as a result of a partial NKA blockade. Overall, the modulation of $Ca_D$ by 100 nM istaroxime might be the consequence of the balance between effects depending on SERCA2a stimulation and NKA inhibition, although negligible.

Abnormalities of the SR uptake function can be due to reduced SERCA2a activity or to increased $Ca^{2+}$ leak through RyRs channels. While functional and structural SERCA2a down-regulation (increased inhibition by PLN and reduced SERCA2a protein level) was observed, RyRs open probability was not significantly changed in

STZ myocytes. Indeed, $Ca^{2+}$ sparks frequency (Fig 5), the incidence of $Ca^{2+}$ waves and the related DADs were not significantly increased in STZ myocytes, thus suggesting the absence of a sharp SR instability at this stage of STZ-induced DCM. These findings lead to limit the detection of potential antiarrhythmic effect of istaroxime as a direct consequence of SERCA2a stimulation.

Moreover, STZ-induced changes in $Ca^{2+}$ sparks characteristics are a mirror image of the reduced SR $Ca^{2+}$ content in STZ myocytes (Fig 5). Indeed, in comparison to CTR myocytes, $Ca^{2+}$ sparks became smaller in amplitude, spatial and time duration, resulting in a smaller spark mass. Istaroxime, by stimulating SERCA2a, blunted these changes and even markedly accelerated $Ca^{2+}$ sparks decay. The last event is relevant for the potential anti-arrhythmic efficacy of istaroxime because of a faster $Ca^{2+}$ release unit (CRU) switch off, that can limit $Ca^{2+}$ waves genesis. Moreover, the acceleration of $Ca^{2+}$ spark decay induced by istaroxime seems independent on STZ-induced changes; thus, we cannot exclude direct effects of the drug on $Ca^{2+}$ spark termination mechanisms.

Temporal dispersion of repolarization, quantified as short-term variability (STV) of APD, is a well-known pro-arrhythmic index because plays an important role in the initiation of ventricular arrhythmias like *torsade de point* (TdP)[47]. STV was significantly increased in STZ myocytes and this was mainly associated to APD prolongation (Fig 3C); istaroxime did not significantly affected STV.

### 4.3 Study limitations

The aim of the study was to test the effect of SERCA2a stimulation on DD in a DCM model. The study spreads from *in vivo* to *in vitro* effects of istaroxime at a concentration marginally affecting NKA. We would like to stress that even though effects dependent on NKA inhibition were detected, the general findings of the study are largely dependent on SERCA2a stimulation by the drug.

## 5. Conclusions and clinical implications

SERCA2a stimulation by istaroxime improves DD in diabetic rats, by controlling intracellular $Ca^{2+}$ compartmentalization. Thus, SERCA2a stimulation can be considered a promising therapeutic approach for DCM treatment. Even though the translation of drug effects from animal models to patients must take into account differences in the pathophysiological mechanisms/picture between animals and patients, STZ model was useful for studying the cardiac mechanical improvement produced by a drug endowed with a SERCA2a stimulatory activity. Accordingly, a recent phase II randomized clinical study in patients hospitalised for acute HF[28] showed that a 24-hour infusion of istaroxime at 0.5 and 1 µg/kg/min improved both diastolic and systolic cardiac function without major cardiac adverse effects. This is a proof-of-concept that SERCA2a stimulation is a novel and valid target for the treatment of high risk patients with reduced LVEF. Therefore, we are confident that the development of small molecules active on SERCA2a only ("pure SERCA2a activators") might be clinically relevant to treat targeted population with unfavorable cardiovascular outcomes with traditional therapies.

## Funding

This work was supported by CVie Therapeutics Limited (Taipei, Taiwan) and FAR2019 of the University of Milano Bicocca.

## Conflict of interests

MF, PB, GB are Windtree employees, PF is a Windtree consultant, S-CH is employee of CVie Therapeutics Limited.

## References

1. Sherwin R, Jastreboff AM. Year in diabetes 2012: The diabetes tsunami. *J Clin Endocrinol Metab* 2012;**97**:4293–4301.
2. Schannwell CM, Schneppenheim M, Perings S, Plehn G, Strauer BE. Left ventricular diastolic dysfunction as an early manifestation of diabetic cardiomyopathy. *Cardiology* 2002;**98**:33–39.
3. Belke DD, Dillmann WH. Altered cardiac calcium handling in diabetes. *Curr Hypertens Rep* 2004;**6**:424–429.

4. Boudina S, Abel ED. Diabetic cardiomyopathy revisited. *Circulation* 2007;**115**:3213–3223.

5. Lebeche D, Davidoff AJ, Hajjar RJ. Interplay between impaired calcium regulation and insulin signaling abnormalities in diabetic cardiomyopathy. *Nat Clin Pract Cardiovasc Med* 2008;**5**:715–724.

6. Choi KM, Zhong Y, Hoit BD, Grupp IL, Hahn H, Dilly KW, Guatimosim S, Jonathan Lederer W, Matlib MA. Defective intracellular Ca2+ signaling contributes to cardiomyopathy in type 1 diabetic rats. *Am J Physiol - Hear Circ Physiol* 2002;**283**:H1398–H1408.

7. Vasanji Z, Dhalla NS, Netticadan T. Increased inhibition of SERCA2 by phospholamban in the type I diabetic heart. *Mol Cell Biochem* 2004;**261**:245–249.

8. Kranias EG, Hajjar RJ. Modulation of cardiac contractility by the phopholamban/SERCA2a regulatome. *Circ Res* 2012;**110**:1646–1660.

9. Zaza A, Rocchetti M. Calcium Store Stability as an Antiarrhythmic Endpoint. *Curr Pharm Des* 2015;**21**:1053–1061.

10. Malek V, Gaikwad AB. Telmisartan and thiorphan combination treatment attenuates fibrosis and apoptosis in preventing diabetic cardiomyopathy. *Cardiovasc Res* 2019;**115**:373–384.

11. Dobrin JS, Lebeche D. Diabetic cardiomyopathy: Signaling defects and therapeutic approaches. *Expert Rev Cardiovasc Ther* 2010;**8**:373–391.

12. Ng HH, Leo CH, Parry LJ, Ritchie RH. Relaxin as a therapeutic target for the cardiovascular complications of diabetes. *Front Pharmacol* 2018;**9**:501.

13. Jaski BE, Jessup ML, Mancini DM, Cappola TP, Pauly DF, Greenberg B, Borow K, Dittrich H, Zsebo KM, Hajjar RJ. Calcium Upregulation by Percutaneous Administration of Gene Therapy in Cardiac Disease (CUPID Trial), a First-in-Human Phase 1/2 Clinical Trial. *J Card Fail* 2009;**15**:171–181.

14. Clark RJ, McDonough PM, Swanson E, Trost SU, Suzuki M, Fukuda M, Dillmann WH. Diabetes and the Accompanying Hyperglycemia Impairs Cardiomyocyte Calcium Cycling through Increased Nuclear O-GlcNAcylation. *J Biol Chem* 2003;**278**:44230–44237.

15. Shao CH, Capek HL, Patel KP, Wang M, Tang K, DeSouza C, Nagai R, Mayhan W, Periasamy M, Bidasee KR. Carbonylation contributes to SERCA2a activity loss and diastolic dysfunction in a rat model of type 1 diabetes. *Diabetes* 2011;**60**:947–959.

16. Kho C, Lee A, Jeong D, Oh JG, Gorski PA, Fish K, Sanchez R, Devita RJ, Christensen G, Dahl R, Hajjar RJ. Small-molecule activation of SERCA2a SUMOylation for the treatment of heart failure. *Nat Commun* 2015;**6**:7229.

17. Peng BY, Dubey NK, Mishra VK, Tsai FC, Dubey R, Deng WP, Wei HJ. Addressing stem cell therapeutic approaches in pathobiology of diabetes and its complications. *J Diabetes Res* 2018;**2018**.

18. Kaneko M, Yamamoto H, Sakai H, Kamada Y, Tanaka T, Fujiwara S, Yamamoto S, Takahagi H, Igawa H, Kasai S, Noda M, Inui M, Nishimoto T. A pyridone derivative activates SERCA2a by attenuating the inhibitory effect of phospholamban. *Eur J Pharmacol* 2017;**814**:1–8.

19. Bidasee KR, Zhang Y, Shao CH, Wang M, Patel KP, Dincer ÜD, Besch HR. Diabetes Increases Formation of Advanced Glycation End Products on Sarco(endo)plasmic Reticulum Ca2+-ATPase. *Diabetes* 2004;**53**:463–473.

20. Shah SJ, Blair JEA, Filippatos GS, MacArie C, Ruzyllo W, Korewicki J, Bubenek-Turconi SI, Ceracchi M, Bianchetti M, Carminati P, Kremastinos D, Grzybowski J, Valentini G, Sabbah HN, Gheorghiade M. Effects of istaroxime on diastolic stiffness in acute heart failure syndromes: Results from the Hemodynamic, Echocardiographic, and Neurohormonal Effects of Istaroxime, a Novel Intravenous Inotropic and Lusitropic Agent: A Randomized Controlled Trial in P. *Am Heart J* 2009;**157**:1035–1041.

21. Rocchetti M, Besana A, Mostacciuolo G, Micheletti R, Ferrari P, Sarkozi S, Szegedi C, Jona I, Zaza A. Modulation of sarcoplasmic reticulum function by Na+/K + pump inhibitors with different toxicity: Digoxin and PST2744 [(E,Z)-3-((2-aminoethoxy)imino)androstane-6,17-dione hydrochloride]. *J Pharmacol Exp Ther* 2005;**313**:207–215.

22. Ferrandi M, Barassi P, Tadini-Buoninsegni F, Bartolommei G, Molinari I, Tripodi MG, Reina C, Moncelli MR, Bianchi G, Ferrari P. Istaroxime stimulates SERCA2a and accelerates calcium cycling in heart failure by relieving phospholamban inhibition. *Br J Pharmacol* 2013;**169**:1849–1861.

23. Alemanni M, Rocchetti M, Re D, Zaza A. Role and mechanism of subcellular Ca2+ distribution in the action of two inotropic agents with different toxicity. *J Mol Cell Cardiol* 2011;**50**:910–918.

24. Adamson PB, Vanoli E, Mattera GG, Germany R, Gagnol JP, Carminati P, Schwartz PJ. Hemodynamic effects of a new inotropic compound, PST-2744, in dogs with chronic ischemic heart failure. *J Cardiovasc Pharmacol* 2003;**42**:169–173.

25. Micheletti R, Palazzo F, Barassi P, Giacalone G, Ferrandi M, Schiavone A, Moro B, Parodi O, Ferrari P, Bianchi G. Istaroxime, a Stimulator of Sarcoplasmic Reticulum Calcium Adenosine Triphosphatase Isoform 2a Activity, as a Novel Therapeutic Approach to Heart Failure. *Am J Cardiol* 2007;**99**:24A-32A.

26. Sabbah HN, Imai M, Cowart D, Amato A, Carminati P, Gheorghiade M. Hemodynamic Properties of a New-Generation Positive Luso-Inotropic Agent for the Acute Treatment of Advanced Heart Failure. *Am J Cardiol* 2007;**99**:41A-

46A.

27. Rocchetti M, Alemanni M, Mostacciuolo G, Barassi P, Altomare C, Chisci R, Micheletti R, Ferrari P, Zaza A. Modulation of sarcoplasmic reticulum function by PST2744 [Istaroxime; (E,Z)-3-((2-aminoethoxy)imino) androstane-6,17-dione hydrochloride] in a pressure-overload heart failure model. *J Pharmacol Exp Ther* 2008;**326**:957–965.

28. Carubelli V, Zhang Y, Metra M, Lombardi C, Felker GM, Filippatos G, O'Connor CM, Teerlink JR, Simmons P, Segal R, Malfatto G, Rovere MT La, Li D, Han X, Yuan Z, Yao Y, Li B, Lau LF, Bianchi G, Zhang J. Treatment with 24 hour istaroxime infusion in patients hospitalised for acute heart failure: a randomised, placebo-controlled trial. *Eur J Heart Fail* 2020;**Jan 23**.

29. Micheletti R, Mattera GG, Rocchetti M, Schiavone A, Loi MF, Zaza A, Gagnol RJP, Munari S De, Melloni P, Carminati P, Bianchi G, Ferrari P. Pharmacological profile of the novel inotropic agent (E,Z)-3-((2-aminoethoxy)imino)androstane-6,17-dione hydrochloride (PST2744). *J Pharmacol Exp Ther* 2002;**303**:592–600.

30. Rocchetti M, Besana A, Mostacciuolo G, Ferrari P, Micheletti R, Zaza A. Diverse toxicity associated with cardiac Na+/K+ pump inhibition: Evaluation of electrophysiological mechanisms. *J Pharmacol Exp Ther* 2003;**305**:765–771.

31. Gheorghiade M, Ambrosy AP, Ferrandi M, Ferrari P. Combining SERCA2a activation and Na-K ATPase inhibition: a promising new approach to managing acute heart failure syndromes with low cardiac output. *Discov Med* 2011;**12**:141–151.

32. Bossu A, Kostense A, Beekman HDM, Houtman MJC, Heyden MAG van der, Vos MA. Istaroxime, a positive inotropic agent devoid of proarrhythmic properties in sensitive chronic atrioventricular block dogs. *Pharmacol Res* 2018;**133**:132–140.

33. Rocchetti M, Sala L, Rizzetto R, Irene Staszewsky L, Alemanni M, Zambelli V, Russo I, Barile L, Cornaghi L, Altomare C, Ronchi C, Mostacciuolo G, Lucchetti J, Gobbi M, Latini R, Zaza A. Ranolazine prevents INaL enhancement and blunts myocardial remodelling in a model of pulmonary hypertension. *Cardiovasc Res* 2014;**104**:37–48.

34. Pasqualin C, Gannier F, Malécot CO, Bredeloux P, Maupoil V. Automatic quantitative analysis of t-tubule organization in cardiac myocytes using ImageJ. *Am J Physiol - Cell Physiol* 2015;**308**:C237-45.

35. Ferrandi M, Tripodi G, Salardi S, Florio M, Modica R, Barassi P, Parenti P, Shainskaya A, Karlish S, Bianchi G, Ferrari P. Renal Na,K-ATPase in genetic hypertension. *Hypertension* 1996;**28**:1018–1025.

36. Altomare C, Bartolucci C, Sala L, Bernardi J, Mostacciuolo G, Rocchetti M,

Severi S, Zaza A. IKr Impact on Repolarization and Its Variability Assessed by Dynamic Clamp. *Circ Arrhythmia Electrophysiol* 2015;**8**:1265–1275.

37. Meo M, Meste O, Signore S, Sorrentino A, Cannata A, Zhou Y, Matsuda A, Luciani M, Kannappan R, Goichberg P, Leri A, Anversa P, Rota M. Reduction in kv current enhances the temporal dispersion of the action potential in diabetic myocytes: Insights from a novel repolarization algorithm. *J Am Heart Assoc* 2016;**5**.

38. Howarth FC, Jacobson M, Qureshi MA, Shafiullah M, Hameed RS, Zilahi E, Haj A Al, Nowotny N, Adeghate E. Altered gene expression may underlie prolonged duration of the QT interval and ventricular action potential in streptozotocin-induced diabetic rat heart. *Mol Cell Biochem* 2009;**328**:57–65.

39. Ku DD, Sellers BM. Effects of streptozotocin diabetes and insulin treatment on myocardial sodium pump and contractility of the rat heart. *J Pharmacol Exp Ther* 1982;**222**:395–400.

40. Hoshijima M, Ikeda Y, Iwanaga Y, Minamisawa S, Date MO, Gu Y, Iwatate M, Li M, Wang L, Wilson JM, Wang Y, Ross J, Chien KR. Chronic suppression of heart-failure progression by a pseudophosphorylated mutant of phospholamban via in vivo cardiac rAAV gene delivery. *Nat Med* 2002;**8**:864–871.

41. Suckau L, Fechner H, Chemaly E, Krohn S, Hadri L, Kockskamper J, Westermann D, Bisping E, Ly H, Wang X, Kawase Y, Chen J, Liang L, Sipo I, Vetter R, Weger S, Kurreck J, Erdmann V, Tschope C, Pieske B, Lebeche D, Schultheiss HP, Hajjar RJ, Poller WC. Long-term cardiac-targeted RNA interference for the treatment of heart failure restores cardiac function and reduces pathological hypertrophy. *Circulation* 2009;**119**:1241–1252.

42. Watanabe A, Arai M, Yamazaki M, Koitabashi N, Wuytack F, Kurabayashi M. Phospholamban ablation by RNA interference increases Ca2+uptake into rat cardiac myocyte sarcoplasmic reticulum. *J Mol Cell Cardiol* 2004;**37**:691–698.

43. Suzuki T, Wang JH. Stimulation of bovine cardiac sarcoplasmic reticulum Ca2+ pump and blocking of phospholamban phosphorylation and dephosphorylation by a phospholamban monoclonal antibody. *J Biol Chem* 1986;**261**:7018–7023.

44. Zhang Y, Wang Y, Yanni J, Qureshi MA, Logantha SJRJ, Kassab S, Boyett MR, Gardiner NJ, Sun H, Howarth FC, Dobrzynski H. Electrical Conduction System Remodeling in Streptozotocin-Induced Diabetes Mellitus Rat Heart. *Front Physiol* 2019;**10**:1–15.

45. Mihm MJ, Seifert JL, Coyle CM, Bauer JA. Diabetes related cardiomyopathy time dependent echocardiographic evaluation in an experimental rat model. *Life Sci* 2001;**69**:527–542.

46. Wu W, Liu X, Han L. Apoptosis of cardiomyocytes in diabetic cardiomyopathy involves overexpression of glycogen synthase kinase-3β. *Biosci Rep*

2019;**39**:BSR20171307.

47. Smoczynska A, Beekman HDM, Vos MA. The increment of short-term variability of repolarisation determines the severity of the imminent arrhythmic outcome. *Arrhythmia Electrophysiol Rev* 2019;**8**:166–172.

## Figure legends

**Figure 1. Istaroxime affinity for rat NKA. Changes in SERCA2, PLN levels and T-tubules expression in STZ vs CTR rats. (A) Top:** Recordings of $Na^+/K^+$ ATPase current ($I_{NKA}$) and Ion NaTRIUM Green-2 fluorescence (Hp -40 mV) during exposure to increasing concentrations of istaroxime and, finally, to 1 mM ouabain (OUA). **Bottom:** concentration-dependent $I_{NKA}$ inhibition by istaroxime in isolated CTR LV myocytes (the best logistic fit and confidence intervals are shown, N=5, n=6-27). Concentration-dependent NKA activity inhibition by istaroxime and OUA in cardiac preparations is shown in the inset (N=5). **B) Left:** Western blot for SERCA2, monomeric (m) and pentameric (p) PLN, $pSer^{16}$-PLN and $pThr^{17}$-PLN in STZ (N=6,7) and CTR (N=5,6) cardiac homogenates. **Right:** densitometric analysis; values are expressed as optical density in arbitrary units. *p<0.05 vs CTR (unpaired t-test). **C) Left:** $Ca^{2+}$ activation curves of SERCA2a activity measured as CPA sensitive component in cardiac SR homogenates from CTR (N=8) and STZ (N=10) rats with or w/o 500 nM istaroxime. **Right:** statistics of the maximum velocity ($V_{max}$) of the $Ca^{2+}$ activation curves estimated by sigmoidal fitting. *p<0.05 vs CTR (unpaired *t*-test), #p<0.05 vs STZ (paired *t*-test). **D) Top:** confocal images of di-3-ANEPPDHQ (20 µmol/L) loaded CTR and STZ myocytes (horizontal bars 2 µm). **Bottom:** mean power spectrum (PS) profile of T-tubules (TT) in CTR (N=5, n=114) and STZ (N=9, n=181) group; average results of the power of the periodic component on the right. *p<0.05 vs CTR (unpaired t-test).

**Figure 2. STZ-induced changes in $Ca^{2+}$ dynamics in field stimulated myocytes. Analysis of istaroxime effects. A) Left:** post-rest potentiation protocol in Fluo4 field stimulated (2Hz) myocytes; steady state $Ca^{2+}$ transients ($ssCa_T$) and superimposed first $Ca^{2+}$ transients ($1^{st}$ $Ca_T$) following increasing resting pauses (1-5-10-20 s) are reported in CTR and STZ myocytes, with or w/o 100 nM istaroxime. Traces were normalized to own diastolic $Ca^{2+}$ level (dotted lines). **Right:** analysis of the $1^{st}$ $Ca_T$ amplitude normalized to the amplitude of the pre-pause $ssCa_T$ and its pause-dependency. CTR N=5 (w/o istaroxime n=44, with istaroxime n=34), STZ N=3 (w/o istaroxime n=35, with istaroxime n=23). *p<0.05 vs CTR w/o istaroxime; #p<0.05

vs STZ w/o istaroxime (two-way ANOVA plus post-hoc Sidak's multiple comparisons). **B)** $ssCa_T$ and caffeine-induced $Ca_T$ evocated in field stimulated CTR and STZ myocytes with or w/o 100 nM istaroxime (the dotted line indicates the diastolic $Ca^{2+}$ ($Ca_D$) in CTR w/o istaroxime). **C)** Statistics for $ssCa_D$, $ssCa_T$ amplitude, caffeine-induced $Ca_T$ (named $Ca_{SR}$) and $ssCa_T$ half decay time ($t_{0.5}$). CTR N=5 (n=36 w/o istaroxime, n=31 with istaroxime), STZ N=7 (n=52 w/o istaroxime, n=42 with istaroxime). *p<0.05 vs CTR w/o istaroxime (one-way ANOVA plus post-hoc Tukey's multiple comparisons). **D)** Changes in $Ca_D$ during the reloading process after caffeine-induced SR depletion. $Ca_D$ values ($Ca_{D,n}$) were normalized to the 1st pulse $Ca_D$ ($Ca_{D,1}$). CTR N=5 (n=36 w/o istaroxime, n=29 with istaroxime), STZ N=7 (n=49 w/o istaroxime, n=43 with istaroxime).

**Figure 3. STZ-induced changes in electrical activity. Analysis of istaroxime effects. A) Top:** representative action potentials (AP) recorded at 1 Hz in CTR and STZ myocytes with or w/o 100 nM istaroxime. **Bottom:** rate dependency of AP parameters ($APD_{50}$, $APD_{90}$, $E_{diast}$) in CTR and STZ myocytes with or w/o 100 nM istaroxime. CTR N=4 (n=29 w/o istaroxime, n=25 with istaroxime), STZ N=3 (n=24 w/o istaroxime, n=19 with istaroxime). *p<0.05 vs CTR w/o istaroxime, #p<0.05 vs STZ w/o istaroxime (two-way ANOVA plus post-hoc Sidak's multiple comparisons). **B)** Effects of 100 nM istaroxime superfusion on diastolic potential (**top,** AP y axis zoomed to highlight changes) and $Na^+_i$ (**bottom**) in comparison to the effect of 1 mM ouabain (OUA) in CTR myocytes loaded with Ion-Natrium Green 2 and stimulated at 7Hz. **C) Top:** Rate-dependency of $APD_{90}$ STV in each experimental group. CTR N=4 (n=27 w/o istaroxime, n=21 with istaroxime), STZ N=3 (n=24 w/o istaroxime, n=20 with istaroxime). *p<0.05 vs CTR w/o istaroxime, (two-way ANOVA plus post-hoc Sidak's multiple comparisons). **Bottom:** linear correlation between STV of $APD_{90}$ and $APD_{90}$ values in CTR and STZ groups; data from all stimulation rates were pooled.

**Figure 4. STZ-induced $Ca^{2+}$ handling changes under control of membrane potential. Analysis of istaroxime effects. A) Top:** APs waveforms (CTR and STZ APs named short and long APs respectively) and corresponding $Ca_T$ evocated in V-

clamped STZ myocyte through AP-clamp experiments (2 Hz). Caffeine-induced $Ca_T$ (caff-$Ca_T$) and the corresponding NCX current ($I_{NCX}$) were recorded at -80 mV following steady state stimulation with short and long AP to estimate changes in SR $Ca^{2+}$ content ($Ca_{SR}$). **Bottom:** statistics of $Ca_T$ amplitude (N=5, n=30) and $Ca_{SR}$ (integral of inward $I_{NCX}$, marked as striped area) (N=5, n=22) under short and long AP stimulation. Fluorescence signals were converted to free $Ca^{2+}$ estimating $F_{max}$ in each cell. *p<0.05 vs short AP (paired *t*-test). **B) Top:** transmembrane currents and $Ca_T$ simultaneously recorded in voltage-clamped cells (Hp -35 mV) from CTR and STZ myocytes with or w/o 100 nM istaroxime. **Bottom:** statistics of $Ca_T$ amplitude, SR $Ca^{2+}$ content ($Ca_{SR}$), $Ca^{2+}$ influx through L-type $Ca^{2+}$ channel ($Ca_L$ influx) and excitation release (ER)-gain. CTR N=3 (n=22-24), STZ N=5 (w/o istaroxime n=26-33, with istaroxime n=28). Fluorescence signals were converted to free $Ca^{2+}$ estimating $F_{max}$ in each cell. *p<0.05 vs CTR (one-way ANOVA plus Tukey's multiple comparison). **C)** Statistics of $Ca_T$ parameters (CaT amplitude, ER-gain and CaT decay time constant) measured during each pulse after SR depletion under NCX blockade (see Fig S2) in CTR and STZ myocytes with or w/o 100 nM istaroxime. *p<0.05 vs CTR; #p<0.05 vs STZ w/o istaroxime (two-way ANOVA); CTR N=5 (n=13-21), STZ N=4 (w/o istaroxime n=13-28, with istaroxime n=19-24).

**Figure 5. STZ-induced changes in $Ca^{2+}$ sparks rate and characteristics. Analysis of istaroxime effects. A)** Representative xt images showing $Ca^{2+}$ sparks at resting in CTR and STZ myocytes with or w/o 100 nM istaroxime. **B)** Statistics of $Ca^{2+}$ sparks characteristics and rate for each group. *p<0.05 vs CTR; #p<0.05 vs STZ w/o istarpoxime (one-way ANOVA plus Tukey's multiple comparison); CTR N=7 (n=62, sparks # =2789), STZ N=5 (w/o istaroxime n=53, sparks # =2019, with istaroxime n=47, sparks # = 1940). FWHM: full width at half maximum, FDHM: full duration at half maximum, Spark mass (spark amplitude*1.206* $FWHM^3$).

# Figures

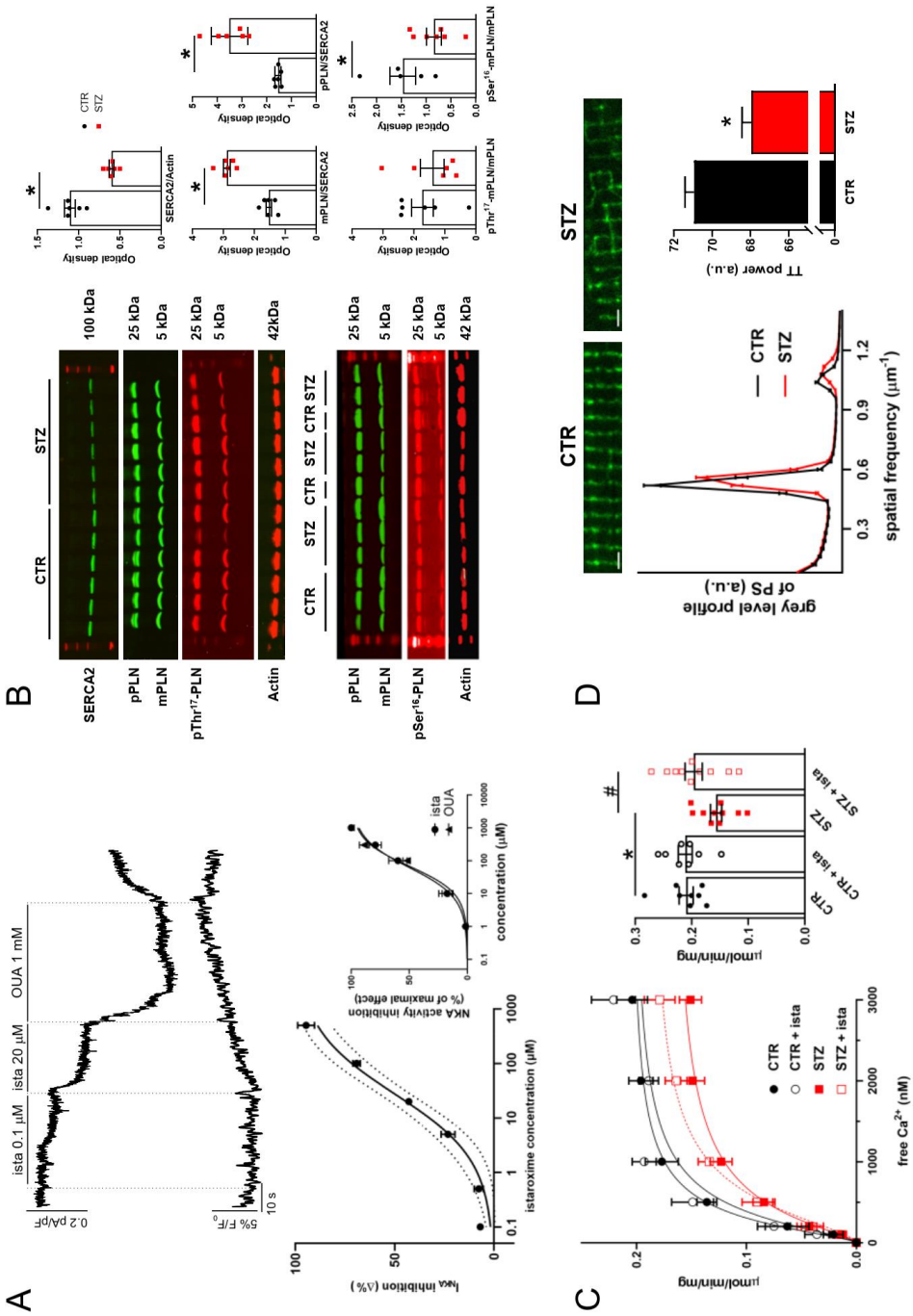


Figure 1

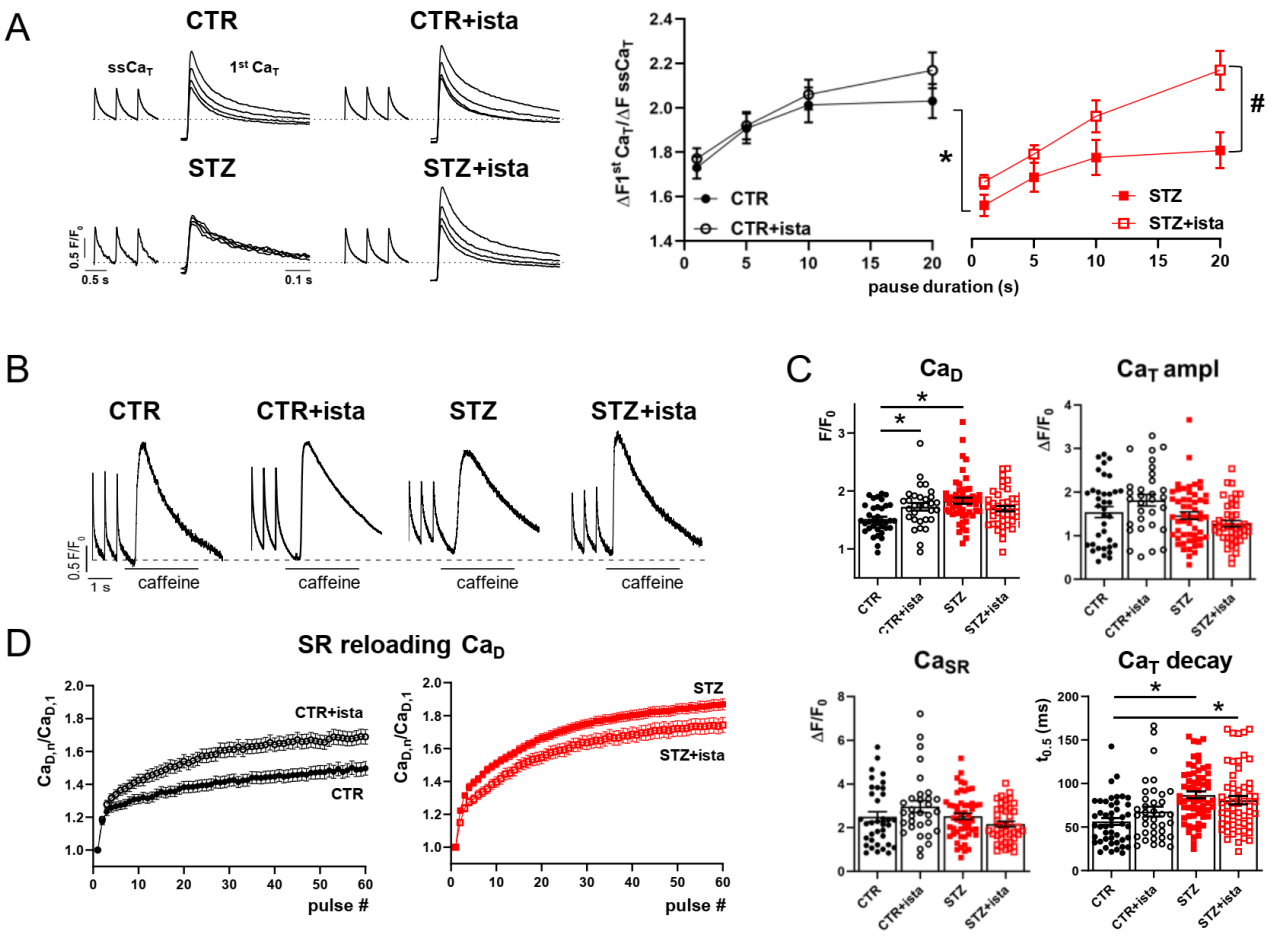
A
CTR
CTR+ista
ssCa$_T$
1$^{st}$ Ca$_T$
STZ
STZ+ista
0.5 F/F$_0$
0.5 s
0.1 s
ΔF1$^{st}$ Ca$_T$/ΔF ssCa$_T$
CTR
CTR+ista
STZ
STZ+ista
pause duration (s)
*
#
B
CTR
CTR+ista
STZ
STZ+ista
0.5 F/F$_0$
1 s
caffeine
C
Ca$_D$
Ca$_T$ ampl
F/F$_0$
ΔF/F$_0$
Ca$_{SR}$
Ca$_T$ decay
t$_{0.5}$ (ms)
D
SR reloading Ca$_D$
Ca$_{D,n}$/Ca$_{D,1}$
pulse #

Figure 2

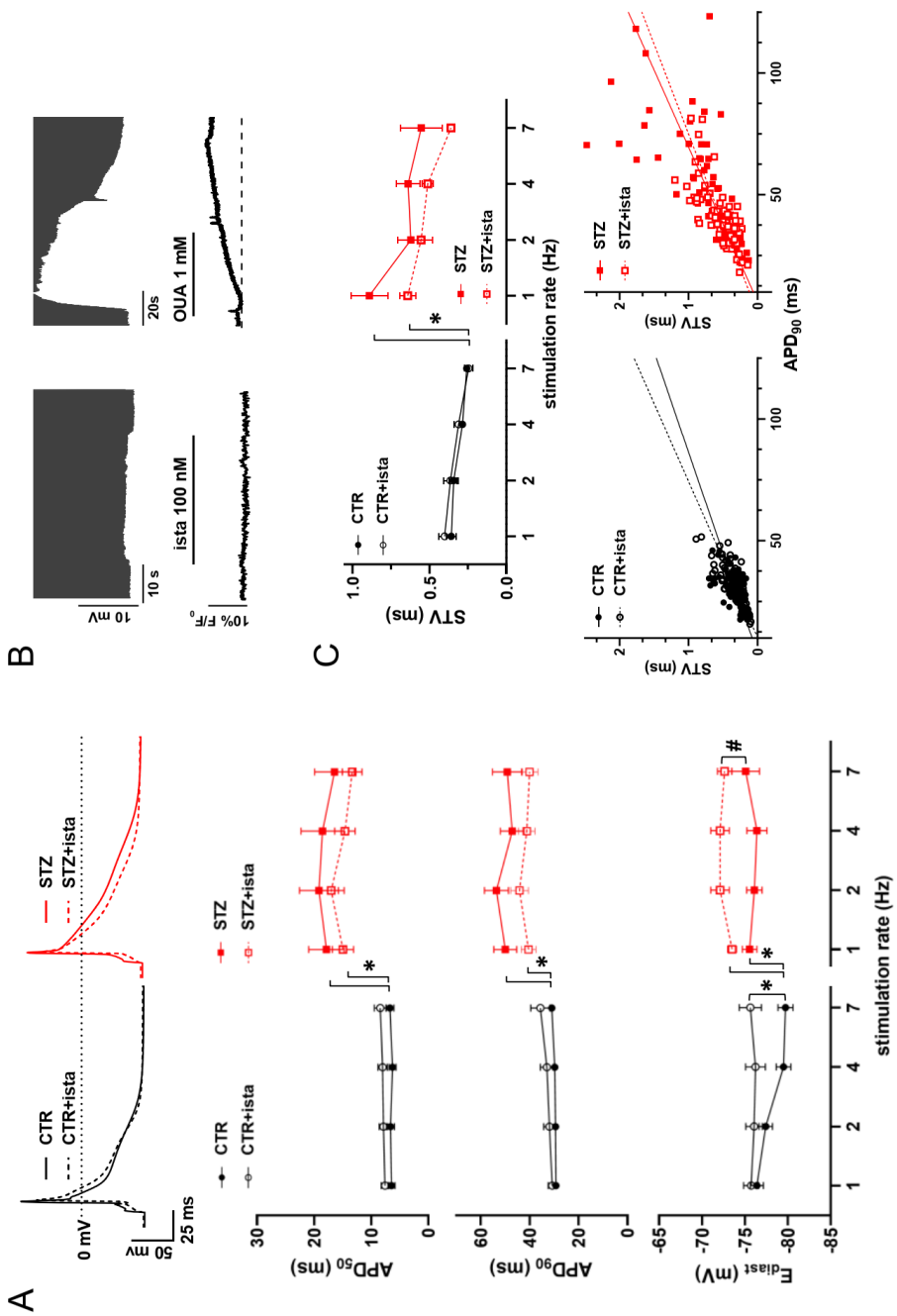
A
CTR
CTR+ista
STZ
STZ+ista
0 mV
50 mV
25 ms
B
10 mV
10 s
ista 100 nM
20s
OUA 1 mM
10% F/F0
C
CTR
CTR+ista
STV (ms)
stimulation rate (Hz)
STZ
STZ+ista
APD90 (ms)
APD50 (ms)
Fdiast (mV)

Figure 3

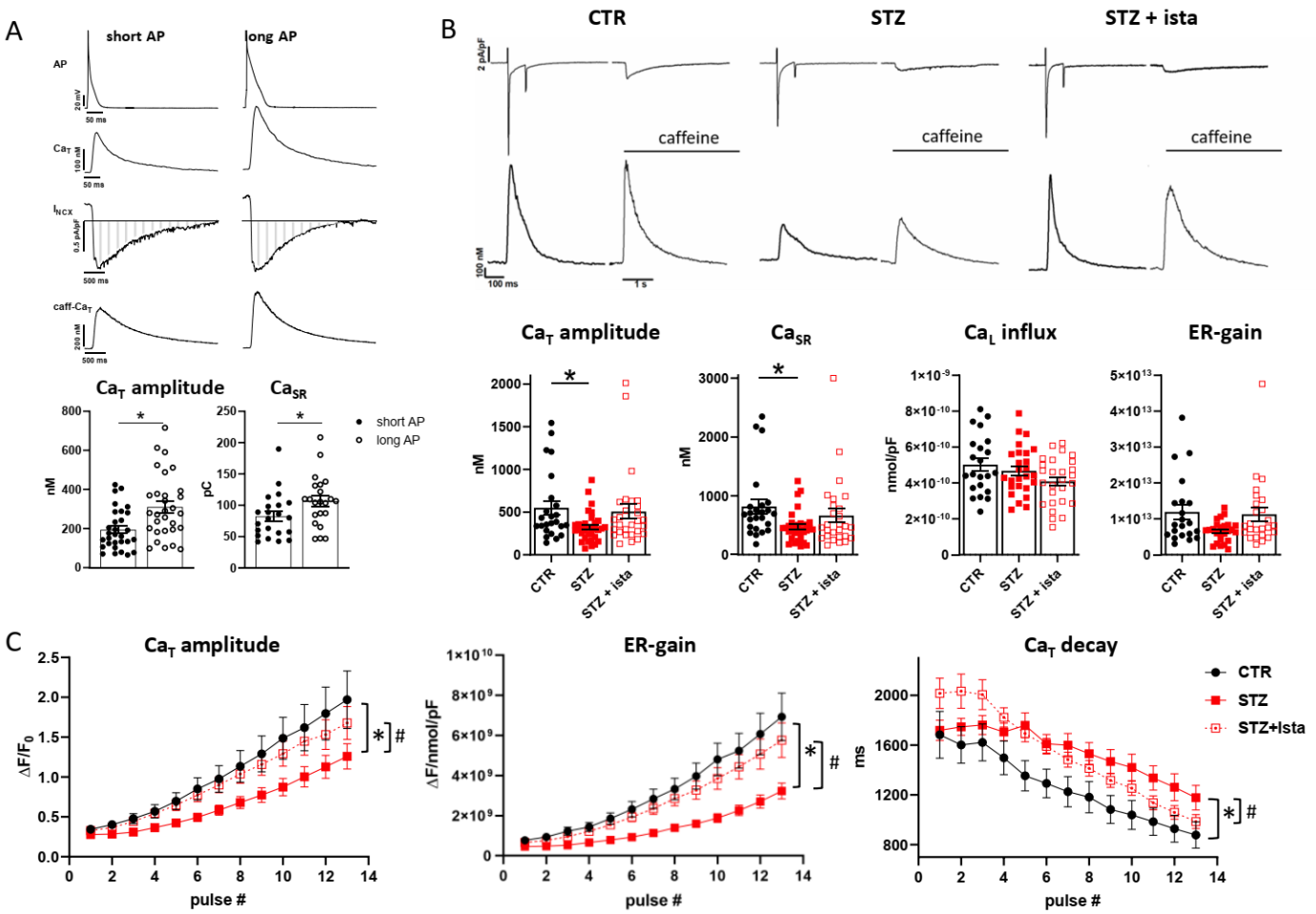
A
short AP
long AP
AP
20 mV
50 ms
Ca_T
109 nM
50 ms
I_NCX
0.5 pA/pF
500 ms
caff-Ca_T
200 nM
500 ms
Ca_T amplitude
Ca_SR
nM
pC
short AP
long AP
B
CTR
STZ
STZ + ista
2 pA/pF
caffeine
100 nM
100 ms
1 s
Ca_T amplitude
Ca_SR
Ca_L influx
ER-gain
nM
nmol/pF
CTR
STZ
STZ + ista
C
Ca_T amplitude
ΔF/F_0
pulse #
ER-gain
ΔF/nmol/pF
Ca_T decay
ms
CTR
STZ
STZ+Ista

Figure 4

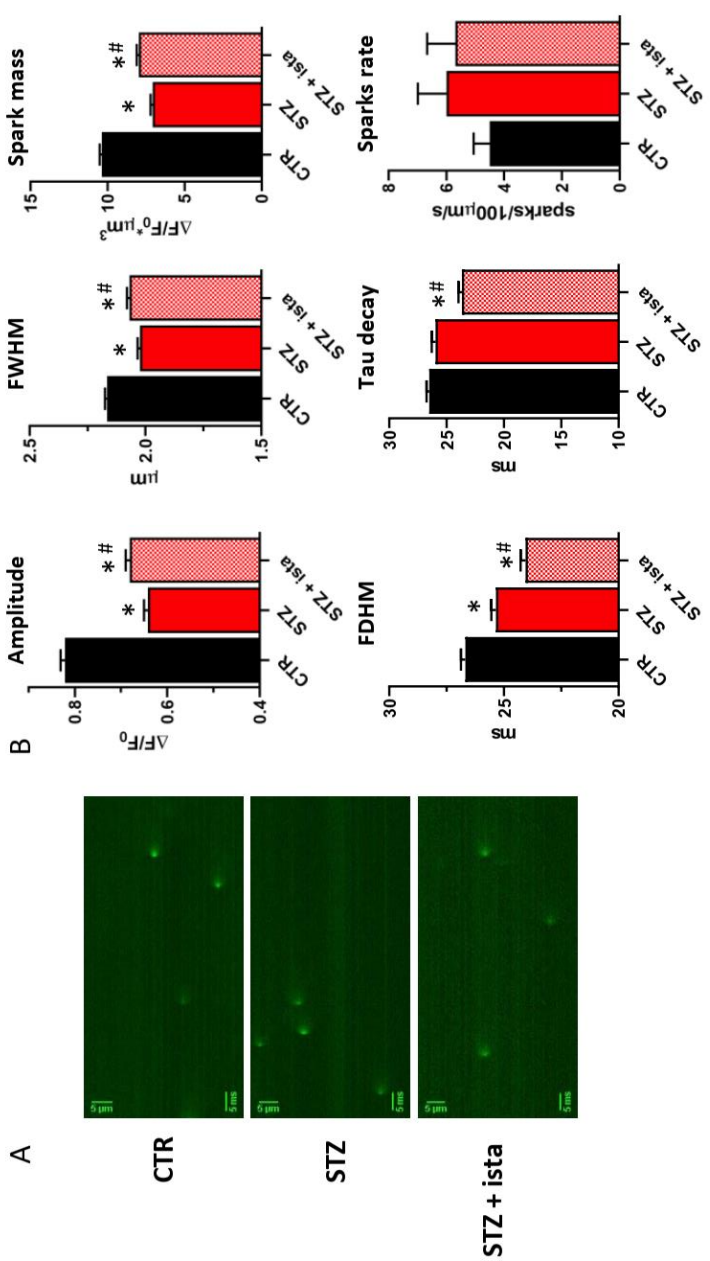
A
CTR
STZ
STZ + ista
B
Amplitude
ΔF/F0
FWHM
μm
FDHM
ms
Tau decay
ms
Sparks rate
sparks/100μm/s
Spark mass
ΔF/F0*μm3
CTR
STZ
STZ + ista

Figure 5

## Table legends

**Table 1. Glycaemia values, morphometric parameters and LV cell dimensions.** Average values of fasting/non fasting glycaemia, morphometric parameters and LV cell dimensions in CTR and STZ animals. Body weight (BW), heart weight (HW), kidney weight (KW), left ventricle weight (LVW), tibia length (TL). *p<0.05 vs CTR (unpaired *t*-test). Morphometric parameters: CTR N=15-21, STZ N=23-34. Cell dimensions: CTR N=4 (n=58), STZ N=6 (n=108). Cell membrane capacitance: CTR N=12 (n=75), STZ N=13 (n=83).

**Table 2. Echocardiographic and Tissue Doppler parameters.** Average values in CTR and STZ animals before (basal) and after infusion with istaroxime at 0.11 mg/kg/min for 15 min. Telediastolic interventricular septum thickness (IVSTd), telediastolic posterior wall thickness (PWTd), left ventricle early-diastolic diameter (LVEDD), telesystolic interventricular septum thickness (IVSTs), telesystolic posterior wall thickness (PWTs), left ventricle early-systolic diameter (LVESD), fractional shortening (FS), early diastolic peak velocity (E, e'), late diastolic peak velocity (A, a'), deceleration time (DT), systolic peak velocity (s'), heart rate (HR), stroke volume (SV), cardiac output (CO), ejection fraction (EF). *p<0.05 vs CTR (unpaired t-test), $p<0.05 vs STZ basal (paired t-test). CTR N=7, STZ N=7.

| | CTR | STZ | P vs CTR |
|---|---|---|---|
| **Fasting glycaemia (mg/dL)** | 94 ± 2 | 390 ± 14 | * |
| **Non fasting glycaemia (mg/dL)** | 126 ± 4 | 560 ± 8 | * |
| **BW (g)** | 400 ± 7 | 202 ± 6 | * |
| **BW gain (g)** | 230 ± 14 | 26 ± 8 | * |
| **HW (g)** | 1.65 ± 0.08 | 1.03 ± 0.03 | * |
| **TL (cm)** | 4.3 ± 0.02 | 3.63 ± 0.03 | * |
| **HW/BW (g/kg)** | 4.11 ± 0.17 | 5.16 ± 0.11 | * |
| **HW/TL (g/cm)** | 0.40 ± 0.03 | 0.28 ± 0.009 | * |
| **LVW/HW (%)** | 67.9 ± 1.0 | 63.4 ± 0.7 | * |
| **KW (g)** | 2.23 ± 0.05 | 2.19 ± 0.07 | NS |
| **KW/TL (g/cm)** | 0.52 ± 0.01 | 0.6 ± 0.02 | * |
| | | | |
| **LV cell length (µm)** | 136 ± 2.8 | 120 ± 2.1 | * |
| **LV cell volume ($10^3$ µm$^3$)** | 65 ± 1.9 | 37 ± 1.03 | * |
| **LV Cross-Sectional Area (CSA, um$^2$)** | 482 ± 13.8 | 309 ± 7.5 | * |
| **LV cell membrane capacitance (pF)** | 179 ± 6 | 136 ± 4 | * |

Table 1

| | CTR | STZ basal | STZ + istaroxime |
|---|---|---|---|
| **IVSTd (mm)** | 1.9 ± 0.09 | 1.81 ± 0.12 | 1.88 ± 0.12 |
| **PWTd (mm)** | 1.71 ± 0.17 | 1.45 ± 0.08 | 1.47 ± 0.07 |
| **LVEDD (mm)** | 6.6 ± 0.35 | 7.08 ± 0.32 | 7.27 ± 0.23 |
| **IVSTs (mm)** | 2.6 ± 0.22 | 2.54 ± 0.18 | 2.57 ± 0.19 |
| **PWTs (mm)** | 2.71 ± 0.2 | 2.52 ± 0.1 | 2.55 ± 0.21 |
| **LVESD (mm)** | 3.07 ± 0.39 | 3.11 ± 0.28 | 3.1 ± 0.34 |
| **FS (%)** | 53.8 ± 5.66 | 56.2 ± 2.4 | 57.7 ± 3.7 |
| **E (m/s)** | 0.88 ± 0.03 | 0.89 ± 0.05 | 0.95 ± 0.05 |
| **A (m/s)** | 0.52 ± 0.07 | 0.7 ± 0.03 * | 0.81 ± 0.05 $ |
| **E/A** | 1.82 ± 0.21 | 1.26 ± 0.03 * | 1.18 ± 0.05 |
| **DT (ms)** | 53.5 ± 1.55 | 61 ± 2.17 * | 48.4 ± 3.8 $ |
| **DT/E ($10^{-3}$ $s^2$/m)** | 61.3 ± 1.43 | 69.3 ± 4.5 | 52.2 ± 5.6 $ |
| **E/DT ($10^3$ $m/s^2$)** | 16.3 ± 0.35 | 14.7 ± 0.9 | 20.8 ± 2.8 $ |
| **s' (mm/s)** | 33.2 ± 1.18 | 24.8 ± 1.19 * | 25.2 ± 1.11 |
| **e' (mm/s)** | 26.7 ± 1.73 | 21.2 ± 0.63 * | 24.5 ± 1.46 $ |
| **a' (mm/s)** | 20.7 ± 1.61 | 27.8 ± 1.99 * | 31.1 ± 2 |
| **e'/a'** | 1.31 ± 0.063 | 0.77 ± 0.03 * | 0.79 ± 0.02 |
| **E/e'** | 33.2 ± 1.56 | 42.3 ± 2.43 * | 39.1 ± 1.57 |
| **HR (bpm)** | 303 ± 9.5 | 233 ± 10 * | 240 ± 13 |
| **SV (mL)** | 0.59 ± 0.1 | 0.73 ± 0.08 | 0.78 ± 0.05 |
| **CO (mL/min)** | 179.8 ± 30.3 | 170.2 ± 17 | 186.9 ± 15 |
| **EF (%)** | 83.6±3.2 | 89.9±1.6 | 90.2±2.3 |
| **N** | 7 | 7 | 7 |

Table 2

## Supplementary figures

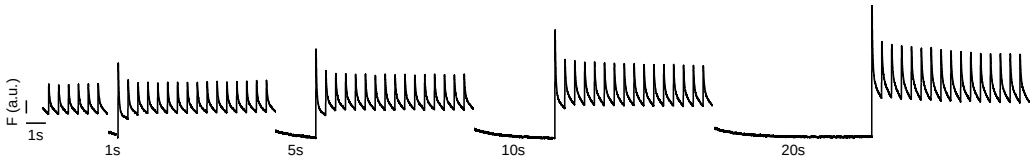


**Figure S1. Post-rest potentiation protocol to evaluate SR $Ca^{2+}$ compartmentalization during rest intervals**. Field stimulated $Ca^{2+}$ transients were evocated at 2 Hz and steady state $Ca_T$ were interrupted by increasing resting pauses (1-5-10-20 s). The amplitude of 1$^{st}$ $Ca_T$ evocated following each resting pause was then normalized to the amplitude of the pre-pause ss$Ca_T$ (see main text Fig 2).

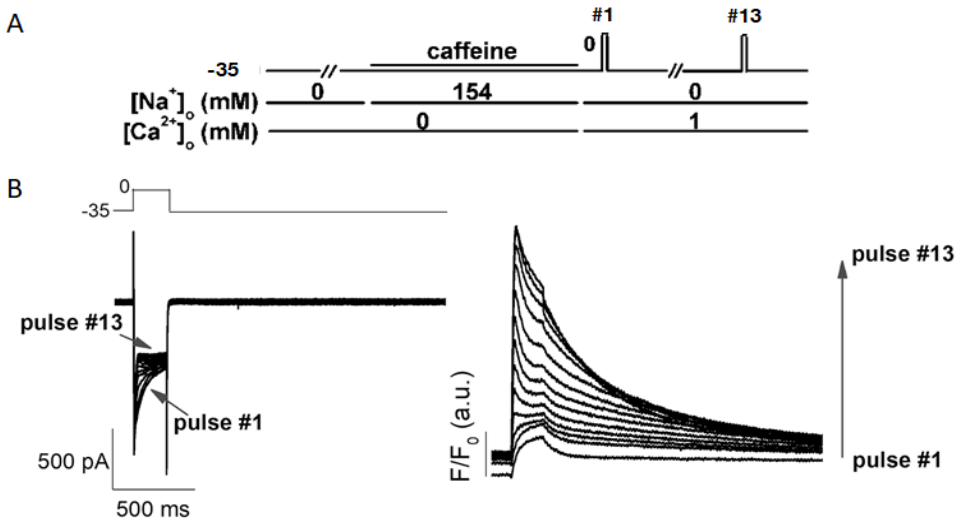


**Figure S2. Protocol to evaluate intracellular $Ca^{2+}$ dynamics in patch-clamped cells under $Na^+$ free condition**. (A) Protocol outline. (B) Transmembrane current (left) and $Ca^{2+}$ transients (right) during SR reloading after caffeine-induced SR depletion in patch-clamped cells; for details see previous work[1] and supplementary Methods below.

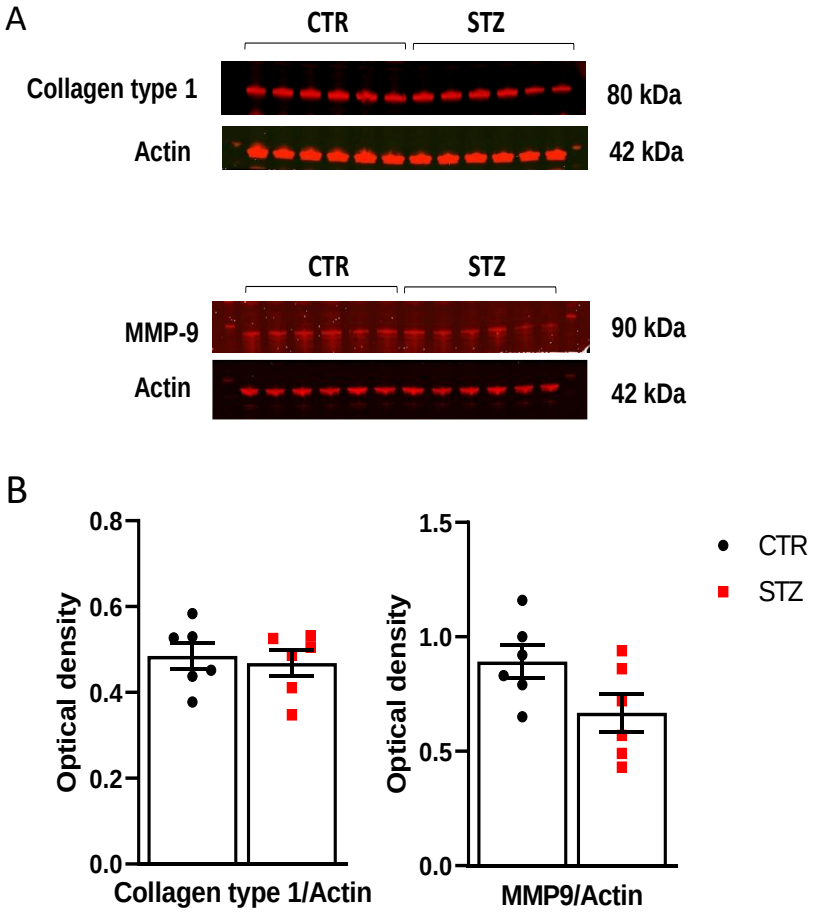


**Figure S3. Protein expression levels of Collagen and MMP-9 in cardiac homogenates from CTR and STZ rats.** (A) Representative Western blots for collagen type 1, matrix metallopeptidase 9 (MMP-9) and corresponding actin in cardiac homogenates from CTR and STZ rats. (B) Average results expressed as optical density in arbitrary units. CTR N=6, STZ N=6 (unpaired *t*-test).

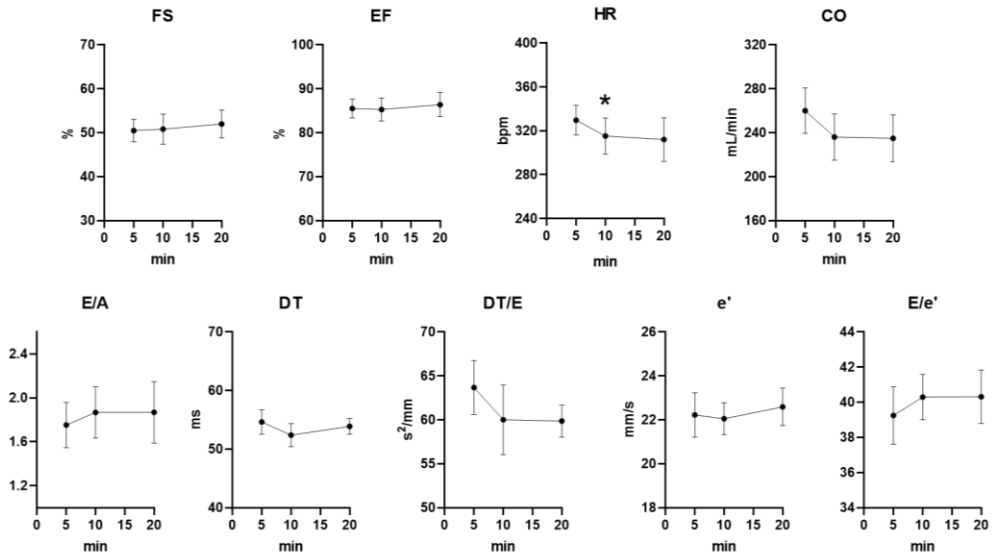


**Figure S4. Time-dependent changes of echocardiographic parameters during urethane anesthesia in CTR rats.** Fractional shortening (FS), ejection fraction (EF), heart rate (HR), cardiac output (CO), early (E, e') and late (A) diastolic peak velocity, deceleration time (DT). N=8. *p<0.05 vs 5 min (one way ANOVA).

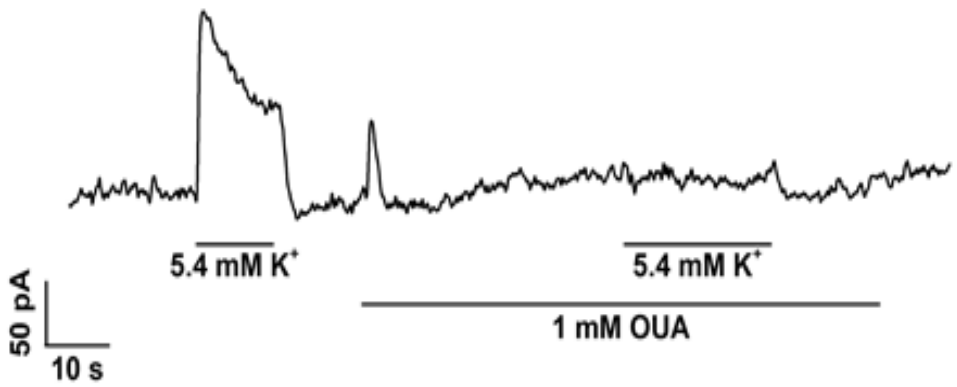


**Figure S5. Saturating concentration of ouabain to block NKA in CTR rat LV cardiomyocytes.** Example of membrane current recorded at -40 mV in the presence of $Ni^{2+}$ (5 mM), nifedipine (5 µM), $Ba^{2+}$ (1 mM) and 4-aminopyridine (2 mM) to block $Na^+/Ca^{2+}$ exchanger, $Ca^{2+}$ and $K^+$ currents, respectively. Switching from extracellular $K^+$ free to 5.4 mM $K^+$ solution, activated an outward current abolished by 1 mM ouabain (OUA) pretreatment, demonstrating that the protocol is suitable to record $I_{NKA}$ and that 1 mM OUA is a saturating concentration to block NKA in rat ventricular myocytes.

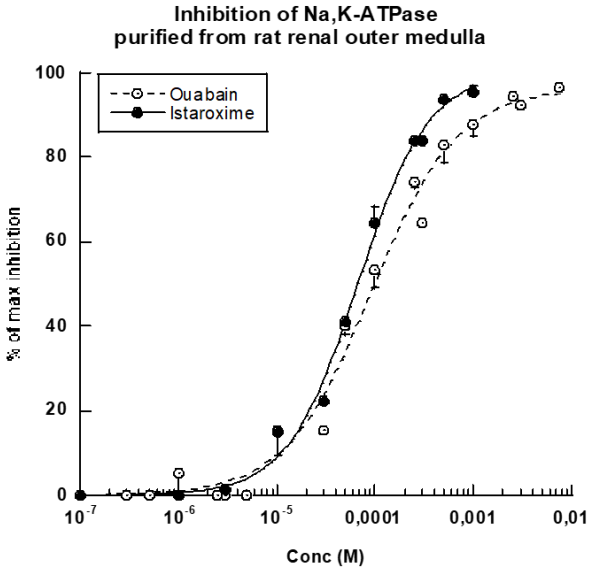


**Figure S6. NKA inhibition by istaroxime and ouabain in purified rat kidneys.** Concentration-response curves for NKA blockade by istaroxime (N=2) and ouabain (N=3) in purified rat kidneys. NKA activity was assayed *in vitro* by measuring the release of $^{32}$P-ATP. The concentration causing 50% inhibition of the NKA activity ($IC_{50}$) was calculated by using a logistic function and was, respectively, 55 ± 19 µM for istaroxime and 96 ± 26 µM for ouabain.

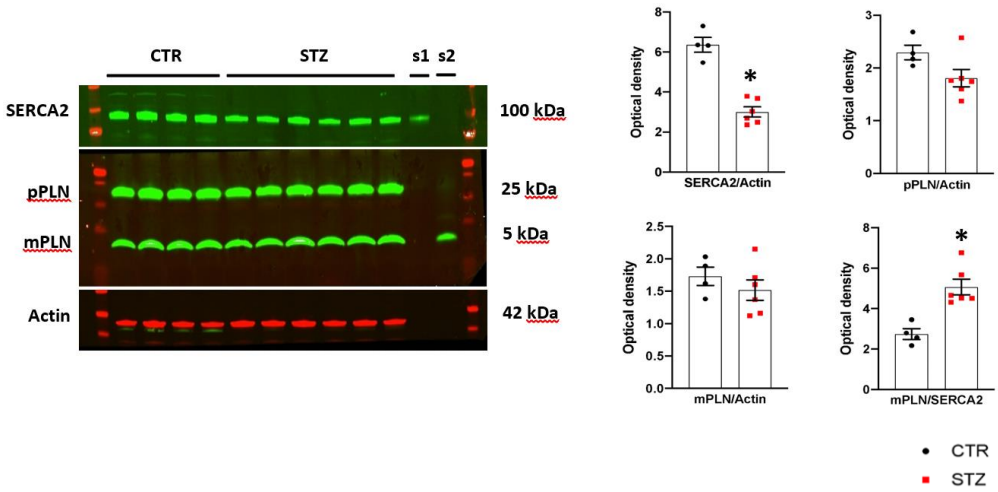


**Figure S7. Protein expression levels of SERCA2 and PLN in LV myocytes from CTR and STZ rats.** Representative Western blot for SERCA2, monomeric (m) and pentameric (p) PLN in CTR and STZ LV myocytes. Densitometric analysis in arbitrary units is shown on the right. CTR N=4, STZ N=6. *p<0.05 vs CTR (unpaired *t*-test).

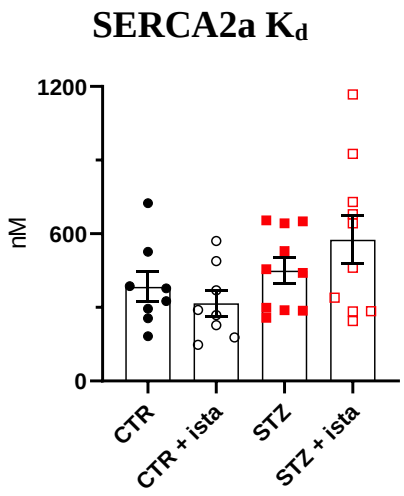


**Figure S8. Effects of STZ and istaroxime on SERCA2a $Ca^{2+}$ affinity ($K_d$) in LV homogenates.** The kinetic parameter was estimated by fitting the $Ca^{2+}$ activation curves through a logistic function (see main text Fig 1). CTR N=8, STZ N=10 (with and w/o istaroxime).

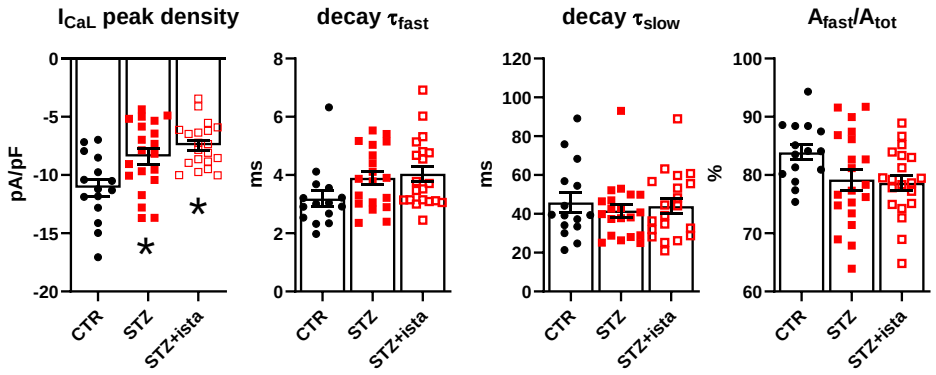


**Figure S9. Effects of STZ (with and w/o istaroxime) on nifedipine-sensitive current ($I_{CaL}$) at 0 mV.** Peak $I_{CaL}$ density (pA/pF) and inactivation kinetic components obtained interpolating $I_{CaL}$ decay with a bi-exponential function. Statistics of decay time constants ($\tau_{fast}$ and $\tau_{slow}$) and contribution of the fast component to the current decay ($A_{fast}/A_{tot}$) are shown. CTR N=3, n=15), STZ N=6 (w/o istaroxime n=20, with istaroxime n=20). * $p<0.05$ vs CTR (one-way ANOVA plus Tukey's multiple comparison).

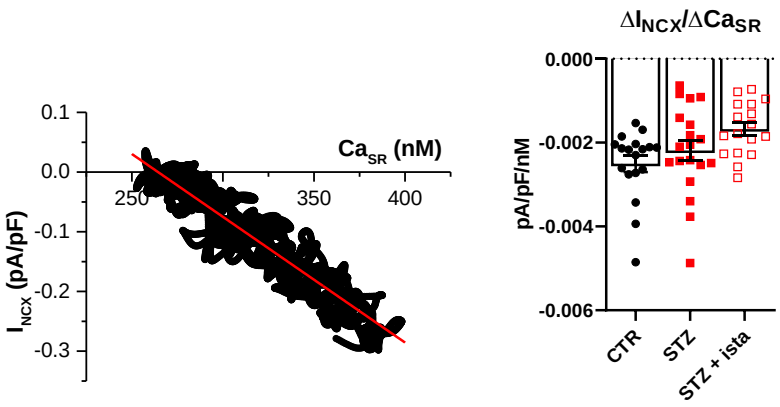


**Figure S10.** Linear correlation between NCX current ($I_{NCX}$) and $Ca_{SR}$ (caffeine induced $Ca_T$) during the final third of the caffeine-induced $Ca_T$; average results of the $\Delta I_{NCX}/\Delta Ca_{SR}$ slope on the right (CTR N=3, n=18), STZ N=6 (w/o istaroxime n=19, with istaroxime n=17). See Fig 4B of the main text.

## Supplementary methods

### Echocardiography

Eight weeks after vehicle/STZ injection, rats were submitted to a transthoracic echocardiographic and Doppler evaluation, performed under urethane (1.25 g/kg i.p.) anesthesia, (M9 Mindray Echographer equipped with a 10 MHz probe, P10-4s Transducer, Mindray, China).

Two-dimensionally guided M-mode recordings were used to obtain short-axis measurements of left ventricular end-diastolic diameter (LVEDD), left ventricular end-systolic diameter (LVESD), posterior wall thickness in diastole (PWTd) and interventricular septum thickness in diastole (IVSTd) according to the American Society of Echocardiography guidelines. Fractional shortening was calculated as FS = (LVEDD - LVESD)/LVEDD.

Mitral inflow was measured by pulsed Doppler at the tips of mitral leaflets from an apical 4-chamber view to obtain early and late filling velocities (E, A), and deceleration time (DT) of early filling velocity. The deceleration slope was calculated as the ratio E/DT. The mitral deceleration index was calculated as the ratio DT/E.

Tissue Doppler Imaging (TDI) was evaluated from the apical 4 chamber view to record mitral annular movements, i.e., peak myocardial systolic (s'), and early and late diastolic velocity (e' and a').

End diastolic volume (EDV) and end systolic volume (ESV) were calculated from the diameters using the Teicholz formula. Ejection fraction, expressed as a percentage (EF%), was calculated by the formula: (EDV-ESV)/EDV*100.

### Heart homogenate preparations

Rats were sacrificed at 9 weeks after STZ injection. Left ventricle (LV) tissues from CTR and STZ rats were rapidly excised, frozen in liquid nitrogen and stored at -80°C. Tissues were homogenized (1g/4ml buffer) in a medium containing 300 mM sucrose, 50 mM K-phosphate, pH 7, 10 mM NaF, 0.3 mM PMSF, 0.5 mM DTT and centrifuged at 35.000g for 30 min. The final pellet was suspended in the same medium and stored in aliquots at -80°C until use.

Protein concentration was determined by Lowry assay[2] using bovine serum albumin as standard, and molecular purity was checked using SDS-polyacrylamide gel electrophoresis.

**Kidney and LV tissues preparations for NKA activity measurements**

Renal outer medulla and LV from CTR rats were dissected and suspended (1g/10 ml) in a sucrose-histidine solution containing 250 mM sucrose, 30 mM histidine and 5 mM EDTA, pH 7.2 and homogenized. The homogenate was centrifuged at 6,000 g for 15 min, the supernatant was decanted and centrifuged at 48,000 g for 30 min. The corresponding pellet contained tissue microsomes. LV microsomes were utilized directly for NKA activity measurements. Conversely, kidney microsomes were further purified on a sucrose gradient. The pellet was suspended in the sucrose-histidine buffer and incubated for 20 min with a sodium-dodecyl-sulphate (SDS) solution, dissolved in a gradient buffer containing 25 mM imidazole and 1 mM EDTA, pH 7.5. The sample was layered on the top of a sucrose discontinuous gradient (10, 15 and 29.4%) and centrifuged at 60,000 g for 115 min. The final pellet was suspended in the gradient buffer.

**SERCA2a and NKA activity measurement**

SERCA2a activity was measured *in vitro* as $^{32}$P-ATP hydrolysis at different $Ca^{2+}$ concentrations (100-3000 nM) as previously described[3]. The heart homogenate (30 µg) was pre-incubated for 5 minutes at 4°C in 80 µL of a solution containing (mM): 100 KCl, 5 $MgCl_2$, 20 Tris, 5 $NaN_3$, 0.001 A23187, 0.001 Ruthenium red, at pH 7.4. After pre-incubation, 20 µl of a 5 mM Tris-ATP solution containing 50 nCi of $^{32}$P-ATP (0.5-3 Ci/mmol, Perkin Elmer) were added. After 15 min at 37°C, the ATP hydrolysis was stopped by acidification with 100 µL ice-cold perchloric acid 20% v/v. $^{32}$P-phosphate was separated by centrifugation with activated charcoal (Norit A, SERVA) and the radioactivity was measured by liquid scintillation counting in a beta counter (Microbeta Trilux, Perkin Elmer). SERCA2a-dependent activity was identified as the portion of total hydrolytic activity inhibited by 10 µM Cyclopiazonic

Acid (CPA). $Ca^{2+}$ concentration-response curves were fitted by using a logistic function to estimate SERCA2a $Ca^{2+}$ affinity ($K_d$ $Ca^{2+}$) and $V_{max}$.

NKA activity was assayed *in vitro* by measuring the release of $^{32}$P-ATP, as previously described[4]. Increasing concentrations of the standard ouabain, or istaroxime, were incubated with 0.3 μg of purified rat kidney enzyme or 20 μg of LV microsomes for 10 min at 37°C in 120 μl final volume of a medium, containing 140 mM NaCl, 3 mM $MgCl_2$, 50 mM Hepes-Tris, 3 mM ATP, pH 7.5. Then, 10 μl of incubation solution containing 10 mM KCl and 20 nCi of $^{32}$P-ATP (3-10 Ci/mmol) were added, the reaction continued for 15 min at 37°C and was stopped by acidification with 20% v/v ice-cold perchloric acid. $^{32}$P was separated by centrifugation with activated Charcoal (Norit A, Serva) and the radioactivity was measured. The inhibitory activity was expressed as percent of the control samples carried out in the absence of ouabain or tested compound. The concentration of compound causing 50% inhibition of the NKA activity ($IC_{50}$) was calculated by using a logistic function.

**Western blot analysis**

Samples of LV homogenates or isolated LV myocytes were separated by SDS-polyacrylamide gel electrophoresis (4-12% Bis-Tris Criterion BIO-RAD gels), blotted for 1h and incubated overnight at 4°C with specific primary antibodies, followed by 1h incubation with specific secondary antibodies, labelled with fluorescent markers (Alexa Fluor or IRDye) and quantified by Odyssey Infrared Imaging System (LI-COR).

Antibodies: polyclonal anti-SERCA2 (N-19; Santa Cruz Biotechnology); monoclonal anti-PLN (2D12, Abcam); polyclonal anti-phospho-Ser$^{16}$-PLN (Upstate Millipore); polyclonal anti-phospho-Thr$^{17}$-PLN (Santa Cruz); polyclonal anti-Collagen type 1 (Chemicon); polyclonal anti-MMP9 (Abcam); polyclonal anti-actin (Sigma).

**Ventricular myocytes preparation**

Male Sprague Dawley LV ventricular myocytes were isolated by using a retrograde coronary perfusion method previously published[5] with minor modifications. Rod-shaped, $Ca^{2+}$-tolerant myocytes were used within 12 h from dissociation.

**Myocyte dimensions and T-tubules (TT) analysis**

Sarcolemmal membranes were stained by incubating isolated LV myocytes with 20 μmol/L di-3-ANEPPDHQ (Life Technologies, Carlsbad, United States)[5] dissolved in high $K^+$ solution (in mmol/L: 40 KCl, 3 MgCl2, 70 KOH, 20 KH2PO4, 0.5 EGTA, 50 L-Glutamic acid, 20 Taurine, 10 HEPES, 10 Glucose, pH 7.4) for 10 min at room temperature. The excitation-contraction uncoupler blebbistatin (17 μmol/L) was added to inhibit cell motion. Cells were then washed before confocal analysis. Images (1024 x 1024 pixels) were collected with Nikon A1R laser-scanning confocal microscopy equipped with a 60x oil-immersion objective; photomultiplier gain and offset were maintained constant throughout each measurement.

Myocyte were stacked (optical sectioning 1.26 μm) to evaluate cell areas over the entire cell thickness; mean cell area was then evaluated. Cell length, defined as the longest length parallel to the longitudinal axis of the myocyte, was measured in the central section of the cell; cell volume was estimated as mean cell area * cell thickness; the myocyte cross-sectional area (CSA) was estimated from the cell volume/cell length ratio.

T-tubules (TT) organization and periodicity was evaluated by a method based on Fast Fourier Transform on 8-bit grayscaled images bu using TTorg plugin (Fiji)[6]. TT images (1024 x 1024 pixels, 50 μm * 50 μm) were collected with Nikon A1R laser-scanning confocal microscopy. The peak amplitude in the Fourier spectrum of the image at the TT frequency (called TT power) and the TT power spectrum profile of each cell were collected.

**Patch clamp measurements**

Ventricular myocytes were clamped in the whole-cell configuration (Axopatch 200-A, Axon Instruments Inc., Union City, CA). During measurements, myocytes were superfused at 2 ml/min with Tyrode's solution containing 154 mM NaCl, 4 mM KCl, 2 mM $CaCl_2$, 1 mM $MgCl_2$, 5 mM HEPES/NaOH, and 5.5 mM D-glucose, adjusted to pH 7.35. A thermostated manifold, allowing for fast (electronically timed) solution switch, was used for cell superfusion. All measurements were performed at 35 ±

0.5°C. The pipette solution contained 110 mM $K^+$-aspartate, 23 mM KCl, 0.2 mM $CaCl_2$ (calculated free-$Ca^{2+}$=$10^{-7}$ M), 3 mM $MgCl_2$, 5 mM HEPES-KOH, 0.5 mM EGTA-KOH, 0.4 mM GTP-$Na^+$ salt, 5 mM ATP-$Na^+$ salt, and 5 mM creatine phosphate $Na^+$ salt, pH 7.3. Membrane capacitance and series resistance were measured in every cell but left uncompensated. Current signals were filtered at 2 KHz and digitized at 5 KHz (Axon Digidata 1200). Trace acquisition and analysis was controlled by dedicated software (Axon pClamp 8.0).

**$Na^+/K^+$ pump current ($I_{NKA}$) recordings**

$I_{NKA}$ was measured as the holding current recorded at -40 mV in the presence of $Ni^{2+}$ (5 mM), nifedipine (5 µM), $Ba^{2+}$ (1 mM) and 4-aminopyridine (2 mM) to minimize contamination by changes in $Na^+/Ca^{2+}$ exchanger, $Ca^{2+}$ and $K^+$ currents, respectively. Tetraethylammonium-Cl (20 mM) and EGTA (5 mM) were added to the pipette solution and intracellular $K^+$ was replaced by $Cs^+$. To optimize the recording conditions, $I_{NKA}$ was enhanced by increasing intracellular $Na^+$ (10 mM) and extracellular $K^+$ (5.4 mM). In each cell, the current was recorded at steady state during exposure to increasing concentrations of the drug under test and, finally, to a saturating concentration of ouabain (1 mM). All drugs were dissolved in dimethyl sulfoxide (DMSO). Control and test solutions contained maximum 1:200 DMSO. Because $I_{NKA}$ inhibition was expressed as percentage of ouabain effect, the latter was used as the asymptote for the estimation of $IC_{50}$ values whenever possible.

A subset of cells was incubated with the $Na^+$ indicator Ion NaTRIUM Green-2 AM (5 µM, Abcam) to evaluate changes in intracellular $Na^+$ ($Na^+_i$) together with changes in membrane current (see below).

**Intracellular $Na^+$ ($Na^+_i$) dynamics**

$Na^+_i$ was monitored in I-clamp condition under physiological condition (Tyrode solution) and in V-clamp condition under modified Tyrode's solution suitable to measure $I_{NKA}$ at the same time (see above). Myocytes were incubated for 30 min with the $Na^+$ indicator Ion NaTRIUM Green-2 AM (5 µM, Abcam) and then washed for 15 min to allow dye de-esterification. Dye emission was collected through a 535 nm

band pass filter, converted to voltage, low-pass filtered (100 Hz) and digitized at 2 kHz after further low-pass digital filtering (FFT, 50 Hz).

**Intracellular $Ca^{2+}$ ($Ca^{2+}_i$) dynamics**

Myocytes were incubated in Tyrode solution for 30 min with the membrane-permeant form of the dye, Fluo4-AM (10 μmol/L), and then washed for 15 min to allow dye de-esterification. Fluo4 emission was collected through a 535 nm band pass filter, converted to voltage, low-pass filtered (100 Hz) and digitized at 2 kHz after further low-pass digital filtering (FFT, 50 Hz).

After subtraction of background luminescence, a reference fluorescence ($F_0$) value was used for signal normalization ($F/F_0$) (see below for details). Whenever possible, fluorescence was calibrated in nmol/L by estimating in each cell the maximal fluorescence ($F_{max}$) by increasing at the end of the experiment the intracellular $Ca^{2+}$ concentration through a gentle patch damage. Fluorescence was converted to $[Ca]_f$ according to Eq. S1:

$$[Ca]_f = F * K_d/(F_{max} - F) \qquad \text{(Eq. S1)}$$

assuming a dye $Ca^{2+}$ dissociation constant ($K_d$) = 400 nmol/L.

*$Ca^{2+}_i$ dynamics in field stimulated cells*

Intracellular $Ca^{2+}$ dynamics were measured in Fluo4-loaded field-stimulated (2 Hz) cardiomyocytes superfused with Tyrode's solution. To highlight the ability of SR to uptake $Ca^{2+}$ at resting (SERCA function) a post-rest potentiation protocol was applied (Fig S1). Briefly, voltage-induced $Ca^{2+}$ transients ($Ca_T$) were evocated at 2 Hz and steady state $Ca_T$ ($ssCa_T$) were interrupted by increasing resting pauses (1-5-10-20 s). The amplitude of 1st $Ca_T$ evocated following each resting pause was then normalized to the amplitude of the pre-pause $ssCa_T$ to evaluate SR $Ca^{2+}$ compartmentalization during rest intervals. $ssCa_T$ was evaluated in terms of diastolic $Ca^{2+}$ ($Ca_D$) and $Ca_T$ amplitude. The SR $Ca^{2+}$ content ($Ca_{SR}$) was estimated at steady-state by applying an electronically timed 10 mM caffeine pulse. SR $Ca^{2+}$ fractional release (FR) was obtained as the ratio between voltage-induced $Ca_T$ and caffeine-induced $Ca_T$ ($Ca_{SR}$)

amplitude. Moreover, $Ca_T$ decay kinetic was estimated by measuring decay $t_{0.5}$. Furthermore, after SR $Ca^{2+}$ depletion by caffeine, cells were de novo stimulated and $Ca_D$ values during the reloading process were monitored. Resting $Ca^{2+}$ following SR depletion was used as reference fluorescence ($F_0$) for signal normalization ($F/F_0$).
Spontaneous $Ca^{2+}$ release (SCR) events were evaluated in each group at resting and during diastole. A fluorescence increase > 3SD the resting fluorescence was considered a SCR.

*$Ca^{2+}{}_i$ dynamics in patch-clamped cells*

Firstly, action potential (AP)-clamp experiments were performed (at 2 Hz) to evaluate changes in $Ca_T$ amplitude and $Ca_{SR}$ strictly dependent on AP durations (APDs) only. To this end two AP waveforms were used as command signals in V-clamp condition and both were applied to the same cell: a "short AP" and a "long AP", representative of the CTR and STZ group in terms of AP characteristics respectively. $Ca_{SR}$ was estimated as usual at steady state by caffeine superfusion and it was quantified by integrating inward NCX current ($I_{NCX}$) elicited during caffeine superfusion at -80 mV. At the end of the experiment, $F_{max}$ was estimated in each cell by gentle patch damage to convert fluorescence signals in $Ca_f$.
Thus, to highlight direct effects on $Ca^{2+}$ handling not depending on electrical activity modifications, $Ca^{2+}{}_i$ dynamics were also evaluated in voltage-clamped cells by standard V-clamp protocols. $BaCl_2$ (1 mM) and 4-aminopyridine (2 mM) were added to Tyrode's solution to block $K^+$ channels. Transmembrane current and cytosolic $Ca^{2+}$ were simultaneously recorded during a train of depolarizing (100 ms) pulses to 0 mV (0.25 Hz) from a holding potential of -40 mV. At steady state condition, an electronically timed 10 mM caffeine pulse was applied at the same cycle length to estimate $Ca_{SR}$. Fluorescence signal was converted to $Ca_f$ (see above) by measuring $F_{max}$ in each cell; $Ca_T$ amplitude, $Ca_{SR}$ and fractional release (FR) were evaluated. $Ca_{SR}$ was estimated by integrating $I_{NCX}$ elicited by caffeine and by measuring the amplitude of caffeine-induced $Ca_T$, obtaining similar results. Data from caffeine-induced $Ca_T$ are reported in Fig 4B. The slope of the $I_{NCX}/Ca_{SR}$ relationship during the final third of the caffeine-induced $Ca_T$ was used to estimate NCX 'conductance'.

$Ca^{2+}$ influx through L-type $Ca^{2+}$ channel ($Ca_L$) was evaluated integrating the nifedipine (10 μM)-sensitive current during the activation pulse at the peak of the evocated $Ca_T$ and then converted to nmol of $Ca^{2+}$. Accordingly, the excitation-release (ER) gain was calculated as the ratio between the fraction of nmol of $Ca^{2+}$ released by SR and nmol of $Ca^{2+}$ entered in the cell ($Ca_T$ amplitude-$Ca_L$)/$Ca_L$). $I_{CaL}$ inactivation kinetic was evaluated interpolating current decay with a bi-exponential function; fast and slow decay time constant ($\tau_{fast}$ and $\tau_{slow}$) and the proportion of fast or slow component to the total decay (e.g. $A_{fast}/A_{tot}$) were estimated.

Finally, to estimate SR uptake function in the absence of NCX and NKA function, SR reloading protocol was applied in V-clamped cells by removing $Na^+$ from both sides of the sarcolemma as previously described[1,7,8]. Cells were incubated in a $Na^+/Ca^{2+}$-free solution (replaced by equimolar $Li^+$ and 1 mM EGTA) added with 4-aminopyridine (2 mM) to block $K^+$ channels. The pipette solution was $Na^+$-free ($Na^+$ salts were replaced by $Mg^{2+}$ or Tris salts). The protocol consisted in emptying the SR by a caffeine pulse (with 154 mM $Na^+$ to allow $Ca^{2+}$ extrusion through NCX) and then progressively refilling it by voltage steps to 0 mV activating $Ca^{2+}$ influx through $I_{CaL}$ in the presence of 1 mM $Ca^{2+}$ (Fig S2). Kinetics of SR $Ca^{2+}$ reloading was evaluated in terms of rate of $Ca_T$ amplitude and ER gain enhancement during the loading process. ER gain in this protocol setting was simply evaluated as the ratio between $Ca_T$ amplitude and $Ca_L$ influx at the peak of $Ca_T$ within each pulse. Moreover, we considered the time constant of $Ca_T$ decay ($\tau_{decay}$) reflecting $Ca^{2+}$ transport rate across the SR membrane, a functional index of SERCA2a activity.

**$Ca^{2+}$ sparks rate and characteristics**

Spontaneous unitary $Ca^{2+}$ release events ($Ca^{2+}$ sparks) were recorded at room temperature in Fluo 4-AM (10μM) loaded myocytes at resting condition. Tyrode's bath solution contained 1 mM $CaCl_2$. Images were acquired at x60 magnification in line-scan mode (*xt*) at 0.5 kHz by confocal Nikon A1R microscope. Each cell was scanned along a longitudinal line and #10 *xt* frames (512 pxls x 512 pxls) were acquired. Non-cell fluorescence was acquired too to allow background fluorescence measurement. Confocal setting parameters were kept constant throughout all

experimental groups to permit group comparison analysis. Images were analyzed by SparkMaster plugin (Fiji) software[9]. Automatic spark detection threshold (criteria) was imposed to 3.8. Only in focus $Ca^{2+}$ sparks (amplitude > 0.3) were considered to quantify their characteristics. In particular, the following spark parameters were measured: frequency (N of events/s/100μm), amplitude ($\Delta F/F_0$), full width at half-maximal amplitude (FWHM, μm), full duration at half-maximal amplitude (FDHM, ms), full width (FW, μm) and full duration (FD, ms), time to peak (ttp, ms) and decay time constant (τ, ms). Spark mass (spark amplitude*1.206* $FWHM^3$) was also calculated as index of $Ca^{2+}$ spark volume[10].

**Compounds**

Stock Fluo4-AM (1 mM in DMSO) and Ion NaTRIUM Green-2 (1 mM in DMSO) solutions were diluted in Tyrode's solution. Istaroxime was dissolved in DMSO at 10-100 mM and then diluted to get final concentrations from 100 nM to 1 mM. The final DMSO did not exceed 0.1% (if it is not different specify). Istaroxime was synthesized at SciAnda (/Changshu) Pharmaceuticals Ltd, Jiangsu (China). Fluo4-AM from ThermoFisher Scientific-Life Technologies Italia, Ion NaTRIUM Green-2 from Abcam and all other chemicals from Merck (Darmstadt, Germany).

**References**


1. Rocchetti M, Besana A, Mostacciuolo G, Micheletti R, Ferrari P, Sarkozi S, Szegedi C, Jona I, Zaza A. Modulation of sarcoplasmic reticulum function by Na+/K + pump inhibitors with different toxicity: Digoxin and PST2744 [(E,Z)-3-((2-aminoethoxy)imino)androstane-6,17-dione hydrochloride]. *J Pharmacol Exp Ther* 2005;**313**:207–215.

2. Lowry OH, Rosebrough NJ, Farr AL, Randall RJ. Protein measurement with the Folin phenol reagent. *J Biol Chem* 1951;**193**:265–275.

3. Micheletti R, Palazzo F, Barassi P, Giacalone G, Ferrandi M, Schiavone A, Moro B, Parodi O, Ferrari P, Bianchi G. Istaroxime, a Stimulator of

Sarcoplasmic Reticulum Calcium Adenosine Triphosphatase Isoform 2a Activity, as a Novel Therapeutic Approach to Heart Failure. *Am J Cardiol* 2007;**99**:24A-32A.

4. Ferrandi M, Tripodi G, Salardi S, Florio M, Modica R, Barassi P, Parenti P, Shainskaya A, Karlish S, Bianchi G, Ferrari P. Renal Na,K-ATPase in genetic hypertension. *Hypertension* 1996;**28**:1018–1025.

5. Rocchetti M, Sala L, Rizzetto R, Irene Staszewsky L, Alemanni M, Zambelli V, Russo I, Barile L, Cornaghi L, Altomare C, Ronchi C, Mostacciuolo G, Lucchetti J, Gobbi M, Latini R, Zaza A. Ranolazine prevents INaL enhancement and blunts myocardial remodelling in a model of pulmonary hypertension. *Cardiovasc Res* 2014;**104**:37–48.

6. Pasqualin C, Gannier F, Malécot CO, Bredeloux P, Maupoil V. Automatic quantitative analysis of t-tubule organization in cardiac myocytes using ImageJ. *Am J Physiol - Cell Physiol* 2015;**308**:C237-45.

7. Rocchetti M, Alemanni M, Mostacciuolo G, Barassi P, Altomare C, Chisci R, Micheletti R, Ferrari P, Zaza A. Modulation of sarcoplasmic reticulum function by PST2744 [Istaroxime; (E,Z)-3-((2-aminoethoxy)imino) androstane-6,17-dione hydrochloride] in a pressure-overload heart failure model. *J Pharmacol Exp Ther* 2008;**326**:957–965.

8. Alemanni M, Rocchetti M, Re D, Zaza A. Role and mechanism of subcellular Ca2+ distribution in the action of two inotropic agents with different toxicity. *J Mol Cell Cardiol* 2011;**50**:910–918.

9. Picht E, Zima A V., Blatter LA, Bers DM. SparkMaster: Automated calcium spark analysis with ImageJ. *Am J Physiol - Cell Physiol* 2007;**293**:C1073–C1081.

10. Hollingworth S, Peet J, Chandler WK, Baylor SM. Calcium sparks in intact skeletal muscle fibers of the frog. *J Gen Physiol* 2001;**118**:653–678.

International Journal of
*Molecular Sciences*

MDPI

*Review*

# Human Induced Pluripotent Stem Cells Derived from a Cardiac Somatic Source: Insights for an In-Vitro Cardiomyocyte Platform

**Alessandra Maria Lodrini [1], Lucio Barile [2,3], Marcella Rocchetti [1] and Claudia Altomare [2,*]**

1 Department of Biotechnology and Biosciences, Università degli Studi di Milano-Bicocca, Milano 20126, Italy; a.lodrini@campus.unimib.it (A.M.L.); marcella.rocchetti@unimib.it (M.R.)
2 Fondazione Cardiocentro Ticino, Lugano 6900, Switzerland; lucio.barile@cardiocentro.org
3 Faculty of Biomedical Sciences, Università della Svizzera Italiana, Lugano 6900, Switzerland
* Correspondence: claudia.altomare@cardiocentro.org

Received: 18 December 2019; Accepted: 10 January 2020; Published: 13 January 2020


**Abstract:** Reprogramming of adult somatic cells into induced pluripotent stem cells (iPSCs) has revolutionized the complex scientific field of disease modelling and personalized therapy. Cardiac differentiation of human iPSCs into cardiomyocytes (hiPSC-CMs) has been used in a wide range of healthy and disease models by deriving CMs from different somatic cells. Unfortunately, hiPSC-CMs have to be improved because existing protocols are not completely able to obtain mature CMs recapitulating physiological properties of human adult cardiac cells. Therefore, improvements and advances able to standardize differentiation conditions are needed. Lately, evidences of an epigenetic memory retained by the somatic cells used for deriving hiPSC-CMs has led to evaluation of different somatic sources in order to obtain more mature hiPSC-derived CMs.

**Keywords:** hiPSC-CMs; epigenetic memory; maturation; cell modelling; drug testing

## 1. Introduction

Human induced pluripotent stem cells (hiPSCs) have assumed a pivotal role in research since their discovery in 2007 [1]. The possibility to differentiate them into functional cardiomyocytes (hiPSC-CMs) awakened excitement for the potential use of those cells in repairing and regenerating damaged cardiac tissue [2,3]; however, even though hiPSC-CMs represent an autologous source that overcomes the immunological limitations and ethical concerns belonging to embryonic stem cells (ESCs), the risk of tumor formation and uncontrolled differentiation have restricted this kind of approach. The possibility to characterize specific phenotypes associated with patient-specific genotypes allows the use of hiPSC-derived cells for disease modelling and drug development with very promising results [4–6].

Several works in the past have reported that hiPSCs are similar to ESCs, but it was recently demonstrated that, because of their somatic origin, epigenetic memory can influence their differentiation and maturation processes [7]. Furthermore, quite a few studies have demonstrated that hiPSC-CMs are molecularly and functionally immature and resemble embryonic and neonatal CMs [8–11]. Differences in structural morphology, gene and protein expression, as well as calcium handling and ionic patterns, have been described using a time-course of hiPSC-CMs maturation in-vitro; electrical properties and physiology of derived CMs can dramatically change in a time-dependent way, thus leading to the crucial need to optimize time and culture conditions during differentiation [12].

The focus of this review is to raise the issue of the different limitations and strengths affecting hiPSC-CMs derived from different somatic sources by the same patient, with particular attention to the role of cell origin and the advantages of CMs derived from a cardiac source.

## 2. Reprogramming

The discovery by Takahashi and Yamanaka in 2006 demonstrated that a defined set of factors is able to directly reprogram a somatic cell to an ESC-like state [13]. Out of 24 candidate ESC-associated genes, just four (i.e., *Oct4*, *Sox2*, *Klf4*, and *c-Myc*) have been determined sufficient to convert fibroblasts to a pluripotent cell type, iPSCs. These four "Yamanaka factors" were first constitutively expressed using retroviral vectors in both mouse [13] and human [1] fibroblasts, inducing these terminally differentiated cells to express genes that are typical of ESCs.

The original iPSCs reprogramming strategy is still being used and remains mostly unaltered, but some advances have been made in the delivery of the four "Yamanaka factors" to improve efficiency. iPSCs have been successfully generated using both integrating and non-integrating methods, but the latter seems to have advantages regarding safety due to a reduced risk of genotoxicity and insertional mutagenesis [14]. Integrating methods include retroviral [13] and lentiviral delivery [15], while non-integrating methods include Sendai viruses [16,17], episomal plasmid transfer [18,19], co-MIP [20], piggyBac transposons [21], small molecules [22], miRNAs [23], and protein-mediated delivery [24].

Many cell types have been successfully reprogrammed to pluripotency, including mononuclear cells from blood [25], umbilical cord and placenta [26], urine-derived cells [27], hair keratinocytes [28] and cardiac progenitor cells [29].

The process to attain pluripotency has been described as consisting of three steps (Figure 1) [30,31]. The first one, called initiation, is characterized by the downregulation of signature somatic genes, a metabolic switch from oxidative phosphorylation to glycolysis, an increase in cell proliferation and reactivation of telomerase activity. This stage also requires changes in cell morphology, in particular a mesenchymal-to-epithelial transition (MET), which involves the acquisition of epithelial characteristics as cell polarity and expression of E-cadherin. These morphological changes are important since it is known that the cell shape itself is involved in epigenetic modifications regulating reprogramming [32].

The second phase of reprogramming, called maturation, involves the upregulation of endogenous pluripotency genes. These genes include the alkaline phosphatase, *SSEA1*, *Fbxo15*, *Sall4*, *Oct4*, *Nanog*, *Tra-1-60*, *Esrrb*, and finally *Sox2* [33]. The maturation step of reprogramming is likely the cause of the low efficiency of the reprogramming process and, indeed, a great number of cells in this phase undergo apoptosis or reversion [34].

Only 1% of the cells that initiate reprogramming make it to the third and final step, called stabilization; these are the cells that manage to repress transgene expression and activate endogenous pluripotency genes, becoming "stabilization-competent" [35]. Other changes occurring during the stabilization phase involve, for example, rearrangements in DNA methylation [33].

The core pluripotency gene cocktail is constituted by *Oct4*, *Sox2* and *Nanog*. These transcription factors form a circuitry for pluripotency which is autoregulatory, since all of them are able to regulate the expression of each other. *Oct4*, *Sox2*, and *Nanog* have the ability to activate genes necessary to maintain ESC-like pluripotency and to repress lineage-specific transcription factors, preventing the exit from the pluripotent state [36,37]. Other factors present in reprogramming cocktails, such as *c-Myc* or *Glis1*, are used to facilitate activation of this autoregulatory circuitry by stimulating gene expression and proliferation in general [38,39].

The original reprogramming strategy has been widely used, leading improvements in the cell reprogramming process. However, the translation of iPSC to a clinical setting is challenged by many obstacles, such as frequent incomplete reprogramming of the cells. Indeed, there are differences in the transcriptomes of iPSCs and ESCs and this may result from iPSCs either not activating pluripotency genes in the same way ESCs do, or not completely silencing somatic genes [40]. Moreover, de novo mutations may occur during the reprogramming process and the culture of generated iPSCs [41]. The lack of a rapid and precise test to evaluate the level of reprogramming in iPSCs aggravates this challenge.

To overcome these issues, an alternative approach that bypasses the pluripotent stage has been developed. This strategy, called transdifferentiation or direct reprogramming, allows for the

reprogramming of one somatic cell type directly into another by delivery of single or multiple specific transcription factors of the desired lineage. Different studies have shown that, with this technique, fibroblasts can be directly converted to several other cell types including neurons [42], cardiomyocytes [43], endothelial cells [44], hepatocytes [45] and chondrocytes [46]. However, in these works transdifferentiation did not always translate to human cells as effectively as it does in murine cells [47]. Recently, it has been reported that fibroblasts from human donors can be efficiently converted to myoblasts by the overexpression of MYOD1 and MYCL [48,49]; the myotubes from this study seem a promising cell source for cell therapy when tested in-vitro, but have yet to be studied in-vivo.

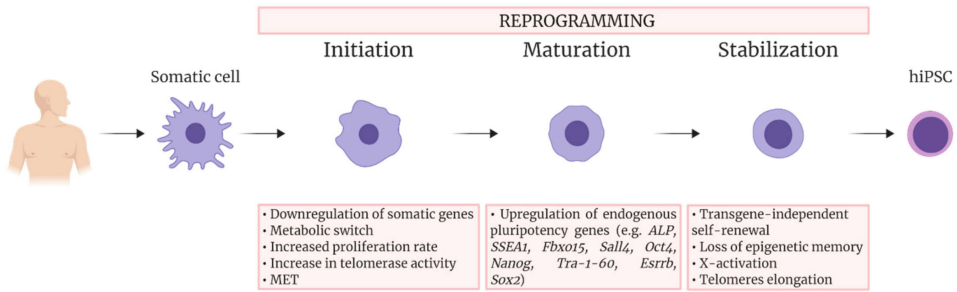


**Figure 1.** Schematic overview of the sequential events occurring during somatic cell reprogramming into human iPSCs. The process consists of three steps, Initiation, Maturation, and Stabilization. The main events occurring during each step are indicated.

## 3. Cardiac Differentiation

Cardiovascular diseases (CVDs) are the greatest cause of mortality among non-communicable and communicable diseases [50]. As such, modelling CVDs in vitro is of great importance to better understand these diseases and to develop new drugs and alternative therapies.

Human CMs can be isolated from patient-derived heart tissue specimens, but the possibility to have access to human cardiac biopsies is rare. Moreover, current protocols to obtain adult primary CMs are still technically challenging making it difficult to obtain large quantities of viable cells. Additionally, after 24–48 h of being kept in culture, in the absence of mechanical and electrical stimuli and of supporting cells (i.e., cardiac fibroblasts), CMs undergo de-differentiation, lose their sarcomeric structure and die [51,52].

The possibility to derive hiPSC-CMs, starting from minimally invasive bioptic samples such as skin tissue, enables the creation of an in-vitro disease- and patient-specific model suitable for preclinical drug screening [53,54], thus replacing non-human cellular and animal models. Indeed, there are several challenges with these models, including their poor predictive capacity owing to inter-species differences in cardiac electrophysiology and human biology [55]. In addition, cell lines such as CHO and HEK293 cells are not ideal models for cardiotoxicity because ectopic expression of a cardiac ion channels does not always recapitulate the physiology of human CMs [56,57].

The initial observation that stem cells could mature into beating CMs was reported when ESCs were first cultured in suspension. These cells spontaneously formed three-dimensional aggregates and inside these "embryoid bodies" (EBs) cells with functional and electrical properties of CMs could be found [58]. A similar process occurring with iPSCs was later reported [59]. Even if it is rather inefficient (~1% purity of CMs) and highly cell line-dependent, the EB method is currently being applied because of its simplicity.

Another method for cardiac differentiation was inspired by embryological cardiovascular development, where the anterior endoderm has a central role in the induction of cardiac mesoderm [60–62]. This method is based on the coculture of iPSCs with END-2 cells, an endoderm-like cell line from mouse carcinoma cells, which may result in the formation of beating clusters [61,63–70]. The preparations resulting from this protocol have a 20–25% purity of CMs.

Different signaling pathways and growth factors have been found involved in successfully inducing cardiac mesoderm in culture [71–73]. Combinations of *BMP4*, *Wnt3a*, and *Activin A* induce gastrulation-like events in iPSCs cultured in a high-density monolayer with a serum- and feeder cell-free system [74]. Spontaneously contracting areas are generally observed after 10 days from induction with BMP/Activin A and, after three weeks, these cell preparations typically consist of ~30% CMs [75]. A similar protocol uses factors that activate the canonical Wnt/β-catenin signaling pathway instead of BMP/Activin *A* to induce cardiac mesoderm [76–78]; this methodology has been described to produce up to 50% CMs [79]. Since all these growth factors don't elicit optimal transcript levels to induce cardiogenesis if used outside the right time frames [80], time-dependent media supplementation is crucial to obtain an efficient lineage-specific differentiation. Commercial kits provide standardized and simplified protocols to increase the reproducibility of the differentiation process [54,81].

## 4. Functional Properties of hiPSC-CMs: Overview and Limitations

The spontaneous beating that appears at the beginning of the differentiation process is generally accepted as sign for the expression, within newly developing hiPSC-CMs, of functional cardiac ion channels and transporters related to generation of action potential (AP) and contractility. Unfortunately, hiPSC-CMs generated with current protocols are still quite immature and existing differentiation techniques appear to work efficiently only with specific cell lines [82–84].

The characterization of electrophysiological properties of differentiating, beating CMs is key to define the level of electrical and mechanical cell maturation. Several ionic currents have been characterized in single hiPSC-CMs by using the patch-clamp technique, such as the sodium ($I_{Na}$), the calcium ($I_{Ca,L}$ and $I_{Ca,T}$) and the potassium ones ($I_{to}$, $I_{Kr}$ and $I_{Ks}$) [85–90]. In particular, sodium and calcium inward components contribute to the depolarizing phases of the electrical activity; while the former is responsible of the fast depolarizing process, the latter has a functional role during the slower depolarization of spontaneous automatic cells together with $I_f$ pacemaker current, or during the plateau in stimulated AP, critical phase for the cell contraction. Otherwise, repolarizing process is due to the outward potassium current contribution of the AP. The balance between inward and outward currents determine the AP duration (APD) and then the refractoriness period, that are crucial in developing arrhythmic events.

The biophysical properties that characterize voltage dependence and activation/inactivation kinetics of each of these ion channels have been studied in relation to time of culture. Furthermore, their current density was found to increase from day 30 to 80 of the differentiation process. Consequently, temporal changes of these properties determine different ionic contribution to the cardiac AP ($I_{Na}$, $I_{CaL}$, $I_{K1}$), leading to heterogeneous AP profiles and parameters (diastolic membrane potential, $E_{diast}$; AP amplitude, APA; AP duration, APD) [91–93].

Based on the AP properties, CMs deriving from a single clone of differentiating iPSCs, frequently results in a mix of cells that can be classified as atrial-, ventricular- and nodal-like CMs [53,59,86]. However, this kind of classification is biased by being operator-dependent and may result in misleading interpretation when comparing CMs with prolonged APD (e.g., hiPSC-CMs from Long QT Syndrome patients) to healthy ones. In this context, tools can be used to identify and/or isolate atrial- or ventricular-like hiPSC-CMs. Recently, Schwach et al. have described a specific marker which is highly enriched in human atrial CMs, but not in ventricular ones, the so called chick ovalbumin upstream promoter transcription factors I and II (COUP-TFI and II) that regulates atrial-specific ion channels gene expression such as KCNA5 encoding $K_v$ 1.5 ($I_{Kur}$ current) and KCNJ3 encoding $K_{ir}$ 3.1 ($I_{KACh}$ current) [94–96]. By fusing this promoter with fluorescent reporter genes (mCherry) and combining it with the well-established human cardiac NKX2.5EGFP/+ reporter, they were able to sort a pure atrial cell population [97].

In Figure 2 the typical features of adult human CM APs are compared to the ones of hiPSC-CMs. In general, nodal-like hiPSC-CMs and sinoatrial CMs APs are comparable, showing spontaneous electrical activity thanks to the contribution of the funny ($I_f$) and calcium ($I_{CaL}$) currents and the

absence of the inward-rectifier potassium channels ($I_{K1}$) that usually maintains negative $E_{diast}$. Major differences between adult and hiPSC-CM AP shapes are present when atrial and ventricular APs are analyzed. Indeed, hiPSC-CMs show more depolarized $E_{diast}$ and they often still have a spontaneous electrical activity, because $I_f$ is still functional and the $I_{K1}$ expression is not enough to maintain an hyperpolarized $E_{diast}$ [98]. As a consequence of the depolarized $E_{diast}$, AP upstroke velocity and APD in hiPSC-CMs are not superimposable to those of adult CMs.

To overcome the lack of $I_{K1}$ expression, the overexpression of Kir 2.1, $I_{K1}$ encoding gene, [99] or an "electronic" maturation by injection of computational $I_{K1}$ in a real time mode (dynamic clamp technique) have been designed [100,101]. In both cases, $E_{diast}$ of derived-CMs hyperpolarizes and the activation of all expressed ion channels allows to develop an AP profile more similar to the one of atrial or ventricular adult CMs. This optimized physiological condition has been used to investigate mechanisms of cardiac cellular disease [4] and predict pharmacological approaches [5,6]. Overall, by adding $I_{K1}$ (through dynamic clamp or channel overexpression), hiPSC-CMs AP becomes more similar to the adult one, suggesting that from the electrophysiological point of view the lack of this channel may be the main reason for the hiPSC-CM immaturity.

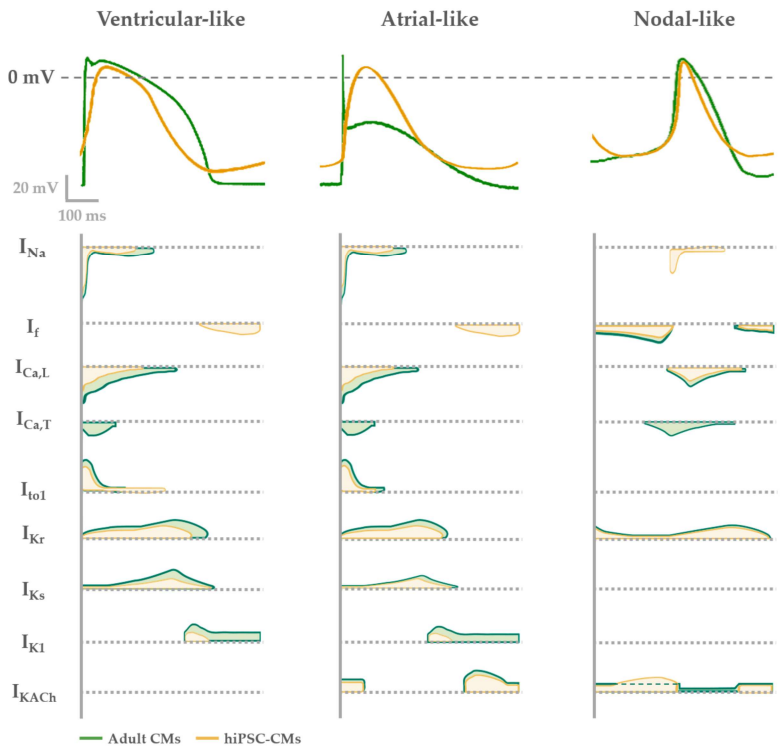


**Figure 2.** Electrophysiological phenotypes of hiPSC-derived (yellow) compared with adult CMs (green). AP shape (upper panel) described in each phenotype (ventricular-, atrial- or nodal-like) is determined by different contribution of cardiac ion currents, represented over time in the lower panel.

Additionally, hiPSC-CMs repolarization reserve is lower in comparison to adult CMs because of the low expression of the slow delayed rectifier channel $I_{Ks}$. Indeed, the functional contribution of this current to the hiPSC-CM AP has been usually seen under β-adrenergic stimulation and reduced repolarization reserve by blocking the rapid component $I_{Kr}$ [102–104]. Only in few papers $I_{Ks}$ has been recorded in basal conditions in hiPSC-CMs [4], a sign of a good cell maturation level. For this reason, the expression of $I_{Ks}$ together with the one of $I_{K1}$ in hiPSC-CMs are usually seen as functional maturation markers of these cells.

Several works have studied $Ca^{2+}$ handling proteins (L-type $Ca^{2+}$ channels, RyR2 in sarcoplasmic reticulum, SERCA2a pump-based $Ca^{2+}$ uptake) and $Ca^{2+}$ transient parameters, as well SR $Ca^{2+}$ release events ($Ca^{2+}$ sparks) [19,105,106]. In hiPSC-CMs there is an immature condition due to a poorly developed sub-cellular T-tubules system and sarcomeric structure; these are crucial elements for $Ca^{2+}$-handling, contractile force and relaxation processes [10,107–110]. U-shaped $Ca^{2+}$ transients in hiPSC-CMs suggest the presence of an immature functional excitation-contraction (EC) coupling compared to native CMs (Figure 3), thus implying that kinetic properties of calcium handling process are slower compared to the adult CMs [106,111].

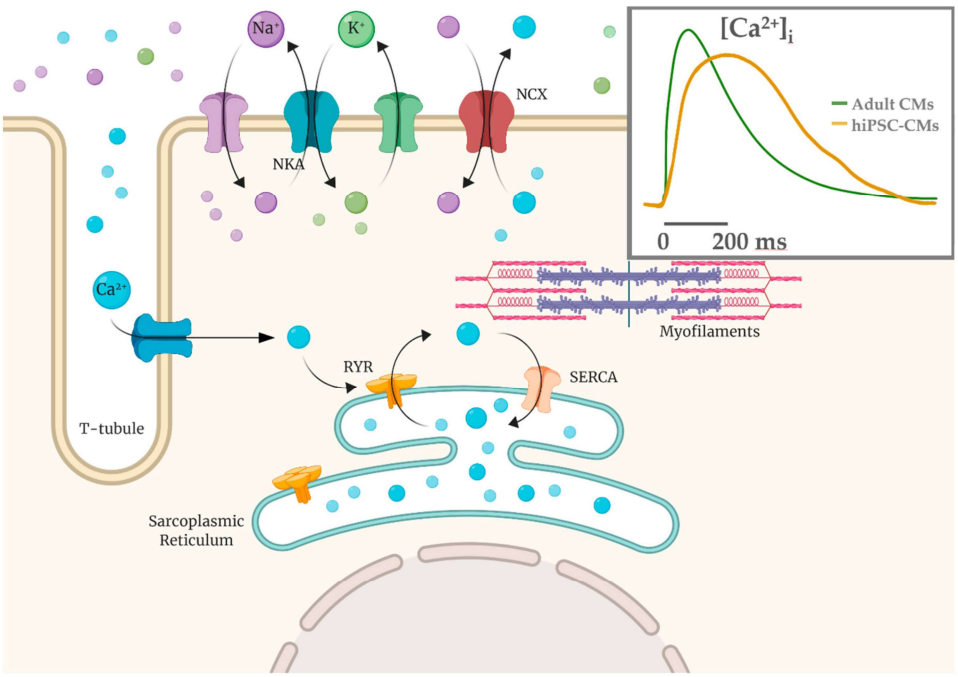


**Figure 3.** Calcium-induced calcium release mechanism (CICR) schematized with T-tubule and sarcomere structures. $Ca^{2+}$ influx via the L-type calcium channels is able to cause a release of the SR $Ca^{2+}$ store via the $Ca^{2+}$-sensitive ryanodine receptors (RYR2). In hiPSC-CMs the $Ca^{2+}$ entry is mainly the extracellular one and calcium handling kinetics are slower (yellow in the inset) compared to adult CMs (green).

Single cells recordings with the patch clamp technique are still the most informative and accurate technique to disclose mechanisms underlying abnormal electrical activity in hiPSC-CMs. However, global electrophysiological information can also be acquired by the multielectrode array (MEA) system by plating spontaneous beating clusters of hiPSC-CM. This technique is useful to evaluate changes in AP rate, duration and conduction velocity.

Platforms of hiPSC-CM to test drug safety by analyzing their proarrhythmic effects have been recently developed. Cardiac electrophysiology models have been applied more and more in the emerging discipline of quantitative system pharmacology (QSP) for cardiac safety prediction [112]. hiPSC-CMs have been applied in screening the proarrhythmic potential of drugs; Sotalol, Dofetilide, and E4031 for hERG channel blockade, Quinidine and Flecainide as sodium channel blockers, and Verapamil and Diltiazem as calcium channel inhibitors represent the main examples [113–115]. These drugs, in conjunction with in silico modelling, have been indeed the major focus of the FDA's Comprehensive In Vitro Proarrythmia Assay (CiPA) initiative [116]. In the last years, the CiPA has been a remarkable initiative that uses in silico models for the assessment of potential proarrhythmic effects of drugs

that are then classified into high, intermediate and low risk for Torsade de Pointes (TdP) tachycardia. In particular, the potential torsadogenic effect of drugs is based on hERG ($I_{Kr}$) or $I_{Ks}$ (slow-delayed rectifier) outward currents inhibition with or without Nav1.5 (transient/late sodium currents, $I_{Na}/I_{NaL}$) and Cav1.2 (L-Type $Ca^{2+}$) inward currents enhancement. The result is a delayed AP repolarization with increased incidence of early afterdepolarization (EADs), leading to ventricular arrhythmias such as TdP and ventricular fibrillation [112,117–119]. Furthermore, a computational approach has been recently developed to recapitulate the human AP profile and drug-induced TdP [120–122].

The CiPA in silico system represents a predictive strategy applied on hiPSC-CMs for development of therapeutic drugs potentially safety in term of cardiac function. Anyway, care must be taken with conclusions about healthy and pathological phenotypes of CMs, that may result misleading because of their immature functional state [89,92,123].

## 5. Pluripotency and Cardiac Differentiation of hiPSCs Derived from Cardiac vs. Non-Cardiac Sources

The reprogramming process can be applied to all type of somatic cells, such as placenta [26] mononuclear cells from blood [25], and keratinocytes [28], from which it is possible to address the differentiation process toward cardiac phenotype. The somatic source may influence the phenotype of iPSCs by affecting both reprogramming and differentiation efficiency. For example, it has been shown how blood-derived iPSCs differentiate into hematopoietic cells more easily in comparison to fibroblast-derived ones [7]; in addition, beta cell derived-iPSCs were more prone to differentiate into insulin-producing cells if compared to ESCs [124].

In agreement with these observations, it has been recently reported the possibility to reprogram explant-derived cells, elsewhere referred as cardiac progenitor cells (CPCs) [125], from human cardiac biopsies obtain functional and terminal differentiated CMs [29]. As schematized in Figure 4, CPC-derived hiPSCs account for improvements in differentiation to CMs in comparison to patient-matched hiPSCs from other somatic sources, such as bone marrow-derived mesenchymal stem cells (BMC) and dermal fibroblasts (HDF) both if cultured in monolayers [126] or EBs [127,128].

These works emphasized the existence of an epigenetic memory retained by iPSCs from their tissue of origin. Reprogramming of somatic cells to pluripotency undergo a reversal in DNA modifications that characterize the cell development, but in some cases these modifications remain unaltered, representing a residual tissue-specific DNA methylation that influences the differentiation potential of iPSCs [129].

Although hiPSC derived from HDFs have been described to produce a higher number of colonies that appear earlier in time, the expression level of pluripotency markers (e.g., *Nanog*, *Oct4*) resulted significantly enhanced in hiPSC from CPCs as compared to both hiPSC from HDFs and from BMCs [126,128]. Inversely, Sanchez-Freire et al. [127] showed that the expression of pluripotency markers was not different between the two hiPSC lineages from different tissues. In both cases, the ability of reprogrammed cells to form three germ layers (i.e., mesoderm, ectoderm, and endoderm), which is considered a hallmark for pluripotency in iPSCs, is not affected by the cell source.

As for the specification potential toward cardiac phenotype, hiPSC derived from cardiac somatic sources showed higher efficiency during the re-differentiation process compared to non-cardiac ones in terms of genes expression for early (NKX 2.5, ISL1) and late cardiogenic transcription factors (HAND2, TBX5, GATA4 and MEF2C) [127,128]. Genes encoding for late cardiac specific markers, such as MYLC2.a, MYH6, TNNI3 and TNNT2, were also overexpressed in cardiac hiPSC-CMs, as well as those encoding for cardiac specific ion channels (HCN1-4, CACNA1C and 1G, RyR2, Cx43) [126,128].

Accordingly, a higher percentage of Troponin T (cTnT)-positive CMs in beating cardiac *Sca1*-iPSC-CMs (cardiac) compared to HDF-iPSC-CMs (non-cardiac) has been reported both by Sanchez-Freire et al. (15 days) [127] and Meraviglia et al. (18–20 days) [128] as a late differentiation marker. Taken together these data support the hypothesis that the cardiac origin of somatic cells to be reprogrammed influences the transcription of cardiac genes during the differentiation of iPSCs.

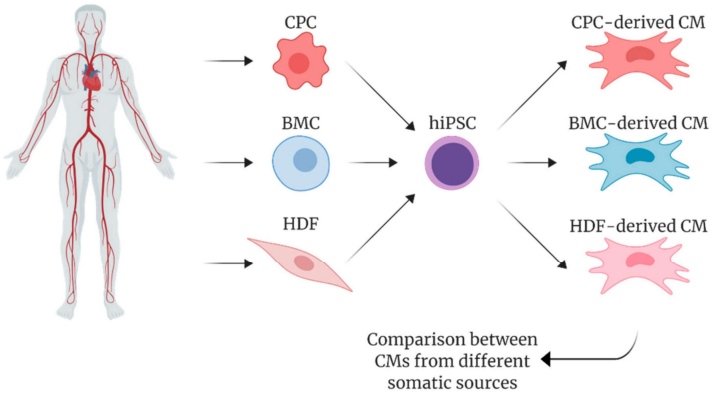


**Figure 4.** Schematic overview of human induced pluripotent stem cells (hiPSCs-CMs) generated from different somatic sources: cardiac progenitor cells (CPCs) from cardiac tissue, bone marrow cells (BMs) from sternal region, and dermal fibroblasts (HDFs) from skin.

While Meraviglia et al. and Pianezzi et al. observed that hiPSC-CMs started beating at 10 days of differentiation, Sanchez-Freire et al. needed five more days to detect the first spontaneous events in their *Sca1*- and HDF-derived CMs. Furthermore, in the studies by Meraviglia et al. and Pianezzi et al. this correlated with an upregulation of cTnI expressed in a sarcomeric pattern. In addition, CPC-derived CMs from Pianezzi et al. are the first population to exhibit early spontaneous beating (at 10 days of differentiation) compared to patient-matched HDF- and BMC-derived ones (15 days), thus suggesting precocity in cell differentiation from cardiac source.

Functionally, Meraviglia et al. and Sanchez-Freire et al. did not observe any differences in term of beating rates between cardiac and non-cardiac sources derived-CMs at 30 days of differentiation. Interestingly, in urine-derived hiPSC-CMs [111] the adaptation of AP to stimulation rates was not observed until 90 days of maturation, while in our hand CPC-derived cells showed $APD_{90}$ shortening when stimulated from 2 to 4 Hz already at 35 days of differentiation (unpublished). Meraviglia et al. noticed that the maturation process affected especially the maximum diastolic potential (MDP) values, that resulted more hyperpolarized in CPC-CMs at 60 day of differentiation. However, Sanchez-Freire et al. did not observe any electrical difference between cardiac- and fibroblast-derived CMs at day 30.

In recent work, it has been observed variability in electrical properties and sensitivity to ion channel blockers in CMs derived from different sources [130]. Accordingly, the MEA measurements by Pianezzi et al. pointed out a higher maturation degree of CPC-CMs by highlighting the presence of $I_{Ks}$, a current more expressed and more functional in CPC-derived CMs in comparison to HDF- and BMC-derived cells. A higher repolarization reserve in CPC-CMs has been demonstrated by highlighting the contribution of $I_{Ks}$ with the specific blocker JNJ303 under $I_{Kr}$ blockade with E4031. In support of this, a JNJ303-dependent QT prolongation resulted strongly enhanced in CPC-CMs in comparison to HDF- and BMC-CMs [126].

In Pianezzi et al. CMs derived from cardiac somatic cells showed differences from an early stage of maturation in calcium handling. Here, not only CPC-, but also HDF- and BMC-CMs at 35 days of differentiation were able to elicit RyR-mediated $Ca^{2+}$ release when exposed to caffeine. However, the quantification of the number of responsive CMs clearly showed that the percentage of CPC-derived ones was significantly greater than the percentages of CMs derived from the other two cell types. On the other hand, the molecular expression of RyR2 and SERCA2a proteins were not different among the three groups. Thus, the "caffeine responsiveness" may represent a functional index, over the expression of cardiac specific genes, for the identification of differentiating CMs. Despite of this, in Sanchez-Freire et al., 30 days of differentiation were not sufficient to evince any differences between CPC- and HDF-CMs, equally immature in $Ca^{2+}$ transient properties.

In general, we can say that, although different somatic cells show a cardiogenic potential when exposed to appropriate cardiac stimuli, cardiac precursor cells seem to be temporally and/or qualitatively more prone to differentiate into functional cardiac cells. Moreover, it must be clarified whether maturation of reprogrammed cells from cardiac sources represents also at late time points a better cellular substrate for cardiac disease modelling, drug testing and tissue regeneration.

## 6. Conclusions

To date, it has been widely described how hiPSC-CMs are able to recapitulate molecular and functional aspects of human heart pathophysiology, thus providing a good tool for disease modelling and development of personalized therapy that involves a pharmacological treatment. A wide range of genetic cardiomyopathies has been modelled using hiPSC-CMs [131], for example familiar long QT (LQT) syndromes [4,85–87,132,133], Brugada syndrome [134,135], Catecholaminergic polymorphic tachycardia (CPVT) [136,137] and atrial fibrillation [138,139].

Unfortunately, the physiological phenotype of iPSC-CMs is heterogeneous both in term of sub-populations of CMs and in term of maturation degree during differentiation protocol, potentially leading to an incorrect interpretation of data. To avoid this, the comparison of their functional parameters with the native and adult counterpart is crucial. The cellular size and morphology, together with the expression of structural proteins and a T-tubular system that ensure the electrical conduction, must be evaluated in order to perform accurate functional analysis and develop 3D platforms; electrophysiological parameters and $Ca^{2+}$ handling features, contractile force, responses to beta-adrenergic stimulation, metabolic profile and conduction velocity must be verified to assess the ability of hiPSC-CM-based models to recapitulate diseases and pathological phenotypes. Furthermore, populations of cells differentiated from iPSCs contain non-cardiomyocyte cells that may interfere with maturation levels, electrophysiological properties and conduction velocity of differentiating CMs, therefore affecting the sensitivity to tested drugs. Standardization of methods and techniques from one laboratory to another is needed for a reliable comparison between healthy and pathological cell models.

Current differentiation protocols that are being tested to optimize the structural and functional maturation degree of hiPSC-CMs use addition of physiological substrates, prolongation of culture time, coculture with endothelial cells or fibroblasts, 3D cell platforms ("organoids") and mechanical and electrical stimulation (dynamic clamp); these techniques, combined with purification methods such as pre-plating or substitution of glucose with lactate in the early maturation phase of CMs, can produce up to 90% cTnT-positive hiPSC-CMs [140–147].

Despite their limitations, thanks to molecular, structural and functional correlations with primary adult CMs, hiPSC-CMs can be considered reliable tool for disease modelling and it represents a valid platform for pharmacological screening [53,54]. Moreover, it is crucial to consider the somatic origin of hiPSC-CMs since it has been clearly demonstrated to impact on time of development and maturation degree of derived CMs in a patient-matched comparison.

The selection of a somatic donor tissue has to be adjusted according to the goal of the study. Since CPCs are derived from cardiac biopsies of patients who undergo heart surgery, the accessibility to human material can be limited. For these reasons, the use of cardiac derived cells as source to generate hiPSCs represents a compromise between the possibility to obtain a more mature CM and the invasiveness and risks of cardiac procedures.

**Author Contributions:** Writing and original draft preparation, A.M.L. and C.A.; figure preparation, A.M.L.; review and editing, C.A., M.R., and L.B. All authors have read and agreed to the published version of the manuscript.

**Funding:** L.B. was supported by research grant of Velux Stiftung (1127), Zurich and by research grant of Swiss National Science Foundation (IZCOZ0_182948) (Switzerland).

**Acknowledgments:** Figures 1, 3 and 4 are created with Biorender.com.

**Conflicts of Interest:** The authors declare no conflict of interest.

## Abbreviations

| | |
|---|---|
| hiPSC | Human Induced Pluripotent Stem Cell |
| CM | Cardiomyocyte |
| ESC | Embryonic Stem Cell |
| MET | Mesenchymal to Epithelial Transition |
| CVD | Cardiovascular Disease |
| CPC | Cardiac Progenitor Cell |
| BMC | Bone Marrow-derived stem Cell |
| HDF | Human Dermal Fibroblast |
| $Na^+$ | Sodium |
| $K^+$ | Potassium |
| $Ca^{2+}$ | Calcium |
| $E_{diast}$ | Diastolic Membrane Potential |
| AP | Action Potential |
| APA | Action Potential Amplitude |
| APD | Action Potential Duration |
| MDP | Maximum Diastolic Potential |
| MEA | Multielectrode Array |
| ECG | Electrocardiogram |
| TdP | Torsade de Pointes |
| LQTS | Long QT Syndrome |
| CPVT | Catecholaminergic Polymorphic Ventricular Tachycardia |
| DCM | Dilated Cardiomyopathies |
| HCM | Hypertrophic Cardiomyopathies |
| QSP | Quantitative System Pharmacology |
| CiPA | Comprehensive In Vitro Proarrythmia Assay |

## References

1. Takahashi, K.; Tanabe, K.; Ohnuki, M.; Narita, M.; Ichisaka, T.; Tomoda, K.; Yamanaka, S. Induction of pluripotent stem cells from adult human fibroblasts by defined factors. *Cell* **2007**, *131*, 861–872. [CrossRef] [PubMed]
2. Li, J.; Minami, I.; Shiozaki, M.; Yu, L.; Yajima, S.; Miyagawa, S.; Shiba, Y.; Morone, N.; Fukushima, S.; Yoshioka, M.; et al. Human Pluripotent Stem Cell-Derived Cardiac Tissue-like Constructs for Repairing the Infarcted Myocardium. *Stem Cell Rep.* **2017**, *9*, 1546–1559. [CrossRef] [PubMed]
3. Funakoshi, S.; Miki, K.; Takaki, T.; Okubo, C.; Hatani, T.; Chonabayashi, K.; Nishikawa, M.; Takei, I.; Oishi, A.; Narita, M.; et al. Enhanced engraftment, proliferation, and therapeutic potential in heart using optimized human iPSC-derived cardiomyocytes. *Sci. Rep.* **2016**, *6*, 19111. [CrossRef] [PubMed]
4. Rocchetti, M.; Sala, L.; Dreizehnter, L.; Crotti, L.; Sinnecker, D.; Mura, M.; Pane, L.S.; Altomare, C.; Torre, E.; Mostacciuolo, G.; et al. Elucidating arrhythmogenic mechanisms of long-QT syndrome CALM1-F142L mutation in patient-specific induced pluripotent stem cell-derived cardiomyocytes. *Cardiovasc. Res.* **2017**, *113*, 531–541. [CrossRef] [PubMed]
5. Laksman, Z.; Wauchop, M.; Lin, E.; Protze, S.; Lee, J.; Yang, W.; Izaddoustdar, F.; Shafaattalab, S.; Gepstein, L.; Tibbits, G.F.; et al. Modeling Atrial Fibrillation using Human Embryonic Stem Cell-Derived Atrial Tissue. *Sci. Rep.* **2017**, *7*, 5268. [CrossRef] [PubMed]
6. Schweizer, P.A.; Darche, F.F.; Ullrich, N.D.; Geschwill, P.; Greber, B.; Rivinius, R.; Seyler, C.; Müller-Decker, K.; Draguhn, A.; Utikal, J.; et al. Subtype-specific differentiation of cardiac pacemaker cell clusters from human induced pluripotent stem cells. *Stem Cell Res. Ther.* **2017**, *8*, 229. [CrossRef]
7. Noguchi, H.; Miyagi-Shiohira, C.; Nakashima, Y. Induced Tissue-Specific Stem Cells and Epigenetic Memory in Induced Pluripotent Stem Cells. *Int. J. Mol. Sci.* **2018**, *19*, 930. [CrossRef]
8. Robertson, C.; Tran, D.D.; George, S.C. Concise review: Maturation phases of human pluripotent stem cell-derived cardiomyocytes. *Stem Cells* **2013**, *31*, 829–837. [CrossRef]

9. Aigha, I.; Raynaud, C. Maturation of pluripotent stem cell derived cardiomyocytes: The new challenge. *Glob. Cardiol. Sci. Pract.* **2016**, *2016*, e201606. [CrossRef]
10. Bedada, F.B.; Wheelwright, M.; Metzger, J.M. Maturation status of sarcomere structure and function in human iPSC-derived cardiac myocytes. *Biochim. Biophys. Acta* **2016**, *1863*, 1829–1838. [CrossRef]
11. Hu, D.; Linders, A.; Yamak, A.; Correia, C.; Kijlstra, J.D.; Garakani, A.; Xiao, L.; Milan, D.J.; van der Meer, P.; Serra, M.; et al. Metabolic Maturation of Human Pluripotent Stem Cell-Derived Cardiomyocytes by Inhibition of HIF1α and LDHA. *Circ. Res.* **2018**, *123*, 1066–1079. [CrossRef] [PubMed]
12. Kumar, N.; Dougherty, J.A.; Manring, H.R.; Elmadbouh, I.; Mergaye, M.; Czirok, A.; Greta Isai, D.; Belevych, A.E.; Yu, L.; Janssen, P.M.L.; et al. Assessment of temporal functional changes and miRNA profiling of human iPSC-derived cardiomyocytes. *Sci. Rep.* **2019**, *9*, 13188. [CrossRef] [PubMed]
13. Takahashi, K.; Yamanaka, S. Induction of pluripotent stem cells from mouse embryonic and adult fibroblast cultures by defined factors. *Cell* **2006**, *126*, 663–676. [CrossRef] [PubMed]
14. Athanasopoulos, T.; Munye, M.M.; Yáñez-Muñoz, R.J. Nonintegrating Gene Therapy Vectors. *Hematol. Oncol. Clin. North. Am.* **2017**, *31*, 753–770. [CrossRef]
15. Somers, A.; Jean, J.C.; Sommer, C.A.; Omari, A.; Ford, C.C.; Mills, J.A.; Ying, L.; Sommer, A.G.; Jean, J.M.; Smith, B.W.; et al. Generation of transgene-free lung disease-specific human induced pluripotent stem cells using a single excisable lentiviral stem cell cassette. *Stem Cells* **2010**, *28*, 1728–1740. [CrossRef]
16. Fusaki, N.; Ban, H.; Nishiyama, A.; Saeki, K.; Hasegawa, M. Efficient induction of transgene-free human pluripotent stem cells using a vector based on Sendai virus, an RNA virus that does not integrate into the host genome. *Proc. Jpn. Acad. Ser. B* **2009**, *85*, 348–362. [CrossRef]
17. Churko, J.M.; Burridge, P.W.; Wu, J.C. Generation of human iPSCs from human peripheral blood mononuclear cells using non-integrative Sendai virus in chemically defined conditions. *Methods Mol. Biol.* **2013**, *1036*, 81–88.
18. Yu, J.; Hu, K.; Smuga-Otto, K.; Tian, S.; Stewart, R.; Slukvin, I.I.; Thomson, J.A. Human induced pluripotent stem cells free of vector and transgene sequences. *Science* **2009**, *324*, 797–801. [CrossRef]
19. Burridge, P.W.; Thompson, S.; Millrod, M.A.; Weinberg, S.; Yuan, X.; Peters, A.; Mahairaki, V.; Koliatsos, V.E.; Tung, L.; Zambidis, E.T. A universal system for highly efficient cardiac differentiation of human induced pluripotent stem cells that eliminates interline variability. *PLoS ONE* **2011**, *6*, e18293. [CrossRef]
20. Diecke, S.; Lu, J.; Lee, J.; Termglinchan, V.; Kooreman, N.G.; Burridge, P.W.; Ebert, A.D.; Churko, J.M.; Sharma, A.; Kay, M.A.; et al. Novel codon-optimized mini-intronic plasmid for efficient, inexpensive, and xeno-free induction of pluripotency. *Sci. Rep.* **2015**, *5*, 8081. [CrossRef]
21. Woltjen, K.; Michael, I.P.; Mohseni, P.; Desai, R.; Mileikovsky, M.; Hämäläinen, R.; Cowling, R.; Wang, W.; Liu, P.; Gertsenstein, M.; et al. piggyBac transposition reprograms fibroblasts to induced pluripotent stem cells. *Nature* **2009**, *458*, 766–770. [CrossRef] [PubMed]
22. Hou, P.; Li, Y.; Zhang, X.; Liu, C.; Guan, J.; Li, H.; Zhao, T.; Ye, J.; Yang, W.; Liu, K.; et al. Pluripotent stem cells induced from mouse somatic cells by small-molecule compounds. *Science* **2013**, *341*, 651–654. [CrossRef] [PubMed]
23. Anokye-Danso, F.; Trivedi, C.M.; Juhr, D.; Gupta, M.; Cui, Z.; Tian, Y.; Zhang, Y.; Yang, W.; Gruber, P.J.; Epstein, J.A.; et al. Highly efficient miRNA-mediated reprogramming of mouse and human somatic cells to pluripotency. *Cell Stem Cell* **2011**, *8*, 376–388. [CrossRef] [PubMed]
24. Zhou, H.; Wu, S.; Joo, J.Y.; Zhu, S.; Han, D.W.; Lin, T.; Trauger, S.; Bien, G.; Yao, S.; Zhu, Y.; et al. Generation of induced pluripotent stem cells using recombinant proteins. *Cell Stem Cell* **2009**, *4*, 381–384. [CrossRef]
25. Loh, Y.H.; Agarwal, S.; Park, I.H.; Urbach, A.; Huo, H.; Heffner, G.C.; Kim, K.; Miller, J.D.; Ng, K.; Daley, G.Q. Generation of induced pluripotent stem cells from human blood. *Blood* **2009**, *113*, 5476–5479. [CrossRef]
26. Cai, J.; Li, W.; Su, H.; Qin, D.; Yang, J.; Zhu, F.; Xu, J.; He, W.; Guo, X.; Labuda, K.; et al. Generation of human induced pluripotent stem cells from umbilical cord matrix and amniotic membrane mesenchymal cells. *J. Biol. Chem.* **2010**, *285*, 11227–11234. [CrossRef]
27. Xue, Y.; Cai, X.; Wang, L.; Liao, B.; Zhang, H.; Shan, Y.; Chen, Q.; Zhou, T.; Li, X.; Hou, J.; et al. Generating a Non-Integrating Human Induced Pluripotent Stem Cell Bank from Urine-Derived Cells. *PLoS ONE* **2013**, *8*, e70573. [CrossRef]
28. Novak, A.; Lorber, A.; Itskovitz-Eldor, J.; Binah, O. Modeling Catecholaminergic Polymorphic Ventricular Tachycardia using Induced Pluripotent Stem Cell-derived Cardiomyocytes. *Rambam Maimonides Med. J.* **2012**, *3*, e0015. [CrossRef]

29. Altomare, C.; Pianezzi, E.; Cervio, E.; Bolis, S.; Biemmi, V.; Benzoni, P.; Camici, G.G.; Moccetti, T.; Barile, L.; Vassalli, G. Human-induced pluripotent stem cell-derived cardiomyocytes from cardiac progenitor cells: Effects of selective ion channel blockade. *Europace* **2016**, *18*, iv67–iv76.
30. Samavarchi-Tehrani, P.; Golipour, A.; David, L.; Sung, H.; Beyer, T.A.; Datti, A.; Woltjen, K.; Nagy, A.; Wrana, J.L. Functional Genomics Reveals a BMP-Driven Mesenchymal-to-Epithelial Transition in the Initiation of Somatic Cell Reprogramming. *Cell Stem Cell* **2010**, *7*, 64–77. [CrossRef]
31. David, L.; Polo, J.M. Phases of reprogramming. *Stem Cell Res.* **2014**, *12*, 754–761. [CrossRef] [PubMed]
32. Downing, T.L.; Soto, J.; Morez, C.; Houssin, T.; Fritz, A.; Yuan, F.; Chu, J.; Patel, S.; Schaffer, D.V.; Li, S. Biophysical regulation of epigenetic state and cell reprogramming. *Nat. Mater.* **2013**, *12*, 1154. [CrossRef] [PubMed]
33. Polo, J.M.; Anderssen, E.; Walsh, R.M.; Schwarz, B.A.; Nefzger, C.M.; Lim, S.M.; Borkent, M.; Apostolou, E.; Alaei, S.; Cloutier, J.; et al. A Molecular Roadmap of Reprogramming Somatic Cells into iPS Cells. *Cell* **2012**, *151*, 1617–1632. [CrossRef] [PubMed]
34. Tanabe, K.; Nakamura, M.; Narita, M.; Takahashi, K.; Yamanaka, S. Maturation, not initiation, is the major roadblock during reprogramming toward pluripotency from human fibroblasts. *Proc. Natl. Acad. Sci. USA* **2013**, *110*, 12172–12179. [CrossRef]
35. Golipour, A.; David, L.; Liu, Y.; Jayakumaran, G.; Hirsch, C.L.; Trcka, D.; Wrana, J.L. A Late Transition in Somatic Cell Reprogramming Requires Regulators Distinct from the Pluripotency Network. *Cell Stem Cell* **2012**, *11*, 769–782. [CrossRef]
36. Pan, G.; Li, J.; Zhou, Y.; Zheng, H.; Pei, D. A negative feedback loop of transcription factors that controls stem cell pluripotency and self-renewal. *FASEB J.* **2006**, *20*, 1730–1732. [CrossRef]
37. Jaenisch, R.; Young, R. Stem Cells, the Molecular Circuitry of Pluripotency and Nuclear Reprogramming. *Cell* **2008**, *132*, 567–582. [CrossRef]
38. Rahl, P.B.; Lin, C.Y.; Seila, A.C.; Flynn, R.A.; McCuine, S.; Burge, C.B.; Sharp, P.A.; Young, R.A. c-Myc Regulates Transcriptional Pause Release. *Cell* **2010**, *141*, 432–445. [CrossRef]
39. Maekawa, M.; Yamaguchi, K.; Nakamura, T.; Shibukawa, R.; Kodanaka, I.; Ichisaka, T.; Kawamura, Y.; Mochizuki, H.; Goshima, N.; Yamanaka, S. Direct reprogramming of somatic cells is promoted by maternal transcription factor Glis1. *Nature* **2011**, *474*, 225–229. [CrossRef]
40. Bilic, J.; Izpisua Belmonte, J.C. Concise review: Induced pluripotent stem cells versus embryonic stem cells: Close enough or yet too far apart? *Stem Cells* **2012**, *30*, 33–41. [CrossRef]
41. Saric, T.; Hescheler, J. Stem cells and nuclear reprogramming. *Minim. Invasive Ther. Allied Technol.* **2008**, *17*, 64–78. [CrossRef] [PubMed]
42. Vierbuchen, T.; Ostermeier, A.; Pang, Z.P.; Kokubu, Y.; Südhof, T.C.; Wernig, M. Direct conversion of fibroblasts to functional neurons by defined factors. *Nature* **2010**, *463*, 1035–1041. [CrossRef] [PubMed]
43. Ieda, M.; Fu, J.D.; Delgado-Olguin, P.; Vedantham, V.; Hayashi, Y.; Bruneau, B.G.; Srivastava, D. Direct reprogramming of fibroblasts into functional cardiomyocytes by defined factors. *Cell* **2010**, *142*, 375–386. [CrossRef] [PubMed]
44. Morita, R.; Suzuki, M.; Kasahara, H.; Shimizu, N.; Shichita, T.; Sekiya, T.; Kimura, A.; Sasaki, K.; Yasukawa, H.; Yoshimura, A. ETS transcription factor ETV2 directly converts human fibroblasts into functional endothelial cells. *Proc. Natl. Acad. Sci. USA* **2015**, *112*, 160–165. [CrossRef]
45. Sekiya, S.; Suzuki, A. Direct conversion of mouse fibroblasts to hepatocyte-like cells by defined factors. *Nature* **2011**, *475*, 390–393. [CrossRef]
46. Yin, S.; Cen, L.; Wang, C.; Zhao, G.; Sun, J.; Liu, W.; Cao, Y.; Cui, L. Chondrogenic transdifferentiation of human dermal fibroblasts stimulated with cartilage-derived morphogenetic protein 1. *Tissue Eng. Part A* **2010**, *16*, 1633–1643. [CrossRef]
47. Pang, Z.P.; Yang, N.; Vierbuchen, T.; Ostermeier, A.; Fuentes, D.R.; Yang, T.Q.; Citri, A.; Sebastiano, V.; Marro, S.; Südhof, T.C.; et al. Induction of human neuronal cells by defined transcription factors. *Nature* **2011**, *476*, 220–223. [CrossRef]
48. Boularaoui, S.M.; Abdel-Raouf, K.M.A.; Alwahab, N.S.A.; Kondash, M.E.; Truskey, G.A.; Teo, J.C.M.; Christoforou, N. Efficient transdifferentiation of human dermal fibroblasts into skeletal muscle: Efficient human skeletal muscle transdifferentiation. *J. Tissue Eng. Regen. Med.* **2018**, *12*, e918–e936. [CrossRef]
49. Shimizu, K.; Ohsumi, S.; Kishida, T.; Mazda, O.; Honda, H. Fabrication of contractile skeletal muscle tissues using directly converted myoblasts from human fibroblasts. *J. Biosci. Bioeng.* **2019**. [CrossRef]

50. World Health Organization. *Noncommunicable Diseases Country Profiles 2018*; World Health Organization: Geneva, Switzerland, 2018.
51. Hoppe, U.C.; Beuckelmann, D.J. Characterization of the hyperpolarization-activated inward current in isolated human atrial myocytes. *Cardiovasc. Res.* **1998**, *38*, 788–801. [CrossRef]
52. Cerbai, E.; Sartiani, L.; DePaoli, P.; Pino, R.; Maccherini, M.; Bizzarri, F.; DiCiolla, F.; Davoli, G.; Sani, G.; Mugelli, A. The properties of the pacemaker current I(F)in human ventricular myocytes are modulated by cardiac disease. *J. Mol. Cell. Cardiol.* **2001**, *33*, 441–448. [CrossRef] [PubMed]
53. Burridge, P.W.; Matsa, E.; Shukla, P.; Lin, Z.C.; Churko, J.M.; Ebert, A.D.; Lan, F.; Diecke, S.; Huber, B.; Mordwinkin, N.M.; et al. Chemically defined generation of human cardiomyocytes. *Nat. Methods* **2014**, *11*, 855–860. [CrossRef] [PubMed]
54. Dell'Era, P.; Benzoni, P.; Crescini, E.; Valle, M.; Xia, E.; Consiglio, A.; Memo, M. Cardiac disease modeling using induced pluripotent stem cell-derived human cardiomyocytes. *World J. Stem Cells* **2015**, *7*, 329–342. [CrossRef] [PubMed]
55. Dixon, J.A.; Spinale, F.G. Large animal models of heart failure: A critical link in the translation of basic science to clinical practice. *Circ. Heart Fail.* **2009**, *2*, 262–271. [CrossRef] [PubMed]
56. Lu, H.R.; Vlaminckx, E.; Hermans, A.N.; Rohrbacher, J.; Van Ammel, K.; Towart, R.; Pugsley, M.; Gallacher, D.J. Predicting drug-induced changes in QT interval and arrhythmias: QT-shortening drugs point to gaps in the ICHS7B Guidelines. *Br. J. Pharmacol.* **2008**, *154*, 1427–1438. [CrossRef] [PubMed]
57. Mathur, A.; Loskill, P.; Shao, K.; Huebsch, N.; Hong, S.; Marcus, S.G.; Marks, N.; Mandegar, M.; Conklin, B.R.; Lee, L.P.; et al. Human iPSC-based Cardiac Microphysiological System for Drug Screening Applications. *Sci. Rep.* **2015**, *5*, 1–7. [CrossRef]
58. Itskovitz-Eldor, J.; Schuldiner, M.; Karsenti, D.; Eden, A.; Yanuka, O.; Amit, M.; Soreq, H.; Benvenisty, N. Differentiation of human embryonic stem cells into embryoid bodies compromising the three embryonic germ layers. *Mol. Med.* **2000**, *6*, 88–95. [CrossRef]
59. Zhang, J.; Wilson, G.F.; Soerens, A.G.; Koonce, C.H.; Yu, J.; Palecek, S.P.; Thomson, J.A.; Kamp, T.J. Functional cardiomyocytes derived from human induced pluripotent stem cells. *Circ. Res.* **2009**, *104*, e30–e41. [CrossRef]
60. Synnergren, J.; Åkesson, K.; Dahlenborg, K.; Vidarsson, H.; Améen, C.; Steel, D.; Lindahl, A.; Olsson, B.; Sartipy, P. Molecular Signature of Cardiomyocyte Clusters Derived from Human Embryonic Stem Cells. *Stem Cells* **2008**, *26*, 1831–1840. [CrossRef]
61. Cao, F.; Wagner, R.A.; Wilson, K.D.; Xie, X.; Fu, J.-D.; Drukker, M.; Lee, A.; Li, R.A.; Gambhir, S.S.; Weissman, I.L.; et al. Transcriptional and Functional Profiling of Human Embryonic Stem Cell-Derived Cardiomyocytes. *PLoS ONE* **2008**, *3*, e3474. [CrossRef]
62. Xu, X.Q.; Soo, S.Y.; Sun, W.; Zweigerdt, R. Global Expression Profile of Highly Enriched Cardiomyocytes Derived from Human Embryonic Stem Cells. *Stem Cells* **2009**, *27*, 2163–2174. [CrossRef] [PubMed]
63. Mummery, C.; Ward-van Oostwaard, D.; Doevendans, P.; Spijker, R.; van den Brink, S.; Hassink, R.; van der Heyden, M.; Opthof, T.; Pera, M.; de la Riviere, A.B.; et al. Differentiation of human embryonic stem cells to cardiomyocytes: Role of coculture with visceral endoderm-like cells. *Circulation* **2003**, *107*, 2733–2740. [CrossRef] [PubMed]
64. Passier, R.; Oostwaard, D.W.; Snapper, J.; Kloots, J.; Hassink, R.J.; Kuijk, E.; Roelen, B.; de la Riviere, A.B.; Mummery, C. Increased Cardiomyocyte Differentiation from Human Embryonic Stem Cells in Serum-Free Cultures. *Stem Cells* **2005**, *23*, 772–780. [CrossRef] [PubMed]
65. Willems, E.; Bushway, P.J.; Mercola, M. Natural and Synthetic Regulators of Embryonic Stem Cell Cardiogenesis. *Pediatr. Cardiol.* **2009**, *30*, 635–642. [CrossRef] [PubMed]
66. Freund, C.; Davis, R.P.; Gkatzis, K.; Ward-van Oostwaard, D.; Mummery, C.L. The first reported generation of human induced pluripotent stem cells (iPS cells) and iPS cell-derived cardiomyocytes in the Netherlands. *Neth. Heart J.* **2010**, *18*, 51–54. [PubMed]
67. Kang, Y.; Nagy, J.M.; Polak, J.M.; Mantalaris, A. Proteomic Characterization of the Conditioned Media Produced by the Visceral Endoderm-Like Cell Lines HepG2 and END2: Toward a Defined Medium for the Osteogenic/Chondrogenic Differentiation of Embryonic Stem Cells. *Stem Cells Dev.* **2008**, *18*, 77–92. [CrossRef] [PubMed]
68. Arrell, D.K.; Niederländer, N.J.; Faustino, R.S.; Behfar, A.; Terzic, A. Cardioinductive Network Guiding Stem Cell Differentiation Revealed by Proteomic Cartography of Tumor Necrosis Factor α-Primed Endodermal Secretome. *Stem Cells* **2008**, *26*, 387–400. [CrossRef]

69. Freund, C.; Oostwaard, D.W.; Monshouwer-Kloots, J.; van den Brink, S.; van Rooijen, M.; Xu, X.; Zweigerdt, R.; Mummery, C.; Passier, R. Insulin Redirects Differentiation from Cardiogenic Mesoderm and Endoderm to Neuroectoderm in Differentiating Human Embryonic Stem Cells. *Stem Cells* **2008**, *26*, 724–733. [CrossRef]
70. Xu, X.Q.; Graichen, R.; Soo, S.Y.; Balakrishnan, T.; Bte Rahmat, S.N.; Sieh, S.; Tham, S.C.; Freund, C.; Moore, J.; Mummery, C.; et al. Chemically defined medium supporting cardiomyocyte differentiation of human embryonic stem cells. *Differentiation* **2008**, *76*, 958–970. [CrossRef]
71. Winnier, G.; Blessing, M.; Labosky, P.A.; Hogan, B.L. Bone morphogenetic protein-4 is required for mesoderm formation and patterning in the mouse. *Genes Dev.* **1995**, *9*, 2105–2116. [CrossRef]
72. Marvin, M.J.; Di Rocco, G.; Gardiner, A.; Bush, S.M.; Lassar, A.B. Inhibition of Wnt activity induces heart formation from posterior mesoderm. *Genes Dev.* **2001**, *15*, 316–327. [CrossRef] [PubMed]
73. Naujok, O.; Diekmann, U.; Lenzen, S. The Generation of Definitive Endoderm from Human Embryonic Stem Cells is Initially Independent from Activin A but Requires Canonical Wnt-Signaling. *Stem Cell Rev. Rep.* **2014**, *10*, 480–493. [CrossRef] [PubMed]
74. Xu, C.; Police, S.; Hassanipour, M.; Gold, J.D. Cardiac Bodies: A Novel Culture Method for Enrichment of Cardiomyocytes Derived from Human Embryonic Stem Cells. *Stem Cells Dev.* **2006**, *15*, 631–639. [CrossRef] [PubMed]
75. Laflamme, M.A.; Chen, K.Y.; Naumova, A.V.; Muskheli, V.; Fugate, J.A.; Dupras, S.K.; Reinecke, H.; Xu, C.; Hassanipour, M.; Police, S.; et al. Cardiomyocytes derived from human embryonic stem cells in pro-survival factors enhance function of infarcted rat hearts. *Nat. Biotechnol.* **2007**, *25*, 1015–1024. [CrossRef]
76. Naito, A.T.; Shiojima, I.; Akazawa, H.; Hidaka, K.; Morisaki, T.; Kikuchi, A.; Komuro, I. Developmental stage-specific biphasic roles of Wnt/β-catenin signaling in cardiomyogenesis and hematopoiesis. *Proc. Natl. Acad. Sci. USA* **2006**, *103*, 19812–19817. [CrossRef]
77. Ueno, S.; Weidinger, G.; Osugi, T.; Kohn, A.D.; Golob, J.L.; Pabon, L.; Reinecke, H.; Moon, R.T.; Murry, C.E. Biphasic role for Wnt/beta-catenin signaling in cardiac specification in zebrafish and embryonic stem cells. *Proc. Natl. Acad. Sci. USA* **2007**, *104*, 9685–9690. [CrossRef]
78. Tran, T.H.; Wang, X.; Browne, C.; Zhang, Y.; Schinke, M.; Izumo, S.; Burcin, M. Wnt3a-Induced Mesoderm Formation and Cardiomyogenesis in Human Embryonic Stem Cells. *Stem Cells* **2009**, *27*, 1869–1878. [CrossRef]
79. Yang, L.; Soonpaa, M.H.; Adler, E.D.; Roepke, T.K.; Kattman, S.J.; Kennedy, M.; Henckaerts, E.; Bonham, K.; Abbott, G.W.; Linden, R.M.; et al. Human cardiovascular progenitor cells develop from a KDR + embryonic-stem-cell-derived population. *Nature* **2008**, *453*, 524–528. [CrossRef]
80. Schlange, T.; Andrée, B.; Arnold, H.H.; Brand, T. BMP2 is required for early heart development during a distinct time period. *Mech. Dev.* **2000**, *91*, 259–270. [CrossRef]
81. Ross, S.; Holliday, M.; Lim, S.; Semsarian, C. Characterization of the first induced pluripotent stem cell line generated from a patient with autosomal dominant catecholaminergic polymorphic ventricular tachycardia due to a heterozygous mutation in cardiac calsequestrin-2. *Stem Cell Res.* **2019**, *37*, 101450. [CrossRef]
82. Matsa, E.; Burridge, P.W.; Wu, J.C. Human stem cells for modeling heart disease and for drug discovery. *Sci. Transl. Med.* **2014**, *6*, 239ps6. [CrossRef] [PubMed]
83. Karakikes, I.; Ameen, M.; Termglinchan, V.; Wu, J.C. Human induced pluripotent stem cell-derived cardiomyocytes: Insights into molecular, cellular, and functional phenotypes. *Circ. Res.* **2015**, *117*, 80–88. [CrossRef] [PubMed]
84. Tu, C.; Chao, B.S.; Wu, J.C. Strategies for Improving the Maturity of Human Induced Pluripotent Stem Cell-Derived Cardiomyocytes. *Circ. Res.* **2018**, *123*, 512–514. [CrossRef] [PubMed]
85. Moretti, A.; Bellin, M.; Welling, A.; Jung, C.B.; Lam, J.T.; Bott-Flügel, L.; Dorn, T.; Goedel, A.; Höhnke, C.; Hofmann, F.; et al. Patient-specific induced pluripotent stem-cell models for long-QT syndrome. *N. Engl. J. Med.* **2010**, *363*, 1397–1409. [CrossRef]
86. Ma, J.; Guo, L.; Fiene, S.J.; Anson, B.D.; Thomson, J.A.; Kamp, T.J.; Kolaja, K.L.; Swanson, B.J.; January, C.T. High purity human-induced pluripotent stem cell-derived cardiomyocytes: Electrophysiological properties of action potentials and ionic currents. *Am. J. Physiol. Heart Circ. Physiol.* **2011**, *301*, H2006–H2017. [CrossRef]
87. Yazawa, M.; Hsueh, B.; Jia, X.; Pasca, A.M.; Bernstein, J.A.; Hallmayer, J.; Dolmetsch, R.E. Using induced pluripotent stem cells to investigate cardiac phenotypes in Timothy syndrome. *Nature* **2011**, *471*, 230–234. [CrossRef]

88. Davis, R.P.; Casini, S.; van den Berg, C.W.; Hoekstra, M.; Remme, C.A.; Dambrot, C.; Salvatori, D.; Oostwaard, D.W.; Wilde, A.A.M.; Bezzina, C.R.; et al. Cardiomyocytes derived from pluripotent stem cells recapitulate electrophysiological characteristics of an overlap syndrome of cardiac sodium channel disease. *Circulation* **2012**, *125*, 3079–3091. [CrossRef]
89. Ivashchenko, C.Y.; Pipes, G.C.; Lozinskaya, I.M.; Lin, Z.; Xiaoping, X.; Needle, S.; Grygielko, E.T.; Hu, E.; Toomey, J.R.; Lepore, J.J.; et al. Human-induced pluripotent stem cell-derived cardiomyocytes exhibit temporal changes in phenotype. *Am. J. Physiol. Heart Circ. Physiol.* **2013**, *305*, H913–H922. [CrossRef]
90. Goversen, B.; van der Heyden, M.A.G.; van Veen, T.A.B.; de Boer, T.P. The immature electrophysiological phenotype of iPSC-CMs still hampers in vitro drug screening: Special focus on IK1. *Pharmacol. Ther.* **2018**, *183*, 127–136. [CrossRef]
91. Otsuji, T.G.; Minami, I.; Kurose, Y.; Yamauchi, K.; Tada, M.; Nakatsuji, N. Progressive maturation in contracting cardiomyocytes derived from human embryonic stem cells: Qualitative effects on electrophysiological responses to drugs. *Stem Cell Res.* **2010**, *4*, 201–213. [CrossRef]
92. Ben-Ari, M.; Naor, S.; Zeevi-Levin, N.; Schick, R.; Ben Jehuda, R.; Reiter, I.; Raveh, A.; Grijnevitch, I.; Barak, O.; Rosen, M.R.; et al. Developmental changes in electrophysiological characteristics of human-induced pluripotent stem cell-derived cardiomyocytes. *Heart Rhythm.* **2016**, *13*, 2379–2387. [CrossRef] [PubMed]
93. Veerman, C.C.; Mengarelli, I.; Lodder, E.M.; Kosmidis, G.; Bellin, M.; Zhang, M.; Dittmann, S.; Guan, K.; Wilde, A.A.M.; Schulze-Bahr, E.; et al. Switch from Fetal to Adult SCN5A Isoform in Human Induced Pluripotent Stem Cell-Derived Cardiomyocytes Unmasks the Cellular Phenotype of a Conduction Disease-Causing Mutation. *J. Am. Heart Assoc.* **2017**, *6*, e005135. [CrossRef] [PubMed]
94. Schwach, V.; Verkerk, A.O.; Mol, M.; Monshouwer-Kloots, J.J.; Devalla, H.D.; Orlova, V.V.; Anastassiadis, K.; Mummery, C.L.; Davis, R.P.; Passier, R. A COUP-TFII Human Embryonic Stem Cell Reporter Line to Identify and Select Atrial Cardiomyocytes. *Stem Cell Rep.* **2017**, *9*, 1765–1779. [CrossRef] [PubMed]
95. Devalla, H.D.; Schwach, V.; Ford, J.W.; Milnes, J.T.; El-Haou, S.; Jackson, C.; Gkatzis, K.; Elliott, D.A.; Chuva de Sousa Lopes, S.M.; Mummery, C.L.; et al. Atrial-like cardiomyocytes from human pluripotent stem cells are a robust preclinical model for assessing atrial-selective pharmacology. *EMBO Mol. Med.* **2015**, *7*, 394–410. [CrossRef]
96. Argenziano, M.; Lambers, E.; Hong, L.; Sridhar, A.; Zhang, M.; Chalazan, B.; Menon, A.; Savio-Galimberti, E.; Wu, J.C.; Rehman, J.; et al. Electrophysiologic Characterization of Calcium Handling in Human Induced Pluripotent Stem Cell-Derived Atrial Cardiomyocytes. *Stem Cell Rep.* **2018**, *10*, 1867–1878. [CrossRef]
97. Elliott, D.A.; Braam, S.R.; Koutsis, K.; Ng, E.S.; Jenny, R.; Lagerqvist, E.L.; Biben, C.; Hatzistavrou, T.; Hirst, C.E.; Yu, Q.C.; et al. NKX2-5(eGFP/w) hESCs for isolation of human cardiac progenitors and cardiomyocytes. *Nat. Methods* **2011**, *8*, 1037–1040. [CrossRef]
98. Doss, M.X.; Di Diego, J.M.; Goodrow, R.J.; Wu, Y.; Cordeiro, J.M.; Nesterenko, V.V.; Barajas-Martínez, H.; Hu, D.; Urrutia, J.; Desai, M.; et al. Maximum Diastolic Potential of Human Induced Pluripotent Stem Cell-Derived Cardiomyocytes Depends Critically on IKr. *PLoS ONE* **2012**, *7*, e40288. [CrossRef]
99. Vaidyanathan, R.; Markandeya, Y.S.; Kamp, T.J.; Makielski, J.C.; January, C.T.; Eckhardt, L.L. IK1-enhanced human-induced pluripotent stem cell-derived cardiomyocytes: An improved cardiomyocyte model to investigate inherited arrhythmia syndromes. *Am. J. Physiol. Heart Circ. Physiol.* **2016**, *310*, H1611–H1621. [CrossRef]
100. Meijer van Putten, R.M.E.; Mengarelli, I.; Guan, K.; Zegers, J.G.; van Ginneken, A.C.G.; Verkerk, A.O.; Wilders, R. Ion channelopathies in human induced pluripotent stem cell derived cardiomyocytes: A dynamic clamp study with virtual IK1. *Front. Physiol.* **2015**, *6*, 7. [CrossRef]
101. Verkerk, A.O.; Veerman, C.C.; Zegers, J.G.; Mengarelli, I.; Bezzina, C.R.; Wilders, R. Patch-Clamp Recording from Human Induced Pluripotent Stem Cell-Derived Cardiomyocytes: Improving Action Potential Characteristics through Dynamic Clamp. *Int. J. Mol. Sci.* **2017**, *18*, 1873. [CrossRef]
102. Zeng, H.; Wang, J.; Clouse, H.; Lagrutta, A.; Sannajust, F. Human-induced pluripotent stem cell-derived cardiomyocytes have limited IKs for repolarization reserve as revealed by specific KCNQ1/KCNE1 blocker. *JRSM Cardiovasc. Dis.* **2019**, *8*. [CrossRef] [PubMed]
103. Braam, S.R.; Tertoolen, L.; Casini, S.; Matsa, E.; Lu, H.R.; Teisman, A.; Passier, R.; Denning, C.; Gallacher, D.J.; Towart, R.; et al. Repolarization reserve determines drug responses in human pluripotent stem cell derived cardiomyocytes. *Stem Cell Res.* **2013**, *10*, 48–56. [CrossRef] [PubMed]

104. Jost, N.; Virág, L.; Comtois, P.; Ordög, B.; Szuts, V.; Seprényi, G.; Bitay, M.; Kohajda, Z.; Koncz, I.; Nagy, N.; et al. Ionic mechanisms limiting cardiac repolarization reserve in humans compared to dogs. *J. Physiol.* **2013**, *591*, 4189–4206. [CrossRef] [PubMed]
105. Mauritz, C.; Schwanke, K.; Reppel, M.; Neef, S.; Katsirntaki, K.; Maier, L.S.; Nguemo, F.; Menke, S.; Haustein, M.; Hescheler, J.; et al. Generation of functional murine cardiac myocytes from induced pluripotent stem cells. *Circulation* **2008**, *118*, 507–517. [CrossRef] [PubMed]
106. Itzhaki, I.; Rapoport, S.; Huber, I.; Mizrahi, I.; Zwi-Dantsis, L.; Arbel, G.; Schiller, J.; Gepstein, L. Calcium handling in human induced pluripotent stem cell derived cardiomyocytes. *PLoS ONE* **2011**, *6*, e18037. [CrossRef] [PubMed]
107. Lee, Y.K.; Ng, K.M.; Lai, W.-H.; Chan, Y.C.; Lau, Y.-M.; Lian, Q.; Tse, H.F.; Siu, C.-W. Calcium homeostasis in human induced pluripotent stem cell-derived cardiomyocytes. *Stem Cell Rev. Rep.* **2011**, *7*, 976–986. [CrossRef] [PubMed]
108. Gherghiceanu, M.; Barad, L.; Novak, A.; Reiter, I.; Itskovitz-Eldor, J.; Binah, O.; Popescu, L.M. Cardiomyocytes derived from human embryonic and induced pluripotent stem cells: Comparative ultrastructure. *J. Cell. Mol. Med.* **2011**, *15*, 2539–2551. [CrossRef]
109. Lundy, S.D.; Zhu, W.Z.; Regnier, M.; Laflamme, M.A. Structural and functional maturation of cardiomyocytes derived from human pluripotent stem cells. *Stem Cells Dev.* **2013**, *22*, 1991–2002. [CrossRef]
110. Cadet, J.S.; Kamp, T.J. A Recipe for T-Tubules in Human iPS Cell-Derived Cardiomyocytes. *Circ. Res.* **2017**, *121*, 1294–1295. [CrossRef]
111. Pioner, J.M.; Guan, X.; Klaiman, J.M.; Racca, A.W.; Pabon, L.; Muskheli, V.; Macadangdang, J.; Ferrantini, C.; Hoopmann, M.R.; Moritz, R.L.; et al. Absence of full-length dystrophin impairs normal maturation and contraction of cardiomyocytes derived from human induced pluripotent stem cells. *Cardiovasc. Res.* **2019**, cvz109. [CrossRef]
112. Li, Z.; Garnett, C.; Strauss, D.G. Quantitative Systems Pharmacology Models for a New International Cardiac Safety Regulatory Paradigm: An Overview of the Comprehensive In Vitro Proarrhythmia Assay In Silico Modeling Approach. *Cpt Pharmacomet. Syst. Pharmacol.* **2019**, *8*, 371–379. [CrossRef] [PubMed]
113. Gibson, J.K.; Yue, Y.; Bronson, J.; Palmer, C.; Numann, R. Human stem cell-derived cardiomyocytes detect drug-mediated changes in action potentials and ion currents. *J. Pharmacol. Toxicol. Methods* **2014**, *70*, 255–267. [CrossRef] [PubMed]
114. Lu, H.R.; Whittaker, R.; Price, J.H.; Vega, R.; Pfeiffer, E.R.; Cerignoli, F.; Towart, R.; Gallacher, D.J. High Throughput Measurement of Ca $^{++}$ Dynamics in Human Stem Cell-Derived Cardiomyocytes by Kinetic Image Cytometery: A Cardiac Risk Assessment Characterization Using a Large Panel of Cardioactive and Inactive Compounds. *Toxicol. Sci.* **2015**, *148*, 503–516. [CrossRef] [PubMed]
115. Patel, D.; Stohlman, J.; Dang, Q.; Strauss, D.G.; Blinova, K. Assessment of Proarrhythmic Potential of Drugs in Optogenetically Paced Induced Pluripotent Stem Cell-Derived Cardiomyocytes. *Toxicol. Sci.* **2019**, *170*, 167–179. [CrossRef]
116. Colatsky, T.; Fermini, B.; Gintant, G.; Pierson, J.B.; Sager, P.; Sekino, Y.; Strauss, D.G.; Stockbridge, N. The Comprehensive in Vitro Proarrhythmia Assay (CiPA) initiative—Update on progress. *J. Pharmacol. Toxicol. Methods* **2016**, *81*, 15–20. [CrossRef]
117. Weiss, J.N.; Garfinkel, A.; Karagueuzian, H.S.; Chen, P.S.; Qu, Z. Early afterdepolarizations and cardiac arrhythmias. *Heart Rhythm.* **2010**, *7*, 1891–1899. [CrossRef]
118. Kussauer, S.; David, R.; Lemcke, H. hiPSCs Derived Cardiac Cells for Drug and Toxicity Screening and Disease Modeling: What Micro- Electrode-Array Analyses Can Tell Us. *Cells* **2019**, *8*, 1331. [CrossRef]
119. Kanda, Y.; Yamazaki, D.; Osada, T.; Yoshinaga, T.; Sawada, K. Development of torsadogenic risk assessment using human induced pluripotent stem cell-derived cardiomyocytes: Japan iPS Cardiac Safety Assessment (JiCSA) update. *J. Pharmacol. Sci.* **2018**, *138*, 233–239. [CrossRef]
120. O'Hara, T.; Virág, L.; Varró, A.; Rudy, Y. Simulation of the undiseased human cardiac ventricular action potential: Model formulation and experimental validation. *PLoS Comput. Biol.* **2011**, *7*, e1002061. [CrossRef]
121. Paci, M.; Hyttinen, J.; Aalto-Setälä, K.; Severi, S. Computational models of ventricular- and atrial-like human induced pluripotent stem cell derived cardiomyocytes. *Ann. Biomed. Eng.* **2013**, *41*, 2334–2348. [CrossRef]

122. Passini, E.; Britton, O.J.; Lu, H.R.; Rohrbacher, J.; Hermans, A.N.; Gallacher, D.J.; Greig, R.J.H.; Bueno-Orovio, A.; Rodriguez, B. Human in Silico Drug Trials Demonstrate Higher Accuracy than Animal Models in Predicting Clinical Pro-Arrhythmic Cardiotoxicity. *Front. Physiol.* **2017**, *8*, 668. [CrossRef] [PubMed]
123. Yang, X.; Pabon, L.; Murry, C.E. Engineering adolescence: Maturation of human pluripotent stem cell-derived cardiomyocytes. *Circ. Res.* **2014**, *114*, 511–523. [CrossRef] [PubMed]
124. Bar-Nur, O.; Russ, H.A.; Efrat, S.; Benvenisty, N. Epigenetic memory and preferential lineage-specific differentiation in induced pluripotent stem cells derived from human pancreatic islet beta cells. *Cell Stem Cell* **2011**, *9*, 17–23. [CrossRef] [PubMed]
125. Barile, L.; Lionetti, V.; Cervio, E.; Matteucci, M.; Gherghiceanu, M.; Popescu, L.M.; Torre, T.; Siclari, F.; Moccetti, T.; Vassalli, G. Extracellular vesicles from human cardiac progenitor cells inhibit cardiomyocyte apoptosis and improve cardiac function after myocardial infarction. *Cardiovasc. Res.* **2014**, *103*, 530–541. [CrossRef]
126. Pianezzi, E.; Altomare, C.; Bolis, S.; Balbi, C.; Torre, T.; Rinaldi, A.; Camici, G.G.; Barile, L.; Vassalli, G. Role of somatic cell sources in the maturation degree of human induced pluripotent stem cell-derived cardiomyocytes. *Biochim. Biophys. Acta Mol. Cell Res.* **2019**, *28*, 118538. [CrossRef]
127. Sanchez-Freire, V.; Lee, A.S.; Hu, S.; Abilez, O.J.; Liang, P.; Lan, F.; Huber, B.C.; Ong, S.G.; Hong, W.X.; Huang, M.; et al. Effect of human donor cell source on differentiation and function of cardiac induced pluripotent stem cells. *J. Am. Coll. Cardiol.* **2014**, *64*, 436–448. [CrossRef]
128. Meraviglia, V.; Wen, J.; Piacentini, L.; Campostrini, G.; Wang, C.; Florio, M.C.; Azzimato, V.; Fassina, L.; Langes, M.; Wong, J.; et al. Higher cardiogenic potential of iPSCs derived from cardiac versus skin stromal cells. *Front. Biosci.* **2016**, *21*, 719–743.
129. Kim, K.; Zhao, R.; Doi, A.; Ng, K.; Unternaehrer, J.; Cahan, P.; Huo, H.; Loh, Y.-H.; Aryee, M.J.; Lensch, M.W.; et al. Donor cell type can influence the epigenome and differentiation potential of human induced pluripotent stem cells. *Nat. Biotechnol.* **2011**, *29*, 1117–1119. [CrossRef]
130. Sheng, X.; Reppel, M.; Nguemo, F.; Mohammad, F.I.; Kuzmenkin, A.; Hescheler, J.; Pfannkuche, K. Human pluripotent stem cell-derived cardiomyocytes: Response to TTX and lidocain reveals strong cell to cell variability. *PLoS ONE* **2012**, *7*, e45963. [CrossRef]
131. Giacomelli, E.; Mummery, C.L.; Bellin, M. Human heart disease: Lessons from human pluripotent stem cell-derived cardiomyocytes. *Cell. Mol. Life Sci.* **2017**, *74*, 3711–3739. [CrossRef]
132. Fatima, A.; Kaifeng, S.; Dittmann, S.; Xu, G.; Gupta, M.K.; Linke, M.; Zechner, U.; Nguemo, F.; Milting, H.; Farr, M.; et al. The disease-specific phenotype in cardiomyocytes derived from induced pluripotent stem cells of two long QT syndrome type 3 patients. *PLoS ONE* **2013**, *8*, e83005. [CrossRef] [PubMed]
133. Sala, L.; Gnecchi, M.; Schwartz, P.J. Long QT Syndrome Modelling with Cardiomyocytes Derived from Human-induced Pluripotent Stem Cells. *Arrhythm. Electrophysiol. Rev.* **2019**, *8*, 105–110. [CrossRef] [PubMed]
134. Selga, E.; Sendfeld, F.; Martinez-Moreno, R.; Medine, C.N.; Tura-Ceide, O.; Wilmut, S.I.; Pérez, G.J.; Scornik, F.S.; Brugada, R.; Mills, N.L. Sodium channel current loss of function in induced pluripotent stem cell-derived cardiomyocytes from a Brugada syndrome patient. *J. Mol. Cell. Cardiol.* **2018**, *114*, 10–19. [CrossRef] [PubMed]
135. Ma, D.; Liu, Z.; Loh, L.J.; Zhao, Y.; Li, G.; Liew, R.; Islam, O.; Wu, J.; Chung, Y.Y.; Teo, W.S.; et al. Identification of an INa-dependent and Ito-mediated proarrhythmic mechanism in cardiomyocytes derived from pluripotent stem cells of a Brugada syndrome patient. *Sci. Rep.* **2018**, *8*, 11246. [CrossRef] [PubMed]
136. Itzhaki, I.; Maizels, L.; Huber, I.; Gepstein, A.; Arbel, G.; Caspi, O.; Miller, L.; Belhassen, B.; Nof, E.; Glikson, M.; et al. Modeling of catecholaminergic polymorphic ventricular tachycardia with patient-specific human-induced pluripotent stem cells. *J. Am. Coll. Cardiol.* **2012**, *60*, 990–1000. [CrossRef]
137. Zhang, X.H.; Haviland, S.; Wei, H.; Sarić, T.; Fatima, A.; Hescheler, J.; Cleemann, L.; Morad, M. Ca2+ signaling in human induced pluripotent stem cell-derived cardiomyocytes (iPS-CM) from normal and catecholaminergic polymorphic ventricular tachycardia (CPVT)-afflicted subjects. *Cell Calcium* **2013**, *54*, 57–70. [CrossRef] [PubMed]
138. Marczenke, M.; Fell, J.; Piccini, I.; Röpke, A.; Seebohm, G.; Greber, B. Generation and cardiac subtype-specific differentiation of PITX2-deficient human iPS cell lines for exploring familial atrial fibrillation. *Stem Cell Res.* **2017**, *21*, 26–28. [CrossRef]

139. Marczenke, M.; Piccini, I.; Mengarelli, I.; Fell, J.; Röpke, A.; Seebohm, G.; Verkerk, A.O.; Greber, B. Cardiac Subtype-Specific Modeling of Kv1.5 Ion Channel Deficiency Using Human Pluripotent Stem Cells. *Front. Physiol.* **2017**, *8*, 469. [CrossRef]
140. Shimko, V.F.; Claycomb, W.C. Effect of mechanical loading on three-dimensional cultures of embryonic stem cell-derived cardiomyocytes. *Tissue Eng. Part. A* **2008**, *14*, 49–58. [CrossRef]
141. Chan, Y.C.; Ting, S.; Lee, Y.K.; Ng, K.M.; Zhang, J.; Chen, Z.; Siu, C.W.; Oh, S.K.W.; Tse, H.F. Electrical stimulation promotes maturation of cardiomyocytes derived from human embryonic stem cells. *J. Cardiovasc. Transl. Res.* **2013**, *6*, 989–999. [CrossRef]
142. Kamakura, T.; Makiyama, T.; Sasaki, K.; Yoshida, Y.; Wuriyanghai, Y.; Chen, J.; Hattori, T.; Ohno, S.; Kita, T.; Horie, M.; et al. Ultrastructural maturation of human-induced pluripotent stem cell-derived cardiomyocytes in a long-term culture. *Circ. J.* **2013**, *77*, 1307–1314. [CrossRef] [PubMed]
143. Tohyama, S.; Hattori, F.; Sano, M.; Hishiki, T.; Nagahata, Y.; Matsuura, T.; Hashimoto, H.; Suzuki, T.; Yamashita, H.; Satoh, Y.; et al. Distinct metabolic flow enables large-scale purification of mouse and human pluripotent stem cell-derived cardiomyocytes. *Cell Stem Cell* **2013**, *12*, 127–137. [CrossRef] [PubMed]
144. Correia, C.; Koshkin, A.; Duarte, P.; Hu, D.; Teixeira, A.; Domian, I.; Serra, M.; Alves, P.M. Distinct carbon sources affect structural and functional maturation of cardiomyocytes derived from human pluripotent stem cells. *Sci. Rep.* **2017**, *7*, 8590. [CrossRef] [PubMed]
145. Lemoine, M.D.; Mannhardt, I.; Breckwoldt, K.; Prondzynski, M.; Flenner, F.; Ulmer, B.; Hirt, M.N.; Neuber, C.; Horváth, A.; Kloth, B.; et al. Human iPSC-derived cardiomyocytes cultured in 3D engineered heart tissue show physiological upstroke velocity and sodium current density. *Sci. Rep.* **2017**, *7*, 5464. [CrossRef]
146. Ronaldson-Bouchard, K.; Ma, S.P.; Yeager, K.; Chen, T.; Song, L.; Sirabella, D.; Morikawa, K.; Teles, D.; Yazawa, M.; Vunjak-Novakovic, G. Advanced maturation of human cardiac tissue grown from pluripotent stem cells. *Nature* **2018**, *556*, 239–243. [CrossRef]
147. Ulmer, B.M.; Stoehr, A.; Schulze, M.L.; Patel, S.; Gucek, M.; Mannhardt, I.; Funcke, S.; Murphy, E.; Eschenhagen, T.; Hansen, A. Contractile Work Contributes to Maturation of Energy Metabolism in hiPSC-Derived Cardiomyocytes. *Stem Cell Rep.* **2018**, *10*, 834–847. [CrossRef]


ESC European Society of Cardiology

Cardiovascular Research (2020) **116**, 1147–1160
doi:10.1093/cvr/cvz217

# Human iPSC modelling of a familial form of atrial fibrillation reveals a gain of function of $I_f$ and $I_{CaL}$ in patient-derived cardiomyocytes

**Patrizia Benzoni [1‡], Giulia Campostrini [1†‡], Sara Landi [1], Valeria Bertini[2], Eleonora Marchina [2], Maria Iascone [3], Gustav Ahlberg [4], Morten Salling Olesen [4], Elisabetta Crescini [2], Cristina Mora[2], Gianluigi Bisleri[5], Claudio Muneretto[6], Roberto Ronca [2], Marco Presta [2], Pier Luigi Poliani[2], Giovanna Piovani [2], Rosanna Verardi [7], Elisa Di Pasquale [8], Antonella Consiglio [2,9,10], Angel Raya [11,12,13], Eleonora Torre[14], Alessandra Maria Lodrini [14], Raffaella Milanesi[1], Marcella Rocchetti [14], Mirko Baruscotti [1], Dario DiFrancesco[1], Maurizio Memo [2], Andrea Barbuti [1]*, and Patrizia Dell'Era [2]***

[1]Department of Biosciences, Università degli Studi di Milano, via Celoria 26, 20133 Milan, Italy; [2]Department of Molecular and Translational Medicine, cFRU lab, Università degli Studi di Brescia, viale Europa 11, 25123 Brescia, Italy; [3]USSD Laboratorio di Genetica Medica, Azienda Socio Sanitaria Territoriale Papa Giovanni XXIII, Piazza OMS, 1, 24127 Bergamo, Italy; [4]The Heart Centre, Rigshospitalet, Laboratory for Molecular Cardiology, Blegdamsvej 9, 2100 Copenhagen, Denmark; [5]Department of Surgery, Division of Cardiac Surgery, Queen's University, 99 University Avenue, Kingston, Ontario K7L 3N6, Canada; [6]Clinical Department of Cardiovascular Surgery, University of Brescia, viale Europa 11, 25123 Brescia, Italy; [7]Department of Trasfusion Medicine, Laboratory for Stem Cells Manipulation and Cryopreservation, ASST Spedali Civili, viale Europa 11, 25123 Brescia, Italy; [8]Department of Cardiovascular Medicine, Humanitas Clinical and Research Center, Via Rita Levi Montalcini, 4, 20090 Pieve Emanuele, Milan, Italy; [9]Department of Pathology and Experimental Therapeutics, Bellvitge University Hospital-IDIBELL, 08908 Hospitalet de Llobregat, C/Feixa Larga s/n, 08907 Barcelona, Spain; [10]Institute of Biomedicine of the University of Barcelona (IBUB), Carrer Baldiri Reixac 15-21, Barcelona 08028, Spain; [11]Center of Regenerative Medicine in Barcelona (CMRB), Hospital Duran i Reynals, Hospitalet de Llobregat, 08908 Barcelona, Spain; [12]Catalan Institution for Research and Advanced Studies (ICREA), Passeig Lluís Companys 23 08010 Barcelona, Spain; [13]Networking Center of Biomedical Research in Bioengineering, Biomaterials and Nanomedicine (CIBER-BBN), 28029 Madrid, Spain; and [14]Department of Biotechnology and Biosciences, Università degli Studi di Milano-Bicocca, iazza dell'Ateneo Nuovo 1, 20126 Milan, Italy

*Received 15 November 2018; revised 19 July 2019; editorial decision 14 August 2019; accepted 26 August 2019; online publish-ahead-of-print 28 August 2019*

**Time for primary review: 40 days**

**Aims** Atrial fibrillation (AF) is the most common type of cardiac arrhythmias, whose incidence is likely to increase with the aging of the population. It is considered a progressive condition, frequently observed as a complication of other cardiovascular disorders. However, recent genetic studies revealed the presence of several mutations and variants linked to AF, findings that define AF as a multifactorial disease. Due to the complex genetics and paucity of models, molecular mechanisms underlying the initiation of AF are still poorly understood. Here we investigate the pathophysiological mechanisms of a familial form of AF, with particular attention to the identification of putative triggering cellular mechanisms, using patient's derived cardiomyocytes (CMs) differentiated from induced pluripotent stem cells (iPSCs).

**Methods and results** Here we report the clinical case of three siblings with untreatable persistent AF whose whole-exome sequence analysis revealed several mutated genes. To understand the pathophysiology of this multifactorial form of AF we generated three iPSC clones from two of these patients and differentiated these cells towards the cardiac lineage. Electrophysiological characterization of patient-derived CMs (AF-CMs) revealed that they have higher beating rates compared to control (CTRL)-CMs. The analysis showed an increased contribution of the $I_f$ and $I_{CaL}$ currents. No differences were observed in the repolarizing current $I_{Kr}$ and in the sarcoplasmic reticulum calcium handling. Paced AF-CMs presented significantly prolonged action potentials and, under stressful conditions, generated both delayed after-depolarizations of bigger amplitude and more ectopic beats than CTRL cells.

* Corresponding authors. Tel: +39 02 50314941; fax: +39 02 50314932, E-mail: andrea.barbuti@unimi.it (A.B.); Tel: +39 030 3717539; fax: +39 030 3717 539, E-mail: patrizia.dellera@unibs.it (P.D.E.)

† Present address. Department of Anatomy and Embryology, Leiden University Medical Center, Einthovenweg 20, 2333ZC Leiden, The Netherlands.

‡ The first two authors contributed equally to the study.

**Conclusions** Our results demonstrate that the common genetic background of the patients induces functional alterations of $I_f$ and $I_{CaL}$ currents leading to a cardiac substrate more prone to develop arrhythmias under demanding conditions. To our knowledge this is the first report that, using patient-derived CMs differentiated from iPSC, suggests a plausible cellular mechanism underlying this complex familial form of AF.

**Graphical Abstract**

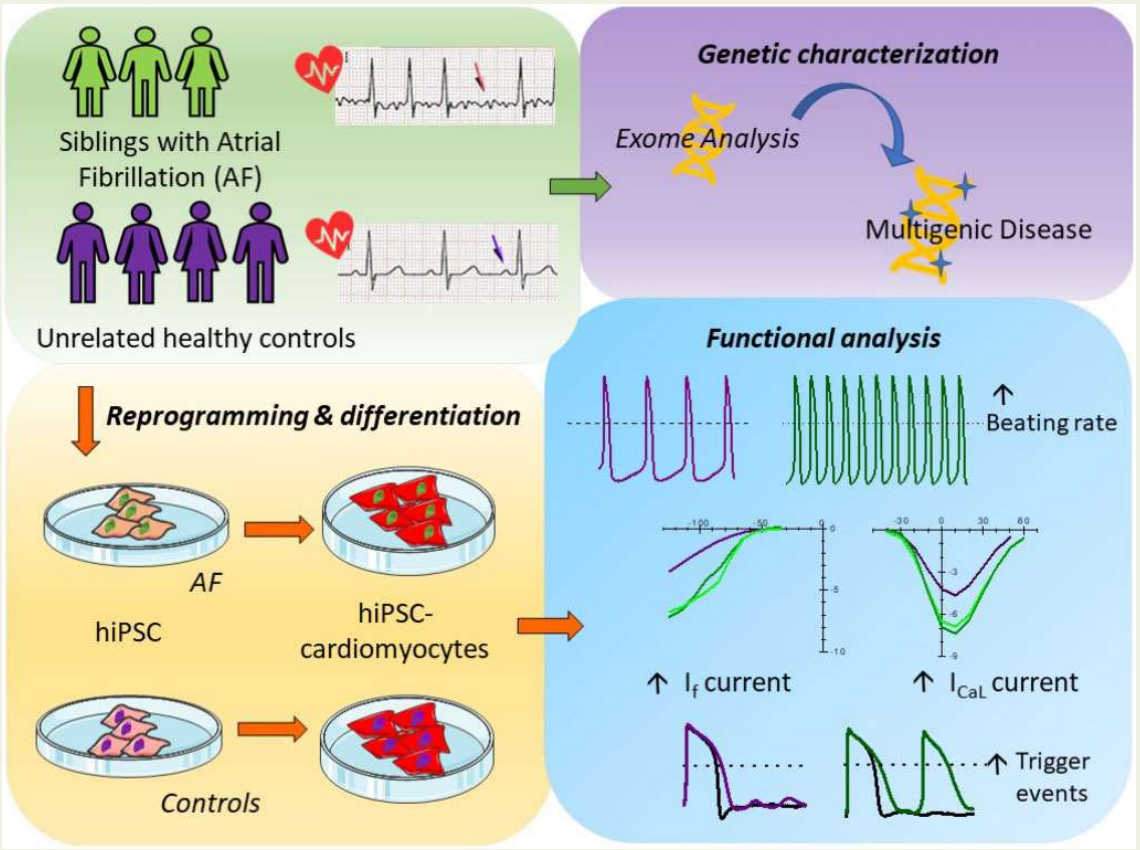


**Keywords** Ion channels • Arrhythmias • Atrial fibrillation • iPSC-derived cardiomyocytes • Precision medicine

## 1. Introduction

Atrial fibrillation (AF) is the most common cardiac arrhythmia, occurring in 1–2% of the general population, but with a greater incidence in the elderly. In this type of arrhythmia, ectopic activity originating outside the sinoatrial node, gives rise to a disorganized electrical activation due to a cellular substrate susceptible to re-entrant circuits. While AF is commonly associated with structural heart diseases and is a major cause of cardiovascular morbidity and mortality in the elderly, it sometimes develops in a subset of patients younger than 60, with no evidence of associated cardiopulmonary or other diseases.

In recent years, evidence for inheritable forms of AF has grown. Beyond the rare cases of monogenic forms of AF and linkage analysis that revealed several genetic loci associated with AF,[1] population-based studies have shown that having first degree relatives with AF increases significantly the probability to develop AF.[2] Familial AF is likely associated with a complex genetic background that predisposes to this arrhythmia and that may or may not manifest itself depending on other non-genetic contributors.

Because of this genetic complexity, the molecular mechanisms underlying the initiation of AF are still poorly understood and possibly involve a complex interplay of various effectors.[3] In addition, electrical disturbances typical of AF cause the remodelling of the atria in a way that may sustain the arrhythmic phenotype.[4] This remodelling, in turn, makes it impossible to discriminate between causes and effects of AF when analysing cardiomyocytes (CMs) obtained from patient's biopsies. Human induced pluripotent stem cells-derived CMs (hiPSCs-CMs) may represent a valuable model to study AF, since they carry the exact genetic background of the patient but are free from the AF-dependent remodelling. hiPSC-CMs are now recognized as a useful human model that recapitulates the functional alterations underlying inherited arrhythmogenic diseases.[5]

In this work, we describe the first iPSC-derived model of human AF, generated from two out of three siblings that developed a drug-resistant form of AF at a relatively young age (<55 years). Using this model, we compared molecular and electrophysiological properties of hiPSC-CMs from AF patients (AF-CMs) and controls (CTRL-CMs), revealing alterations in ionic currents that may represent one of the cellular mechanisms that contribute to AF initiation.

# 2. Methods

## 2.1 AF patients

The three siblings were referred to Spedali Civili of Brescia (Italy), where they were diagnosed for AF (for details on method see Supplementary material online). Since all three patients were non-responsive to antiarrhythmic medication and failed previous transcatheter ablation, they underwent surgical ablation as described in Supplementary material online. A detailed clinical history of the patients is reported in the Supplementary material online, *Table S1*.

## 2.2 Generation of hiPSCs and cardiac differentiation

Blood and skin biopsies have been obtained from all three siblings following approved protocols by the Ethical Committee of Brescia (protocol number 1737) and a written consent obtained from the patients, in agreement with the declaration of Helsinki. hiPSC were generated as reported in Supplementary material online.

Cardiac differentiation of hiPSC was carried out either by embryoid bodies (EBs), as previously described[6] or by monolayer culture using the PSC Cardiomyocyte Differentiation Kit (Thermo Fisher Scientific). Differentiation in EBs was used for experiments on beating clusters to record the spontaneous rate. All the other experiments were carried out using the monolayer differentiation.

## 2.3 Electrophysiological and $Ca^{2+}$ handling analysis

Electrophysiological and $Ca^{2+}$ handling experiments were performed on dissociated hiPSC-CMs from at least three independent differentiation experiments, using the patch-clamp technique in whole-cell configuration. For protocols and solutions see Supplementary material online.

## 2.4 Statistics

Statistical analysis was carried out with Origin Pro 9, IBM SPSS Statistics and R software. Groups were compared with one-way ANOVA followed by pairwise comparison using Fisher's test or by nested one-way ANOVA with Holm *P*-value adjustment. Difference in events percentage among groups was assessed by Fisher's exact test, adjusting the *P*-value with Bonferroni correction. *P*-value <0.05 defines statistical significance. Data are presented as mean ± SEM.

# 3. Results

## 3.1 Characteristics of patients: genetic screening for mutations in AF-related genes

We identified three siblings with untreatable AF (see exemplified electrocardiogram in Supplementary material online, *Figure S1* and clinical characteristics in Supplementary material online, *Table S1*) who, due to failure of pharmacological treatment, underwent surgical ablation. Although they present other comorbidities (e.g. high body mass index and hypertension) that may importantly contribute to the poor control of the pathology, the familiarity, and their young age of onset of AF, strongly support a genetic basis for this form of arrhythmia.

In an attempt to identify potential AF-related mutations within the family we performed a whole exome sequencing in which data obtained from the three siblings (dubbed AF1, AF2, and AF3) were compared with 6000 human reference genomes (GRC37/hg19). We identified more than one hundred variants common only to the three siblings (see Supplementary material online, *Table S2*). Only few of these variants were in genes previously associated with AF (*ZFHX3*) and expressed also in the heart (*PDE4DIP*, *CNN2*, *RYR3*, *NEFM*, *FLNC*, and *MYLK*). Because of the complex genetic background of the family and the lack of unquestionably healthy relatives, we decided to address the molecular basis of this form of AF from a functional point of view.

## 3.2 Generation of hiPSC clones

To highlight possible common functional cardiac alterations in these patients, we generated patient-derived iPSCs and differentiated them into CMs. The reprogramming procedure was effective for fibroblasts obtained from AF1 and AF2, which allowed the generation of three hiPSC clones (AF1 $n = 2$; AF2 $n = 1$).

In the absence of unquestionably healthy parental or isogenic controls, AF clones were compared with at least three of four different unrelated control clones: one derived from dermal fibroblasts of an age-matched healthy woman[7] (CTRL1); one derived from epidermal keratinocytes[8] (CTRL2); one derived from dermal fibroblasts of a young male (CTRL3 shown in *Figure 1B* and *C*); and the last one from blood cells of a 62-year-old male not affected by AF or other cardiac pathologies (CTRL4).

The clones obtained from AF1 and AF2 were tested for the expression of both exogenous (t) and endogenous (e) pluripotency genes *OCT4*, *SOX2*, *NANOG*, and *REX1* by qPCR (*Figure 1A*) or by immunocytochemistry (*Figure 1B*). They were further screened for morphological properties typical of pluripotent colonies, such as sharp borders, the absence of a central dark area, and the expression of alkaline phosphatase (*Figure 1B*). The maintenance of a normal karyotype was also verified by quinacrine staining of metaphase plates (*Figure 1B*). Finally, the capacity to differentiate towards the three germ layers was confirmed by immunostaining with specific antibodies recognizing the ectodermal protein Nestin or Class III beta-Tubulin (TUJ1), the mesodermal protein smooth muscle actin, and the endodermal protein alpha fetoprotein (*Figure 1C*).

## 3.3 AF and CTRL hiPSCs differentiate into CMs with similar efficiency

For the experiments evaluating beating rate of clusters of hiPSC-CMs, clones were differentiated towards the cardiac lineage using a previously published procedure that involves spontaneous formation of EBs.[6] For all remaining experiments, we switched to a commercially available cardiac differentiation kit that ensured a higher yield of CMs.

Besides the appearance of beating areas, CMs in AF and CTRL groups were evaluated for the expression of the cardiac troponin gene (TNNT2) and the atrial gene sarcolipin (SLN) at day 30 of differentiation, by qPCR. The plots in *Figure 2A* (top panels) show that the levels of TNNT2 and SLN were similar in all groups.

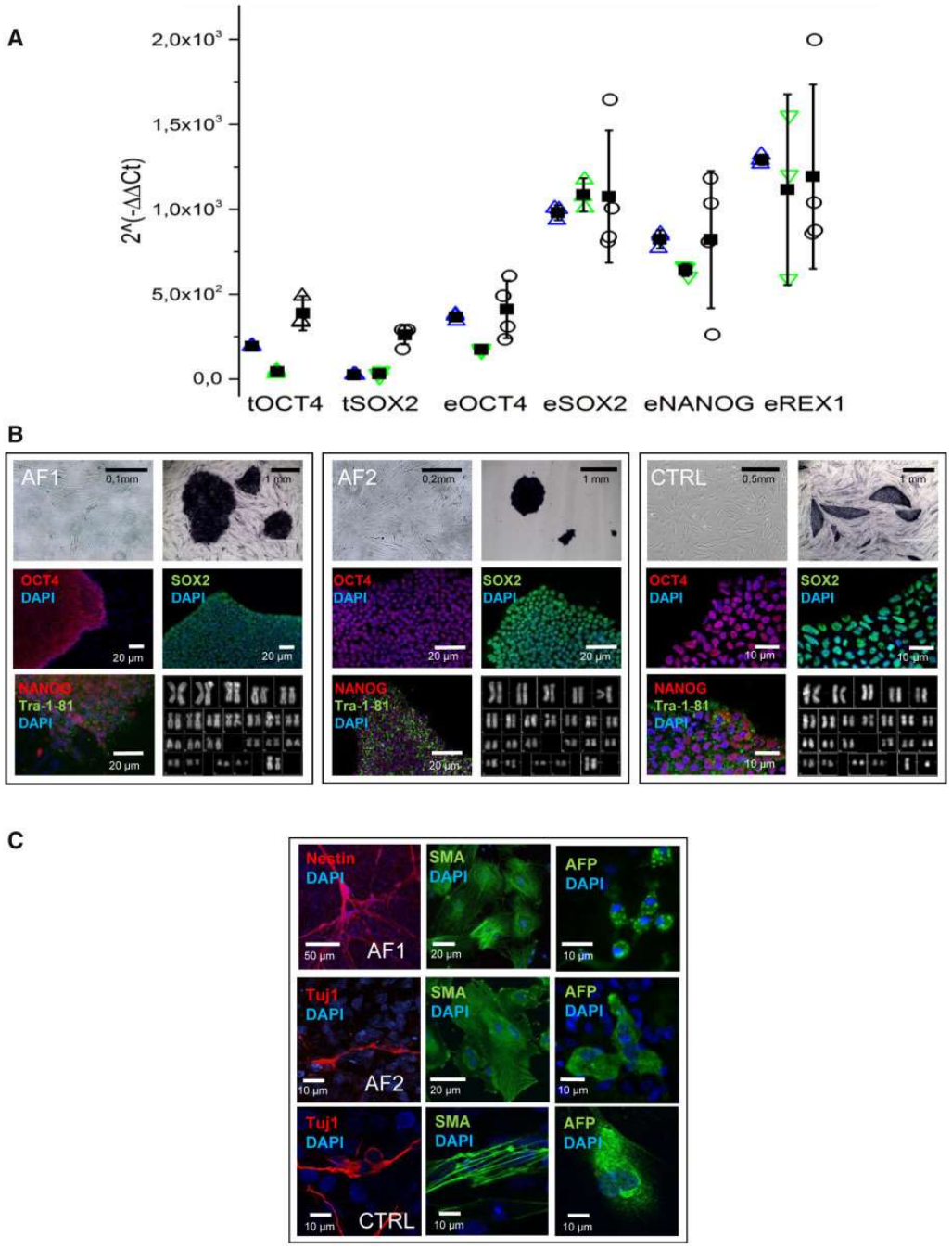


**Figure 1** Pluripotency characterization. (*A*) qPCR analysis of pluripotency gene expression in hiPSC using dermal fibroblasts as reference control equal to 1. *tOCT4* and *tSOX2* indicate the specific expression of transgenes, while *eOCT4* and *eSOX2* refer to expression of endogenous genes. Differences in gene expression levels were compared using one-way ANOVA followed by Fisher's *T*-test. (*B*) Summary panels for AF1, AF2, and CTRL hiPSC lines, as indicated (from left to right): bright-field images of primary fibroblasts, alkaline phosphatase activity in hiPSC-colonies, immunostaining of hiPSC for pluripotency markers and karyotype. (*C*) Immunostaining of differentiated hiPSCs with antibodies recognizing ectodermal, mesodermal, and endodermal markers as indicated.

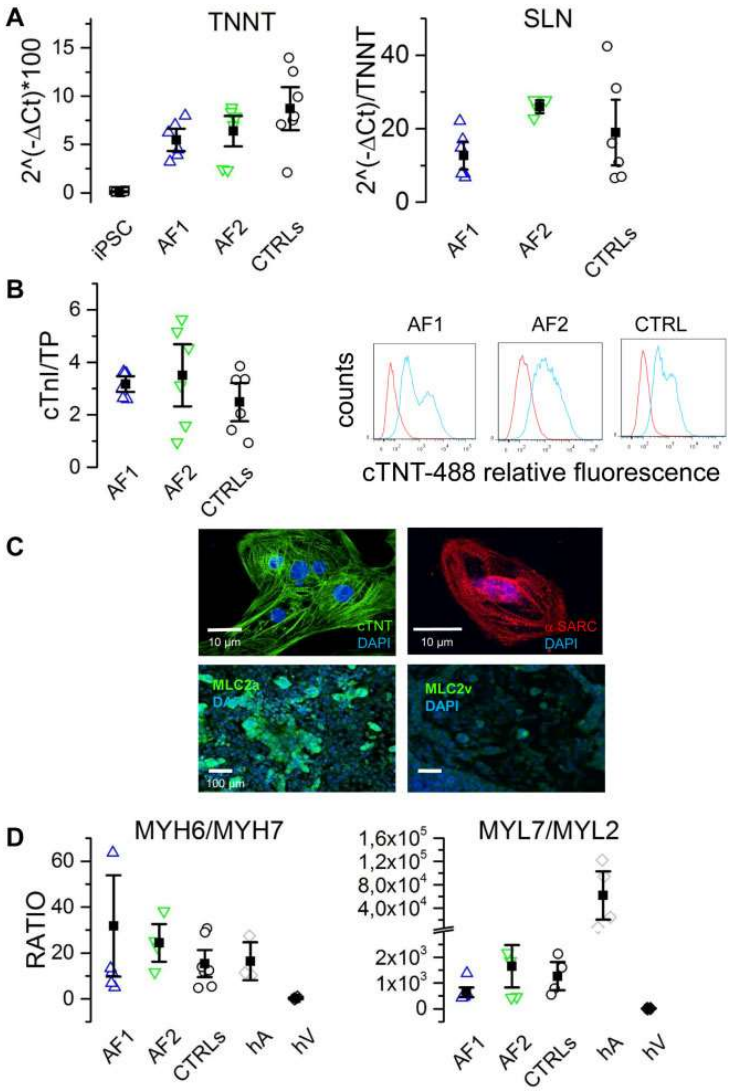


**Figure 2** hiPSC-derived cardiomyocyte differentiation. (*A*) qPCR analysis of cardiac troponin T (TNNT2) and sarcolipin (SLN) expression at day 30 of differentiation for AF1-, AF2-, and CTRL-CMs, as indicated. Undifferentiated hiPSC were used as negative control. (*B*) Quantification of cardiac troponin I (µg) on total protein content (TP, mg) of AF1 (2.9 ± 0.46; $n = 3$), AF2 (2.4 ± 1.37; $n = 3$), CTRL (2.36 ± 1.08; $n = 6$), and hiPSCs (0.002 ± 0.01; $n = 2$) (left). Representative flow cytometry analysis on hiPSC-differentiated cells using an anti-cardiac troponin T antibody: AF1 (45.1 ± 11 $n = 3$), AF2 (55.2 ± 19 $n = 3$), CTRL (52 ± 12 $n = 6$) (right). (*C*) Representative images of isolated AF1-CM and AF1-differentiated monolayers stained for cardiac troponin T (cTNT), sarcomeric actin (α-SARC), atrial (MLC2a), and ventricular (MLC2v) myosin light chains; nuclei were counterstained with DAPI. (*D*) Ratios between the qPCR expression levels of heavy (left) and light (right) chain isoforms of myosin. Human atria (hA) and ventricles (hV) were used as positive and negative controls, respectively. Differences in gene expression and protein quantification were assessed by one-way ANOVA followed by Fisher's *T*-test.

We further investigated cardiac differentiation at the protein level by assessing the expression of cardiac troponin I in cellular lysates using a commercially available diagnostic kit (*Figure 2B*, left panel), finding no differences among clones. CMs yield was evaluated by flow cytometry using an anti-cardiac troponin T (cTNT) antibody. This analysis revealed that around half of the population was composed by CMs (*Figure 2B*, right panel). Again, no significant differences were found between AF and CTRL clones. Top panels of *Figure 2C* show representative images of isolated AF1-CMs, stained with cTNT and sarcomeric actin, displaying clear sarcomeric structures. In differentiating monolayers (*Figure 2C*, bottom panels), we evaluated the expression of the atrial myosin light chain (MLC2a) typical of immature/atrial CMs; conversely, very poor

staining was obtained using anti-ventricular light chain (MLC2v) antibodies.

To better characterize the maturation stage reached at 30 days and the subtype of CM obtained, we measured the expression of the genes corresponding to the alfa (atrial) and beta (ventricular) myosin heavy chain (MYH6 and MYH7, respectively) and atrial and ventricular light chains (MYL7 and MYL2, respectively) by qPCR. *Figure 2D* shows that the mean MYH6/MYH7 ratio values were similar among hiPSC-CMs and comparable to values found in human adult atrium but not human ventricles. These data together with SLN expression, further suggest an immature/atrial rather than a ventricular phenotype for hiPSC-CMs.

Taken together these data confirm the reproducibility of the differentiating procedure among different groups and indicate that no significant differences in CM differentiation were found between AF and CTRL hiPSC lines.

## 3.4 hiPSC-CMs from AF patients display a higher beating rate than CTRL

In order to investigate the molecular mechanisms contributing to AF in our patients, we compared the electrophysiological properties of AF- and CTRL-CMs. Because data obtained from CMs of different CTRL clones were similar (Supplementary material online, *Figure S2* and *Tables S3–S5*), they were pooled together.

Representative action potential (AP) traces, recorded from spontaneously beating hiPSC-CM aggregates derived from AF1, AF2, and CTRL lines are shown in *Figure 3A*; even if the intra-clone variability was relatively large, on average aggregates derived from the two patients were beating at significantly higher rates than those derived from control lines (*Figure 3B*; see also Supplementary material online, *Movies S1 and S2*).

No significant differences in maximum diastolic potential, amplitude, and rate-corrected duration[9] were observed (Supplementary material online, *Table S3*). To test if the higher rate could result from elevated concentrations of intracellular cyclic AMP (cAMP), cells were challenged with a saturating concentration of the β-adrenergic agonist isoproterenol (Iso 1 μM). Panels of *Figure 3C* show representative time courses of spontaneous action potential rate in control, during superfusion of isoproterenol and after washout. The mean graph of *Figure 3D* shows that the fractional rate acceleration caused by isoproterenol was similar in all groups, suggesting that the higher basal beating rate does not depend on the modulatory pathway but likely derives from an intrinsic modification of the pacemaking mechanisms. On the other hand, we evaluated the effect of superfusion of the bradycardic agent ivabradine (3 μM). Panels in *Figure 3E* show representative time courses of spontaneous action potential rate in control, during ivabradine perfusion and after washout. The mean graph of *Figure 3F* shows that the fractional rate reduction caused by ivabradine was significantly higher in AF groups, abolishing the rate difference. These data suggest a higher than normal contribution of $I_f$ to the pacemaker activity of beating AF-CMs.

## 3.5 hiPSC-CMs from AF patients show a gain of function of f-channels

Since the $I_f$ current is a major contributor to control beating rate,[10,11] we measured the pacemaker $I_f$ current in isolated AF-CMs at day 15 and day 30 of differentiation, while controlling at the same time the expression of the HCN genes responsible for this current (*Figure 4*). Expression analysis revealed that HCN1, HCN2, and HCN3 isoforms were expressed at comparable low levels in all groups while HCN4, the most abundant isoform, was significantly more expressed in CTRL than in AF1- and AF2-CMs (*Figure 4A*).

Such increase in HCN4 expression could not be confirmed by immunofluorescence analysis; representative confocal images shown in *Figure 4B* display similar HCN4 expression in CMs derived from the various hiPSC lines.

Functional data instead demonstrated a significant gain of function of f-channels in AF-CMs compared to CTRL cells, as shown by the representative families of $I_f$ traces recorded from 30-day-old hiPSC-CMs (*Figure 4C*) and by the mean current density-voltage relations for AF1-, AF2-, and CTRL-CMs (*Figure 4D*, top). Interestingly, besides having higher density, f-channels of AF-CMs also activated at significantly more positive potentials than in CTRL-derived cells, as apparent from the mean activation curves shown in *Figure 4D* (bottom). It is noteworthy that at an earlier stage of differentiation (between day 15 and 20), while the current density does not differ among groups, f-channels activation is already shifted by 7 and 10 mV towards more positive potentials in AF1- and AF2-CMs, respectively, compared to CTRL (see Supplementary material online, *Figure S3*). Superfusion with isoproterenol (100 nM), which is known to cause a cAMP-dependent positive shift of $I_f$ activation curve,[12] had similar effects in all groups (shift: AF1 = 4.0 ± 0.5 mV, $n = 15$; AF2 = 4.1 ± 0.5 mV, $n = 21$; CTRL = 5.0 ± 0.7 mV, $n = 9$), indicating that the more positive activation depends on changes in the intrinsic properties of the channel rather than a functional modulation due to alteration in cytosolic cAMP homeostasis. Since a mis-interaction of HCN channels with caveolin-3 (CAV3) may cause both a shift of their voltage dependence and decrease in membrane expression,[13,14] we evaluated if the more positive activation in AF-CMs could be due to either a decreased expression of CAV3 or a mis-localization of the channel and CAV3. We found that CAV3 was equally expressed in AF- and CTRL-CMs and HCN4 co-localized with CAV3 (Supplementary material online, *Figure S4*).

## 3.6 AF-CMs display an increase in the L-type calcium current with a preserved calcium handling

Antiarrhythmic drugs aimed at controlling heart rhythm often target calcium currents and in particular L-type calcium currents. We thus evaluated the expression levels and functional properties of calcium channels. qPCR analysis revealed that CACNA1C and CACNA1D genes, responsible for the $I_{CaL}$ current, were similarly expressed in AF- and CTRL-CMs with CACNA1C as the prevalent isoform (*Figure 5A*). Electrophysiological analysis revealed instead that AF-derived cells show a significantly larger nifedipine-sensitive $I_{CaL}$ current than CTRL-CMs as shown by representative traces in *Figure 5B* and by the mean current density-voltage relations plotted in *Figure 5C* (top). All samples had similar activation and inactivation curves (*Figure 5C*, bottom).

Notably, the difference in $I_{CaL}$ density was already detectable at an early stage of differentiation (see Supplementary material online, *Figure S3*). We did not detect the expression of CACNA1G gene (*Figure 5A*) and indeed we could never record a T-type calcium current (data not shown).

To verify whether $I_{CaL}$ enhancement in AF-CMs might alter the excitation-contraction coupling mechanism, intracellular $Ca^{2+}$ handling was evaluated. In order to analyse only the primary effects on the intracellular $Ca^{2+}$ handling, cells were voltage-clamped and stimulated at 1 Hz and diastolic calcium ($Ca_{diast}$), $Ca^{2+}$ transient (CaT) amplitude, and sarcoplasmic reticulum (SR) $Ca^{2+}$content (CaSR) measured. In *Figure 5D* left, representative traces are shown together

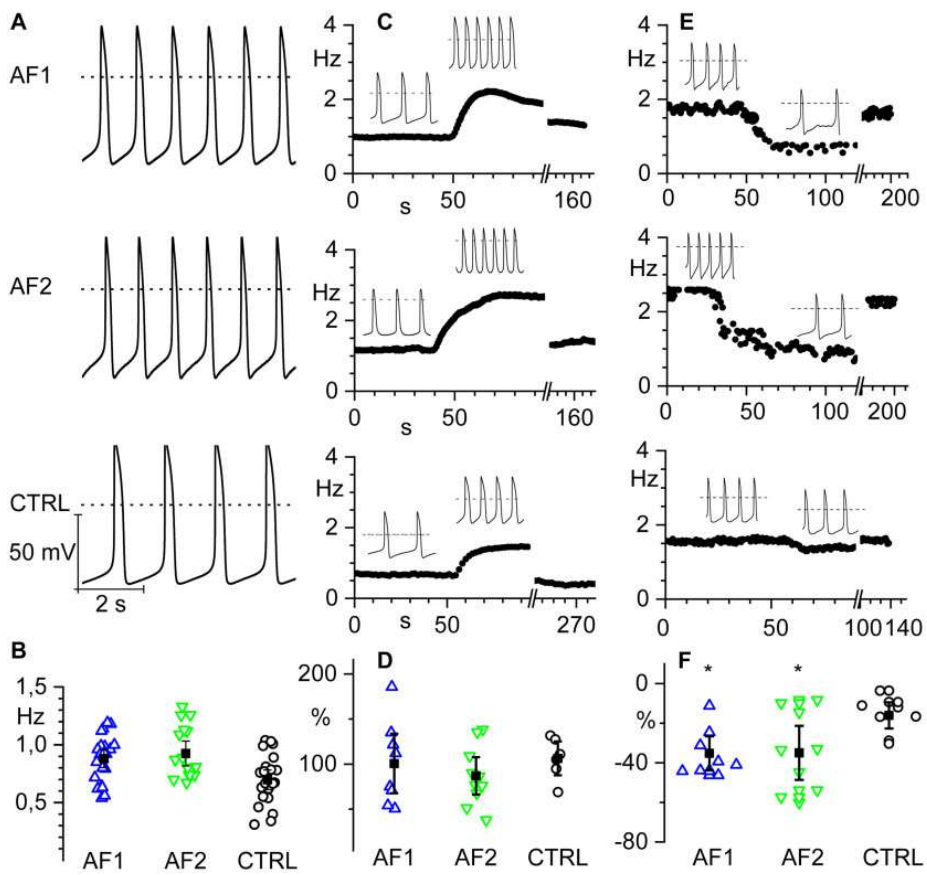


**Figure 3** hiPSC-CMs from AF patients show increased spontaneous firing rate and similar response to β-adrenergic stimulation compared to controls. (*A*) Representative voltage traces of spontaneous firing recorded from hiPSC-CM clusters from AF1 and AF2 patients and CTRL as indicated. (*B*) Scatter plot of the firing rate (open circles) and mean values (filled squares) of AF1 (0.88 ± 0.04 Hz, *n*/exp = 24/6), AF2 (0.99 ± 0.07 Hz, *n*/exp = 19/8), and CTRL (0.72 ± 0.05 Hz, *n*/exp = 25/9) hiPSC-CMs. (*C*) Time course of the firing rate of representative hiPSC-CM clusters from AF1, AF2, and CTRL from top to bottom, respectively; the black line indicates the time of isoproterenol perfusion. Insets show representative voltage traces before and during isoproterenol stimulation. (*D*) Dot plot graph of the percentage increase in firing rate after isoproterenol stimulation. (AF1 100.6 ± 16.5%; *n*/exp = 8/3, AF2 87.0 ± 10.4%; *n*/exp = 10/6, and CTRL 106.4 ± 9.4%; *n*/exp = 6/5). (*E*) Time course of the firing rate of representative hiPSC-CM clusters from AF1, AF2, and CTRL before, during, and after ivabradine superfusion. Insets show representative voltage traces before and during ivabradine stimulation. (*F*) Dot plot of the percentage decrease in firing rate after ivabradine superfusion (AF1 -35.2 ± 4.3%; *n*/exp = 8/3; AF2 -34.9 ± 6.8%; *n*/exp = 9/3; CTRL -16 ± 3.3%; *n*/exp = 8/3). Data were compared using nested one-way ANOVA *$P < 0.05$.

with the protocol. The analysis revealed that $Ca_{diast}$ was similar in all groups, while AF1-CMs showed an increased CaT amplitude and an increase in CaSR, compared to CTRL-CMs and AF2-CMs. AF2-CMs values were similar to those of CTRL-CMs. However, fractional release (FR) did not change among groups, suggesting a preserved SR stability in AF as in CTRL cells under resting condition (*Figure 5D*, right). The $Ca^{2+}$ parameters for the three separate CTRL lines can be found in Supplementary material online, *Table S5*. In agreement with these data, Western blot analyses on SERCA2 and phospholamban did not reveal any difference (Supplementary material online, *Figure S5*).

## 3.7 AF-CMs show longer action potential duration without changes in repolarizing currents

Once isolated, the great majority of hiPSC-CMs were quiescent but when stimulated (at 1 Hz) they fired action potentials. In *Figure 6*, the histograms of action potential duration (APD)90 obtained from AF1-, AF2-, and CTRL-CMs show that, despite the large variability of data, intrinsic to this cell model, AF-CMs have a wider distribution of APD (*Figure 6A*) with action potentials lasting as much as 300 ms, while none of the action potentials recorded from CTRL-CMs lasted more than 200 ms. In *Figure*

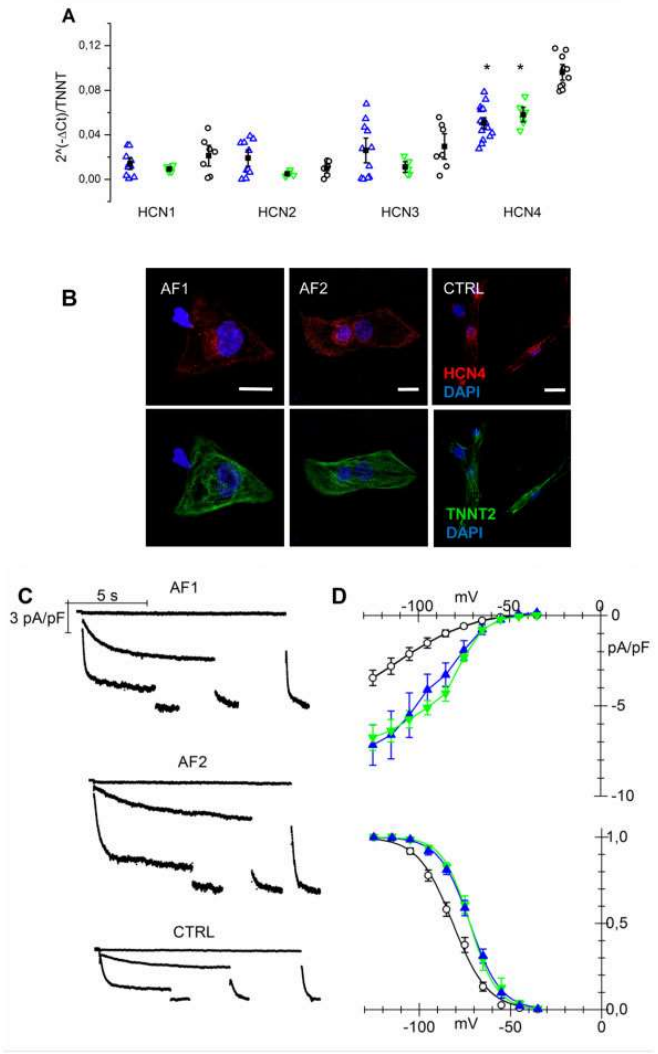


**Figure 4** $I_f$ current is increased in AF-CMs. (*A*) qPCR analysis of *HCN* isoforms normalized to troponin T expression at day 30 of differentiation. (*B*) Representative images of isolated AF1-, AF2-, and CTRL-CMs stained for HCN4 and cardiac troponin T (calibration bar = 10μm). (*C*) Representative traces of $I_f$ current density recorded at -35, -75, and -105 mV followed by a step at -125 mV from AF1-, AF2-, and CTRL-CMs. (*D* Top) Plot of mean $I_f$ current density voltage relation from AF1-CMs (blue triangles), AF2-CMs (green inverted triangles), and CTRL-CMs (white circles); Peak current density (at -125mV): AF1 = -7.17 ± 1.1*pA/pF, *n*/exp = 14/8; AF2 = -6.75 ± 0.72*pA/pF, *n*/exp = 13/3; CTRL = -3.45 ± 0.43 pA/pF, *n*/exp = 28/9. (Bottom) Mean activation curves of $I_f$ current from AF1-CMs, AF2-CMs, and CTRL-CMs (symbols as in top panel). $V_{1/2}$ values: AF1 = -71.2 ± 1.6* mV, *n*/exp = 21/6; AF2 = -72.7 ± 1.3* mV, *n*/exp = 15/4; CTRL = -81.5 ± 1.4 mV, *n*/exp = 28/9. Inverse slope factor values: AF1 = 8.4 ± 0.25, *n* = 21; AF2 = 7.5 ± 0.5, *n* = 15; CTRL = 9.5 ± 0.5, *n* = 28. *$P$ < 0.005. Data were compared using nested one-way ANOVA *$P$ < 00.5.

6*B* representative traces recorded from the three groups highlight the prolongation of APD in AF-CMs.

On average patient-derived cells displayed significantly longer APD at 30, 50, and 90% of repolarization (see *Table 1*), in agreement with the presence of a larger $I_{CaL}$.

Because of this APD prolongation, we decided not to categorize the CM population in nodal-, atrial-, or ventricular-like cells based on the APD ratio. Indeed, the classifications based on either the APD90/APD50[15] or the APD30–40/APD70–80 ratios,[16] revealed that 66.5 or 68.5% of CTRL-CMs seems to be atrial-like, while these percentages were substantially lower for AF1-CMs (52.5–47.5%) and AF2-CMs (48.7–41.0%). However, as apparent in the Supplementary material online, *Figure S6*, most of the AF-derived CMs fall close to the cut-off values separating atrial from ventricular cells. Since AF-CMs

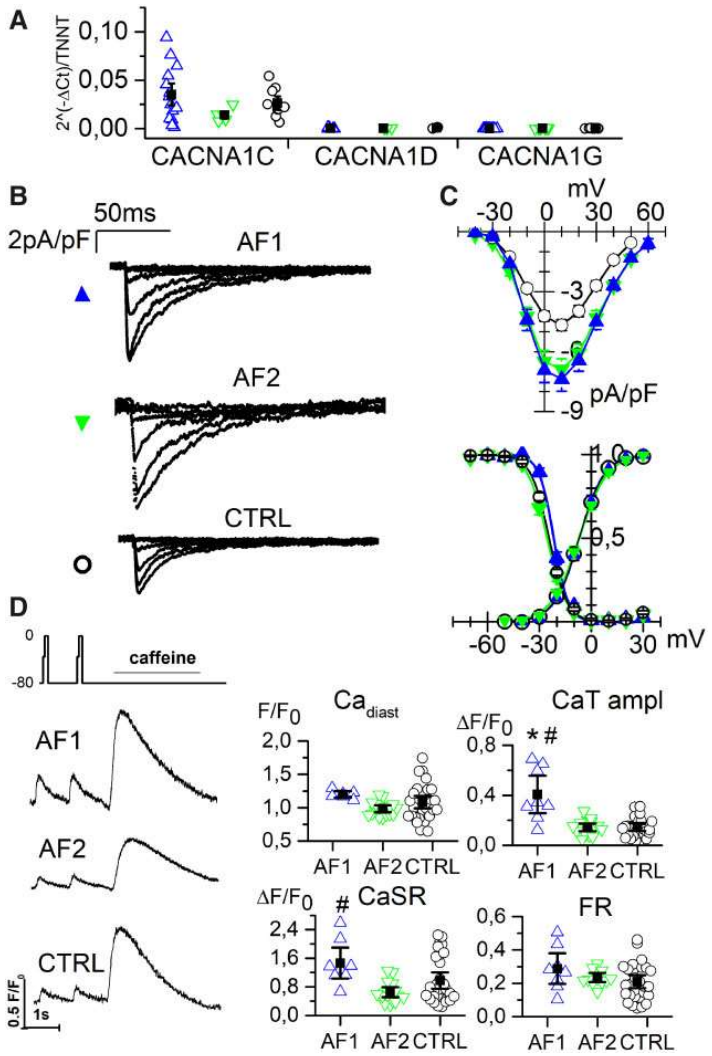


**Figure 5** L-type calcium current is increased in AF-CMs. (*A*) qPCR analysis of L-type calcium channel isoforms (1C, 1D) and T-type isoform (1G) expression normalized to troponin level at day 30 of differentiation. (*B*) Representative traces of $I_{CaL}$ current density recorded by 10 mV steps to the range of -40/+10 mV from AF1-, AF2-, and CTRL-CMs. (*C* Top) Plot of mean $I_{CaL}$ current density voltage relation from AF1-CMs (blue triangles), AF2-CMs (green inverted triangles), and CTRL-CMs (white circles). Peak current density (at 10 mV): AF1 = -7.4 ± 0.6*pA/pF, *n*/exp = 34/6; AF2 = -6.9 ± 0.5*pA/pF, *n*/exp = 30/8; CTRL = -4.7 ± 0.3 pA/pF, *n*/exp = 52/11. (Bottom) Mean activation and inactivation curves of $I_{CaL}$ current from AF1-CMs, AF2-CMs, and CTRL-CMs (symbols as in top panel) $V_{1/2}$ values of activation: AF1 = -6.6 ± 1.2 mV, *n*/exp = 29/6; AF2 = -6.8 ± 1.0 mV, *n*/exp = 31/8; CTRL = -7.4 ± 0.5 mV, *n*/exp = 51/11. $V_{1/2}$ values of inactivation: AF1 = -21.8 ± 0.7 mV, *n*/exp = 16/6; AF2 = -25.4 ± 0.8 mV, *n*/exp = 25/8; CTRL = -24.5 ± 0.5 mV, *n*/exp = 36/11. (*D*) Left, examples of calcium transients recorded from AF1-, AF2-, and CTRL-CMs applying the protocol shown. Right, dot blot graphs of the Ca diast, CaT amplitude, CaSR, and FR data in the three groups, as indicated. For values see Supplementary material online, *Table S5*. Data were compared using nested one-way ANOVA $^{*}P < 0.05$ vs. CTRL; $^{\#}P < 0.05$ vs. AF2.

show a larger $I_{CaL}$ and, as a consequence, a APD prolongation, a certain number of atrial-like cells would indeed pass the threshold and enter the 'ventricular-like' category even if they are not actually ventricular cells. Therefore, in this specific case, a selection of cells based on these criteria would obviously introduce a bias in the results.

Of the main repolarizing currents, we were able to analyse the delayed rectifier current $I_{Kr}$, whose density and kinetics did not differ between AF- and control-CMs (Supplementary material online, *Figure S7*). Under our differentiation conditions $I_{Ks}$ was absent while, in agreement with the depolarized resting potential, $I_{K1}$ was expressed at very low levels (data not shown), as previously reported.[17]

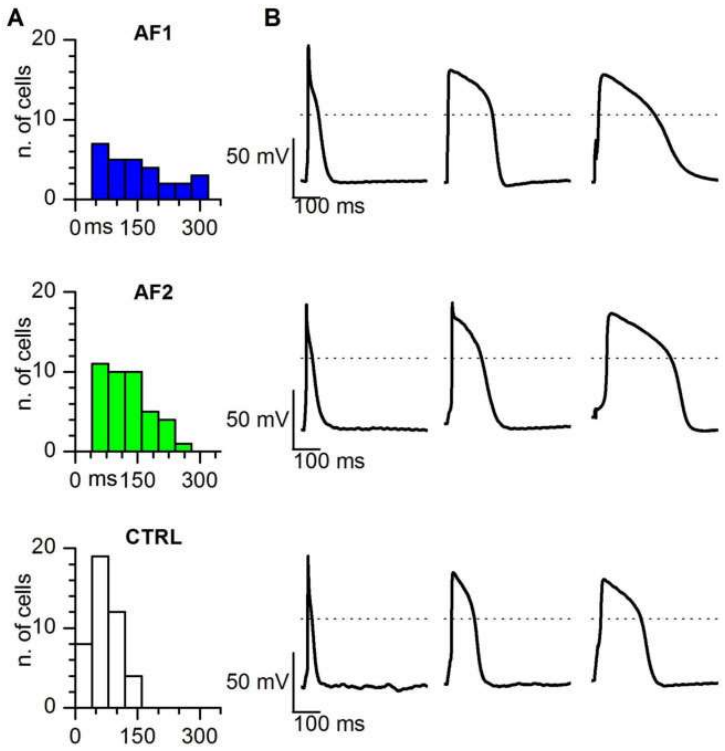


**Figure 6** Action potential duration is longer in AF-CMs compared to CTRL-CMs. (*A*) Histograms of the distribution of the APD90 in AF1, AF2, and CTRL cells, as indicated. Bin size = 40 ms. (*B*) Representative action potentials with the shortest (left), average (centre), and longest (right) APD90 recorded at 1 Hz stimulation in AF1 (top), AF2 (middle), and CTRL (bottom) CMs. Dashed lines indicate the 0 mV level.

**Table 1 Stimulated action potential analysis**

| | APD30 (ms) | APD50 (ms) | APD90 (ms) | MDP (mV) | dV/dT | APA (mV) |
|---|---|---|---|---|---|---|
| AF1 (*n*/exp = 40/11) | 80.2 ± 9.4* | 105.1 ± 11.2* | 137.3 ± 12.7* | -55.7 ± 1.4 | 57.6 ± 11.9 | 92.78 ± 3.9 |
| AF2 (*n*/exp = 39/12) | 71.2 ± 6.7* | 92.6 ± 8.2 * | 120.6 ± 8.8* | -58.8 ± 0.9 | 46.6 ± 6.6 | 93.9 ± 3.4 |
| CTRLs (*n*/exp = 61/13) | 39.9 ± 3.2 | 52.4 ± 3.7 | 74.1 ± 4.1 | -56.9 ± 0.9 | 41.3 ± 8.4 | 86.7 ± 2.4 |

Stimulated action potential properties of hiPSC-CMs paced at 1 Hz: action potential duration (APD30, 50, and 90), maximum diastolic potential (MDP), slope (dV /dT), and action potential amplitude (APA) *$P$< 0.05 by one-way ANOVA.

Because of the difference in the L-type calcium current, we evaluated the presence of calcium-dependent $K^+$ currents. Application of both apamin (100 nM), a specific blocker of the SK3 channel and charybdotoxin (100 nM), a blocker of the BK channel, did not have any effect on stimulated action potentials, thus suggesting a negligible expression of these channels (data not shown).

## 3.8 AF-CMs display larger delayed-after-depolarizations and an increased number of ectopic beats under stressful conditions

Finally, we evaluated if the electrophysiological alterations found in AF-CMs may be pro-arrhythmic by pacing both CTRL- and AF-CMs at 0.5 Hz and superfusing them with isoproterenol (100 nM) and E4031 (300 nM). This treatment, as expected, caused a significant prolongation of the APD and eventually the development of delayed-after-depolarizations (DADs) and/or triggered AP (*Figure 7A*). In *Figure 7B*, the proportion of CMs showing DADs, triggered AP, or the APD prolongation only (no events) for AF1, AF2, and CTRL-CMs is plotted. A significantly higher percentage of AF cells displayed triggered AP than CTRL cells, under this stressful condition (*Figure 7B*).

Furthermore, even if the proportion of cells with DADs was not different among the three cell populations, on average, DADs from AF1 and AF2 cells had a higher amplitude than those from CTRL cells (*Figure 7C*).

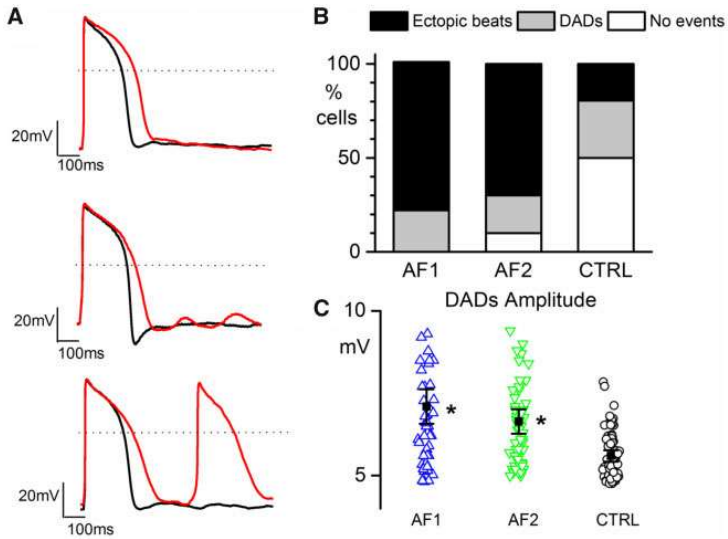


**Figure 7** AF-CMs are more arrhythmogenic. (*A*) Representative action potentials in Tyrode (black line) and during perfusion of 100 nM isoproterenol + 300 nM E4031 (red line) showing no events (top), DADs (middle), and ectopic beats (bottom) recorded from AF2-CMs paced at 0.5 Hz; dashed lines indicate the 0 mV level. (*B*) Plot of the percentage of cells showing ectopic beats (AF1 7 out of 9/3 cells/exp, 78.8%*; AF2 7 out of 10/3 cells/exp, 70.0%*; CTRL 7 out of 36/6 cell/exp, 19.5%), DADs (AF1 2 out of 9, 22.2%; AF2 2 out of 10, 20.0%; CTRL 11 out of 36, 30.5%), and no events (AF1 0 out of 9, 0%; AF2 1 out of 10, 10.0%; CTRL 18 out of 36, 50%). (*C*) Plot of DADs amplitude in AF1-CMs (blue triangles), AF2-CMs (green inverted triangles), and CTRL-CMs (white circles). Values are AF1 = 6.95 ± 0.62* mV, *n*/exp = 60/3; AF2 = 6.73 ± 0.26* mV, *n*/exp = 66/3; CTRL = 5.66 ± 0.16 mV, *n*/exp = 70/6. Percentage data were compared using Fisher's exact test, adjusting the *P*-value with Bonferroni correction. Amplitude data were compared using nested one-way ANOVA *$P < 0.05$.

# 4. Discussion

## 4.1 Whole exome screening reveals a complex genetic background in the siblings affected by AF

Although AF is the most prevalent cardiac arrhythmia in the developed world,[18] the pathophysiology of this complex heart rhythm disorder is still incomplete. The changes leading to the initial occurrence of AF are still elusive because (i) it is a progressive disease, (ii) human cardiac diseased tissues have undergone extensive remodelling, and (iii) no animal models fully recapitulate the disease.

The discovery of genetic forms of AF, linked to single gene mutations, and genome-wide association studies have improved our knowledge of causative mechanisms underlying AF.[1] Monogenic forms of AF are rare but, since the probability to develop AF increases in the presence of affected relatives,[2] a complex genetic background can be hypothesized. Indeed, we described a family in which three siblings, diagnosed with AF, share several mutations that can contribute to determine this arrhythmia.

Among these genes, only *ZFHX3* has been previously associated with AF in GWAS studies.[1] Nevertheless, the contribution of the other cardiac and non-cardiac mutated genes to AF onset is hard to dissect.

## 4.2 Generation of functional hiPSC-CMs overcomes the problems linked to genetic complexity of the disease

Because of this genetic complexity, an approach based on the evaluation of the contribution of each single mutation is clearly unfeasible and unlikely to provide a comprehensive description of the pathology. In order to estimate the full range of the effects of genetic alterations, we thus approached the problem from a functional point of view. We decided to use patient-derived hiPSCs to obtain a human cardiac cell model that possesses the entire patient's genetic background. Although the limitation linked to the well-known phenotypic immaturity of hiPSC-CMs,[19] these cells have already been widely used to study monogenic forms of cardiomyopathies and arrhythmias.[5] On the contrary, their use for modelling complex genetic pathologies is a rarely adopted approach.[20,21]

Here, we analysed for the first-time hiPSC-CMs from patients with a complex genetic form of AF. It must be emphasized that this model does not intend to recapitulate either the complexity of the atria or the entire clinical aspects of the disease but represents a novel tool to understand the molecular mechanisms underlying excitability alterations in diseased human CMs.

Because of the lack of healthy controls within the family and the unfeasibility to generate isogenic hiPSCs, due to the complex genetic alterations, AF clones were compared with four different lines generated from

unrelated healthy controls. These controls were chosen based on different variables that could potentially affect the comparison with CMs derived from our patients: sex (female and male), age (middle aged), and reprogramming procedure (retroviral infection from skin fibroblast and keratinocyte).

Once established the pluripotency of the clones, we choose those clones displaying a good cardiac differentiation capacity for further characterization. Our molecular data on the expression of the myosin heavy and light chain isoforms indicate that hiPSC-CMs are mainly immature/atrial rather than ventricular cells, independently of the cell line. Because a certain degree of maturation can be achieved in culture, especially in the electrical properties,[19] we decided to compare the AF and control lines at an early (15–20 days) and at a late stage of differentiation (30–35 days).

## 4.3 AF-CMs show a high beating rate due to increased $I_f$ and $I_{CaL}$ currents

We started to analyse the spontaneous beating rate of small aggregates and found that AF-CMs beat at a significantly higher rate than those from the controls, while no differences were found in the other parameters. Since the beating rate is physiologically modulated by the β-adrenergic/adenylate cyclase/cAMP pathway and an increase in rate may derive from an imbalance of this system, we tested the ability of the cells to respond to the β-adrenergic agonist isoproterenol. A saturating concentration of isoproterenol caused similar increases in rate in all the lines thus excluding differences in intracellular cAMP concentration as a cause of the higher rate in AF-CMs. AF onset is often associated with elevated heart rates. A few studies have indeed shown that initiation of post-operative AF, in patients undergoing coronary artery bypass surgery, was preceded by a significant increase in sinus rate mediated by either high levels of circulating norepinephrine[22] or by an unbalance of the autonomic tone towards the sympathetic input.[23]

The funny current is the pacemaker current critical to the initiation and regulation of cardiac pacemaker activity[10] and an increase in its contribution can indeed be arrhythmogenic.[24] The expression of f-channels (HCN1–HCN4) has been demonstrated also in non-pacemaker cardiac cells and in the working myocardium where it is abundant during fetal and neonatal life or under pathological conditions.[25] We found that the *HCN4* gene is the most expressed isoform in hiPSC-CMs and is less expressed in AF-CMs than in control-CMs. Direct recording of the $I_f$ current from isolated hiPSC-CMs, however, demonstrated a significant gain of function of f-channels due to both a rightward shift of the activation curve (both at early and late differentiation time-points) and an increase in current density (at later stages of differentiation) in AF compared to controls. Although molecular and functional data are discordant, they are in agreement with previous data from Stillitano *et al.*[26] These authors found that mRNA of HCN4 was down-regulated in chronic atrial fibrillation (cAF) CMs while the protein level tended to be higher. Although they have found similar current densities, the cAF cells displayed f-channels with activation curve shifted to more positive potentials than control cells by about 10 mV,[26] similar to our results.

Since CAV3 is known to interact with HCN4[13] and it has been already reported in pluripotent-derived CMs that different expression of CAV3 can shift $I_f$ activation curve,[14] we analysed the CAV3 expression both at mRNA and protein levels without detecting any difference between AF and CTRL groups (Supplementary material online, *Figure S4*).

A possible contribution of an increased $I_f$ current to abnormal automaticity in the atrium in paroxysmal AF has been described by Nattel and Dobrev[4] in a recent review.

Our results on L-type calcium current seem to be less in accordance with the evidence that AF induces a reduction of calcium currents. Indeed, atrial CMs derived either from patients with AF or from animal models of fast atrial pacing show a significant reduction of the effective refractory period (ERP) and of the $I_{CaL}$ current, compared to controls.[4,27] The reduction of calcium current and ERP seems, however, the consequence rather than the cause of AF and is attributable to the maladaptive remodelling of atrial tissue. In support of a role of an increased $I_{CaL}$ to AF, a few studies have shown that an initial calcium overload can be the stimulus that triggers maladaptive changes in atrial protein expression, based on the evidence that the calcium blocker verapamil prevents such remodelling.[28,29]

Albeit the magnitude of $I_{CaL}$ density has not been regularly associated with a higher probability to develop post-cardiac surgery AF,[30] it is interesting to note that Van Wagoner *et al.*[27] have shown that patients in sinus rhythm who developed AF following cardiac surgery had a significantly higher pre-operative $I_{CaL}$ density than those that did not experience post-operative AF. This observation, together with our data showing that CMs from AF patients display an $I_{CaL}$ twice as big as that of controls, is consistent with the concept that calcium overload may be an important factor in the initiation of AF, while $I_{CaL}$ depression is a consequence of AF.

## 4.4 AF-CMs display a prolonged APD and an increased susceptibility to arrhythmic activity

Despite the lack of any evident modulation of specific calcium channel isoforms, many mechanisms may contribute to an increased $I_{CaL}$ current such as, for example: miRNA-mediated modulation of expression,[31] altered channel trafficking/recycling,[32] channel oligomerization,[33] and modulation by accessory subunits.[34] The observed increase of the inward calcium current not accompanied by a counterbalancing increase in outward currents is expected to prolong the APD. Indeed, Sato *et al.*[35] has shown that an increased cooperative gating of L-type calcium channels increases current density and causes APD prolongation, in *in silico* experiments. Despite the large variability in APD duration typical of the CMs derived from hiPSCs (*Figure 6*),[17] we observed a significant prolongation of the APD in paced AF-CMs compared to controls. Usually, variability in APD is decreased by dividing CMs in nodal-, atrial-, and ventricular-like cell based on the slope of fast depolarization and APD ratio.[15,16] In our specific case, the selection of the cardiac cell type using the criteria based on the APD ratio is not applicable since APD is in fact exactly the parameter which is altered in AF-CMs, according to our results.

Although data on calcium handling do not indicate a significant instability of the SR, at least under 'basal' conditions (fixed stimulus duration and Tyrode solution), this situation may, however, be quite different in a scenario in which calcium dynamics are affected by the duration of the action potential and/or under the prevalence of sympathetic tone. It is known from the literature, for example, that the catecholamine-mediated trigger for inducing AF involves a significant increase of atrial $I_{CaL}$.[36] In agreement with this situation, our data on paced cells show that under stressful conditions (isoproterenol + E4031) AF-CMs are significantly more prone to generate arrhythmic events than CTRL-CMs, as indicated by larger DADs that more easily give rise to ectopic beats. The

underlying mechanism may be related to the very long action potential during β-adrenergic stimulation in AF-CMs in which the contribution of $I_{CaL}$ become more relevant than in CTRL-CMs. Together, our data suggest that the increase in $I_{CaL}$ and in $I_f$ current are likely to be the trigger for the initiation of AF.

### 4.5 Study limitations

Because sibling's parents are deceased, and their sons/daughters are still too young for ruling out AF, we could not derive hiPSCs from healthy relatives. We bypassed this limitation by comparing data with those obtained from at least three unrelated healthy controls, which displayed similar results among them. At the time we started to collect data, no protocols for selecting specifically atrial-like hiPSC-derived CMs were available. However, even if we did not select a specific hiPSC-CM atrial subpopulation, and despite the fact that the arrhythmogenesis due to a gain of function of inward currents can be more easily demonstrated in hiPSC-CMs lacking $I_{K1}$, we believe that the changes observed in $I_f$ and $I_{CaL}$ could induce triggered automaticity also *in vivo*, specifically in the atria, due to the fact that the adult atrium shows a significantly lower conductance than ventricle, near the resting potential.[3,37]

## 5. Conclusions

In conclusion, we provide in the present work the first demonstration that hiPSCs can be used as a cellular model of a human cardiac pathology with a complex genetic background. Independently of the genetic alterations, we demonstrated that hiPSC-CMs from two sisters with AF show a higher spontaneous rate of contraction and a gain of function of both the $I_f$ and the $I_{CaL}$ currents relative to CMs derived from any of four control individuals. We suggest that the increase of these depolarizing currents and other still unknown factors can contribute to the induction of abnormal automaticity in atrial cells and can thus be the triggering event of this specific type of AF.

## Supplementary material

Supplementary material is available at *Cardiovascular Research* online.


## Acknowledgements

We acknowledge Angela De Luca, Marialaura Serzanti, Giulia Savio, and Laura Tononi for technical assistance; Gianluigi Condorelli for helpful discussions; and Paola Aldegheri for the informations on patients' clinical history.

**Conflict of interest:** none declared

## Funding

E.C. was a recipient of the Giuseppe Marai INN fellowship. This work was supported by the European Research Council-ERC (2012-StG-311736-PD-HUMMODEL) to A.C., the Spanish Ministry of Economy and Competitiveness-MINECO (SAF2015-69706-R and BFU2016-80870-P), Instituto de Salud Carlos III-ISCIII/FEDER (Red de Terapia Celular - TerCel RD16/0011/0024), AGAUR (2014-SGR-1460) to A.R. and A.C. and CERCA Programme / Generalitat de Catalunya to A.R. Fondazione Cariplo (Grant numbers 2014-0822 to P.D.E.; 2014-1090 to A.B.; and 2014-0728 to D.D.).


## References


1. Tucker NR, Ellinor PT. Emerging directions in the genetics of atrial fibrillation. *Circ Res* 2014;**114**:1469–1482.
2. Mahida S, Lubitz SA, Rienstra M, Milan DJ, Ellinor PT. Monogenic atrial fibrillation as pathophysiological paradigms. *Cardiovasc Res* 2011;**89**:692–700.
3. Iwasaki YK, Nishida K, Kato T, Nattel S. Atrial fibrillation pathophysiology: implications for management. *Circulation* 2011;**124**:2264–2274.
4. Nattel S, Dobrev D. Electrophysiological and molecular mechanisms of paroxysmal atrial fibrillation. *Nat Rev Cardiol* 2016;**13**:575–590.
5. Dell'Era P, Benzoni P, Crescini E, Valle M, Xia E, Consiglio A, Memo M. Cardiac disease modeling using induced pluripotent stem cell-derived human cardiomyocytes. *World J Stem Cells* 2015;**7**:329–342.
6. Di Pasquale E, Song B, Condorelli G. Generation of human cardiomyocytes: a differentiation protocol from feeder-free human induced pluripotent stem cells. *J Vis Exp* 2013;**76**:e50429.
7. Nakahama H, Di Pasquale E. Generation of cardiomyocytes from pluripotent stem cells. *Methods Mol Biol* 2016;**1353**:181–190.
8. Aasen T, Raya A, Barrero MJ, Garreta E, Consiglio A, Gonzalez F, Vassena R, Bilic J, Pekarik V, Tiscornia G, Edel M, Boue S, Izpisua Belmonte JC. Efficient and rapid generation of induced pluripotent stem cells from human keratinocytes. *Nat Biotechnol* 2008;**26**:1276–1284.
9. Cordeiro JM, Nesterenko VV, Sicouri S, Goodrow RJ Jr, Treat JA, Desai M, Wu Y, Doss MX, Antzelevitch C, Di Diego JM. Identification and characterization of a transient outward K+ current in human induced pluripotent stem cell-derived cardiomyocytes. *J Mol Cell Cardiol* 2013;**60**:36–46.
10. DiFrancesco D, Noble D. The funny current has a major pacemaking role in the sinus node. *Heart Rhythm* 2012;**9**:299–301.
11. Baruscotti M, Barbuti A, Bucchi A. The cardiac pacemaker current. *J Mol Cell Cardiol* 2010;**48**:55–64.
12. DiFrancesco D, Tortora P. Direct activation of cardiac pacemaker channels by intracellular cyclic AMP. *Nature* 1991;**351**:145–147.
13. Barbuti A, Scavone A, Mazzocchi N, Terragni B, Baruscotti M, Difrancesco D. A caveolin-binding domain in the HCN4 channels mediates functional interaction with caveolin proteins. *J Mol Cell Cardiol* 2012;**53**:187–195.
14. Bosman A, Sartiani L, Spinelli V, Del Lungo M, Stillitano F, Nosi D, Mugelli A, Cerbai E, Jaconi M. Molecular and functional evidence of HCN4 and caveolin-3 interaction during cardiomyocyte differentiation from human embryonic stem cells. *Stem Cells Dev* 2013;**22**:1717–1727.
15. Moretti A, Bellin M, Welling A, Jung CB, Lam JT, Bott-Flügel L, Dorn T, Goedel A, Höhnke C, Hofmann F, Seyfarth M, Sinnecker D, Schömig A, Laugwitz K-L. Patient-specific induced pluripotent stem-cell models for long-QT syndrome. *N Engl J Med* 2010;**363**:1397–1409.
16. Ma J, Guo L, Fiene SJ, Anson BD, Thomson JA, Kamp TJ, Kolaja KL, Swanson BJ, January CT. High purity human-induced pluripotent stem cell-derived cardiomyocytes: electrophysiological properties of action potentials and ionic currents. *Am J Physiol Heart Circ Physiol* 2011;**301**:H2006–H2017.
17. Barbuti A, Benzoni P, Campostrini G, Dell'Era P. Human derived cardiomyocytes: a decade of knowledge after the discovery of induced pluripotent stem cells. *Dev Dyn* 2016;**245**:1145–1158.
18. Schnabel RB, Yin X, Gona P, Larson MG, Beiser AS, McManus DD, Newton-Cheh C, Lubitz SA, Magnani JW, Ellinor PT, Seshadri S, Wolf PA, Vasan RS, Benjamin EJ, Levy D. 50 year trends in atrial fibrillation prevalence, incidence, risk factors, and mortality in the Framingham Heart Study: a cohort study. *Lancet* 2015;**386**:154–162.
19. Robertson C, Tran DD, George SC. Concise review: maturation phases of human pluripotent stem cell-derived cardiomyocytes. *Stem Cells* 2013;**31**:829–837.
20. Brennand KJ, Simone A, Jou J, Gelboin-Burkhart C, Tran N, Sangar S, Li Y, Mu Y, Chen G, Yu D, McCarthy S, Sebat J, Gage FH. Modelling schizophrenia using human induced pluripotent stem cells. *Nature* 2011;**473**:221–225.
21. Laksman Z, Wauchop M, Lin E, Protze S, Lee J, Yang W, Izaddoustdar F, Shafaattalab S, Gepstein L, Tibbits GF, Keller G, Backx PH. Modeling atrial fibrillation using human embryonic stem cell-derived atrial tissue. *Sci Rep* 2017;**7**:5268.
22. Kalman JM, Munawar M, Howes LG, Louis WJ, Buxton BF, Gutteridge G, Tonkin AM. Atrial fibrillation after coronary artery bypass grafting is associated with sympathetic activation. *Ann Thorac Surg* 1995;**60**:1709–1715.
23. Dimmer C, Tavernier R, Gjorgov N, Van Nooten G, Clement DL, Jordaens L. Variations of autonomic tone preceding onset of atrial fibrillation after coronary artery bypass grafting. *Am J Cardiol* 1998;**82**:22–25.
24. Baruscotti M, Bucchi A, Milanesi R, Paina M, Barbuti A, Gnecchi-Ruscone T, Bianco E, Vitali-Serdoz L, Cappato R, DiFrancesco D. A gain-of-function mutation in the cardiac pacemaker HCN4 channel increasing cAMP sensitivity is associated with familial inappropriate sinus tachycardia. *Eur Heart J* 2017;**38**:280–288.
25. Cerbai E, Mugelli A. I(f) in non-pacemaker cells: role and pharmacological implications. *Pharmacol Res* 2006;**53**:416–423.
26. Stillitano F, Lonardo G, Giunti G, Del Lungo M, Coppini R, Spinelli V, Sartiani L, Poggesi C, Mugelli A, Cerbai E. Chronic atrial fibrillation alters the functional properties of If in the human atrium. *J Cardiovasc Electrophysiol* 2013;**24**:1391–1400.
27. Van Wagoner DR, Pond AL, Lamorgese M, Rossie SS, McCarthy PM, Nerbonne JM. Atrial L-type Ca2+ currents and human atrial fibrillation. *Circ Res* 1999;**85**:428–436.

28. Daoud EG, Knight BP, Weiss R, Bahu M, Paladino W, Goyal R, Man KC, Strickberger SA, Morady F. Effect of verapamil and procainamide on atrial fibrillation-induced electrical remodeling in humans. *Circulation* 1997;**96**:1542–1550.
29. Tieleman RG, De Langen C, Van Gelder IC, de Kam PJ, Grandjean J, Bel KJ, Wijffels MC, Allessie MA, Crijns HJ. Verapamil reduces tachycardia-induced electrical remodeling of the atria. *Circulation* 1997;**95**:1945–1953.
30. Workman AJ, Pau D, Redpath CJ, Marshall GE, Russell JA, Kane KA, Norrie J, Rankin AC. Post-operative atrial fibrillation is influenced by beta-blocker therapy but not by pre-operative atrial cellular electrophysiology. *J Cardiovasc Electrophysiol* 2006;**17**:1230–1238.
31. Barana A, Matamoros M, Dolz-Gaitón P, Pérez-Hernández M, Amorós I, Núñez M, Sacristán S, Pedraz A, Pinto A, Fernández-Avilés F, Tamargo J, Delpón E, Caballero R. Chronic atrial fibrillation increases microRNA-21 in human atrial myocytes decreasing L-type calcium current. *Circ Arrhythm Electrophysiol* 2014;**7**:861–868.
32. Ghosh D, Nieves-Cintron M, Tajada S, Brust-Mascher I, Horne MC, Hell JW, Dixon RE, Santana LF, Navedo MF. Dynamic L-type CaV1.2 channel trafficking facilitates CaV1.2 clustering and cooperative gating. *Biochim Biophys Acta Mol Cell Res* 2018;**1865**:1341–1355.
33. Dixon RE, Yuan C, Cheng EP, Navedo MF, Santana LF. Ca2+ signaling amplification by oligomerization of L-type Cav1.2 channels. *Proc Natl Acad Sci USA* 2012;**109**:1749–1754.
34. Kashihara T, Nakada T, Kojima K, Takeshita T, Yamada M. Angiotensin II activates CaV 1.2 Ca(2+) channels through beta-arrestin2 and casein kinase 2 in mouse immature cardiomyocytes. *J Physiol (Lond)* 2017;**595**:4207–4225.
35. Sato D, Dixon RE, Santana LF, Navedo MF. A model for cooperative gating of L-type Ca2+ channels and its effects on cardiac alternans dynamics. *PLoS Comput Biol* 2018;**14**:e1005906.
36. Workman AJ. Cardiac adrenergic control and atrial fibrillation. *Naunyn Schmiedebergs Arch Pharmacol* 2010;**381**:235–249.
37. Opthof T. The membrane current (I(f)) in human atrial cells: implications for atrial arrhythmias. *Cardiovasc Res* 1998;**38**:537–540.

## Translational perspective

This is the first time a human cellular model of atrial fibrillation (AF), based on the analysis of iPSC-derived cardiomyocytes from patients, is presented. Comparing cells from two sisters of a family with a complex genetic form of AF with those from healthy controls, we found peculiar alterations in two ion currents potentially involved in AF aetiology. Despite progresses in the management of AF, efficacy in maintaining sinus rhythm is modest. Human-based models elucidating the molecular mechanisms underlying AF will help define the best therapeutic approach. We propose to personalize AF therapy based on functional alterations found in patient-specific cardiomyocytes.